University of Alberta

Modelling of bypassed oil recovery in EOS compositional simulation

by

Bo Zhang

A thesis submitted to the Faculty of Graduate Studies and Research
in partial fulfillment of the requirements for the degree of

Master of Science

in

Petroleum Engineering

Department of Civil and Environmental Engineering

Spring 2014
Edmonton, Alberta

I dedicate this work to my parents who always encourage and support me.

Abstract

The local equilibrium assumption in the conventional composition simulation allows for no bypassing of oil at the sub-grid scale. Oil bypassing by gas, however, always occurs due to micro and macroscopic heterogeneities, gravity, and front instability.

This research presents an efficient two-step method to model bypassed oil recovery in multiphase compositional flow simulation of gas floods. The oil bypassing is first quantified by use of the dual-porosity flow with three dimensionless groups: the bypassed fraction, throughput ratio, and longitudinal Péclet number. To represent bypassed oil recovery in single-porosity flow, a new flow-based fluid characterization is applied to part of the heavy fractions of the fluid model used. Properties for pseudo components are determined based on the throughput ratio estimated in the dual-porosity flow. Case studies for various reservoir/fluid properties show that single-porosity flow with the new method successfully represents bypassed oil recovery observed in core-flooding experiments and fine-scale heterogeneous simulations.

Acknowledgements

First and foremost, I give my sincere appreciation to Dr. Ryosuke Okuno for his support and insightful ideas throughout the research. This work would not have been finished without his continued guidance and unlimited patience during the whole parts of this study. I am also grateful to my committee members, Dr. Juliana Leung and Dr. Huazhou Li for giving me constructive comments and feedbacks.

My gratitude goes to the funding by research grants from the Natural Sciences and Engineering Research Council of Canada (RGPIN 418266), Japan Petroleum Exploration Co., Ltd. (JAPEX), and Japan Canada Oil Sands Ltd. (JACOS).

I would like to thank Mr. Takeshi Hiraiwa，Dr. Koichi Suzuki and Dr. Tayfun Babadagli for technical comments on this research. I am also thankful to Mr. Ashutosh Kumar, Zhongguo Xu and Jindong Shi who gave me help to finish the thesis.

I am truly grateful to my parents, for their love, understanding, and support throughout my life. Finally, I would like to express my deepest gratitude to my girlfriend Xinming Li for her love and companion.

Table of Contents

List of Tables

List of Figures

List of Nomenclature

Roman Symbols

a	Attraction parameter in a cubic equation of state
a(T)	Temperature dependant attraction parameter
A_m	Dimensionless attraction parameter for mixtures
B	Bypassed fraction
B_m	Dimensionless covolume parameter for mixtures
b	Covolume parameter in a cubic equation of state
H	Reservoir thickness
k	Permeaiblity
k_{ij}	Binary interaction parameter matrix with elements k_{ij} for components i and j
L	Reservoir length
m	Parameter in the Peng–Robinson EOS (1978) defined in Equations 2.1.6 and 2.1.7
N_C	Number of components
N_{CV}	Characterized capillary number
N_{pe}	Péclet number
n	Number of fine grids in the corresponding coarse region
n_P	Number of phases
P	Pressure
P_C	Critical pressure
P_c	Capillary pressure
q	Injection rate
R_L	Aspect ratio
R	Universal gas constant
S	Saturation
S_i	Shale fraction in coarse grid block i
T	Temperature
T_C	Critical temperature
M	Mobility ratio
V	Volume
$\underline{V}$	Molar volume
v_j	Flow velocity of phase j
x_i	Composition for component i
x_j	Composition for component j
Z	Compressibility factor

Abbreviations

°API	API (American Petroleum Institute) gravity
BIP	Binary interaction parameter
CN	Carbon number
FCM	First contact miscible
EOS	Equation of state
MMP	Minimum miscibility pressure, bars
MW	Molecular weight, gm/mol
P_C	Pseudo component
PR	Peng-Robinson
PVI	Pore-volume injected

Greek symbols

α_{ij}	Alpha-factors for component i in phase j
$\alpha(T)$	Temperature dependence factor
Ω_a	Constant term in the attraction parameter of a cubic EOS
Ω_b	Constant term in the covolume parameter of a cubic EOS
ϕ	Porosity
φ_i	Fugacity coefficient for component i
ψ	ai / bi^2
γ_A	Attraction index
γ_B	Covolume index
Δ	Difference
ξ	Dimensionless length
τ	Dimensionless time

Subscripts/Superscript symbols

av	Average in vertical direction
al	Average in longitudinal direction
B	Bypassed fraction
e	Constant for permeability based on porosity
F	Flowing fraction
f	Index for permeability based on permeability
H	Introduced heavy oil components
i	Component i
j	Phase j
m	Mixture
Pen	Peneloux volume correction
T	Transverse direction

CHAPTER 1 INTRODUCTION

1.1 Problem description

Gas injection is a widely used method for enhanced oil recovery. Oil displacement by gas is explained fundamentally using 1-D dispersion-free flow in porous media, where the interaction of fluid flow with phase behaviour can yield multicontact miscibility between reservoir oil and injection gas. Therefore, design of gas injection processes often requires compositional simulation that can accurately model properties of equilibrium phases using a cubic equation of state (EOS). Compositional simulation attempts to consider complexities that exist in actual reservoir processes by increasing the generalization level of the conservation equations for multidimensional, multiphase, compositional flow in heterogeneous porous media. Fundamental assumptions always made, however, include the local equilibrium assumption, where fluids are completely mixed and at equilibrium within individual grid blocks. This assumption allows for no bypassing of oil at the sub-grid scale in gas injection simulation. The capacitance (bypassing) effects discussed in this research are defined as the phenomenon that oil is first stored in the stagnant volume and then gradually recovered by the mass transfer between the stagnant volume and flowing stream.

Oil bypassing by gas occurs at different scales because of micro and macroscopic heterogeneities, gravity, and front instability. Part of the bypassed oil is recovered by the crossflow between the bypassed and flowing regions. The transverse flux between the two regions can occur because of diffusion, dispersion, viscous forces, capillarity and gravity. The channelling of injection gas into high permeability layers significantly accelerates the breakthrough time. The gradual migration of oil from the bypassed region to the flowing region can lead to a longer tailing in effluent concentration profiles that significantly deviates from the simple diffusion model. These results indicate the importance of considering capacitance in compositional simulation to improve the oil recovery prediction.

Reservoir simulation can explicitly model the heterogeneities at the scale of grid block and greater. At the sub-grid scale, however, the local equilibrium assumption in simulation allows for no oil bypassing in gas floods. There are a few attempts to model oil bypassing by gas at the sub-grid scale. The alpha-factor method applies transport coefficients to adjust the flux term for different components in compositional simulation (Fayers et al. 1992). It is a purely numerical concept to adjust the flux for components, somewhat analogous to pseudo relative permeabilities to adjust the flux for phases (Barker et al. 2005). It is physically impossible to control the mass flux of a certain component in a phase

in a given region of a reservoir. It has been used to retain a desired amount of residual oil in history matching for predominantly single-phase flow (Barker and Fayers 1994; Christie and Clifford 1998; Ballin et al. 2002; Barker et al. 2005; Bourgeois et al. 2011, 2012). Its applicability in partial miscibility conditions is not fully understood. This is likely because the presence of more phases that are partially miscible yields more non-linearity and non-uniqueness in the history matching process.

Hiraiwa and Suzuki (2007) successfully applied the alpha-factor method to retain the residual oil in their gas injection simulations. They split the original oil components into two fractions; the mobile fraction with an alpha-factor of 1.0, and the immobile fraction with an alpha-factor of 0.0. The method of Hiraiwa and Suzuki (2007) is similar to the S_{orm} method that is currently available in commercial simulators. The S_{orm} method excludes the immobile oil from flash calculations and explicitly models the oil bypassed by the injection gas. The main disadvantage of the S_{orm} method is that no mass flux is allowed between the bypassed and flowing fractions so that the recovery of bypassed oil cannot be modelled.

The previous attempts mentioned above are unsuitable for modelling the recovery of bypassed oil for gas floods in partially miscible conditions in EOS

compositional simulation. This is fundamentally because the mass conservation equations used in the conventional compositional simulation do not consider the bypassed fraction and the mass transfer between the bypassed and flowing fractions. As discussed in the publications (Burger and Mohanty 1997; Barker et al. 2005), compositional flow using the dual-porosity method is likely the most straightforward representation of oil bypassing and recovery of the bypassed oil in gas injection. However, it can be unacceptably time-consuming to build and run a dual-porosity model for field-scale applications (Coats et al. 2007).

1.2 Research objectives

The optimum level of gas enrichment or pressure for gas floods depends on the level of capacitance and the recovery of bypassed oil. Ideally fine-scale field simulation needs to be conducted to determine the optimum for each field. However, the fine-scale simulation which can explicitly model the capacitance effects is too time consuming to be acceptable. An improved method for modelling the capacitance effects at the sub-grid scale is needed to replace the fine-scale field simulations of gasfloods in conventional compositional simulation. The transverse mass flux between the bypassed region and flowing region plays an important role in the recovery of gasfloods. It needs to be measured in

experiments and properly represented in simulations. Advancement in modelling capacitance at the sub-grid scale will significantly improve the design of gas floods.

The main objective of this research is to develop an efficient method to model the recovery of bypassed oil in the multiphase compositional simulation with no change in the governing equations. This method should be able to reproduce the characteristics of fluid flow in a dual-porosity model (dual-porosity flow or DPF). The dual-porosity method in this research successfully characterizes and quantifies the capacitance with the bypassed fraction and throughput ratio introduced in this research. A fluid characterization method applied in single-porosity flow (SPF) is then proposed to reduce the computational time. It considers the sub-grid scale capacitance effects by correcting the fluid model in a SPF. Case studies of n-alkanes and real reservoir fluids are given to present that the recovery of bypassed oil in the DPF can be quantitatively reproduced using a SPF with fluid model correction. Simulation results indicate that the efficient modelling of bypassed oil recovery with the local equilibrium assumption (i.e., using single-porosity simulation) for field-scale applications can be done in two steps: 1. Characterization of representative flow behaviour using a 1-D DPF model, and 2. Correction of the fluid model for the DPF characteristics.

This research proposed a systematic two-step procedure to model the sub-grid scale capacitance effects that exist in gas floods but cannot be modelled in conventional composition simulation. The first step is to quantify the capacitance by use of a dual-porosity flow with the bypassed fraction and throughput ratio. The flow-based characterization method is then applied to model the sub-grid scale heterogeneity in conventional compositional simulation with the local equilibrium assumption. The attraction and covolume parameters for the introduced pseudo heavy components are adjusted to account for the faster displacement front and longer tailing in the effluent concentration profile in the presence of capacitance effect. The new fluid characterization method requires no change in the governing equations and substantial computational time is saved compared to a fine-scale geological model for field applications.

1.3 Organization of thesis

This thesis is consisted of seven chapters. Chapter 1 gives the motivation and objective for this research. Chapter 2 summarizes the background knowledge of this research to model the oil bypassing in gas floods. The limitation of the finite-difference compositional simulation in modelling the sub-grid scale heterogeneity is explained. The literature survey for the capacitance effects in experimental and field observations and modelling of the capacitance effect is also

included. The uncertainties in EOS fluid model are given to explain why the proposed fluid characterization method can be used to characterize the capacitance effects in reservoirs with reasonable influence in phase behavior predictions.

Chapter 3 presents that the dual-porosity flow in conventional compositional simulation is applied to reproduce the flow characteristics of the capacitance effects in gas floods. The highlight of this chapter is to quantify the capacitance effects by three dimensionless groups: bypassed fraction, throughput ratio and longitudinal Péclet number. The 1-D dual-porosity flows are successfully applied to match the core flooding data for different gas floods. The capacitance effects in the fine-scale heterogeneous reservoir are well characterized by use of the coarse-scale simulation with the DPF.

Chapter 4 proposes a flow-based fluid characterization method in the SPF to model the capacitance effects for n-alkanes mixtures. The original EOS fluid model is split into two fractions: one with original components to represent the swept oil and the other with introduced pseudo heavy components to compose the bypassed oil. The correlations for n-alkanes on the basis of molecular weight (MW) are used to generate the EOS parameters for the introduced pseudo heavy components. The relationships between the two adjust parameters in the flow-based fluid characterization method and the throughput ratios characterized in

the DPFs are studied for empirical predictions from core floods data to field-scale simulations.

In chapter 5, the flow-based fluid characterization method is extended to real reservoir fluids. The directly adjustment of the attraction and covolume parameters for the introduced pseudo heavy components avoids the restrictions that only n-alkanes mixtures can be used. The adjustment parameters in the fluid characterization method exhibit an empirical linear relationship with different throughput ratios. The effects on phase behaviour are minimized within the uncertainties in fluid model by use of the appropriate tuning strategy and volume-shift parameters for the introduced pseudo heavy components. A case study shows that the component propagation speed in the SPF with corrected EOS is matched with the DPF which explicitly models the capacitance effect.

Chapter 6 proposes a two-step method on the basis of the DPF and flow-based characterization method in the SPF. Case studies of core flooding data and fine-scale heterogeneous simulations considering gravity forces are investigated for different reservoir and fluid properties. It is observed that the effects of the proposed fluid characterization method on the phase behaviour in P-T-x space are within the uncertainties in fluid models.

Chapter 7 summarizes conclusions and limitations for the proposed two-step method to model the sub-grid scale capacitance effects. Potential topics and recommendations for further research are also identified and discussed.

CHAPTER 2 BACKGROUND

This chapter provides the required basic knowledge for this research. Section 2.1 gives a brief introduction for the determination of the miscibility in gas flooding process. The limitations of finite-difference compositional simulation in modelling sub-grid scale heterogeneity are explained in section 2.2. Section 2.3 summarizes the capacitance effects discussed in experiments and field observations. The previous attempts in modelling the recovery of bypassed oil are presented in section 2.4. Section 2.5 explains the cubic equation of state (EOS), mixing rules and volume-shift parameters used to model the compositional and volumetric phase behaviour in simulations. The reasons for the uncertainties in fluid EOS model are explained in section 2.6. Finally, the correlations of T_C, P_C and ω proposed by Kumar and Okuno (2013) are introduced in section 2.7. The correlations are used to generate the EOS parameters for the introduced pseudo heavy components on the basis of the increased MW in the flow-based fluid characterization method.

2.1 Miscibility in gas floods

Gas injection is a widely used method for enhanced oil recovery since 1950. Oil displacement by gas is explained fundamentally using 1-D dispersion-free flow in porous media, where the interaction of fluid flow with phase behaviour can yield

multicontact miscibility between reservoir oil and injection gas (Johns 1992; Dindoruk 1992; Orr 2007).

The multicontact miscible displacement occurs in a ternary system when either the initial tie line or the injection tie line is a critical tie line, a tie line of zero length that is tangent to the bimodal curve at the critical point. Condensing gas drives are multicontact miscible when the injection gas tie line is the critical tie line, and vaporizing gas drives are multicontact miscible when the initial oil tie line is critical. The composition of the injection gas is easy to be adjusted in field applications, so it is easy to determine minimum enrichment for miscibility (MME) for condensing gas drives. In contrast to condensing gas drives, it is generally impossible to adjust the composition of the initial oil in oil field in vaporizing gas drives. As a result, the pressure is adjusted to find the minimum miscibility pressure (MMP) for a given injection gas composition.

Figure 2.1 gives a ternary diagram and marks the corresponding MME for given temperature and pressure. The partially miscible conditions used in this research are the conditions when reservoir pressure is below MMP or the composition of the injection gas is leaner than MME. Most of the gas injection processes are in partially miscible conditions where multiphase flows occur in the presence of dispersion.

2.2 Limitations of finite-difference compositional simulation

Design of gas injection process often requires compositional simulation that can accurately model properties of equilibrium phases using a cubic equation of state (EOS). Compositional simulation attempts to consider complexities that exist in actual reservoir processes by increasing the generalization level of the conservation equations for multidimensional, multiphase, compositional flow in heterogeneous porous media.

The component conservation equations are not possible to be solved in individual channels because the phase boundaries in flow channels are extremely tortuous and their locations are unknown in porous medium. The practical way of avoiding this difficulty is to apply the continuum assumption to the flow so that a point within a permeable medium is associated with a representative elementary volume (REV) (Lake 1989).

The REV is defined as the smallest volume over which a measurement can be made that will yield a representative value of the whole porous medium (Hill 1963). The definitions including porosity, permeability, tortuosity, and dispersivity for the porous medium, are made locally smooth on the basis of REV. For volumes smaller than the REVs, a representative property cannot be defined. Under the continuum assumption, the locally discontinuous porous medium is

approximated to a locally smooth porous medium. The component conservation equations now apply for each REV and the problem of determining the phase boundaries in flow channels no longer exists.

A microscopic view of pores and grains within a porous medium is used to understand the REV scale by Lake (1989). Figure 2.2 illustrates a cube of small volume placed within a porous medium. The porosity in the cube is defined as the pore volume within the cube divided by the bulk volume of the cube. The volume of the cube is increased from a point with infinite small volume. If the cube volume is small enough, the porosity will be either unity or zero depending on its original location. As the cube volume increases, the porosity changes unpredictably as grains and pores are included inside the cube as presented in Figure 2.3 by Lake (1989). The porosity varies in microscopic domain until the cube volume increased to REV. The porosity approaches a constant value of porosity at the REV scale. Above the REV size, the cube porosity remains constant at the scale of the porous medium. However, the cube porosity is affected by layering and other heterogeneities if the cube volume is increased further. This layering and heterogeneities are defined as the macroscopic heterogeneities in this research.

The volume of gird block in finite difference simulation should be larger than the REV size so that the continuum assumption can be used for component conservation equation. The microscopic heterogeneity in pore structures reported in the literature cannot be modelled by use of the finite-difference simulation with the continuum assumption. That is part of the reasons that the conventional compositional simulation might overestimate the oil recovery in gas floods because the bypassed oil remaining in the dead-end pore volume is vaporized in the simulations.

In field-scale simulations, the grid block size is usually larger than the porous medium domain to save the computational time. The local equilibrium assumption is always made in conventional finite-difference simulation. This assumption allows for no heterogeneity at the sub-grid scale because fluids are assumed to be completely mixed and at equilibrium within individual grid blocks. Fine-scale geological model with a grid block small enough to include the macroscopic heterogeneity is the most straightforward way to model the recovery of bypassed oil in gas floods. However, the computational time would be too large to be accepted. The limitation in modelling the macroscopic heterogeneity at the sub-grid scale is due to the local equilibrium assumption in conventional compositional simulation.

As explained in this section, the continuum and local equilibrium assumption make it impossible to model the capacitance effects in gas floods due to microscopic and macroscopic heterogeneity, respectively. However, the oil bypassing (capacitance) effects are widely observed in both experiments and field observations according to the literature listed in section 2.3.

2.3 Investigations of oil bypassing (capacitance) effects in literature

Oil bypassing by gas occurs at different scales because of micro and macroscopic heterogeneities, gravity, and front instability. Microscopic oil bypassing is related to the pore structures with bimodal or wide pore-size distributions (Baker 1977; Salter and Mohanty 1982; Dai and Orr 1987; Bahralolom et al. 1988; Spence and Watkins 1980). Campbell and Orr (1985) showed that the microscopic bypassing can also occur without actual dead-end pores, where oil in pores that are perpendicular to the local flow direction is not swept and can be recovered by the mass transfer with adjacent flowing streams. Shielding of oil by water films in pores can increase the level of microscopic oil bypassing (Baker 1977; Gardner and Ypma 1984; Campbell and Orr 1985). Gas channelling creates slow-flow or stagnant region in heterogeneous oil reservoirs. Thin shales with a thickness of only a few inches can cause marked oil bypassing by gas (McGuire et al. 1995).

The degree of miscibility between oil and gas also affects the level of oil bypassing (Burger and Mohanty 1997; Mohanty and Johnson 1993). Experimental results in Burger et al. (1994) indicate that the bypassed oil fraction is less significant for less miscible processes. They stated that the optimum gas enrichment can be below the minimum miscibility enrichment for a secondary gas flood with a high-viscosity ratio, where the sweep and local displacement efficiency could take a balance. Partially miscible (near-miscible) displacement of oil can result in efficient recovery of bypassed oil (Burger et al. 1994) due to better sweep efficiency compared to miscible floods. In the mechanistic investigation of bypassed oil recovery in CO_2 injection by Khosravi et al. (2014), maximum recovery is achieved in near-miscible tests when CO_2 is injected in the flowing region because swelling and vaporization enhances oil recovery significantly. Moreover, it is often not economical or technically feasible to inject a gas that is miscible with oil as mentioned by Al-Wahaibi et al. (2007). In this research, we focus on partially miscible conditions where interactions between multiphase behaviour and capacitance are not fully investigated before.

Part of the bypassed oil can be recovered by mixing of fluids between the bypassed and flowing regions (Baker 1977; Salter and Mohanty 1982; Stern 1991; Burger et al. 1994, 1996; Burger and Mohanty 1997; Pande and Orr 1994a, b).

The transverse flux between the two regions can occur because of diffusion, dispersion, viscous forces, and capillarity. Gradual migration of the oil from the bypassed region to the flowing region can lead to significant deviations in effluent concentration profiles. High residual oil saturations were observed in the flowing region due to the interaction of phase behaviour with oil bypassing (Gardner and Ypma 1984; Campbell and Orr 1985; Dai and Orr 1987; Bahralolom et al. 1988; Mohanty and Johnson 1993). These results indicate the importance of considering the recovery of bypassed oil.

2.4 Literature review on modelling capacitance

Capacitance effects in a mathematical model to reproduce core flooding data have been studied since late 1950s. The convection-dispersion model developed by Aronofsky and Heller (1957) in explaining the mixing of flowing miscible fluids was confirmed to be inaccurate in reproducing the capacitance effects in core flooding experiments.

Deans (1963) proposed a capacitance model of single-phase flow in which the pore space was divided into the flowing and stagnant volumes and used lumped mass transfer coefficients to model the mass flux between the two volumes. Coats and Smith (1964) included a dispersion term in the flowing fraction in Dean's model and matched the experimental core flooding data by use of their

capacitance-dispersion model. The capacitance effects are observed as earlier breakthrough time and a longer tailing in the effluent concentration profile as mentioned by Barker (1977). Three key dimensionless groups in the dispersion-capacitance model are defined as flowing fraction, Péclet number and Damköler number by Dai and Orr (1987). The Damkhöler number is the dimensionless mass-transfer rate expressed as a ratio of characteristic times for the transverse mass transfer and longitudinal convection.

Batycky et al. (1982) developed an algorithm that provided rapid and accurate determination of the three dimensionless groups to minimize the error criteria in the Laplace-transform domain and real-time domain. The sensitivity of the three dimensionless groups on effluent concentration profile was also investigated. Salter and Mohanty (1982) separated the original bypassed fraction into dendritic and isolated fraction by whether they have contact with the flowing fraction. The isolated fraction is completely surrounded by water so no mass flux can occur between the isolated oil and flowing stream. Dai and Orr (1987) extended the four parameter model by Salter and Mohanty in two phase displacements by use of a pseudo-ternary phase diagram fitted to experimental data to represent the phase behaviour in the simulations. The dispersion-capacitance model was also used to

characterize the gas trapping in foam floods in core flooding experiments by Smith and Jikich (1994) and Nguyen et al. (2009).

The capacitance-dispersion model was successfully applied to capture the capacitance effects in core scale experiments, but the applicability in the field-scale is uncertain because of the scale dependency of the dimensionless groups as mentioned in many publications (Barker 1977; Bartycky et al. 1982; Brigham 1974; Bretz and Orr 1987 and Jasti et al. 1988). Applications of the capacitance model in field-scale models showed that the longer tailing observed in laboratory tests using short cores are not as pronounced in a longer system. The resulting flowing fraction is larger, and the Damköler number is smaller at the field-scale with a longer system length. The dispersion-capacitance model is not successfully implemented in conventional composition model. The local equilibrium assumption is made for individual grid blocks so we cannot split the dead-end pore volume from the flowing cell to use the dispersion-capacitance model.

Reservoir simulation can explicitly consider the level of heterogeneity at the scale of grid blocks or greater. However, detailed geological models in the field-scale would be unacceptably time consuming (Salehi et.al. 2013). At the sub-grid scale, the local equilibrium assumption in simulations allows for no

capacitance in gas injection process. Several papers demonstrated that the simulation results with the local equilibrium assumption could be erroneous compared to core floods data (Gardner and Ypma 1984; Nghiem 1997; Al-Wahaibi et al. 2007). Compositional simulation is necessary for accurate representation of the fluid flow associated with phase behaviour to determine the optimal enrichment or injection pressure (Burger et al. 1994 and Salehi et al. 2013). A few previous attempts to model the capacitance effects at the sub-grid scale in reservoir simulations are discussed in the following section.

Unstable fluid propagation speed is modelled empirically, statistically and numerically for capacitance effects caused by viscous fingering in several publications (Koval 1963; Todd and Longstaff 1972; Yong 1990; Fayers et al. 1992; Blunt and Christie 1994). The extended empirical model has been successfully applied in conventional compositional simulator in both continuous gas injection and water-alterative-gas (WAG) process by generating pseudo relative permeabilities and alpha-factors by Barker and Evans (1995). However, it is not mechanistically sound, and the accuracy of the empirical models is less satisfactory without the diffusive term in large amplitude heterogeneities with short correlation length (Fayers et al. 1992).

Diffusion and dispersion in porous media have been studied and tried to model the mixing of fluids in both pore and field scale (Arya et al. 1988; Garmeh et al. 2009; Abraham et al. 2010). However, Coats and Smith (1964) demonstrated that the dispersion term alone was confirmed to be insufficient to reproduce the experimental asymmetrical effluent concentration profile. Effective dispersion coefficients are introduced to account for capacitance effects by matching the mixing zone length in the capacitance-dispersion model (Bretz and Orr, 1987; Mohanty and Johnson, 1993). This method is only effective in the reservoirs where the bypassed fraction is small and transverse mass flux rate is sufficiently high. The asymmetrical effluent concentration profile representing the capacitance effect cannot be reproduced by use of simple diffusion/dispersion model. Comparisons were conducted between the Coats-Smith model and the porous-spheres model at lengths of 20 and 140 m by Bretz and Orr (1987). The paper presented that an effective dispersion coefficient is not suitable to match the experimental data even at relatively large displacement lengths where the corresponding Damköler number is relatively large.

The S_{orm} method is available in commercial simulators to explicitly model the bypassed oil in reservoirs. It excludes the immobile oil from flash calculation so that the main disadvantage of this method is that no mass flux is allowed between

the bypassed and flowing regions. Lizuka et al. (2013) historically matched the corefloods experiments by use of the S_{orm} method in 1-D simulation and 2-D fine-scale simulation without the S_{orm} method. As the bypassed oil is unrecoverable in the S_{orm} method, it is equivalent to assign zero Damköler number in the dispersion-capacitance model.

The alpha-factor method was proposed by Barker and Fayers in 1994. The transport coefficients (alpha factors) are used to adjust the components' flux in compositional simulation. It is a purely numerical concept because controlling the mass flux of a certain component in a phase in a given region of the reservoir is physically impossible (Barker et al 2005). The Alpha-factor method alone can only be applied in single phase dominant flow (Ballin et al. 2002) and pseudo relative permeability is required in partially miscible conditions where the presence of more phases yields more non-linearity and non-uniqueness for the alpha factors. Christie and Clifford (1998) combined the alpha-factor method with streamline techniques and re-calculate the boundary conditions for certain grid blocks to deal with the potential error in multidimensional cases. The alpha-factor method was used to improve the accuracy in matching experimental data for MCM displacements (Al-Wahaibi 2007) and recently a thermodynamically consistent

alpha-factors on the basis of non-equilibrium approach was also developed for existing simulators (Salehi et al. 2013).

The failure of the previous attempts is mainly because the mass conservation equations in conventional compositional simulation do not consider the bypassed fraction and the mass flux between the bypassed regions and flowing regions. The dual-porosity method introduced by Coats et al. (2007) is the most straightforward representation of oil bypassing and the recovery of the bypassed oil in gas floods in commercial simulators as mentioned by Barker et al. (2005). The applicability of dual-porosity method in WAG process was also tested by tracking the changes in composition of the trapped and mobile fluids (Brown et al. 2013). However, the dual-porosity model for the field-scale application might be too computational expensive to be accepted. The detailed procedure of the application for the dual-porosity method in conventional composition simulation is not shown in the previous literature. In chapter 3, we define the three dimensionless groups to quantify the capacitance effects in the dual-porosity flow.

2.5 Cubic Equation of state, mixing rules and volume-shift parameters

The EOS method is typically used for modelling the equilibrium phases for high pressure mixtures of hydrocarbons in gas flooding process because of its accuracy and simplicity. The vapor and liquid phases are described through the

fugacity coefficients by use of an EOS. The most important assumption in a cubic EOS is that molecules are spherical so that it is possible to separate the effects of free volume and molecular interactions.

Before Van der Waals derived the first EOS, he researched on the phase behaviour of a pure component. With the increase of pressure, the molar volume approaches an asymptotical value for the pressure going towards infinity. This asymptotical value of the molar volume for a pure component is the covolume parameter (b). The attraction force (a) between molecules is found to be proportional to $1/\underline{V}^2$. Based on the defined attraction and covolume parameter, he proposed the final form of the van der Waals EOS:

$$P = (RT)/(\underline{V} - b) - a/\underline{V}^2, \qquad (2.5.1)$$

where $\underline{V}$ is the molar volume, and R is the gas constant. The first term $(RT)/(\underline{V} - b)$ is the free volume term and the second term $a/\underline{V}^2$ represents the interaction term.

The accuracy of those cubic EOSs is determined by the empirically determined parameters and cancellation of errors between the attraction and covolume parameters. Different types of EOS are proposed after the van der Waals EOS based on the attraction and covolume parameters to improve the accuracy in predicting the vapor pressure or phase properties. The PR EOS (1976)

is applied for the phase behaviour modelling for compositional simulation throughout this thesis. The final form of the PR equation is

$$P = (RT)/(\underline{V} - b) - a(T)/\left[\underline{V}(\underline{V} + b) + b(\underline{V} - b)\right], \quad (2.5.2)$$

where the attraction (a) and covolume parameter (b) are calculated based on the critical pressure, temperature and acentric factors for a fixed temperature. The equations for attraction and covolume parameter are shown as follows:

$$a(T) = \Omega_a R^2 T_C^2 \alpha(T)/P_C, \quad (2.5.3)$$

$$b_i = \Omega_b R T_C/P_C, \quad (2.5.4)$$

$$\alpha(T) = \left[1 + m\left(1 - \sqrt{T/T_C}\right)\right]^2, \quad (2.5.5)$$

$$m = 0.37464 + 1.54226\omega - 0.26992\omega^2 \quad , \quad \text{for} \quad \omega < 0.49, \quad (2.5.6)$$

$$m = 0.37464 + \omega(1.48503 + \omega(-0.16442 + 0.01667\omega)), \text{ for } \omega > 0.49. \quad (2.5.7)$$

To extend a cubic EOS to mixtures of N_C components, the van der Waals mixing rules are used to generate the attraction and covolume parameters used in the PR EOS:

$$a_m = \sum_{i=1}^{Nc} \sum_{j=1}^{Nc} x_i x_j a_{ij}, \quad (2.5.8)$$

$$b_m = \sum_{i=1}^{Nc} \sum_{j=1}^{Nc} x_i x_j b_{ij}. \quad (2.5.9)$$

The combining rule for a_{ij} is:

$$a_{ij} = \sqrt{a_i a_j}\left(1 - k_{ij}\right), \quad (2.5.10)$$

where k_{ij} is the binary interaction parameter (BIP) between components i and j.

The fugacity coefficients for component i in a mixture using the PR EOS is:

$$\ln \varphi_i = \frac{B_i}{B_m}(Z-1) - \ln(Z-B_m) - \frac{A_m}{(\delta_1-\delta_2)B_m}\left(\frac{2\sum_{j=1}^{N_c} x_j A_{ij}}{A_m} - \frac{B_i}{B_m}\right) \ln\left[\frac{Z+\delta_1 B_m}{Z+\delta_2 B_m}\right], \tag{2.5.11}$$

where $\delta_1 = 1 + 2^{0.5}$ and $\delta_2 = 1 - 2^{0.5}$. The definitions for the dimensionless attraction and covolume parameters are

$$A_m = a_m P/(RT)^2, \tag{2.5.12}$$

$$A_{ij} = a_{ij} P/(RT)^2, \tag{2.5.13}$$

$$B_m = a_m P/(RT)^2. \tag{2.5.14}$$

To improve the liquid density predictions in the SRK EOS, Peneloux presented a modification to the SRK EOS with a volume-shift parameter in 1982. The SRK EOS with the Peneloux equation (SRK-Peneloux) takes the form:

$$P = \frac{RT}{\underline{V}-b} - \frac{a(T)}{(\underline{V}+c)(\underline{V}+b+2c)}. \tag{2.5.15}$$

The parameter c is called the volume-shift parameter. It is possible to relate the molar volumes and covolume parameters in the SRK and SRK-Peneloux equations as follows:

$$\underline{V}_{Pen} = \underline{V}_{SRK} - c, \tag{2.5.16}$$

$$b_{Pen} = b_{SRK} - c. \tag{2.5.17}$$

The volume-shift parameter c has no influence on gas-liquid phase equilibrium calculation results. It is a parameter controlling the molar volumes and phase densities without influencing the phase equilibrium.

The Peneloux volume-shift concept is also applicable to the PR EOS as presented by Jhaveri and Youngren in 1988. With the Peneloux volume correction, the PR equation becomes (PR-Peneloux):

$$P = \frac{RT}{\underline{V}-b} - \frac{a(T)}{(\underline{V}+c)(\underline{V}+b+2c)+(b+c)(\underline{V}-b)}. \quad (2.5.18)$$

The phase equilibrium results obtained with the PR-Peneloux equation is identical to those obtained with the original PR EOS with no volume correction. The reason is explained on the basis of the equation of fugacity coefficients obtained from the PR EOS and PR-Peneloux equation. The PR and PR-Peneloux fugacity coefficients for component i are interrelated through:

$$\ln\varphi_{i,PR} = \ln\varphi_{i,Pen} + \frac{C_i P}{RT}, \quad (2.5.19)$$

where φ_i is fugacity coefficient for component i.

At equilibrium between a vapour phase (V) and a liquid phase (L), the following relation will apply for component I in the PR EOS:

$$\frac{y_i}{x_i} = \frac{\varphi^L_{i,PR}}{\varphi^V_{i,PR}}. \quad (2.5.20)$$

If Peneloux correction is applied, the equation above can be rewritten as:

$$\frac{y_i}{x_i} = \frac{\varphi^L_{i,Pen}}{\varphi^V_{i,Pen}} = \frac{\varphi^L_{i,PR}\exp(\frac{C_i P}{RT})}{\varphi^V_{i,PR}\exp(\frac{C_i P}{RT})} = \frac{\varphi^L_{i,PR}}{\varphi^V_{i,PR}}. \quad (2.5.21)$$

It shows that the PR and PR-Peneloux equation will result in exactly the same results for phase compositions. The volume-shift parameters only change the molar volume and phase densities predictions to match the experimental data.

However, volume-shift parameters could affect compositional phase behaviour predictions when used as regression parameters in fluid characterization as demonstrated by Kumar and Okuno (2013). The P-T-x conditions used in laboratory measurements are only a small part of actual P-T-x conditions in reservoir process. Therefore, volume-shift parameters should be carefully selected in regression since it can substantially affect the oil recovery predictions through altered phase behaviour predictions in P-T-x space where PVT data is not available.

2.6 Uncertainties in EOS fluid model

In section 2.6, the reasons for the uncertainties in EOS fluid model are discussed in different aspects. First, the uncertainties can be caused in the step of component analysis. The oil and gas mixtures are consisted of thousands of different components making it impossible to carry out a complete component analysis. According to Pedersen and Christensen (2010), two standard analytical techniques are used in compositional analyses: One is gas chromatography (GC) and the other is true boing point (TBP) distillation.

The GC technique is well suited for analyzing gas samples up to C_9. In the process of GC, a small gas sample is injected into a GC column, through which it is transported at a rate that depends on molecular structure, size, and boiling point. Each component can be quantitatively identified because the number of different component is limited in gas samples. However, GC is less suited for oil samples due to the number of components increases rapidly with carbon number. Furthermore, identification of individual components becomes increasing difficult as the carbon number goes up because high molecular weight hydrocarbons are present in lower concentration than hydrocarbons of a lower molecular weight. A complete component analysis may be carried out for fractions up to around C_9.

A TBP analysis separates the components of oil into boiling point cuts. Each distillation cut contains sufficient components to measure the density and molecular weight. Because there is a limited span in molecular weight within a carbon number fraction, its molecular weight can be measured with a higher accuracy than the average molecular weight of the oil sample. The uncertainties on the molecular weight of the individual carbon number fraction is around 2%, whereas it is around 5% for the plus fraction as reported in Pedersen and Christensen (2010).

However, the true boiling point data might not be possible for each reservoir fluid and most composition analyses are based on gas chromatography. In such conditions, molecular weight and density of individual C_{10+} fractions reported from a GC analysis will be default values. In reality, the comparison of the molecular weights and densities reveals some difference especially for the molecular weights as shown in Table 2.1 (GC) and 2.6 (TBP) in Pedersen and Christensen (2010). The uncertainties on the measured average molecular weight of the oil samples can be as large as 20%. For a GC composition, this uncertainties is transferred into the molecular weight of a plus fraction. This uncertainties is defined as experimental uncertainties in this research.

The uncertainties caused in fluid characterization part are also presented in the following part. To perform the phase equilibrium calculation on reservoir fluid using an EOS, T_C, P_C and ω are required for each component contained in the mixture. The defined components contained in petroleum reservoir fluids are N_2, CO_2, H_2S, C_1, C_2, C_3, iC_4, nC_4, iC_5, nC_5, and C_6. However, the T_C, P_C and ω for C_{7+} fraction are needed to be characterized by in fluid characterization.

A distribution function is required to fit to the composition data provided in the first step of characterization method. Distribution functions proposed in the literature include the gamma, chi-squared and logarithmic distributions. The most

general form is the gamma distribution and it reduces to the other two when certain assumptions are made. The logarithmic distribution is a widely used form for conventional oil characterization, where composition analysis can provide composition information for a large fraction of the fluid. Heavy oils often require more flexible distribution functions to match their composition data. Regardless of the type of distribution function used, the reliability of the resulting molar distribution depends primarily on how much uncertainties is left as a plus fraction in composition analysis.

After the determination of molar fraction of each component, different correlations are used to estimate properties of the split components because critical properties measured for heavy hydrocarbons are not available. The correlations used for characterization is various and uncertainties can occur if different correlations are used. The widely used correlations of Pederson et al. (2010) are developed for an EOS to reproduce vapor pressures and the critical point for the pseudo component for a given carbon number. However, the PR EOS with these correlations is not able to accurately model densities of heavy hydrocarbons until volume-shift parameters are used.

Considering the modelling efficiency, the number of components used in fluid model is limited. However, the fewer components might result in worse

predictions in phase behaviour due to reduced dimensionality in composition space. Joergensen and Stenby (1995) conducted a comparative study of 12 different grouping methods and concluded that it was difficult to select a single grouping method.

Regression of pseudo components' properties to match experimental data available is often conducted because the previous three steps make certain assumptions resulting in deviations of predictions from actual phase behaviour. Typical parameters adjusted in regression step include T_C, P_C, ω, volume-shift parameters and BIPs for pseudo components heavier than C_7. These adjustment parameters offer flexibilities required to match different PVT data. Different EOS fluid models can be generated depending on the adjustment parameters and how much they are adjusted. It is called the uncertainties in EOS fluid models in this research.

The fluid model uncertainties in fluid characterization can result in a large deviation in the phase behaviour prediction in P-T-x space. Figure 2.4 shows the P-T envelope for mixture of n-alkanes (methane, n-C_{10}, n-C_{18}, and n-C_{30}) presented by Kumar and Okuno (2014b). The P-T envelopes are calculated for the mixture using the optimized critical parameters (Kumar and Okuno 2012) and estimated physical critical parameters (Constantinou and Gani 1994). The resulting P-T

envelope is compared with the experimental data for P-T envelope from Daridon et al. (1996). It is evident that the different characterization methods can lead to different phase behaviour predictions for n-alkane mixtures.

Kumar and Okuno (2012) made comparisons between the PR EOS with their correlation for critical parameters and correlation of Gao et al. (2001). The deviations of saturation pressure for C_6-C_{36} binary mixtures in P-x space are shown in Figure 2.5. More severe uncertainties can be observed for heavy oil mixing with gas. Figures 2.6 and 2.7 present the notably different predictions in phase behaviour in P-T-x space when different characterization methods are applied for real reservoir fluid. In the figures, NM stands for the PnA method developed in Kumar and Okuno (2013) and CM_WV is the conventional method using volume-shift parameters.

2.7 Correlation for n-alkanes and PnA method of Kumar and Okuno

The PR EOS can exhibit erroneous phase behaviour predictions when applied to heavy hydrocarbon mixtures. New correlations for critical temperature (T_C), critical pressure (P_C) and acentric factors (ω) that enable the PR EOS to accurately predict phase behaviour of n-alkanes from C_7 to C_{100} were developed by Kumar and Okuno (2012). The new correlations for n-alkanes are only based on the molecular weight:

$$T_C = 1154.35 - 844.83(1.0 + 1.7557 \times 10^{-3}\mathrm{MW})^{-2.0}, \quad (2.7.1)$$

$$P_C = 559.93(\mathrm{MW})^{-0.638} - 1.49, \quad (2.7.2)$$

$$m = 0.4707 + 2.4831(\mathrm{MW})^{-(39.933/MW)}. \quad (2.7.3)$$

Predictions using the PR EOS with the new correlations give 3.0% average deviation (AAD) for 3583 density data, and 3.4% for 1525 vapor pressure data for n-alkanes from C_7 to C_{100}. Significant improvement is also observed for bubble point pressure and density predictions for n-alkane mixtures. Compared to conventional critical parameter correlations in the literature, the new correlations give more accurate phase behaviour predictions while requiring only MW as the tuning parameter. To limit the flexibility in selecting heavier components to be added, we assume that reservoir fluids are n-alkane mixtures in chapter 4 so that only MW for the heavy oil component is required to be estimated to generate the corresponding EOS parameters.

The optimum T_C and P_C developed for n-alkanes can serve as the lower boundary for the pseudo components of reservoir oils that are characterized using the PR EOS. The new characterization method by Kumar and Okuno (2013) considers a PNA distribution of a plus fraction as perturbation from a limiting distribution of 100% n-alkanes. Considering the physical trend of T_C, P_C and ω with respect to the PNA distribution, the equations combines the perturbation

concept and the correlation of Kumar and Okuno (2012) are given in equations 2.2.4, 2.2.5 and 2.2.6.

$$T_C = 1154.35 - 844.83(1.0 + 1.7557 \times 10^{-3} f_T MW)^{-2.0}, \quad (2.7.4)$$

$$P_C = 559.93(MW/f_P)^{-0.638} - 1.49, \quad (2.7.5)$$

$$m = 0.4707 + 2.4831(f_m MW)^{-(39.933/MW)}. \quad (2.7.6)$$

These perturbation factors are the deviation of pseudo component from the corresponding n-alkane. The values of the perturbation factors are determined by matching the saturation pressure and density data.

The PnA method is extended to lighter fluid by considering proper relationship ($\psi = a/b^2$) between the attraction and covolume parameter of pseudo components. The regression algorithm controls the trend of the ψ parameter with respect to molecular weight using a further adjustment parameter γ.

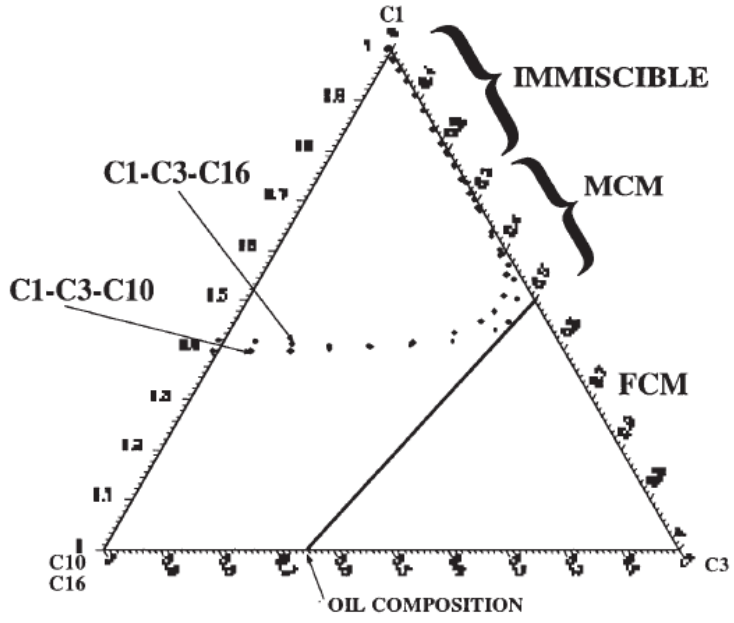

Figure 2.1 The ternary diagram for $C_1/C_3/C_{10}$ and $C_1/C_3/C_{16}$ ternary diagrams at 1500 psia and 70 ℉ in Figure 1 of Burger et al. (1996).

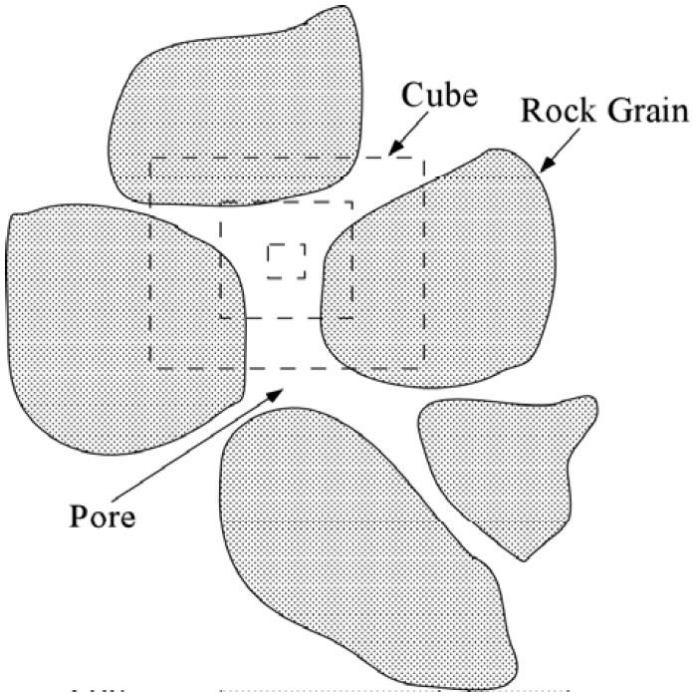

Figure 2.2 The illustration of microscopic cube placed within a porous medium by Lake (1989). The cube is initially within a pore so that its porosity is 1.0. As the cube volume increases, it takes in more grains so that its porosity decreases.

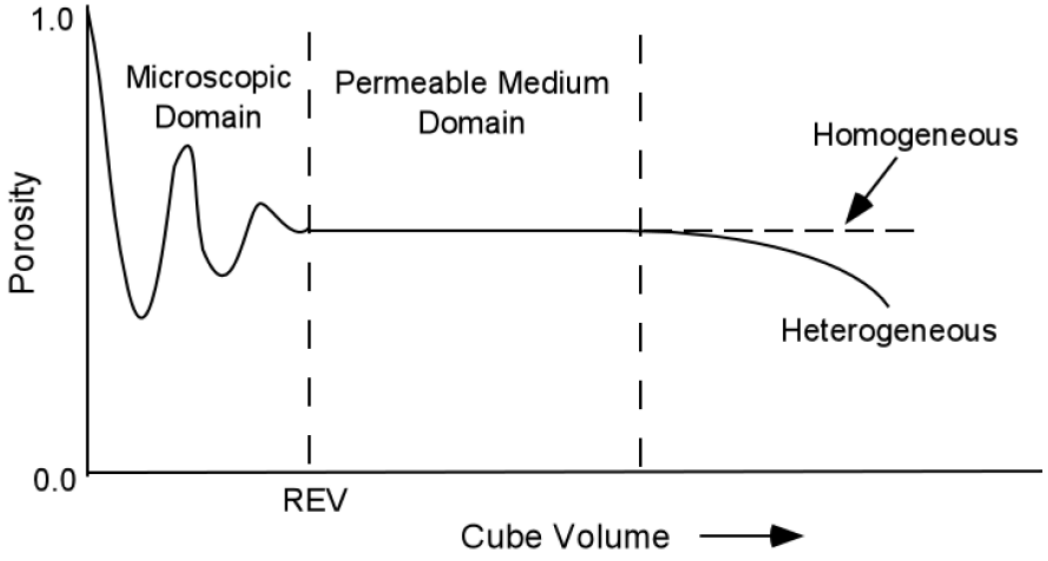

Figure 2.3 The idealizations of the microscopic, porous medium and macroscopic domains by Lake (1989). The REV size separates the microscopic and porous medium.

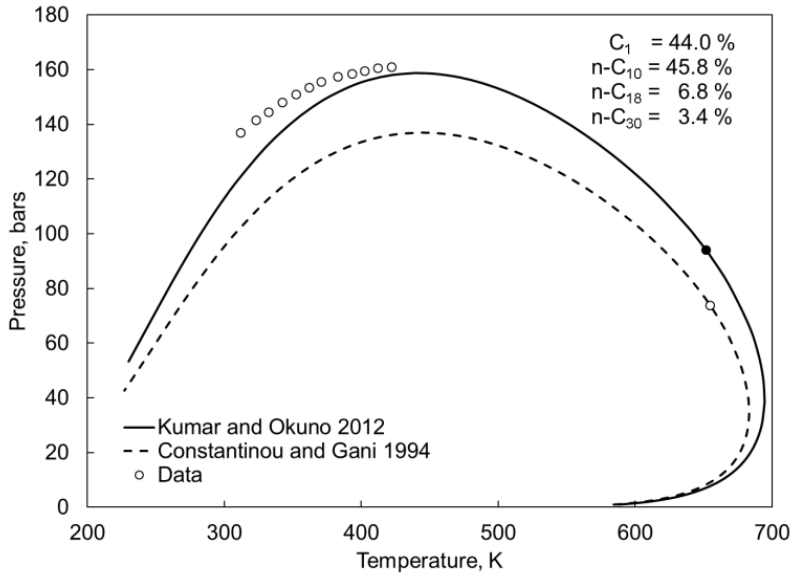

Figure 2.4 The P-T envelope predictions for n-alkane mixture with the PR EOS using the critical parameters from Kumar and Okuno (2012) and Constantinou and Gani (1994). The BIPs are zero for both cases. The experimental data used are from Daridon et al. (1996).

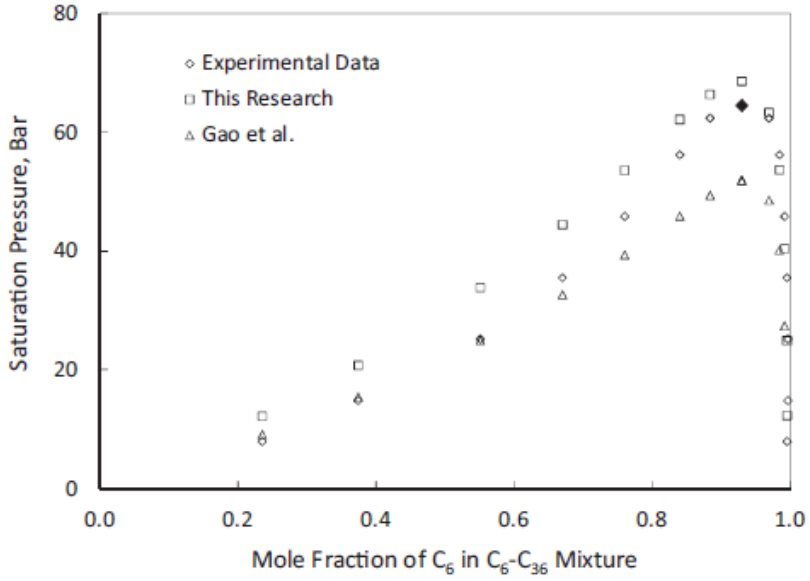

Figure 2.5 The comparisons of saturation pressure prediction with experimental data for C_6-C_{36} binary mixture at 621.8 K. For the predictions, the PR EOS is used with the critical parameters developed in Kumar and Okuno (2012) and those by Gao et al. (2001).

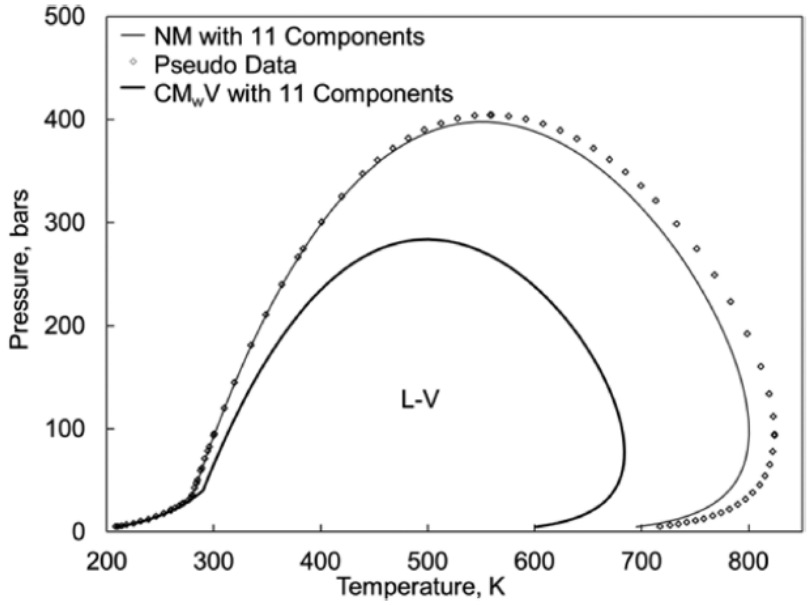

Figure 2.6 The two-phase P-T diagrams for a mixture of oil 6 10% and C_2 90% based on the PnA method and conventional method with volume-shift parameter presented in Figure 10 of the paper by Kumar and Okuno (2014).

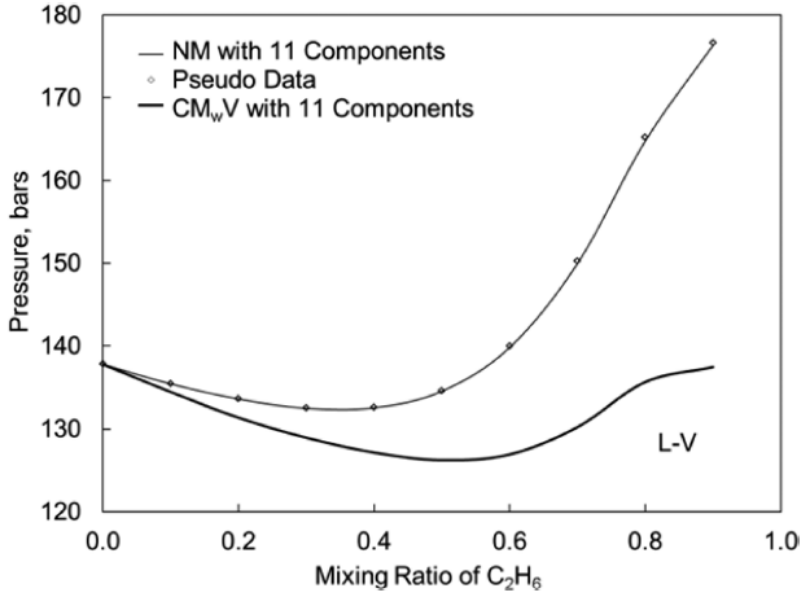

Figure 2.7 P-x diagrams for the oil-6/C_2 pseudo binary pair at 333.15 K based on the PnA method and conventional method with 11 components illustrated in Figure 15 of the paper by Kumar and Okuno (2014).

CHAPTER 3: QUANTIFICAITION OF THE CAPACITANCE EFFECTS BY USE OF THE DUAL-POROSITY FLOW

The capacitance effects are widely observed in both experiments and field applications of gas injection process at different levels. The typical values for bypassed oil are around 10% according to literature. Flow with capacitance effects exhibits earlier breakthrough of the injection gas and long tailing in the effluent concentration profile. The capacitance model originally proposed by Dean (1963) is a mixing cell model which spilt the flowing stream and stagnant volume. The mass transfer from dead-end pore volume to flowing stream is used to account for the longer tailing of the effluent concentration profile in core floods. However, in conventional compositional simulation, the local equilibrium assumption is made for individual grid block so it is not possible for us to split the dead-end pore volume from the flowing cell.

This chapter presents that these flow characteristics of capacitance effects can be captured by flow in a dual-porosity model (dual-porosity flow or DPF). A dimensionless parameter, the throughput ratio (R_T), is introduced to represent the ratio of characteristic times for intra-block mass flux in transverse direction and mass flux in the longitudinal direction in the DPF. This is a gross form of the

Damkhöler number in the dispersion-capacitance model, but closer related to oil recovery.

The capacitance effects observed in core flooding experiments and heterogeneous fine-scale simulation are both quantified by use of the dual-porosity method with given bypassed fraction and throughput ratio. Accurate recovery prediction can be obtained with an optimized value of the bypassed fraction and throughput ratio. The bypassed fraction distribution is recommended for each coarse grid to improve the concentration profile matching result with the fine-scale simulation.

3.1 Flow characteristics of the capacitance effects in the dual-porosity flow

3.1.1 Dual-porosity flow and relevant assumptions

Each grid block is split into a flowing fraction and a bypassed fraction in the dual-porosity flow to represent the flowing and bypassed region at the sub-grid scale. Figure 3.1 presents the schematic for the dual-porosity flow proposed in this research. The flowing and bypassed fractions are represented by the primary (fracture) and secondary (matrix) pore systems in a DPF, respectively. Oil in the flowing fraction is directly displaced by the injected solvent. The bypassed fraction has no contribution to the longitudinal convection. The two fractions

have intra-block mass flux in the transverse direction within individual grid block. The intra-block mass flux contains diffusion/dispersion, convection, gravity and capillary crossflow between the bypassed and flowing fraction. Other relevant assumptions for the dual-porosity flow in this research are listed as follows:

- Isothermal flow
- No mobile water
- Continuous gas injection

The multiphase flow at partially miscible conditions is investigated in this research because the capacitance effects are notable and the mass flux in transverse direction is substantial at these conditions as described in Pande and Orr (1994a, b), Burger et al. (1994), and Burger and Mohanty (1997).

The bypassed fraction is explicitly modelled using bypassed grids blocks that are attached horizontally to the corresponding grid blocks representing the flowing fraction in the single-porosity method for 1-D and vertical 2-D simulations in this research. Results of these flow simulations are identical to those using the dual-porosity option available in commercial simulators as long as the transmissibility between the bypassed and flowing fractions is the same. The dual-porosity option for the 3-D DPF simulations is applied in this research because

it is impossible to attach bypassed grid blocks horizontally to the grid blocks in the flowing fraction to avoid gravity effects.

3.1.2 The capacitance effects modelled in the dual-porosity flow

The 1-D dual-porosity and single-porosity flow are compared in this section to give a clear picture of the capacitance effects modelled by the DPF. Table 3.1 illustrates the reservoir properties used for the DPF simulations. For the SPF simulations, the flowing fraction is set to 1.0. Phase behaviour of the ternary system given in Table 3.2 is calculated using the PR EOS with the van der Waals mixing rules. All BIPs are zero for this n-alkane mixture. C_2 is injected to displace the reservoir oil consisting of 20% C_1 and 80% C_{10}. The reservoir temperature and pressure are 158 °F and 1015.27 psia, respectively. The pressure is fixed at 1025.27 psia for the injector and at 1015.27 psia for the producer to control the influences of pressure on phase behaviour. The minimum miscibility pressure for this displacement is calculated to be 1174.27 psia using the tie-line approach in the PVTsim software (Calsep 2011). Viscosity calculations are based on the Lohrenz-Bray-Clark method (Lohrenz et al. 1964). The Wilke-Chang correlation (Wilke 1950) is used to estimate the diffusion coefficients listed in Table 3.1. All flow simulations in this research are performed using Eclipse 300 of Schlumberger (2011). Numerical dispersion is controlled by the number of grid

blocks using a uniform time step and grid block size. Physical dispersion is neglected in this research for simplicity.

The capacitance effects is observed as earlier breakthrough time and longer tailing in the effluent concentration profiles as we discussed in chapter 2. The dual-porosity flow with the input value listed in Table 3.1 and 3.2 successfully reproduces the flow characteristics of capacitance effects in core floods reported in literature. Figure 3.2 presents the C_2 concentration histories at the outlet for the three cases: dual-porosity flow with 500 grid blocks, single-porosity flow with 500 grid blocks, and single-porosity flow with 250 grid blocks. The DPF exhibits earlier breakthrough and longer tailing of C_2 compared to the SPF with same numerical dispersion level. The earlier breakthrough occurs in the DPF because the injection gas cannot sweep the low permeability region and the effective area open to flow is reduced. The main reason for the longer tailing observed in the effluent C_2 concentration histories is that the bypassed oil gradually migrates to the flowing fraction by the transverse mass flux. The SPF with 250 grid blocks results in a longer transition period than the case with 500 grid blocks due to the increased level of numerical dispersion. The use of effective longitudinal dispersion has been mentioned in the literature to mimic thecapacitance effects. However, the

longitudinal dispersion cannot mimic the capacitance effects in this case as clearly shown by the differences among the three cases.

The breakthrough of C_2 occurs after 1.0 PVI in Figure 3.2 due to the volume change on mixing considered in the simulation. Figure 3.3 compares the C_2 concentrations using the single-porosity models with and without volume change on mixing. For the latter, 1-D dispersion-free compositional flow was numerically solved with the ideal mixing assumption using the codes developed by Okuno (2009).

Figure 3.4 shows oil recovery histories for the DPF and SPF with 500 grid blocks. Gradual recovery of the bypassed oil is the major difference between the two cases. The recovery at breakthrough time for the dual-porosity flow is smaller than the single-porosity flow because the breakthrough time is earlier. The pore-volume injected to achieve the ultimate recovery is later because bypassed oil is held up in the low permeability region and gradually migrates to the flowing region.

Figure 3.5 presents the C_2 concentration profile at 0.8 pore-volume injected (PVI) for the DPF. The profiles in the flowing and bypassed fractions are used to calculate the total C_2 concentration profile. The C_2 concentration gradually

increases in the bypassed fraction because of the mass flux between the two volume fractions.

Figure 3.6 compares the C_2 concentration profiles at 0.8 PVI for three cases; DPF, SPF, and SPF with the S_{orm} method. These three cases use 500 gridblocks to maintain the numerical dispersion in the same level. The displacement fronts for the DPF and the S_{orm} method propagate faster than that in the SPF without the S_{orm} method because of the reduced area open to the longitudinal flow. The capacitance effects are observed in the gradual variation of the C_2 concentration for the DPF.

The C_{10} concentration profile at 10 PVI in Figure 3.7 shows that C_{10} still migrates from the bypassed fraction to the flowing fraction after the evaporation wave in the flowing fraction reaches the outlet. The recovery of the oil stored in the bypassed fraction takes more throughputs than the recovery of the oil in the flowing fraction. The total C_{10} profile in Figure 3.7 and the C_2 front in Figure 3.6 indicate that the capacitance effects resemble displacement of heavier oil in the SP model with the local equilibrium assumption. The displacement front moves faster, and the evaporation wave moves slower in displacement of heavier oil for a given injection gas composition, temperature, and pressure.

Figure 3.8 show the composition variations in ternary diagram for the DP and SP cases at 0.8 PVI, which is before gas breakthrough. The composition variation in the bypassed fraction is totally different from that in the flowing fraction, but does not affect very much the variation of the total composition in this case. However, the recovery prediction is substantially different between the two cases as shown in Figure 3.4. From Figure 3.8, we can conclude that capacitance effects do not change composition path much in composition space but it do have a significant effect on oil recovery because of the earlier breakthrough and longer tailing of the effluent of the injected solvent.

3.2 Dual-porosity flow parameters

The bypassed fraction, throughput ratio and longitudinal Péclet number are defined to parameterize capacitance effects in the dual-porosity flow. One of the most important one is throughput ratio, which is the ratio of characteristic time for intra-block mass flux in transverse direction and mass flux in the longitudinal direction in the DPF. It is a scale and dimensionality dependent parameter as investigated later.

3.2.1 Bypassed fraction

Bypassed fraction is the volume fraction of bypassed region in the pore volume. It is defined as the fraction of the bypassed volume in the pore volume:

$$B = V_B/V. \quad (3.2.1)$$

The bypassed fraction can be measure by conducting core flooding test. However, experimental data might not always be available. An empirical correlation is developed by Lange (1998) to predict the bypassed fraction based on the solubility parameters of the fluids, gas density and average molecular weight. Typical values of bypassed fraction in the literature are on the order of 10% measured in pore volumes in literatures. In our procedure to generate the corresponding DPF, the value of bypassed fraction is determined by matching the recovery at breakthrough time compared to core floods data or fine-scale simulation result.

3.2.2 Longitudinal Péclet number

Longitudinal Péclet number is used to quantify the level of total dispersion in longitudinal direction of the reservoir. It is the ratio of the characterized times for dispersive transport of a particle in the longitudinal direction to convective transport in the same direction. The spatial difference form is back difference (BD) and time difference form is implicit in this research. According to the definition of truncation error expression in BD, implicit simulations for miscible flow by Lantz (1971), the numerical dispersion is $(\Delta\xi + \Delta\tau)/2$.

where ξ is the dimensionless length, τ is the dimensionless time.

The dimensionless length is defined as the ratio between the grid block length and total reservoir length:

$$\Delta\xi = \Delta x/L. \quad (3.2.2)$$

The dimensionless time is the ratio of the pore-volume injected per time step and the pore volume of the reservoir:

$$\Delta\tau = q\Delta t/PV, \quad (3.2.3)$$

where q is the injection rate of the solvent, PV is the pore volume of the reservoir.

In this research, we specify zero physical dispersion in the simulation and control the numerical dispersion with the number of grid block in longitudinal direction and time step size. The longitudinal Péclet number is determined by the numerical dispersion:

$$N_{pe} = 2/(\Delta\xi + \Delta\tau). \quad (3.2.4)$$

A Péclet number of zero implies that dispersive transport completely dominates over convection. The longitudinal Péclet number for the generated dual-porosity model should fit the corresponding core floods experiment or field simulation.

3.2.3 Throughput ratio

Oil recovery with capacitance effects takes more throughput than without capacitance effects to achieve the same level of oil recover as shown in Figure 3.4. To measure capacitance effects, we define the throughput ratio (R_T) as follows:

$$R_T = PVI_1/PVI_2, \quad (3.2.5)$$

where PVI_1 and PVI_2 are the pore-volume injected (i.e., throughputs measured in pore volumes) required for ultimate oil recovery without and with intra-block mass flux in the DPF. PVI_1 is measured by setting the intra-block transmissibilities and diffusion coefficients to zero in a DPF simulation. Figure 3.9 shows C_{10} recoveries in the 1-D DP model with and without intra-block mass flux. Simulation conditions are given in Tables 3.1 and 3.2. In this example, PVI_1 and PVI_2 are 9.93 and 24.34, respectively. R_T is then calculated to be 0.408.

R_T is zero for the case without intra-block mass flux, which corresponds to SPF with the S_{orm} method where bypassed oil is excluded from flash calculation. The reason is that PVI_2 tends to be infinity for bypassed oil to be recovered in the DP case without intra-block mass flux. R_T becomes unity as the intra-block mass flux approaches infinity because intra-block flow rate is sufficiently large to equal PVI_1 and PVI_2. Thus, SPF without the S_{orm} method has a limiting R_T of unity since equilibrium is instantaneously achieved within individual grid blocks with the local equilibrium assumption. Similar to the Damkhöler number in the dispersion-capacitance model, R_T represents the relative magnitude of transverse mass flux to the longitudinal mass flux. R_T, however, is more directly related to oil recovery in the presence of capacitance effects as it shows in Figure 3.10. It

presents C_{10} recoveries with different R_T values. Oil recoveries with different degrees of capacitance effects are well characterized using R_T. These different R_T values are generated by multiplying the intra-block diffusion coefficients by factor C. This method of controlling R_T is also used in the subsequent sections.

Figure 3.11 shows that R_T monotonically increases with the C multiplier. The transverse permeability between bypassed region and flowing region is minimized to restrict the convective crossflow. As a result, the diffusion becomes the dominant source of the mass flux in transverse direction. As diffusion rate is faster for larger multiplier for molecular diffusion coefficients, the corresponding PVI_2 becomes smaller for a fixed bypassed fraction.

Mechanical equilibrium between the bypassed and flowing fractions causes the convective crossflow in these DP simulations. This transverse convection along with molecular diffusion should cause transverse crossflow in reality. The transverse convection, however, is not considered here because it is easier to control the intra-block mass flux by changing the C multiplier alone in this fundamental research.

The scale dependency of capacitance effects are observed in both experiments and simulations as reported in chapter 2. For larger scale such as field cases with longer process time, capacitance becomes smaller enough to be reproduced by

effective dispersion. Throughput ratio (R_T) properly considers the effects of recovery process time on oil recovery in the presence of capacitance. Table 3.3 presents that R_T values resulting from different system lengths for two different C values 100 and 500. R_T becomes larger as the recovery process takes longer for a fixed C, bypassed fraction, and longitudinal dispersion level. From Table 3.3, we can conclude that R_T properly considers the effects of recovery process time on oil recovery in the presence of capacitance.

As system length is changed, the injection rate will be different if the pressure difference is the same between injector and producer. The dimensionless time step will inevitably change according to the definition in equation 3.2.3. In order to retain the longitudinal Péclet number, the time step size is adjusted to control the dimensionless time step size. Table 3.4 shows the different time step size used to maintain the longitudinal dispersion level for all of the six cases shown in Table 3.3. Influences of dispersion are excluded to analyze effects of system length on throughput ratios. For longer system length, the throughput ratio tends to be larger because the process time becomes larger. This dependency of R_T on recovery process time should be considered for estimating R_T at a field-scale based on R_T at model scales (e.g., R_T from a 1-D DPF model fitted to core flood data).

The increase of dimensionality of reservoir can also increase the value of throughput ratio for a fixed C and reservoir length. Multiple flow paths will coexist from the injector to the producer for 2-D and 3-D simulations. The different flow paths have different travel lengths from the injector to the producer. The flow rate is also different based on the permeability for different flow path. The process time in multidimensional flow is longer than one dimension flow because it is determined by the slowest flow path. It is reasonable for us to make a prediction that throughput ratio (R_T) will become larger if we transfer from 1-D flow to a 2-D/3-D flow as process time is longer.

2-D simulations with different throughput ratios are generated based on the reservoir model used for the 1-D simulations. The reservoir dimensions, fluid properties, pressures, temperature, and relative permeability are the same for the 1-D and 2-D flow. The number of grid blocks in the longitudinal direction is also kept the same so the longitudinal Péclet number is retained for the two cases. Reservoir properties for the 2-D flow are given in Table 3.5. Figure 3.12 compares R_T values for different C values in 1-D and 2-D flow. Consistent with the prediction, throughput ratio (R_T) in the 2-D flow is systematically higher than that in the 1-D flow as illustrated in the figure. For a C value of 500, the recovery process time is 90.21 years for the 2-D case and 16.07 years for the 1-D case. The

recovery process becomes much longer for the 2-D flow than the 1-D flow for a given C. This dimensionality dependency also requires to be considered for estimating the throughput ratio from 1-D flow to 2-D/3-D flow together with scale dependency. It is in line with less capacitance effects are observed in large field simulation cases where a 3-D model with the local equilibrium assumption.

Gardner and Ypma (1984) qualitatively showed capacitance effects on ultimate oil recovery in CO_2 floods with different Damkhöler numbers in capacitance-dispersion model. Because of the similarity of throughput ratio and Damkhöler numbers, it is believed that ultimate recovery should also be a function of throughput ratio. Instead of showing the schemes of the relationship between ultimate oil recovery and Damkhöler numbers, simulation studies with different throughput ratios are investigated for 1-D, 2-D and 3-D reservoir. Fluid properties are the same for cases in different dimensionalities. Reservoir properties for 1-D and 2-D flow are still based on Table 3.1 and Table 3.5, respectively. Reservoir properties for the 3-D flow have the same reservoir dimension, porosity and permeability as 1-D and 2-D flow. The detailed reservoir properties are given in Table 3.6.

A similar relationship between ultimate oil recovery and throughput ratios are plotted in Figure 3.13, where C_{10} recoveries are shown for different R_T values for

1-D, 2-D, and 3-D flow. Ultimate recovery is measured at 15 PVI, 25 PVI, and 35 PVI for the 1-D, 2-D, and 3-D flow, respectively. R_T of unity corresponds to the local equilibrium assumption in conventional compositional simulation. R_T of zero corresponds to the S_{orm} method, which is currently available in commercial simulators. By use of the definition of throughput ratios, the transition zone of the ultimate oil recovery between local equilibrium assumption and the S_{orm} method are successfully modelled in conventional composition simulation which is not possible without the dual-porosity method together with the three dimensionless groups. Efficient modelling and quantifying of the transition between these two limiting assumptions in reservoir simulation is the long-existing technical issue pointed out by Burger et al. (1994), and now is solved by introducing the three dual porosity parameters in the dual-porosity method.

3.3 Mathematical development for the dual-porosity flow

This section presents the mathematical development from a fine-scale simulation explicitly modelling capacitance effects to a coarse-scale simulation with the dual-porosity method. The working equation for coarse-scale simulation with the DPF to match the recovery prediction in the fine-scale simulation is obtained through the derivation. A main flow pattern based on the dominant flow direction is assumed for the fluid flow in real porous medium. In

the simplified one dimension flow in real porous medium, the dispersion term is neglected in the flow direction. The material balance equation for hydrocarbon component i in the fine grid compositional simulation model is:

$$\frac{d}{dt}\int_V \phi \sum_{j=1}^{n_p} x_{ij}\rho_j S_j \, dV + \oint_A \vec{n} \cdot \sum_{j=1}^{n_p} x_{ij}\rho_j \vec{v_j} \, dS = 0, \quad (3.3.1)$$

where i = 1, 2…n_c, j = oil, gas.

In the alpha-factor method by Barker and Fayers (1994), transport coefficients α_{ij} are introduced in the flux terms to adjust the flow:

$$\frac{d}{dt}\int_V \phi \sum_{j=1}^{n_p} x_{ij}\rho_j S_j \, dV + \oint_A \vec{n} \cdot \sum_{j=1}^{n_p} x_{ij}\rho_j \boldsymbol{\alpha_{ij}} \vec{v_j} \, dS = 0. \quad (3.3.2)$$

By tabulating a table of $\boldsymbol{\alpha_{ij}}$ for different components and phases, the desired x_{ij} is able to be obtained in the coarse grid simulation to mimic the composition in original fine-scale simulation. The detailed explanation for the alpha-factor method is included in section 2.4. In the DPF, we maintain the flux term in the same form but spilt the coarse grid block into flowing and bypassed fraction to get the desired x_{ij}.

In the flowing and bypassed region, flash calculation is done separately. The longitudinal flow only occurs in flowing region between the injector and producer. The material balance equation for component i in the coarse-scale simulation with the DPF is obtained by splitting the original coarse grid into flowing region V^F and bypassed region V^B:

$$\frac{d}{dt}\int_{V^F}\phi^F\sum_{j=1}^{n_p}x_{ij}^F\rho_j^F S_j^F\,dV+\oint_{A^F}\vec{n}\cdot\sum_{j=1}^{n_p}x_{ij}^F\rho_j^F\overrightarrow{v_j^F}\,dS+\int_V\sum_{j=1}^{n_p}q_{ij}^T dV=0, \quad (3.3.3)$$

where q_{ij}^T is the moles of component i in phase j transferring from bypassed region to flowing region.

If we consider the whole reservoir, the flux term will be replaced by the injection amount and production amount. The material balance equation for component i in the whole reservoir for fine-scale simulation is:

$$\frac{d}{dt}\int_V\phi\sum_{j=1}^{n_p}x_{ij}\rho_j S_j\,dV+\int_V\sum_{j=1}^{n_p}q_{ij}^I\,dV-\int_V\sum_{j=1}^{n_p}q_{ij}^P\,dV=0. \quad (3.3.4)$$

Similar to fine-scale simulation, the material balance equation for component i in the whole porous medium for coarse-scale simulation with the DPF can be written as:

$$\frac{d}{dt}\int_{V^F}\phi^F\sum_{j=1}^{n_p}x_{ij}^F\rho_j^F S_j^F\,dV+\int_V\sum_{j=1}^{n_p}q_{ij}^I\,dV-\int_V\sum_{j=1}^{n_p}q_{ij}^P\,dV+\int_V\sum_{j=1}^{n_p}q_{ij}^T dV=0. \quad (3.3.5)$$

From equation (3.3.4) and (3.3.5), the working equation for coarse-scale simulation with the DPF to match the recovery prediction in fine-scale simulation is obtained:

$$\frac{d}{dt}\int_V\phi\sum_{j=1}^{n_p}x_{ij}\rho_j S_j\,dV-\frac{d}{dt}\int_{V^F}\phi^F\sum_{j=1}^{n_p}x_{ij}^F\rho_j^F S_j^F\,dV=\int_V\sum_{j=1}^{n_p}q_{ij}^T dV \quad .$$

(3.3.6)

The key information expressed by the working equation is to equalize the variation of component i in the fine-scale and coarse-scale simulation to the amount of

component i transferring from bypassed region to flowing region. The throughput ratio R_T is introduced to control q_{ij}^T to satisfy the desired composition variation between fine-scale simulation and coarse-scale simulation with DPF.

As defined in our DPF, there is no mass flux in the longitudinal direction of bypassed region. The material balance equation for the bypassed region in the whole reservoir can be written as:

$$\frac{d}{dt}\int_{V^B} \phi^B \sum_{j=1}^{n_p} x_{ij}^B \rho_j^B S_j^B \, dV = \int_V \sum_{j=1}^{n_p} q_{ij}^T dV \quad . \tag{3.3.7}$$

The only source term of q_{ij}^T is the composition variation in the bypassed region of the DPF. A proper value of bypassed fraction B should be determined to quantify the amount of bypassed oil fraction in the reservoir. Also an appropriate throughput ratio should be estimated to match the mass flow rate between the bypassed fraction and flowing fraction.

If the concentration profile is required to be matched, the working equation (3.3.8) needs to be satisfied to develop the corresponding coarse-scale simulation with DPF:

$$\frac{d}{dt}\int_V \phi \sum_{j=1}^{n_p} x_{ij} \rho_j S_j \, dV =$$

$$\frac{d}{dt}\int_{(1-B)V} \phi^F \sum_{j=1}^{n_p} x_{ij}^F \rho_j^F S_j^F \, dV + \frac{d}{dt}\int_{BV} \phi^B \sum_{j=1}^{n_p} x_{ij}^B \rho_j^B S_j^B \, dV \quad . \tag{3.3.9}$$

Various bypassed fraction distribution which has individual bypassed fraction B for each coarse grid gives additional flexibility to match the concentration for each grid blocks. In section 3.5.5, the bypassed fraction distribution is generated based on the shale fraction in the fine-scale simulation resulting in a satisfactory matching result.

Based on the mathematical development, it is clear that bypassed fraction and throughput ratio are the two key parameters to satisfy the working equation. In the following two sections, the dual-porosity method is validated in case studies. Capacitance effects in core flooding experiments and fine-scale heterogeneous simulations are reproduced by DPF, respectively.

3.4 The dual-porosity method applied in core flooding experiment

In this section, two case studies of using 1-D homogenous simulation with DPF to reproduce the core flooding data are presented. The first case is the core flooding experiment of a lean gas mixture injected into synthetic oil consisted of n-alkanes by Burger et al. (1996). The second case is the laboratory experiments of representative core samples with reservoir fluids from Hassi-Messaoud Field undertaken by Bardon et al. (1994). Both of the case studies are at partially miscible condition when the recovery of bypassed oil is important.

3.4.1 Core flooding case 1 of C_1, C_3 and C_{16} mixture

This section shows a case study using core floods data given in Burger et al. (1996). A series of core flooding experiments are conducted with different gas enrichment to research on the mass transfer rate from the bypassed region to the flowing region. According to their result, this mass transfer rate is quite substantial for near-miscible condition at the laboratory scale. This coreflood with 74% C_1 and 26% C_3 injection which is at partially miscible condition is used in our research. The fluid properties for the used three n-alkane components are shown in Table 3.7. All BIPs are zero for this n-alkane mixture.

The Péclet number for this coreflood was estimated to be 500 according to literature. A same level of dispersion is used in the 1-D DPF model using 0.002 for both of the dimensionless time-step and grid block sizes with the fully implicit formulation. The 1-D DPF model is then fitted to the coreflood data as shown in Figure 3.14, yielding a bypassed fraction of 0.12 and a R_T value of 0.365. The resulting model parameters are summarized in Table 3.8.

Figure 3.14 shows that the core floods recovery history cannot be matched using the 1-D SPF models with and without the S_{orm} method available in conventional composition simulation. The 1-D SPF model overestimates the recovery because capacitance effects cannot be considered with local equilibrium

assumption. The 1-D SPF model with the S_{orm} method corresponds to the 1-D DPF with the R_T value of 0.0. The recovery of bypassed oil cannot by modelled because the residual oil is excluded from flash calculation. Capacitance effects must be properly quantified by a fitted bypassed fraction and throughput ratio in DPF to reproduce the core flooding experimental data.

3.4.2 Core flooding case 2 of reservoir oil sample from Hassi-Messaoud field

The Hassi-Messaoud Field is one of the largest oil field in the world, made to produce by miscible gas injection since 1964. In some blocks, the pressure declines greatly to the pressure close to MMP. In order to determine the lowest operation pressure below MMP, Bardon et al. (1994) undertook a series of laboratory experiments on representative core samples with reservoir fluids from Hassi-Messaoud field.

The oil in place is light (45° API) with a saturation pressure of 2824.04 psia. The minimum miscibility pressure of the reservoir oil is determined to be 3790.39 psia by slim tube experiments. A medium gas consisted of 80% C_1, 15% C_2 and 5% C_3 is injected to displace the reservoir oil at reservoir temperature 245.30 °F and pressures below MMP. Two different pressures 3480.91 psia and 3190.83 psia are used in our research to validate the dual-porosity method in different pressures. The reservoir fluid is characterized by the PnA method developed by Kumar and

Okuno (2013) to match the given PVT data. Table 3.9 presents the characterized EOS model of reservoir oil and injection gas. Table 3.10 gives the corresponding BIPs for this characterized EOS model.

A composite core built with ten plugs with similar petrophysical properties is used for the core floods. A 1-D single-porosity simulation is developed first based on the given characterized EOS model and core properties given in Table 3.11. The Péclet number for the core flooding experiment is not mentioned in the Burger's paper, so we just make it reasonable for core scale. The Pectlet number is calculated to be 833.6 with 500 gird blocks and 0.01 hour time step.

Figure 3.15 shows that experiment data at pressure 3480.91 psia is reproduced by 1-D DPF simulation. The resulting bypassed fraction is 0.1 and throughput ratio is approaching zero because the recovery of bypassed oil is too slow to be observed. However, if we do not consider capacitance effects, the recovery will be overestimated because of the local equilibrium assumption in conventional composition simulation.

As the reservoir pressure continues to decline, one more core flooding experiment is undertaken at a lower pressure 3190.83 psia. The dual-porosity method also successfully reproduces the recovery prediction as Figure 3.16

presents and resulting bypassed fraction is 0.14 which is slightly higher than the estimated value in 3480.91 psia.

In core flooding case 2, two different pressures at partially miscible condition are tested for our dual-porosity method in modelling capacitance effects. The recovery predictions of the core flooding data are all accurately reproduced by our dual porosity method with proper bypassed fraction and throughput ratios. In conclusion, capacitance effects observed in core floods can be quantified or parameterized by the dimensionless group defined in the dual-porosity method.

3.5 Case studies for the coarse-scale dual-porosity simulation to reproduce fine-scale simulation results

3.5.1 Generation heterogeneous reservoir models

A heterogeneous XY-2D reservoir is constructed by use of S-GeMS V2.1, a geostatistical earth modelling software from Standford University. The reservoir is consisted of 120 grid blocks in X direction and 30 grid blocks in Y direction. The dimension of each grid block is 1 ft×1 ft×1 ft. It contains two different facies which are sandstones and shales to represent the flowing region and bypassed region, respectively. The shales occupy 0.2 volume of the reservoir and distribute in the REV with a correlation length of 10 ft in both X and Y direction. The histogram of the porosity of the reservoir is given in Figure 3.17. It is a bimodal

distribution with an average porosity of 0.28 for sandstone and 0.01 for shales. The resulting porosity distribution for the reservoir is shown in Figure 3.18. Gas is injected along the left side of the reservoir and oil is produced along the right side of the reservoir. The blue region is the shales with low porosity, which is expected to be bypassed region in gas flooding process.

The permeability distribution is generated based on the porosity distribution of the reservoir. A widely used form of calculating permeability from porosity is used in this research:

$$k = e\varphi^{f} \quad . \tag{3.5.1}$$

Constant f (1.2) is used in this research. Different e is applied for shales to characterize the different rate of the recovery from bypassed region. Three different cases are generated here and the equations for permeability based on porosity are given as below:

For case 1, permeabilities are $1200\varphi^{1.2}$ for both sandstones and shales.

For case 2, permeabilities are $1200\varphi^{1.2}$ for sandstones and $120\varphi^{1.2}$ for shales.

For case 3, permeabilities are $1200\varphi^{1.2}$ for sandstones and $12\varphi^{1.2}$ for shales.

For all of three cases above, the location of shales is exactly the same and permeabilities of sandstone are also the same (around 250 md). However, the permeabilities for shales are different.

For case 1, shale permeability is around 5.00 md.

For case 2, shale permeability is around 0.50 md.

For case 3, shale permeability is around 0.05 md.

The histogram of permeability for case 1 is given in Figure 3.19. The permeability distribution for case 1 is shown in Figure 3.20. The blue region is the shale with low permeability which is going to be the bypassed region in gas flooding process.

3.5.2 Capacitance effects in fine-scale heterogeneous simulation

The 3 component EOS of C_1, C_2 and C_{10} mixtures in Table 3.2 is used in the fine-scale simulation for the heterogeneous reservoir. Figure 3.21 presents the oil and gas relative permeability used for the fine and coarse-scale simulation in section 3.5. Capillary pressure is neglected in this subsection.

The reservoir temperature is 158 °F and pressure is 1015.27 psia. The fine-scale heterogeneous reservoir generated in section 3.5.1 is used to explicitly consider capacitance effects. Figure 3.22 presents the concentration profile of C_2 which is the only injectant in case 1 at different PVIs. The bypassing of oil is

clearly shown in the concentration profile at different PVIs. The injected solvent C_2 channels through the sandstone with relatively high permeability and the oil near the shale is bypassed. As the gas injection continues, the oil which is previously bypassed at early PVIs (0.7 and 1 PVI) will be slowly recovered as it shows in late PVI (1.5 PVI). At last, most of the bypassed oil is recovered because of the mass transfer between the bypassed region and flowing region as it shows in 10.0 PVI. The recovery of bypassed oil is relatively fast in case 1 because the relative high permeability of shales (5 md) results in a considerable mass transfer between bypassed region and flowing region. The breakthrough time is after 1 PVI because of the volume change on mixing.

Comparisons of C_2 concentration for the cases with lower permeability for shale in case 2 and 3 are discussed in the following part. C_2 concentration profile at 1.0 and 10.0 PVIs are compared in Figure 3.23 and Figure 3.24. As the concentration profiles show, the rate of the recovery of bypassed oil strongly depends on the permeability of the shale which is considered as bypassed region. For case 3 with lowest permeability for shales, the recovery of bypassed oil is the slowest. At 10.0 PVI, the difference in residual oil saturation is significant.

If the dual-porosity method is applied in coarse-scale simulation to reproduce the recovery prediction in fine-scale simulation, it is predictable that case 3 results

in smaller throughput ratio compared to case 1. The fine-scale heterogeneous reservoir is upscaled into a coarse-scale reservoir with 12×3 gird blocks. Figure 3.25 presents the upscaled porosity distribution for the corresponding coarse case 1, 2 and 3 generated by the calculating the arithmetric mean of the porosity in selected region. The permeability is calculated by equation $k = 1200\varphi^{1.2}$ for case 1, 2, 3 based on the upscaled porosity for each coarse grid block. Figure 3.26 gives the permeability distribution calculated for the coarse-scale simulation.

C_2 concentration profiles for fine and coarse-scale simulation at 1.0 PVI in case 3 are plotted in Figure 3.27. It is clearly observed the upscaled coarse-scale simulation cannot model bypassed effects due to the local equilibrium assumption at the sub-grids. Figure 3.28 illustrates the resulting recovery predictions for the fine-scale simulations and upscaled coarse-scale simulation. Coarse-scale simulation dramatically overestimates the recovery compared to the fine-scale simulation because capacitance effects at the sub-grid scale of the coarse grid cannot be considered as it shows in Figure 3.28. The recovery efficiency keeps decreasing with the decrease of the permeabilities for shales from case 1 to case 3. The major difference between fine-scale simulation and upscaled coarse-scale simulation is the earlier breakthrough time and longer tailing which are the characteristics of capacitance effects modelled in the dual-porosity flow.

Similar to definition of throughput ratios in the dual-porosity method in equation 3.2.5, the throughput ratios can also be calculated for fine-scale simulations to quantify the bypassed effects in the fine-scale simulation. The PVI needed for fine-scale simulation to reach the ultimate recovery is considered as PVI_2 which is corresponding to the dual-porosity method explicitly modelling capacitance effects at the sub-grid scale. The PVI needed for coarse-scale simulation to achieve the ultimate recovery is regarded as PVI_1. The throughput ratios for the three cases are 0.73, 0.46 and 0.14 from case 1 to case 3, respectively. The parameterization of bypassed effects in fine-scale simulation is really helpful to create the corresponding upscaled coarse-scale simulation with the dual-porosity method as presented in section 3.5.4.

3.5.3 Effects of capillary crossflow on recovery of bypassed oil

Capillary crossflow can be considerably important for the recovery of bypassed oil especially for the case with high capillary number. In this section, the effects of capillary crossflow on the recovery of bypassed oil will be further discussed based on the corresponding capillary number. The capillary function used in the simulation for the case with capillary pressure is shown in Figure 3.29.

Aspect ratio R_L is calculated to determine whether the transverse direction perturbation is important for this reservoir. As gas is injected along the left side to

the right side, it is reasonable to consider the X direction as the longitudinal direction and Y direction as the transverse direction for the flow in the reservoir. Aspect ratio (R_L) is defined a ratio of a characteristic time for fluid to cross the reservoir in the longitudinal direction to that in the transverse direction. If R_L is large, saturation or pressure fluctuations in the transverse direction decay much faster than those in the longitudinal direction. Therefore, the transverse direction perturbations such as crossflow in transverse direction can be neglected. The definition of aspect ratio is given in equation 3.5.1:

$$R_L = \frac{L}{H}\left(\frac{k_{av}}{k_{al}}\right)^{0.5}, \qquad (3.5.1)$$

where L is the reservoir length in longitudinal direction,

H is the reservoir thickness in transverse direction,

k_{av} is the average permeability in transverse direction,

k_{al} is the average permeability in longitudinal direction.

As reported in Lake (2010), the vertical equilibrium assumption is applicable when aspect ratio is more than ten. For the XY-2D heterogeneous reservoir in this research, the aspect ratio is calculated to be four which is smaller than ten, which means the crossflow in transverse direction between bypassed fraction and flowing fraction cannot be neglected.

The crossflow in transverse direction can be viscous or capillary crossflow in XY-2D case. The capillary number is often used to compare the capillary force and viscous force in the reservoir. In the paper by Zhou et al. (1994) and Cinar et al. (2005), characteristic time ratios for fluid to flow in the transverse direction due to capillary forces to that in horizontal direction due to viscous forces are defined to characterize the capillary effects compared to viscous effects. In this research, the same definition is used to characterize the capillary effects as it shows in equation 3.5.1:

$$N_{cv} = \frac{Lp_c^* k_{av}}{H^2 v \mu_o} \quad , \tag{3.5.2}$$

where L is reservoir length in longitudinal direction, cm

k_{av} is the average permeability in transverse direction, D

H is the reservoir thickness in transverse direction, cm

v is total Darcy flow velocity, cm/s

μ_o is oil viscosity, mPa*s

p_c^* is characteristic capillary pressure, kpa

The characteristic capillary pressure is defined as the average capillary pressure in different saturation as shown in Equation 3.5.3:

$$p_c^* = \int_{S_{gc}}^{1-S_{or}} p_c(S_g) \frac{dS}{1-S_{or}-S_{gc}}. \tag{3.5.3}$$

According to the input values, the calculated capillary number (N_{cv}) is165.79. As defined in Cinar et al. (2005), the flow is capillary dominant when the scaling numbers $\frac{MN_{cv}}{1+M}$ is larger than 5.0. The scaling number for this gas flooding conducted in the XY-2D heterogeneous reservoir is more than 5.0 as shown below:

$$\frac{\mathrm{MN_{cv}}}{1+\mathrm{M}} = 8.6 > 5.0. \quad (3.5.4)$$

For the XY-2D case which considers capillary pressure (case with P_c), it is a capillary dominated case. For the case without capillary pressure, the calculated characterized capillary number is zero as the characteristic capillary pressure is zero so that it is a viscous dominated case.

The comparisons for the C_2 concentration profile at 1.0 and 10.0 PVI for case 3 with and without capillary pressure are shown in Figure 3.30 and Figure 3.31. As observed in the concentration profile, the effects of capillary pressure are significant. Capillary effects decrease component propagation speed as it shows in Figure 3.30 at 1.0 PVI. However, capillary crossflow enhances the recovery of bypassed oil notably as observed in Figure 3.31 at 10.0 PVI. The recovery predictions for case 3 with and without capillary pressure are presented in Figure 3.32. It is consistent with concentration profile that breakthrough time is earlier for the case without capillary pressure. The recovery efficiency of bypassed oil is

higher for the case with capillary pressure because capillary crossflow migrates the bypassed oil to the flowing region.

Capillary crossflow is confirmed to be considerable important for the recovery of bypassed oil for the case with large capillary number. The local equilibrium assumption at the sub-grid scale result in much smaller error because of the substantial capillary crossflow to recover the bypassed oil as illustrated in Figure 3.33. For case 3 with smaller throughput ratio, the difference between fine-scale and coarse-scale simulation is still visible

In the next section, the dual-porosity method will be validated in the case with and without capillary pressure in the upscaled coarse-scale simulation to reproduce the recovery prediction in fine-scale simulation. Results demonstrate that the dual-porosity method can significantly improve the recovery prediction for coarse-scale simulation in both capillary and viscous dominated case.

3.5.4 The Coarse-scale dual-porosity simulation to reproduce fine-scale simulation results

In section 3.5.2, the significant difference for the recovery prediction in fine-scale simulation and upscaled coarse-scale simulation is observed in Figure 3.28. The main reason of the erroneous prediction in recovery for upscale coarse-scale simulation is that capacitance effects at the sub-grid scale is not

modelled properly because of the local equilibrium assumption in conventional composition simulation. In this section, the dual-porosity method is validated in the upscaled coarse-scale simulation to improve the recovery prediction compared to fine-scale simulation case.

Each coarse grid is split into bypassed and flowing fraction to consider capacitance effects at the sub-grid scale. For case 3 without capillary pressure, the DPF is fitted to the fine-scale simulation result as it shows in Figure 3.34. The resulting throughput ratio is 0.14 and bypassed fraction is 0.08 for this case. It is observed that DPF significantly improves the recovery prediction for the coarse-scale simulation. Capacitance effects because of the sub-grid heterogeneity in coarse grid are explicitly considered as the bypassed region in DPF. Capacitance effects can also be parameterized by the throughput ratio, bypassed fraction as it shows here.

If capillary pressure is considered as in section 3.5.3, capacitance effects will be greatly decreased by the capillary crossflow as it shows in Figure 3.33. However, there is still a visible difference between the fine-scale simulation and coarse-scale simulation for case 3. The dual-porosity method is also applied for case 3 which considers the effects of capillary pressure. The recovery prediction is improved by use of the dual-porosity method in case 3 with capillary pressure as

presented in Figure 3.35. The throughput ratio R_T for this case is 0.139, which is close to the case without capillary pressure. The corresponding bypassed fraction is 0.025 which is much smaller compared to the case which is viscous dominant for DPF. The reason should be the derogation of capacitance effects are considered as the deduction of bypassed fraction because the capillary crossflow is so fast that it already produces large amount of bypassed oil before breakthrough time which is used to estimate the bypassed fraction.

3.5.5 Distribution of bypassed fraction applied in the dual-porosity method

In previous section, the dual-porosity method with average bypassed fraction in coarse-scale simulation successfully reproduces the recovery prediction in fine-scale simulation. However, the DPF with averaged bypassed fraction only considers that the recovery of oil at outlet equals to the fine-scale simulation in order to reproduce recovery. The concentration profile matching result for the coarse-scale simulation with DPF and fine-scale simulation needs further modification as it shows in Figure 3.36.

Distributing the bypassed fraction in the upscaled coarse-scale simulation is one possible solution for to improve the concentration prediction in each coarse grid. The bypassed fraction is distributed as a function of shale amount in each coarse grid as the original permeability distribution is a bimodal distribution with

shales and sandstones. The procedures for calculating the bypassed fraction for each coarse gird are presented as below:

Step 1: For each coarse grid i, the number of shale grid blocks are counted in the corresponding region in the fine-scale case. The amount of shale fine girds in coarse gird block i is C_i.

Step 2: Calculate the shale fraction based on the number of fine grids and the counted number of shale grid blocks for each coarse grid i:

$$S_i = \frac{C_i}{n}, \tag{3.5.5}$$

where S_i is the shale fraction in coarse gird block i, n is the number of fine grids in the corresponding coarse region.

Step 3: Estimate the average bypassed fraction (B) from the dual-porosity case with averaged bypassed fraction matching the recovery prediction of the fine-scale simulation.

Step 4: The bypassed fraction for coarse grid block i can be calculated based on the shale fraction:

$$B_i = BmS_i / \sum_m S_i, \tag{3.5.6}$$

where m is total gird block numbers for the coarse-scale simulation.

Based on the procedure, the resulting distribution for bypassed fraction is given in Figure 3.37.

Using the bypassed fraction distribution is the coarse-scale simulation for case 3, it is observed that both averaged bypassed fraction and various bypassed fraction distribution can result in accurate recovery prediction as shown in Figure 3.38. It is concluded that the recovery prediction is accurate once the appropriate bypassed fraction and throughput ratio is used in the coarse-scale simulation with DPF. However, the dual-porosity method with various bypassed fraction distribution is able to qualitative consider the influences of locations of shales on concentration profile as shown in Figure 3.39. The concentration profile at row 2 for fine-scale and coarse-scale simulation with averaged and various bypassed fraction distribution are plotted in Figure 3.40. The averaged concentration for fine-scale simulation is the average concentration for fine-scale simulation in the region of the corresponding coarse grid. A notable improvement of the concentration profile matching is observed by use of various bypassed fraction distribution compared to DPF with averaged bypassed fraction in row 2**.** Additional flexibility in bypassed fraction helps to improve the concentration prediction in the coarse-scale simulation with DPF as well as keeping the accuracy in reproducing the recovery prediction.

TABLE 3.1– RESERVOIR PROPERTIES FOR THE 1-D DUAL-POROSITY SIMULATION	
Dimensions (F*/B*)	$2 \times 900 \times 50$ ft^3/$2 \times 100 \times 50$ ft^3
Number of gird blocks	$500 \times 2 \times 1$
Porosity	0.3
Permeability (F*/B*)	2000 md (X,Z), 2000 md(Y)/ 0.0 md(X,Z), 0.2 md (Y)
Reservoir pressure	1015.27 psia
Reservoir temperature	158 ℉
Injection pressure	1025.27 psia
Production pressure	1015.27 psia
Relative permeability model	Corey
Residual saturation (Oil/Gas)	0.24/0.0
Endpoint relative permeability (Oil/Gas)	1.0/0.6
Exponent (Oil/Gas)	2.1/1.8
Initial saturation (Oil/Gas)	1.0/0.0
Molecular diffusion coefficents in oil phase (C_1/C_2/C_{10})	0.002575/0.001465/0.000625 ft^3/day
Molecular diffusion coefficents in gas	25.75/14.65/6.25 ft^3/day

phase ($C_1/C_2/C_{10}$)	
*F: Flowing grid block; *B: Bypassed grid block.	

TABLE 3.2 – FLUID PROPERTIES FOR THREE-COMPONENT N-ALKANE MIXTURES OF C_1, C_2 AND C_{10}

	Oil (mole fraction)	Gas (mole fraction)	Molecular weight (g/mol)	T_C (℉)	P_C (psia)	ω	V_C (ft^3/lb-mol)
C_1	0.2	0.0	16.043	-116.590	667.20	0.0080	1.59
C_2	0.0	1.0	30.070	90.050	708.35	0.0980	2.37
C_{10}	0.8	0.0	142.285	644.620	321.78	0.5032	9.66

TABLE 3.3 –THROUGHPUT RATIOS FOR THE 1-D DUAL-POROSITY SIMULATIONS USING DIFFERENT SYSTEM LENGTHS AND C MULTIPLIERS.

C	System length (ft)	R_T	Process time without intra-block mass flux (year)	Process time with intra-block mass flux (year)
100	500	0.0919	2.482	15.788
100	1000	0.1566	5.870	22.654
100	2000	0.2829	15.918	38.497
500	500	0.2631	2.482	6.485
500	1000	0.3981	5.870	11.349
500	2000	0.5678	15.918	24.728

TABLE 3.4 –DIFFERENT TIME STEP SIZE USED TO RETAIN THE LONGITUDINAL DISPERSION LEVEL FOR THE 1-D DUAL-POROSITY SIMULATIONS USING DIFFERENT SYSTEM LENGTHS AND C MULTIPLIERS.

C	System length (ft)	Stable injection rate (ft^3/day)	Time step (day)	Dimensionless time step	Dimensionless grid size
100	500	162070.6	0.0403	0.000871	0.002
100	1000	130623.3	0.1000	0.000871	0.002
100	2000	94128.5	0.2776	0.000871	0.002
500	500	161997.6	0.0403	0.000871	0.002
500	1000	130595.2	0.1000	0.000871	0.002
500	2000	94128.5	0.2776	0.000871	0.002

TABLE 3.5 – RESERVOIR PROPERTIES FOR THE VERTICAL 2-D DUAL-POROSITY SIMULATION.

Dimensions (F*/B*)	$2 \times 900 \times 5$ ft^3/$2 \times 100 \times 5$ ft^3
Number of gird blocks	$500 \times 2 \times 10$
Porosity	0.3
Permeability (F*)	2000 md (X,Y), 1000 md (Z)
Permeability (B*)	0.0 md(X,Z), 0.2 md(Y)
Injection well	1,1,10
Production well	500,1,10
*F: Flowing grid block; *B: Bypassed grid block.	

TABLE 3.6 – RESERVOIR PROPERTIES FOR THE 3-D DUAL-POROSITY SIMULATION.

	Flowing region	Bypassed region
Number of gird blocks	$20 \times 20 \times 5$	$20 \times 20 \times 5$
Dimensions	$50 \times 50 \times 9$ ft^3	$50 \times 50 \times 1$ ft^3
Porosity	0.3	0.3
Permeability	2000 md(X,Y), 1000 md(Z)	0.2 md

Injection well	1, 1, 10
Production well	20, 20, 10

TABLE 3.7 – FLUID PROPERTIES FOR C_1, C_3 AND C_{16} MIXTURES IN COREFLOODING CASE 1

	Oil (mole fraction)	Gas (mole fraction)	Molecular weight (g/mol)	T_C (℉)	P_C (psia)	ω	V_C (ft^3/lb-mol)
C_1	0.00	0.74	16.043	-116.59	667.20	0.0080	1.59
C_3	0.35	0.26	44.097	205.97	615.76	0.1520	3.25
C_{16}	0.65	0.00	226.400	839.51	233.72	0.7634	14.74

TABLE 3.8 – RESERVOIR PROPERTIES USED FOR THE 1-D DUAL-POROSITY SIMULATION OF COREFLOODING CASE 1.

Dimensions (F*/B*)	$0.020 \times 1.386 \times 1.969 in^3$/ $0.020 \times 0.189 \times 1.969\ in^3$
Number of girdblocks	$500 \times 2 \times 1$
Porosity	0.262
Permeability (F*/B*)	700 md/0 md(X,Z) 0.7md(Y)
Reservoir pressure	1500 psia
Reservoir temperature	70 ℉
Injection rate	95.191 in^3/min
Production pressure	1500 psia
Relative permeability model	Corey
Residual saturation (Oil/Gas)	0.2/0.0
Endpoint relative permeability (Oil/Gas)	1.000/0.263
Exponent (Oil/Gas)	1.5/6.0
Initial saturation (Oil/Gas)	1.0/0.0
Molecular diffusion coefficents in oil phase (C_1/C_3/C_{16})	0.008/0.005/0.002 ft^3/day
Molecular diffusion coefficents in gas phase (C_1/C_3/C_{16})	0.07/0.05/0.02 ft^3/day
*F: Flowing grid block; *B: Bypassed grid block.	

TABLE 3.9 – FLUID PROPERTIES FOR HASSI-MESSAOUD RESERVOIR OIL MODEL FOR COREFLOODING SIMULATION 2.							
	Oil (mole fraction)	Gas (mole fraction)	MW (g/mol)	T_C (°F)	P_C (psia)	ω	V_C (ft^3/lb-mol)
N_2	0.016	0.000	28.010	-232.510	492.26	0.0400	1.44
CO_2	0.011	0.000	44.010	87.890	1069.80	0.2250	1.51
C_1	0.346	0.800	16.040	-116.590	667.18	0.0080	1.59
C_2	0.135	0.150	30.070	90.050	708.37	0.0980	2.37
C_3	0.09	0.050	44.100	205.970	615.83	0.1520	3.25
C_4	0.056	0.000	58.120	305.690	551.15	0.1930	4.08
C_5	0.037	0.000	72.150	385.610	489.36	0.2510	4.87
C_6	0.029	0.000	86.180	453.650	430.62	0.2960	5.93
PC1	0.113	0.000	121.810	586.022	386.82	0.2189	9.66
PC2	0.079	0.000	173.430	773.744	329.53	0.3975	11.40
PC3	0.056	0.000	244.170	972.734	280.21	0.6273	13.94
PC4	0.034	0.000	409.580	1252.616	216.83	1.0179	16.60

TABLE 3.10 – BINARY INTERACTION PARAMETERS FOR HASSI-MESSAOUD RESERVOIR OIL MODEL FOR COREFLOODING SIMULATION 2.

	N_2	CO_2	C_1	C_2	C_3	C_4	C_6	PC1	PC2	PC3	PC4
N_2											
CO_2	0.00										
C_1	0.10	0.10									
C_2	0.10	0.10	0.00								
C_3	0.10	0.10	0.00	0.00							
C_4	0.10	0.10	0.00	0.00	0.00						
C_5	0.10	0.10	0.00	0.00	0.00						
C_6	0.10	0.10	0.00	0.00	0.00	0.00					
PC1	0.13	0.10	0.00	0.00	0.00	0.00	0.00				
PC2	0.13	0.10	0.00	0.00	0.00	0.00	0.00	0.00			
PC3	0.13	0.10	0.00	0.00	0.00	0.00	0.00	0.00	0.00		
PC4	0.13	0.10	0.00	0.00	0.00	0.00	0.00	0.00	0.00	0.00	

TABLE 3.11 – CORE PROPERTIES USED FOR 1-D SINGLE-POROSITY SIMULATION OF COREFLOODING

SIMULATION 2.	
Dimensions	0.0305×1.3956×1.3956 in^3
Number of gird blocks	500×1×1
Porosity	0.103
Permeability	56 md (X, Y, Z)
Reservoir pressure	3190.83/3480.91 psia
Reservoir temperature	245.30 ℉
Injection rate	7.32 in^3/min
Production pressure	3190.83/3480.91 psia
Relative permeability model	Corey
Residual saturation (Oil/Gas)	0.1/0.0
Endpoint relative permeability (Oil/Gas)	1.0/0.7
Exponent (Oil/Gas)	3.0/3.0
Initial saturation (Oil/Gas)	1.0/0.0

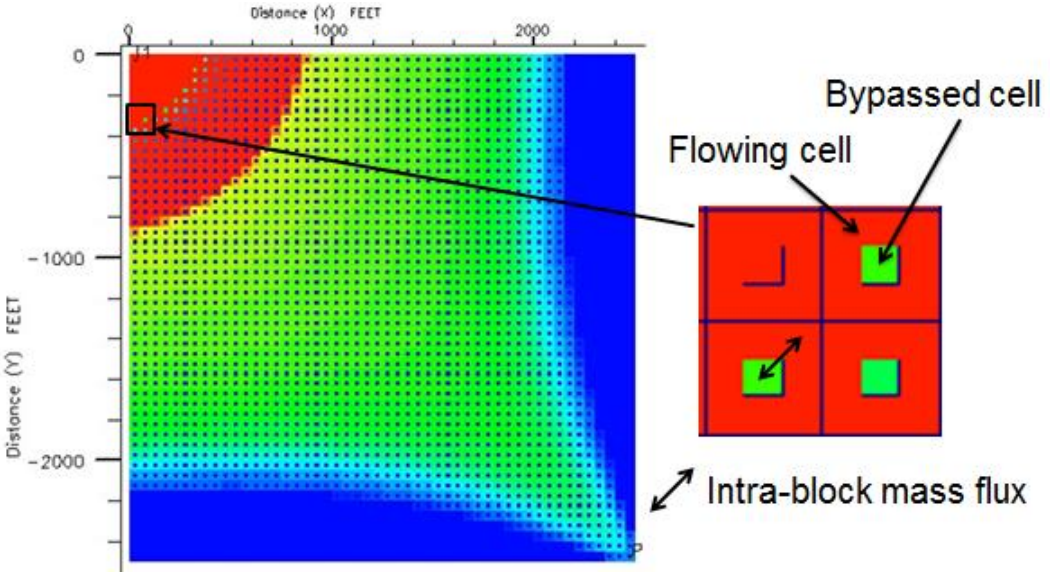

Figure 3.1 The schematic for the dual-porosity flow to model the recovery of bypassed oil.

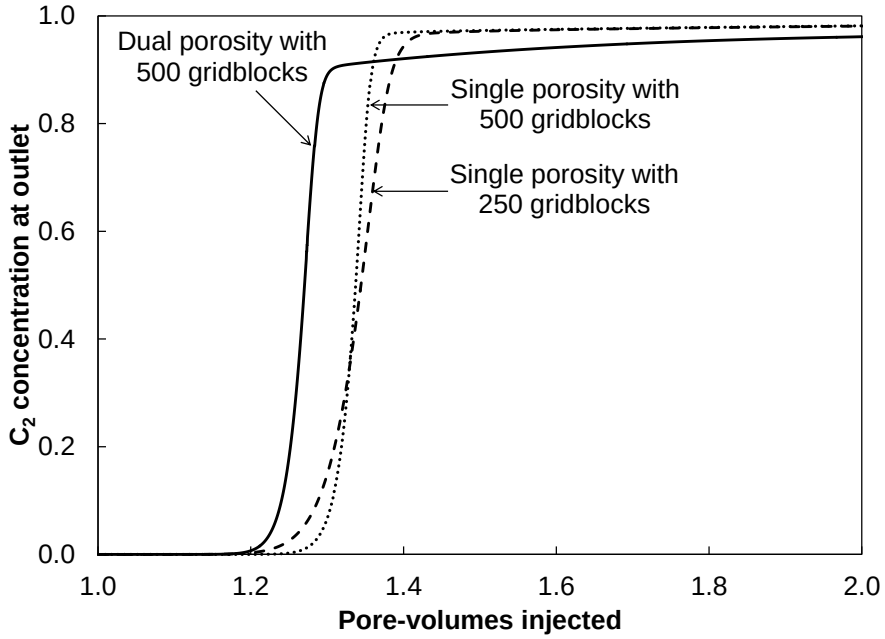

Figure 3.2 C_2 effluent concentration profiles for three cases: dual-porosity (DP) model with 500 gridblocks, single-porosity (SP) model with 500 gridblocks, and SP model with 250 gridblocks.

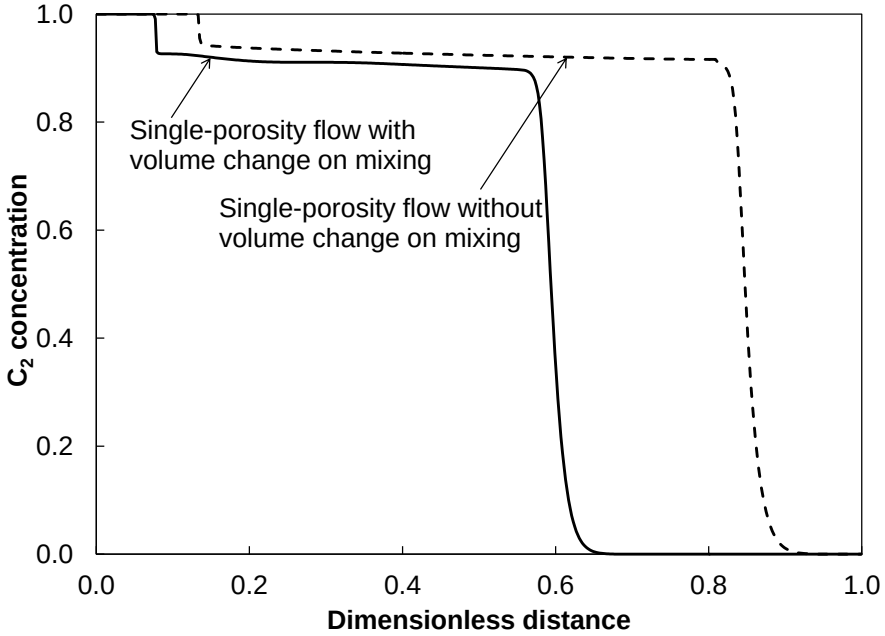

Figure 3.3 C_2 concentration profile at 0.8 PVI for single porosity flow with and without volume change on mixing. The C_2 breakthrough after 1.0 PVI in Figure 3.1 is because of the effects of volume change on mixing.

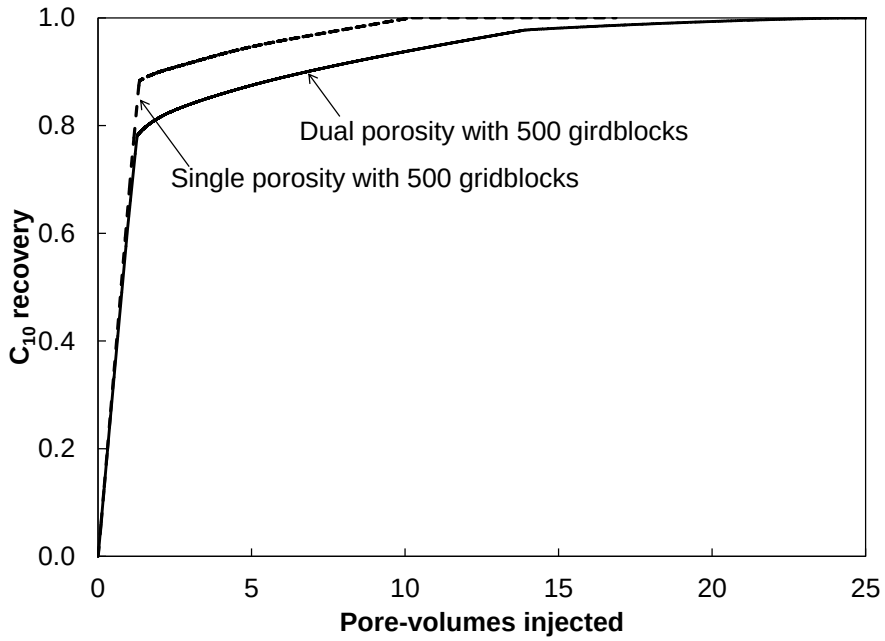

Figure 3.4 Recovery histories for the DP and SP cases with 500 grid blocks. Capacitance effects are observed as the earlier breakthrough and gradual recovery of bypassed oil in the DP simulation.

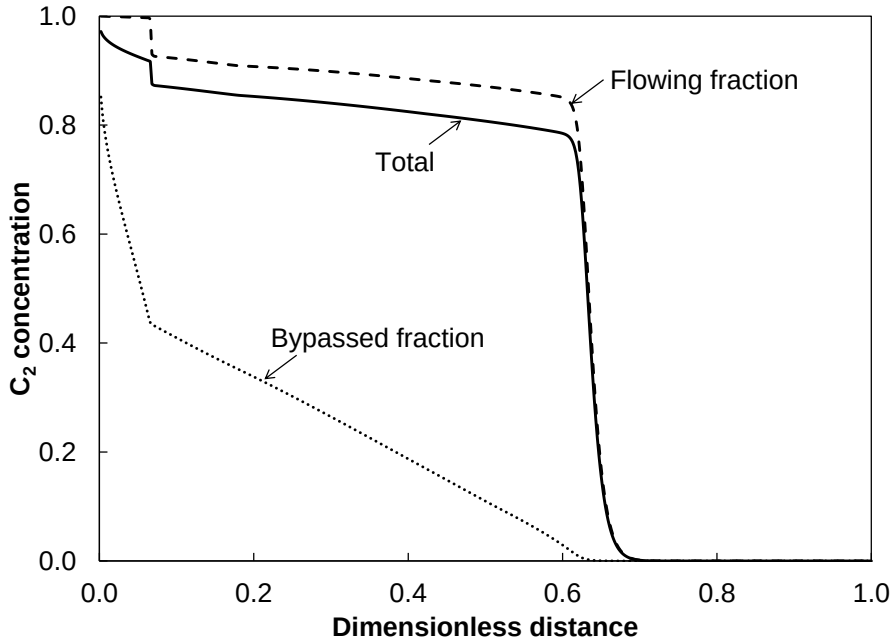

Figure 3.5 C_2 concentration profiles for the flowing fraction, bypassed fraction and total region in the reservoir at 0.8 PVI in the DP case with 500 grid blocks. Reservoir and fluid properties are given in Tables 3.1 and 3.2.

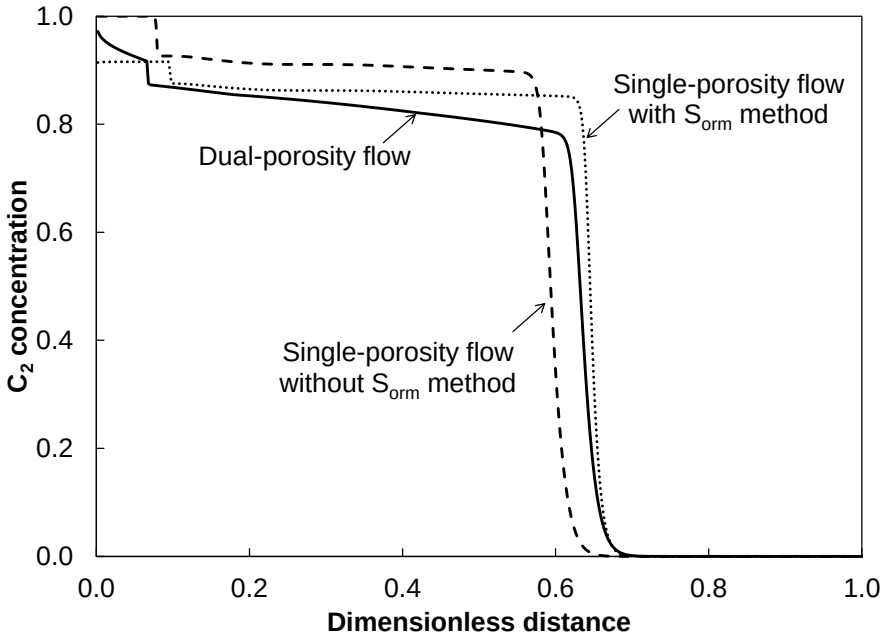

Figure 3.6 C_2 concentration profiles at 0.8 PVI for three cases; DP, SP, and SP with the Sorm method.

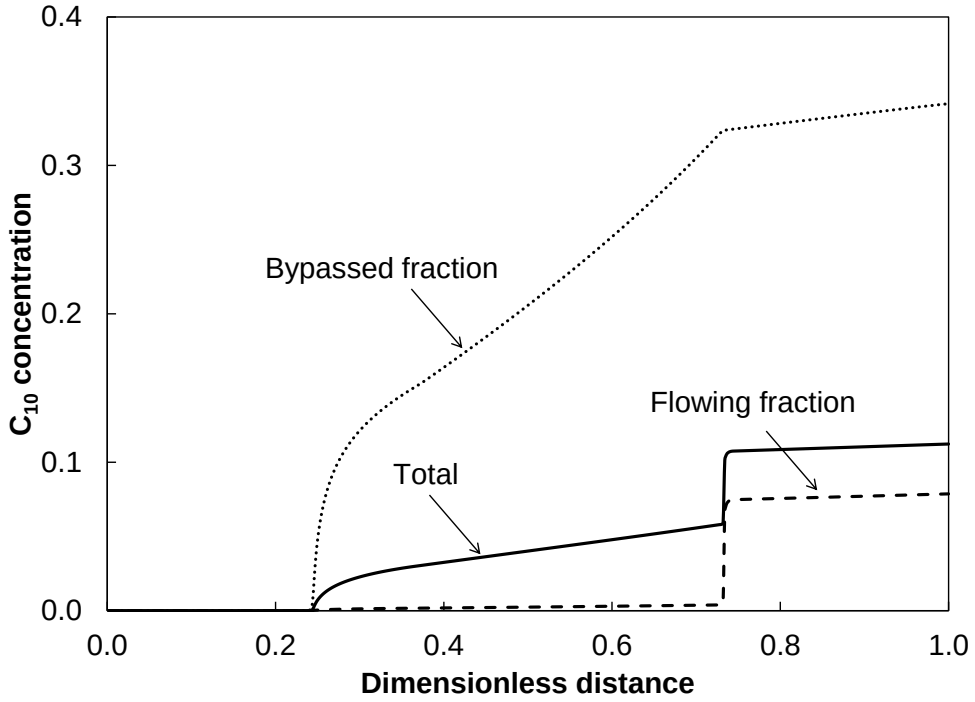

Figure 3.7 C_{10} concentration profile at 10 PVI in the DP simulation, for which reservoir and fluid properties are given in Tables 3.1 and 3.2.

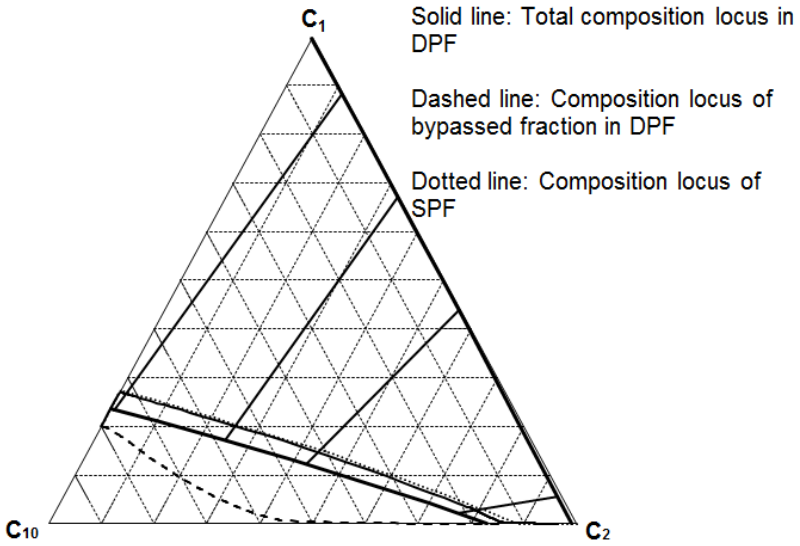

Figure 3.8 Composition variations for the DP and SP cases at 0.8 PVI, which is before gas breakthrough time.

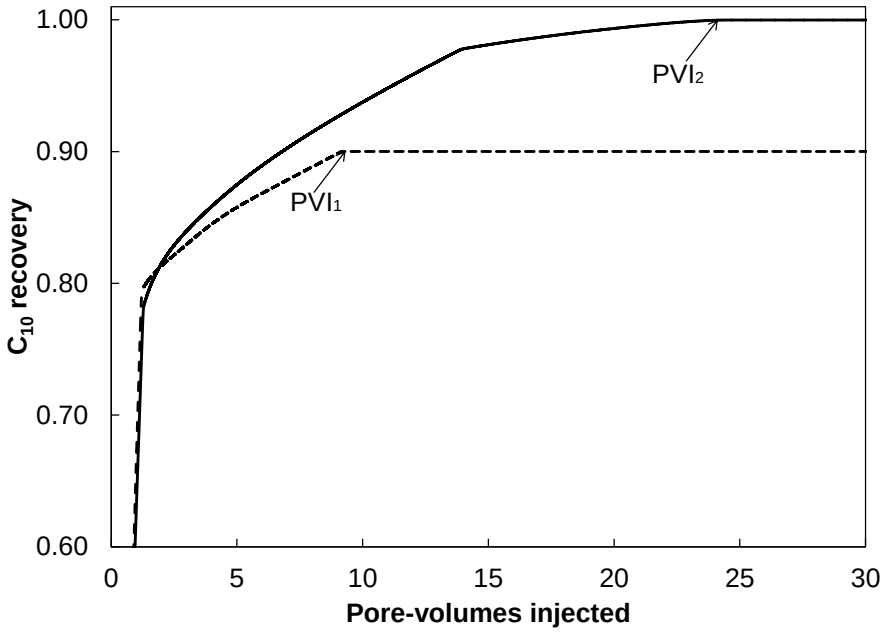

Figure 3.9 C_{10} recovery predictions for the 1-D DP models with and without intra-block mass flux. PVI_1 and PVI_2 stand for the PVIs required for ultimate recovery without and with intra-block mass flux in DPF, respectively.

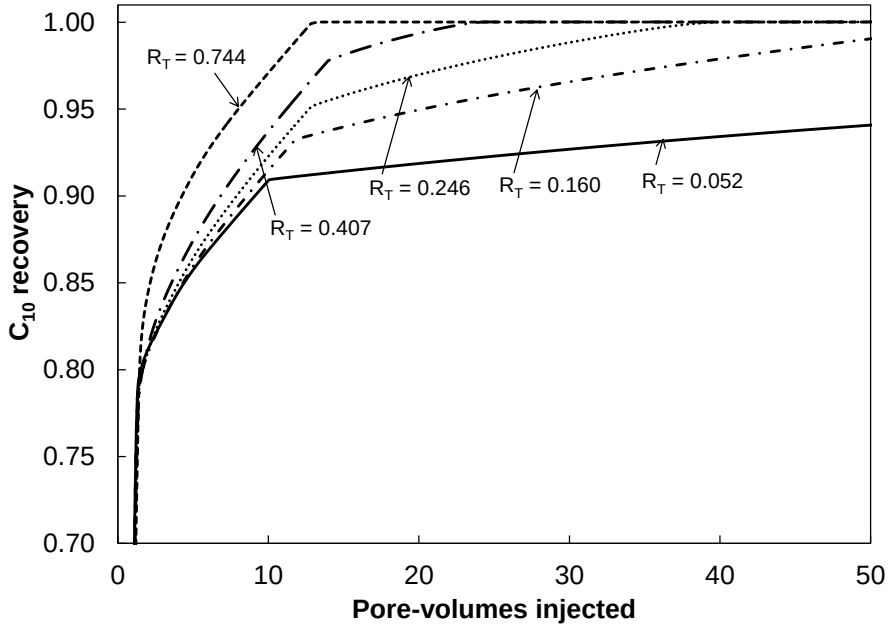

Figure 3.10 C_{10} recovery predictions for the 1-D dual-porosity simulations with different throughput ratios (RT) from 0.052 to 0.744. Oil recoveries with different degrees of capacitance effects are well characterized using R_T.

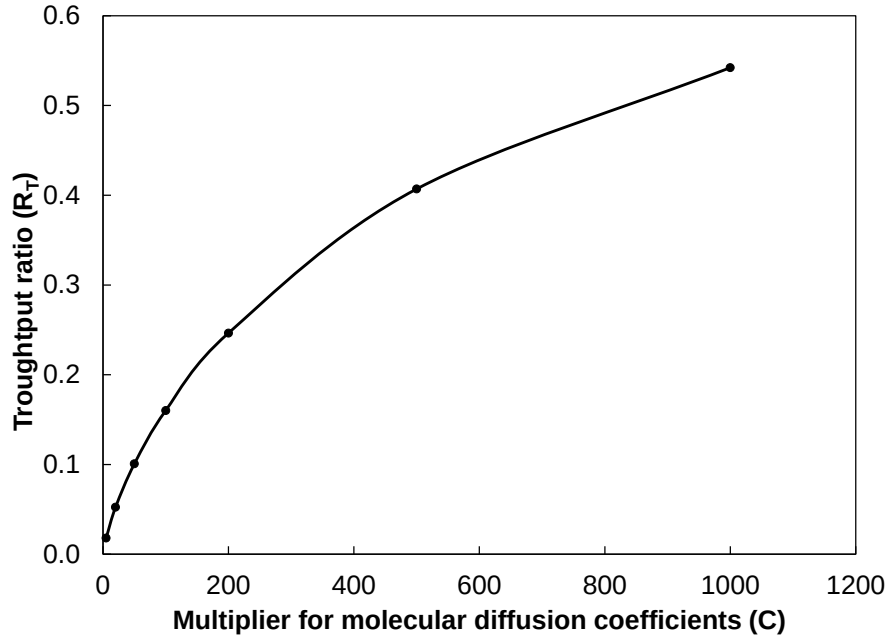

Figure 3.11 Throughput ratio (R_T) monotonically increases with the C multiplier for molecular diffusion coefficients.

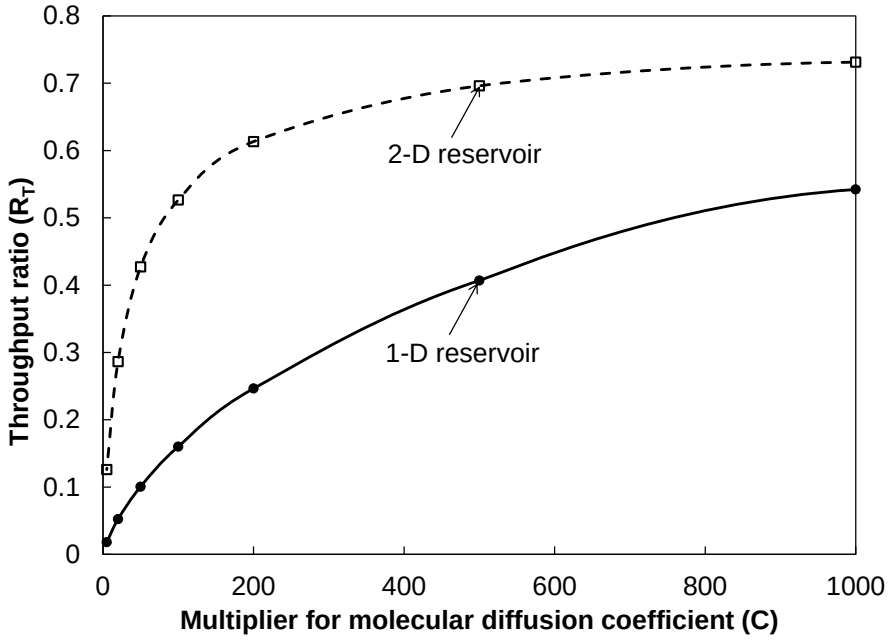

Figure 3.12 Throughput ratios (R_T) for different C values in 1-D and 2-D flow. For a C value of 500, the recovery process time is 90.21 years for the 2-D case and 16.07 years for the 1-D case.

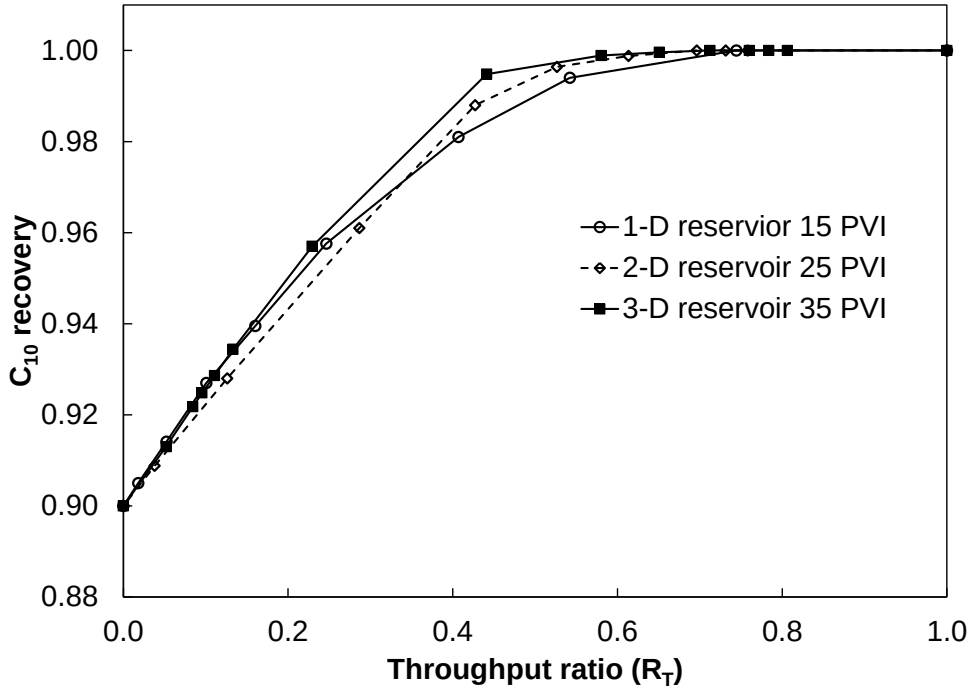

Figure 3.13 C_{10} ultimate recoveries for the 1-D, 2-D and 3-D dual-porosity flow with different throughput ratios.

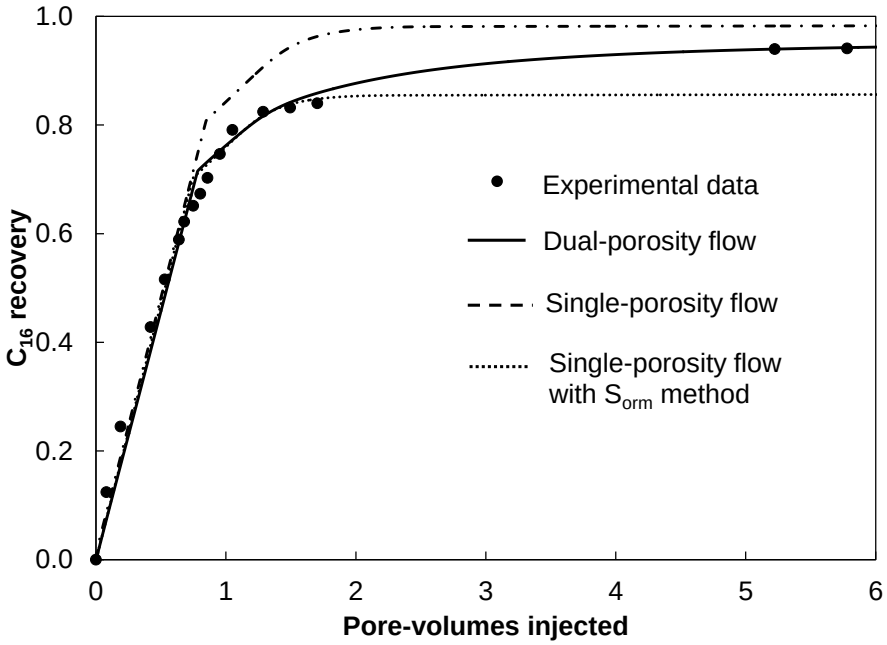

Figure 3.14 1-D DPF model fitted to core floods data of Burger et al. (1996) gives a bypassed fraction of 0.12 and a R_T value of 0.365.

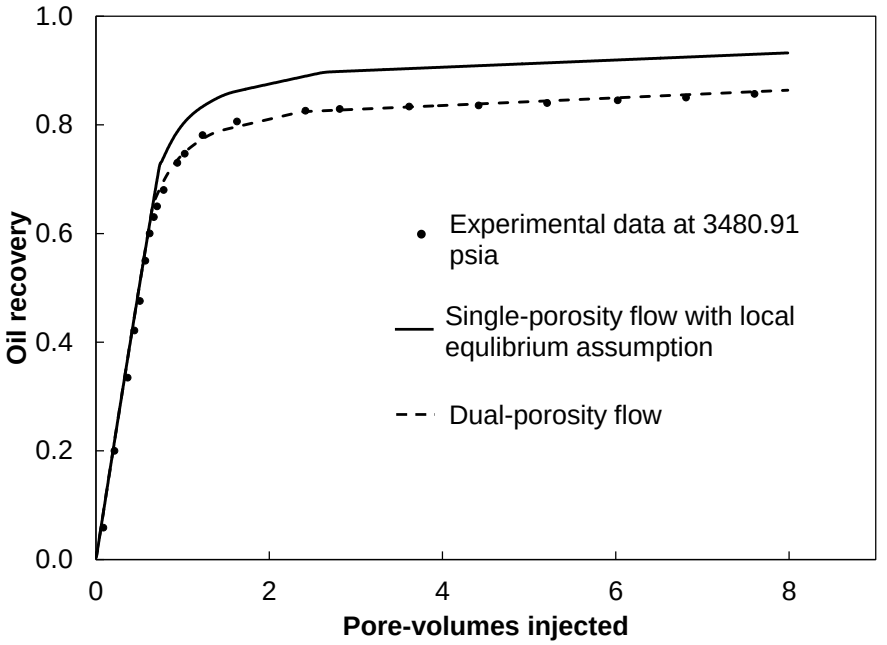

Figure 3.15 1-D DPF model fitted to core floods data of case 2 with P = 3480.91 psia gives a bypassed fraction of 0.1 and a throughput ratio of nearly 0, which represents that the recovery of bypassed oil is almost zero.

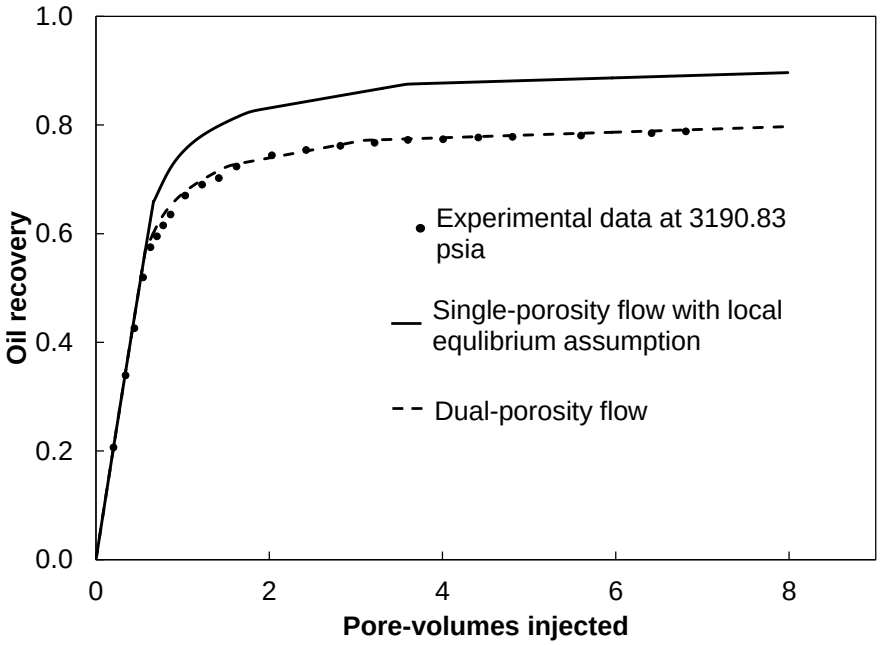

Figure 3.16 1-D DPF model fitted to core floods data of case 3 with P = 3190.83 psia gives a bypassed fraction of 0.14 and a throughput ratio of nearly 0.

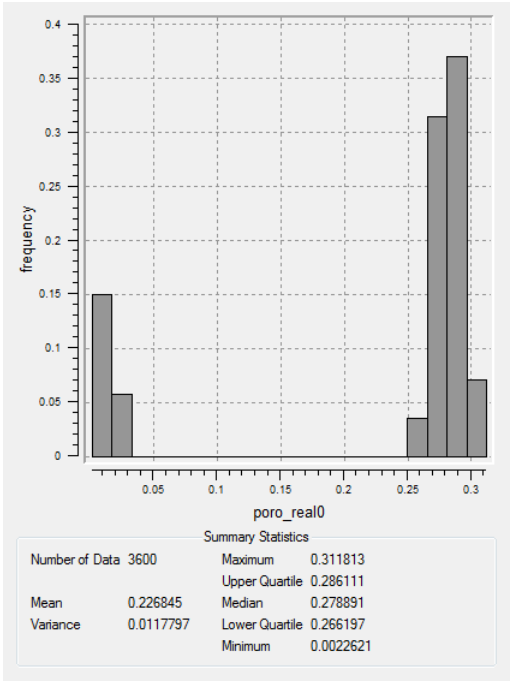

Figure 3.17 The histogram of the porosity for the heterogeneous XY-2D reservoir showing a bimodal distribution for sandstones and shales.

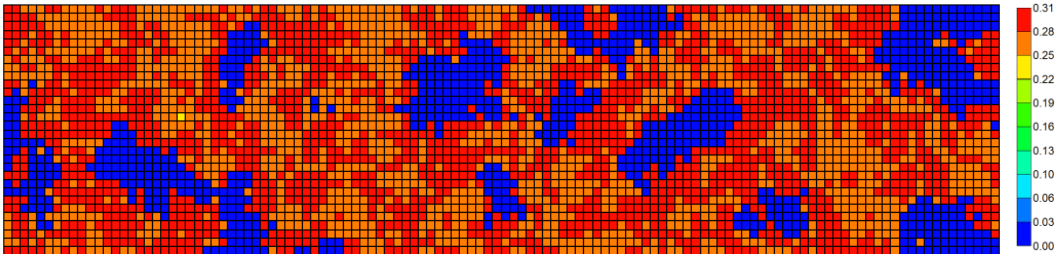

Figure 3.18 The porosity distribution of the heterogeneous XY-2D REV with 0.2 shales distributed with a correlation length of 10 ft according to the histogram given in Figure 3.16.

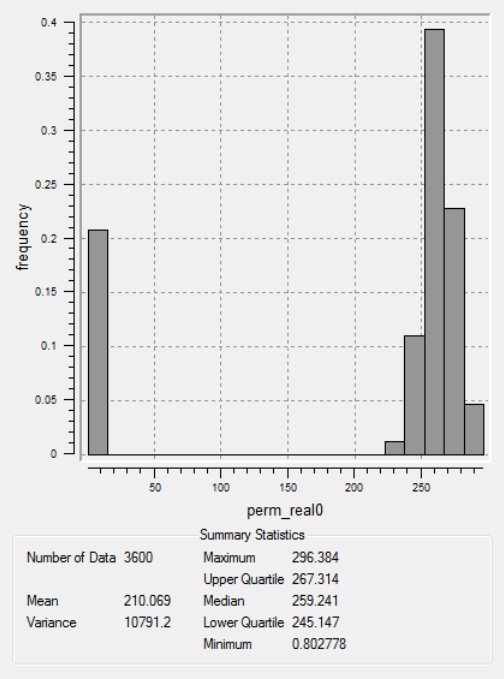

Figure 3.19 The histogram of the permeability for the heterogeneous XY-2D reservoir showing a bimodal distribution for sandstones and shales.

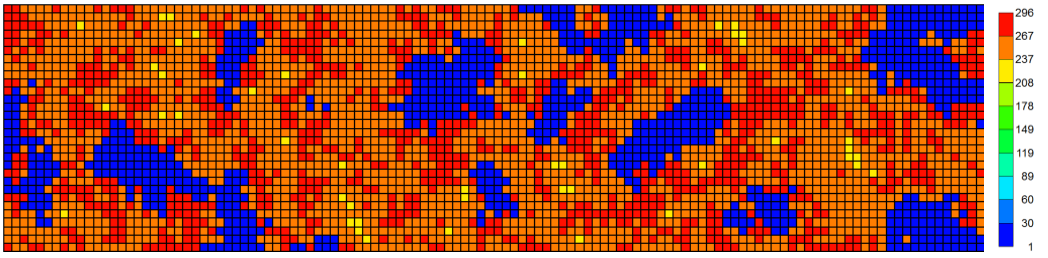

Figure 3.20 The permeability distribution of the heterogeneous XY-2D REV with 0.2 shales distributed with a correlation length of 10 ft according to the histogram of permeability given in Figure 3.18.

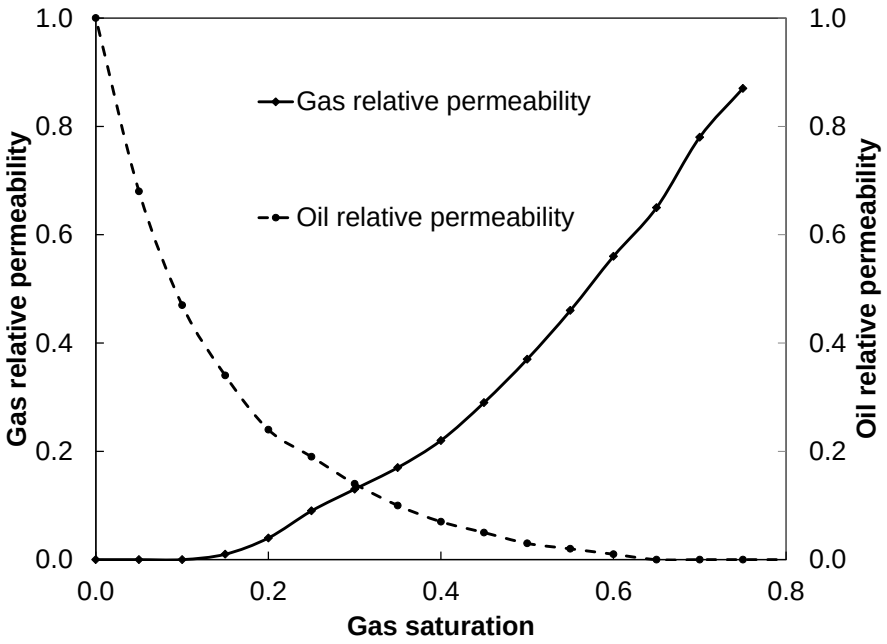

Figure 3.21 Oil and gas relative permeability used for the heterogeneous reservoir in fine and coarse-scale simulations of section 3.5.

@0.7 PVI

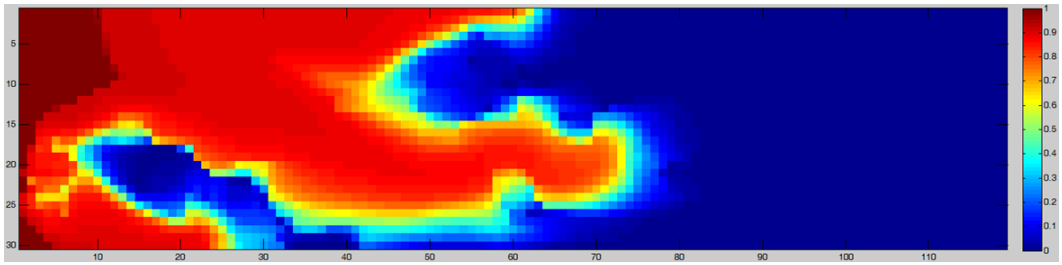

@1.0 PVI

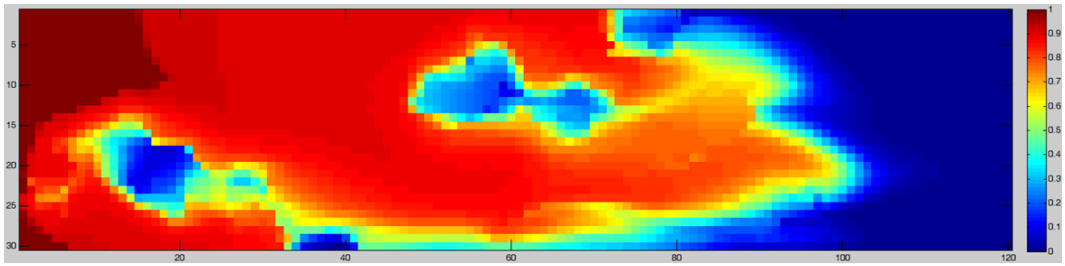

@ 1.5 PVI

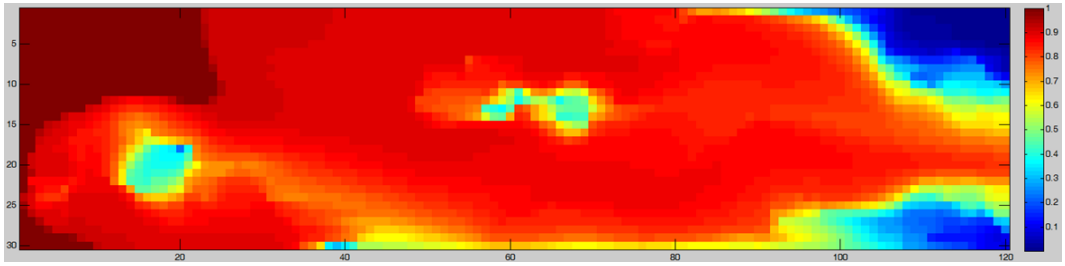

@ 10.0 PVI

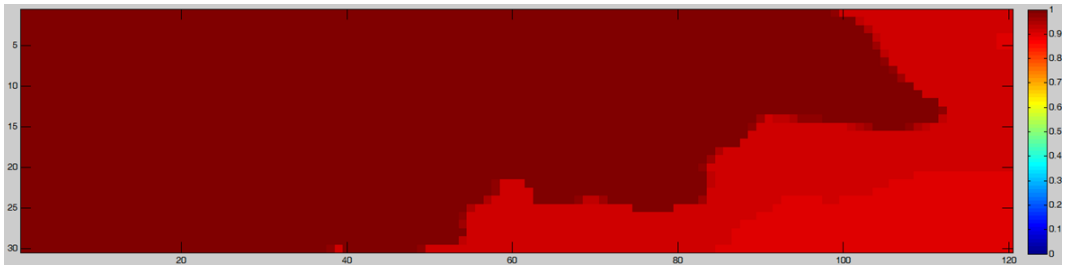

Figure 3.22 The C_2 concentration profile at different PVIs listed above the figures. The bypassing of oil because of channelling can be clearly observed.

Case 1: 5 md for shale

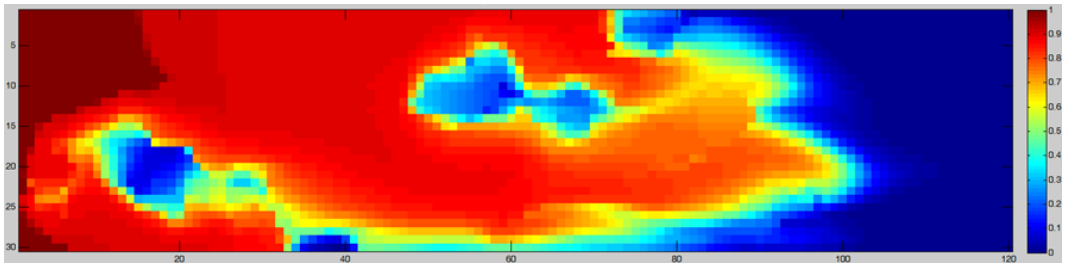

Case 2: 0.5 md for shale

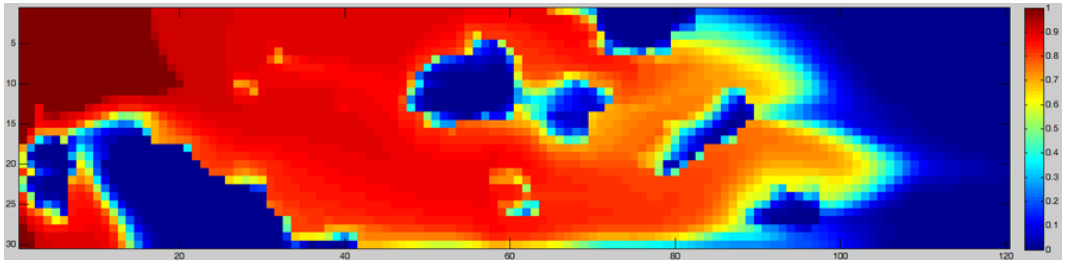

Case 3: 0.05 md for shale

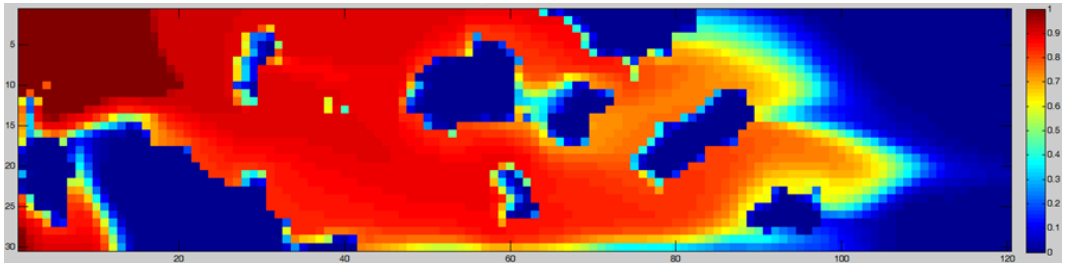

Figure 3.23 C_2 concentration profiles at 1.0 PVI for case 1, 2 and 3. Different permeabilities are assigned to the shales representing the bypassed fraction.

Case 1: 5 md for shale

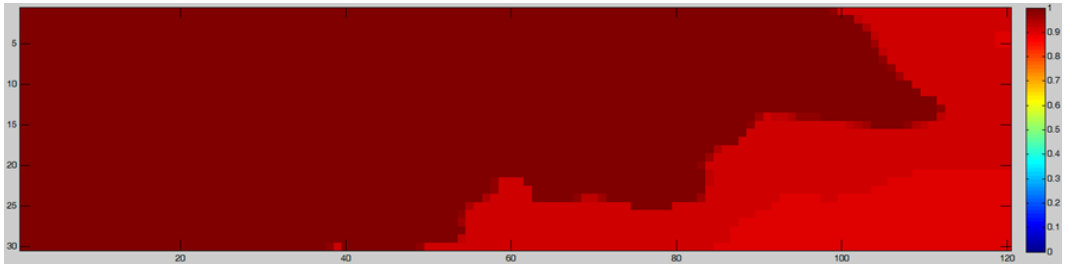

Case 2: 0.5 md for shale

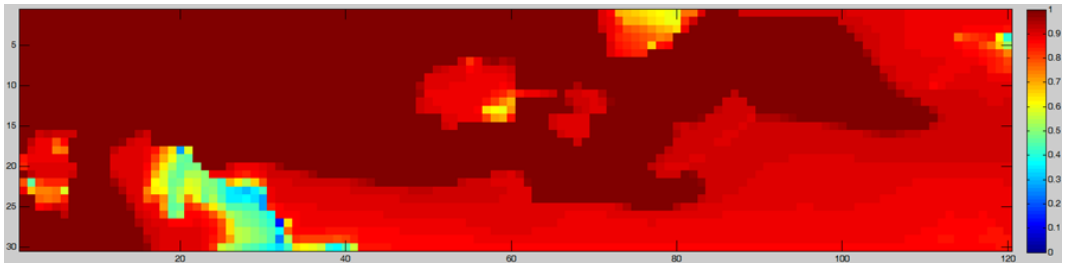

Case 3: 0.05 md for shale

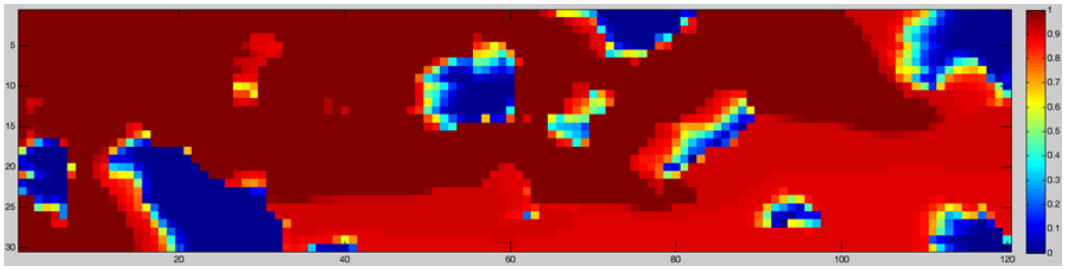

Figure 3.24 The C_2 concentration profiles at 10.0 PVI for case 1, 2 and 3. Different permeabilities are assigned to the shales representing the bypassed fraction.

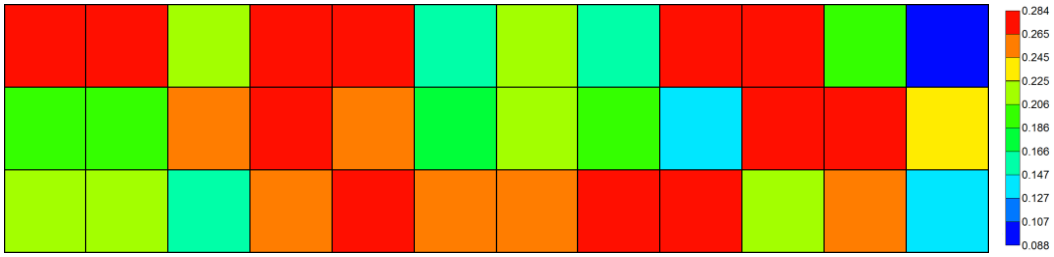

Figure 3.25 The porosity distribution for the upscaled coarse-scale simulations.

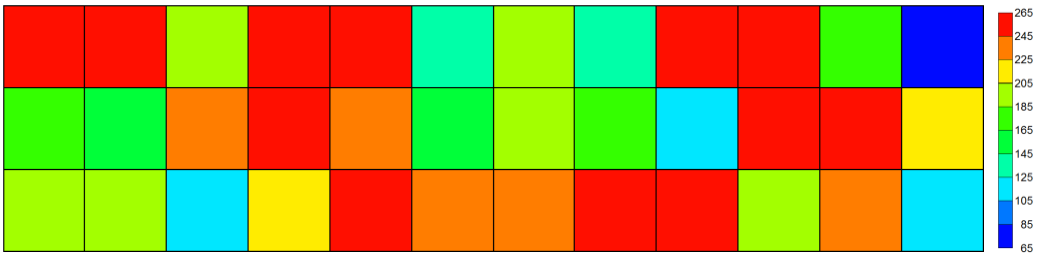

Figure 3.26 The permeability distribution for the upscaled coarse-scale simulations

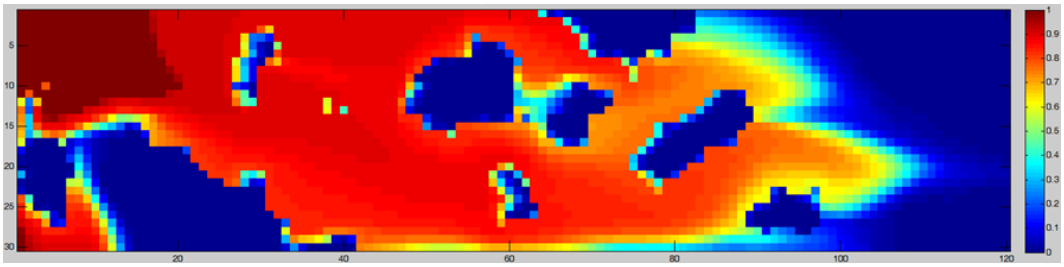

a. Fine-scale simulation for case 3 at 1.0 PVI

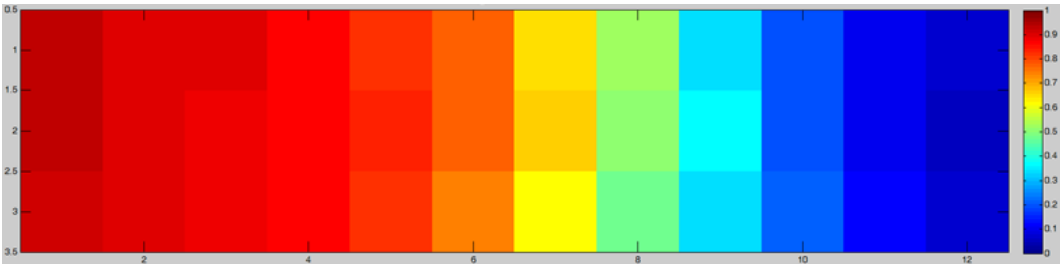

b. Coarse-scale simulation for case 3 at 1.0 PVI

Figure 3.27 Comparisons between C_2 concentration profiles for fine-scale simulation and upscaled coarse-scale simulation in case 3 at 1.0 PVI.

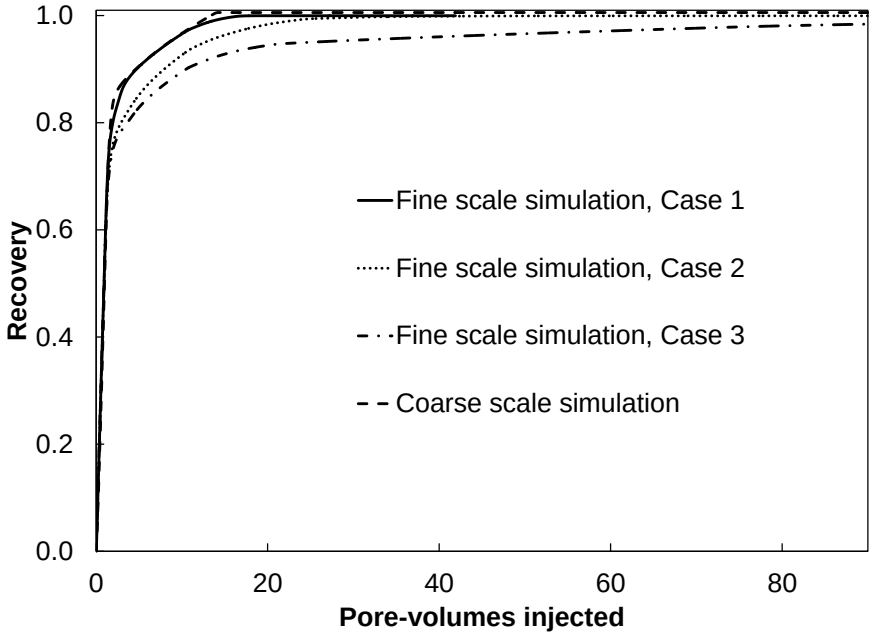

Figure 3.28 Recovery predictions for the fine-scale simulations and upscaled coarse-scale simulation. Different permeabilities are assigned to shale representing bypassed fraction.

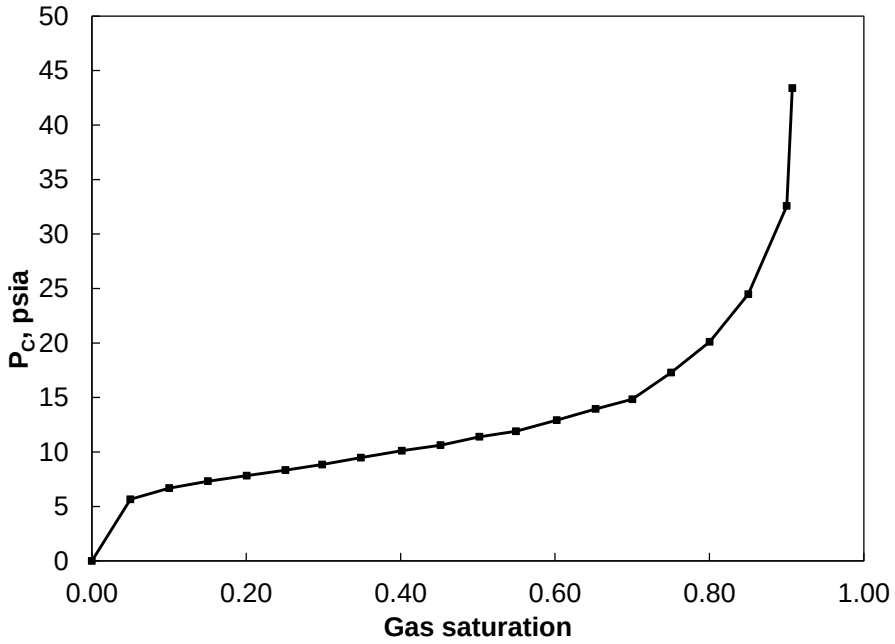

Figure 3.29 Capillary function used for the fine and coarse-scale simulations with capillary pressure.

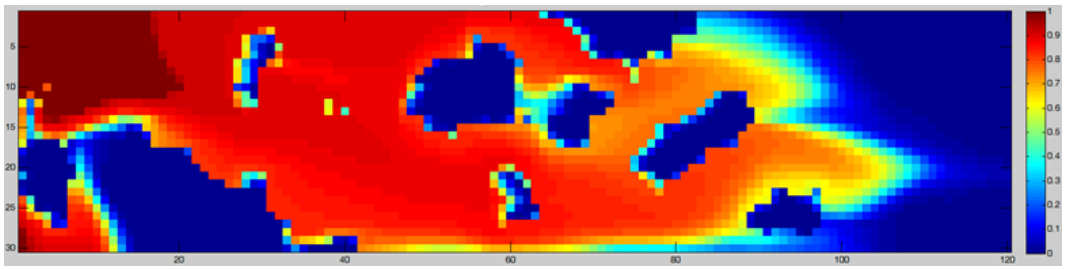

a. Without capillary pressure: $\frac{MN_{cv}}{1+M} = 0$

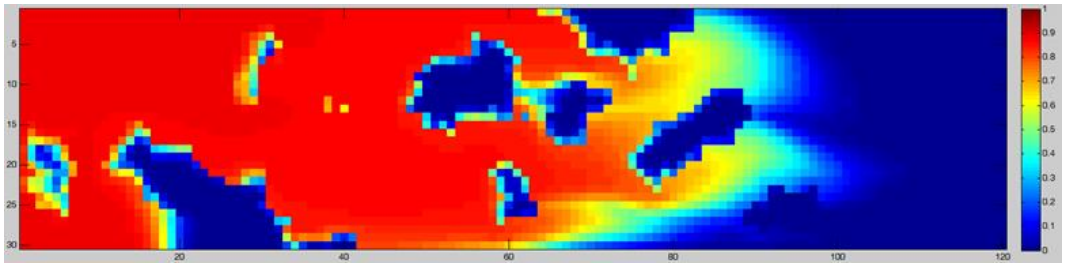

b. With capillary pressure: $\frac{MN_{cv}}{1+M} = 8.6$

Figure 3.30 Comparisons between C_2 concentration profiles for fine-scale simulation with and without capillary pressure at 1.0 PVI in case 3.

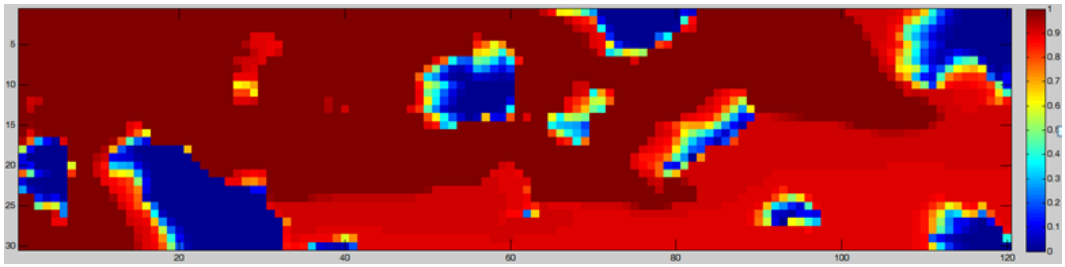

a. Without capillary pressure: $\frac{MN_{cv}}{1+M} = 0$

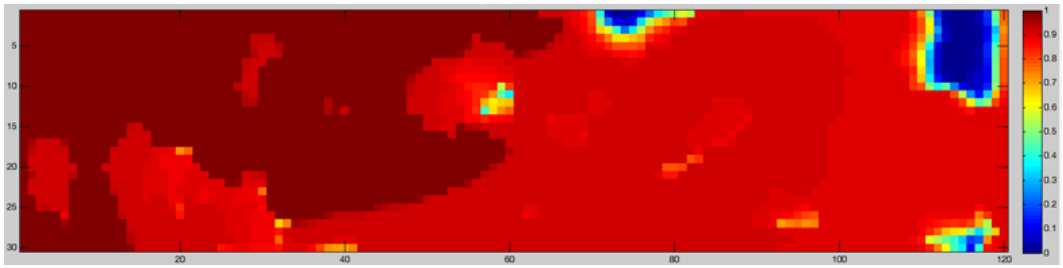

b. With capillary pressure: $\frac{MN_{cv}}{1+M} = 8.6$

Figure 3.31 Comparisons between C_2 concentration profiles for fine-scale simulation with and without capillary pressure at 10.0 PVI in case 3.

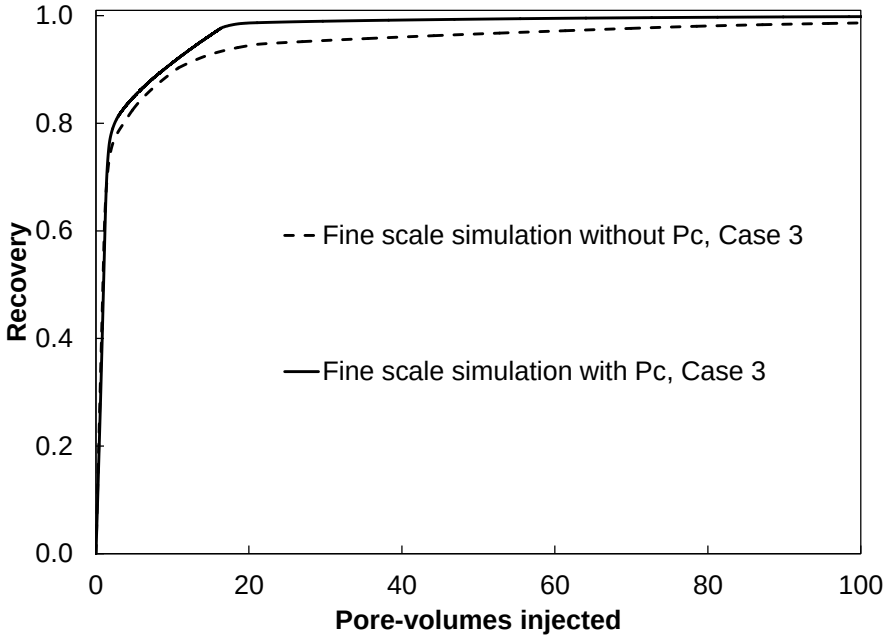

Figure 3.32 Comparisons of recovery prediction for fine-scale simulation with and without capillary pressure in case 3.

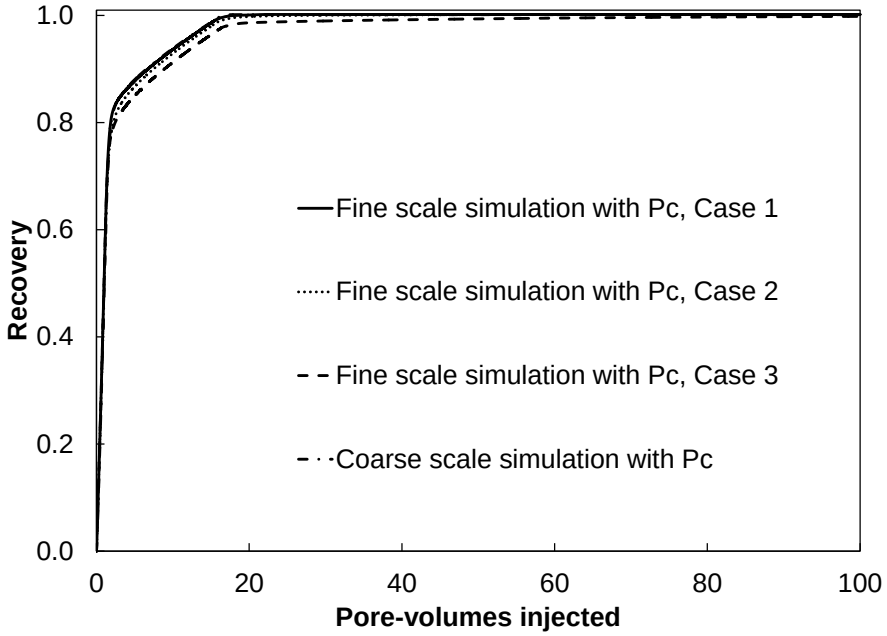

Figure 3.33 Comparisons of recovery prediction for fine-scale simulation and coarse-scale simulation with capillary pressure from case 1 to case 3.

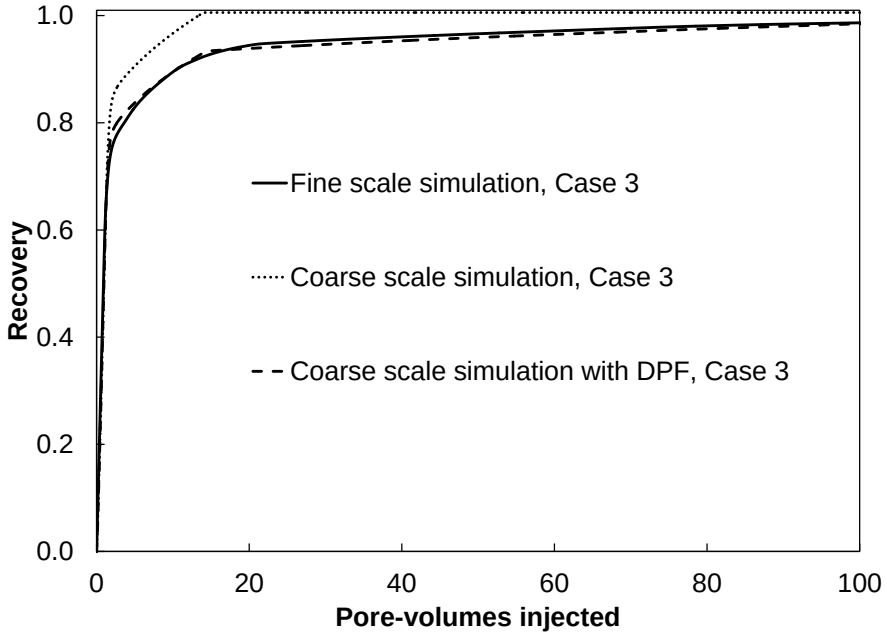

Figure 3.34 Recovery predictions for fine-scale simulation and coarse-scale simulation with and without the dual-porosity method for case 3 (capillary pressure is not considered in this example).

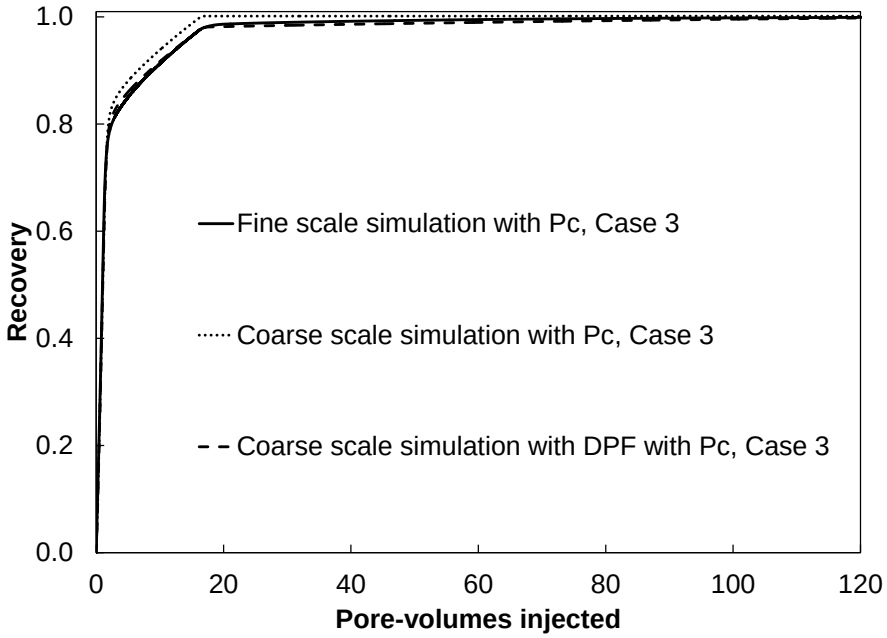

Figure 3.35 Recovery predictions for fine-scale simulation and coarse-scale simulation with and without the dual-porosity method for case 3 considering capillary effects.

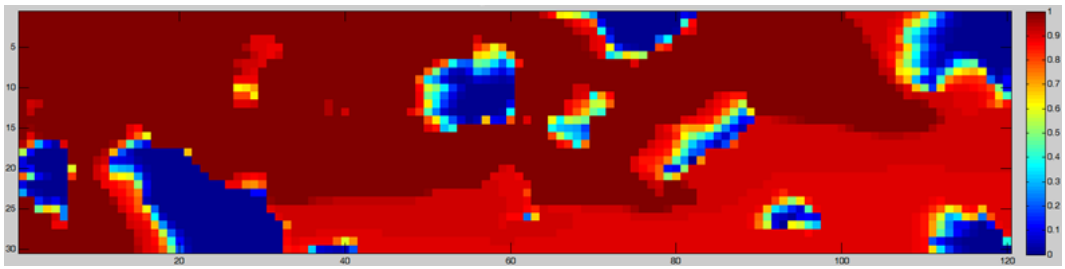

a. Fine-scale simulation

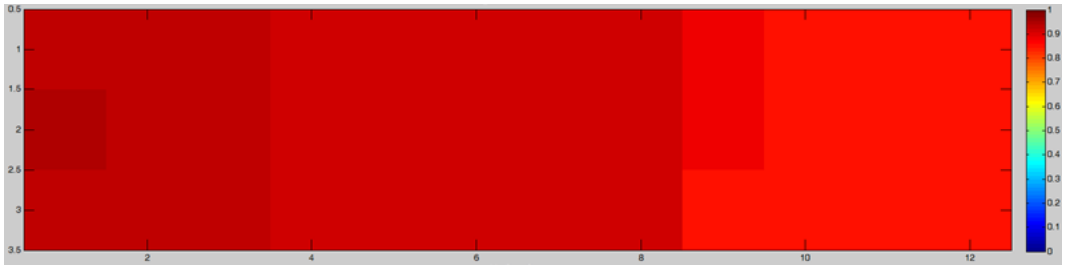

b. Coarse-scale simulation with DPF in average bypassed fraction

Figure 3.36 C_2 concentration profile for fine-scale simulation and coarse-scale simulation with DPF in averaged bypassed fraction for case 3 without capillary pressure at 10.0 PVI.

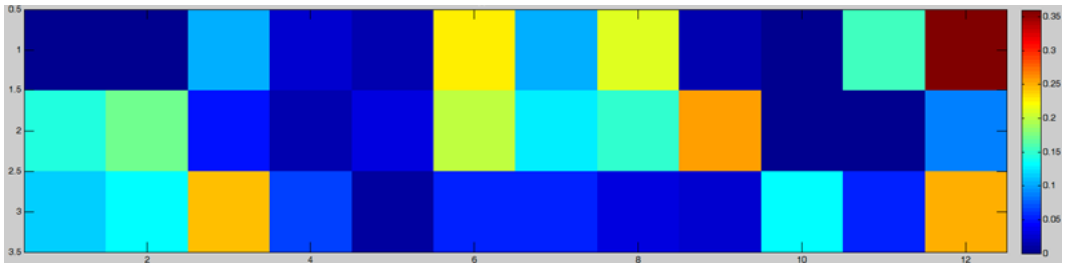

Figure 3.37 Bypassed oil fraction distributions for case 3 without capillary pressure.

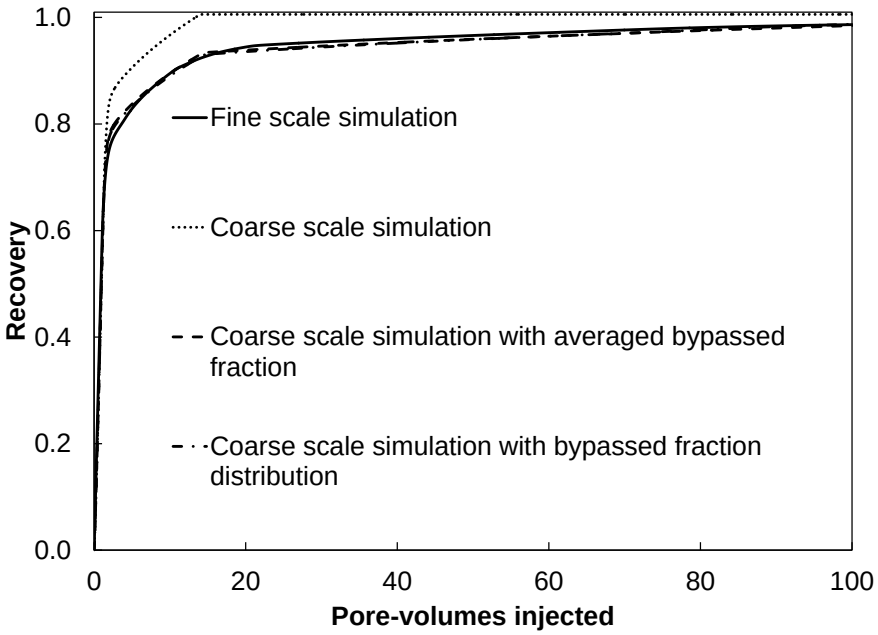

Figure 3.38 Recovery predictions showing that both averaged and various bypassed fraction distribution result in an accurate result with fine-scale simulation.

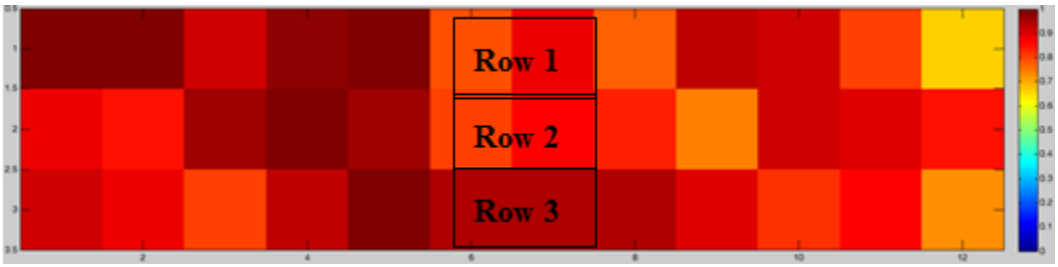

Figure 3.39 C_2 concentration profile for coarse-scale simulation with DPF in various bypassed fraction distribution for case 3 without capillary pressure at 10.0 PVI.

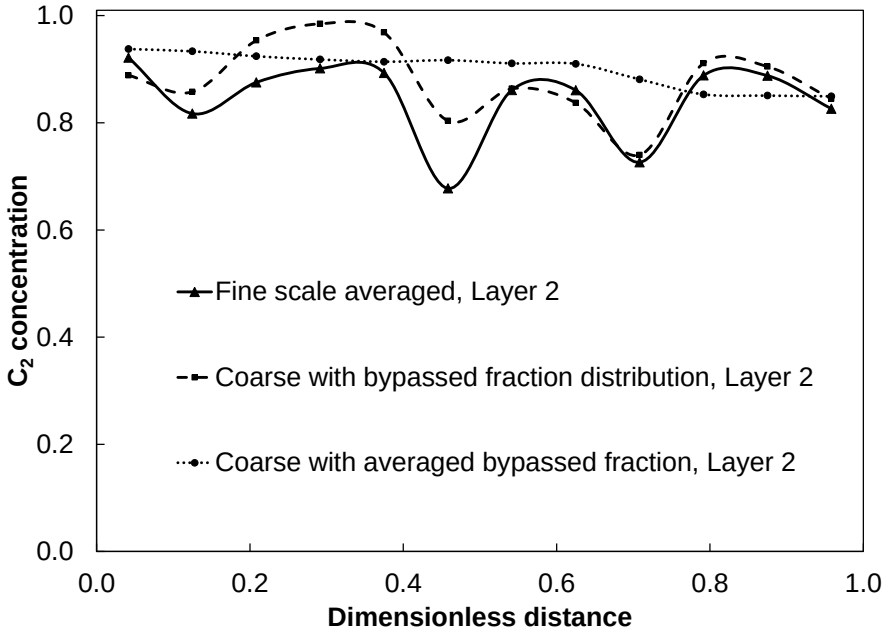

Figure 3.40 C_2 concentration profile for fine-scale simulation and coarse-scale simulation with various and averaged bypassed fraction in DPF for case 3 without capillary pressure at 10.0 PVI in row 2.

CHAPTER 4: FLUID CHARACTERIZATION METHOD FOR CAPACITANCE EFFECTS FOR N-ALKANES MIXTURES

The previous section showed that flow characteristics of DPF resemble those in displacement of heavier oil. Addition of heavy components to model bypassed oil is mentioned in literatures but no specifics have been discussed in the literature for such fluid characterization. This section presents a fluid characterization method that corrects an EOS fluid model for capacitance by adding fictitious heavier components. The SPF with a corrected fluid model successfully mimics the flow characteristics of capacitance effects modelled by DPF in previous section.

The alpha-factor method directly controls components' fluxes in phases to match local fluxes in fine-scale simulation with those in upscaled simulation. We control propagation rates of overall compositions in SPF by correcting an EOS fluid model for capacitance effects. Our method essentially equates the accumulation terms of the mass conservation equations for DPF and SPF along a representative 1-D flow path at different PVIs. The alpha-factor method equates the local flux terms of the mass conservation equations for fine-scale and upscaled simulations.

4.1 Introduction of fictitious heavy oil component

Addition of heavy components vaporizing slowly to model bypassed oil is mentioned in Barker et al. (2005) and the Eclipse manual (Schlumberger 2011). However, it is mentioned that experimental PVT properties cannot be matched if heavy components are introduced. Actually experimental PVT properties such as density and viscosity are possible to be matched by use of volume-shift parameters. In this section, we are going to describe how the introduced heavy components are split from the original oil components.

The original idea of splitting the original EOS comes from the work of Kim (1993) to track the injected components. Typical injected components such as CO_2, methane, ethane, or propane often exist in the initial reservoir hydrocarbon fluid. In order to distinguish between injected and resident components in the convention composition simulation, the common components in the EOS are split into two pseudo-components with identical equation of state parameters: one initially present in the resident reservoir fluid, the other to be carried in the injection gas.

Based on the idea of splitting the common components in the EOS, Hiraiwa and Suzuki (2007) partition the original fluid system into mobile & immobile fraction to consider the non-vaporizing residual oil saturation as it shows in Figure

4.1. Alpha-factors of unity and zero are specified for mobile and immobile components, respectively. However, the "immobile" component is confirmed to be recoverable by mass transfer between the bypassed region and flowing region so zero alpha-factor will underestimate the recovery of the "immobile" component.

The flow characteristics of DPF resemble the faster displacement front and slower evaporation wave in displacement of heavier oil as presented in Figures 3.5 and 3.6. If fictitious heavy oil components are introduced, a slower evaporation wave will be obtained because of larger K value. Also the propagation speed of the displacement front will become faster. These are the two main reasons to introduce fictitious heavy components in single-porosity flow to resemble the flow characteristics modelled by the dual-porosity method.

4.2 Mathematical development for new fluid characterization method

The mathematical development for modelling bypassed oil in the dual-porosity flow is proposed in section 3.3. In this section, the mathematical development is extended to the new fluid characterization method in single-porosity flow to reproduce the flow characteristics modelled by the dual-porosity method.

For the new fluid characterization method, one more fictitious component is introduced for component i to represent the component i which is bypassed in

stagnant volume. The material balance equation for component i in a coarse gird block for the coarse-scale simulation with corrected EOS can be written as:

$$\frac{d}{dt}\int_V \phi \sum_{j=1}^{n_p}(x_{ij+}x_{Hij})\rho_j S_j \, dV + \oint_A \vec{n}\cdot\sum_{j=1}^{n_p}(x_{ij+}x_{Hij})\rho_j\vec{v_j}dS = 0, \qquad (4.2.1)$$

where x_{Hij} is mole fraction of introduced heavy component i in phase j.

If we consider the whole reservoir, the flux term $\oint_A \vec{n}\cdot\sum_{j=1}^{n_p}(x_{ij+}x_{Hij})\rho_j\vec{v_j}dS$ will be cancelled out between the neighbourhood grid block. Instead, the injection and production amount need to be considered in the material balance:

$$\frac{d}{dt}\int_V \phi \sum_{j=1}^{n_p}(x_{ij}+x_{Hij})\rho_j S_j \, dV + \int_V \sum_{j=1}^{n_p} q_{ij}^I \, dV - \int_V \sum_{j=1}^{n_p} q_{ij}^P \, dV = 0. \qquad (4.2.2)$$

From the material balance equation for DPF (equation 3.3.5) and SPF with corrected EOS (Equation 4.2.2), the injection and production amount should be identical if recovery prediction requires to be matched. The objective function for the new fluid characterization method to mimic the recovery prediction of DPF is obtained as below:

$$\frac{d}{dt}\int_V \phi \sum_{j=1}^{n_p}(x_{ij}+x_{Hij})\rho_j S_j \, dV - \frac{d}{dt}\int_{V^F} \phi^F \sum_{j=1}^{n_p} x_{ij}^F \rho_j^F S_j^F \, dV = \int_V \sum_{j=1}^{n_p} q_{ij}^T dV. \qquad (4.2.3)$$

The key to satisfy equation (4.2.3) is to match the propagation speed of the introduced heavy oil component with the transverse mass transfer rate from bypassed region to flowing region as presented in the algorithm in section 4.4.

If it is required to match the concentration profiles for DPF and SPF with corrected EOS, the objective function is listed as below:

$$\frac{d}{dt}\int_V \phi \sum_{j=1}^{n_p}(x_{ij}+x_{Hij})\rho_j S_j \, dV =$$

$$\frac{d}{dt}\int_{(1-B)V} \phi^F \sum_{j=1}^{n_p} x_{ij}^F \rho_j^F S_j^F \, dV + \frac{d}{dt}\int_{BV} \phi^B \sum_{j=1}^{n_p} x_{ij}^B \rho_j^B S_j^B \, dV. \quad (4.2.4)$$

According to the characteristics of capacitance effects reproduced by DPF, the appropriate phase behaviour of the introduced heavy component i should be possible to mimic the faster displacement front and slower evaporation wave. The algorithm of determining the EOS parameters and mole fraction ratio of the introduced heavy component is developed in the following sections by use of the two adjustment parameter together with correlations of Kumar and Okuno (2013).

4.3 f_{MW} and z_{Hi} in the fluid characterization method

The properties of equilibrium phases are modelled with an EOS in compositional flow simulation. Different kinds of EOS are proposed after van der Waals equation to improve the accuracy in predicting the vapor pressure or phase properties. In this research, the PR EOS (1976) is used. The three decisive parameters to determine the phase behaviour are critical temperature (T_C), critical pressure (P_C) and acentric factors (ω) in the PR EOS. To limit the flexibility in selecting heavier components to be added, fluid system consisted of n-alkane mixtures is used in this section. The correlations of Kumar and Okuno (2013)

introduced in chapter 2 are used to estimate critical temperatures (T_C), critical pressures (P_C), and acentric factors (ω) of n-alkanes in the PR EOS. As this correlation only depends on molecular weight (MW) for each component, we only need to estimate the potential MW for the introduced heavy oil component to calculate the corresponding EOS parameters.

One of the key tuning parameter f_{MW} is defined as the ratio of the MW for the introduced heavy oil component and original component:

$$f_{MW} = MW_{Hi}/MW_i, \tag{4.3.1}$$

where MW_{Hi} is the estimated molecular weight for the introduced heavy oil component. In this research, a single f_{MW} is used for each component to limit the flexibility. The increased MWs are only used to generate the EOS properties for the introduced heavy component. The original MWs are still used for both original fraction and introduced heavy fraction in the simulations to maintain the material balance.

The mole fraction ratio of the introduced heavy components in original components is another important adjustment parameter. It determines the height of the evaporation wave of the introduced heavy component corresponding to the slower trailing front in DPF because of the bypassing of the original component. The definition of z_{Hi} is presented as below:

$$z_{Hi} = \sum_{j=1}^{n_p} x_{Hij} / \sum_{j=1}^{n_p} (x_{ij} + x_{Hij}), \quad (4.3.2)$$

where x_{Hij} is the mole fraction of heavy component i in phase j. Similar to f_{MW}, z_{Hi} for each component is identical in this research to limit the flexibility. In composition space, z_{Hi} determines the initial oil tie line.

The introduced heavy component gives the flexibility in component phase behaviour between the injection and initial oil compositions, which enables to control components' propagation speed in our method. However, it also alters volumetric phase behaviour such as original oil density and viscosity. Volume-shift parameter is used to retain volumetric phase behaviour along the mixing lines between the gas and two oils: one consisting of original component, and the other consisting of the introduced heavy component. In this research, the dimensionless volume-shift parameter is used to retain the original oil density and viscosity. The definition of the dimensionless volume-shift parameter is defined as the ratio of volume-shift parameter and covolume parameter for component i:

$$c_{Di} = c_i / b_i, \quad (4.3.3)$$

where c_i is the volume-shift parameter and b_i is the covolume parameter for component i.

Based on the two tuning parameters f_{MW} and z_{Hi}, we are able to reproduce the compositional phase behaviour considering capacitance effects. The volumetric

phase behaviour is also retained by use of the dimensionless volume-shift parameter for the introduced heavy component. A systematic procedure is proposed for the new flow-based characterization method for n-alkane mixtures in the next section.

4.4 Algorithm for the fluid characterization method based on the correlation for n-alkanes

The algorithm for the fluid characterization method is proposed based on a sample case in reproducing the recovery prediction of a 1-D DPF with a C multiplier of 100. The determination of the two tuning parameter f_{MW} and z_{Hi} is the two main steps in the procedure. The quaternary diagram of the corrected EOS explains the flexibility given by the introduced heavy component in composition space.

The C_{10} recovery prediction for the DPF is presented in Figure 4.2. The bypassed fraction is assigned to be 10% for this sample case. R_T for this case is 0.155, which indicates that capacitance effects cannot be modelled using effective longitudinal dispersion. Fluid and reservoir properties are the same as listed in Tables 3.1 and 3.2. In Figure 4.2, Time 1 is the PVI at the breakthrough time. The PVI when the evaporation wave reaches the outlet in the flowing region is defined as Time 2.

The first step for the fluid characterization method is to partition oil components in the EOS fluid model into two fractions: one with the original components and the other with heavier components. In this case, we only split the oil component C_{10} into the C_{10} and C_{H10} (heavier C_{10}). That is, z_{C10} in the original model is the sum of z_{C10} and z_{CH10} in the new model, where z_i is the overall mole fraction of component i.

The EOS properties for the introduced heavy oil component are determined in the step 2. EOS properties of C_{H10} are determined by increasing MW from the MW of C_{10} in the correlation of Kumar and Okuno (201) given in chapter 2 until the total C_{10} (i.e., C_{10} and C_{H10}) recovery matches that from the 1-D DPF for the period after Time 2 in Figure 4.2. This adjustment of MW is performed using the f_{MW} multiplier for MW in Equations 4.3.1. Note that the f_{MW} multiplier is different from the perturbation factors used in the fluid characterization method of Kumar and Okuno (2013). In this case, f_{MW} of 1.43 yields a good match for the recovery after Time 2 as shown in Figure 4.2.

The C_{H10} component gives one more dimension to composition space of the fluid model. Figure 4.3 shows the resulting quaternary composition space at the reservoir temperature and pressure, 158 ℉ and 1020.85 psia. Two phases span a

volumetric region, giving a variation between the C_1-C_2-C_{10} ternary and the C_1-C_2-C_{H10} ternary.

C_{H10} gives the flexibility in compositional phase behaviour between the injection and initial compositions, which enables to control components' propagation in our method. However, C_{H10} also alters volumetric phase behaviour because of different EOS parameters are applied. Volume shift is used to retain volumetric phase behaviour along the mixing lines between the gas and two oils in step 3: one consisting of C_1, C_2, and C_{10}, and the other consisting of C_1, C_2, and C_{H10}.

The original gravity number will be inevitably changed because the pore volumes open to flow is different between DPF and SPF. Volume correction for gas components is also made to retain the original gravity number and oil recovery before breakthrough (Time 1 in Figure 4.2). As we keep the original oil density and relative permeability for both oil and gas phase, the density of injection gas needs to be adjusted to match the original gravity number in step 4.

Once we set up a new composition space, the last step is to determine the concentrations of the heavier components z_{Hi} (i.e., z_{CH10} in this case) to match oil recovery between Time 1 and Time 2. Figure 4.3 illustrates the composition path for the corrected EOS at 0.8 PVI. Flexibilities are introduced in the composition

path between the injection-gas and original oil to model the capacitance effect. z_{CH10} determines the oil composition on the red mixing line $z_{C10} + z_{CH10} = 0.8$ in the C_2-free ternary subsystem in Figure 4.3. z_{CH10} is determined to be 0.5375 in this case. The resulting four components are presented in Table 4.4.1. The binary interaction parameters (BIPs) are all zero for this n-alkane mixture.

The procedure for fluid characterization method for n-alkanes mixtures presented above is summarized as the algorithm listed below:

Step 1: Obtain compositional information for the original EOS: MWs and mole fractions.

Step 2: Create simulations of DPF for a given bypassed fraction and longitudinal dispersion level with/without intra-block mass flux to measure throughput ratio (R_T) and recovery history.

Step 3: Estimate f_{MW} for introduced heavier oil components to match the oil recovery after Time 2. Time 2 is when the evaporation wave in the flowing fraction reaches the outlet.

Step 4: Determine volume-shift parameters for the introduced oil components to retain the original oil density and viscosity.

Step 5: Resolve volume-shift parameters for gas components to match the original gravity number and breakthrough time (Time 1).

Step 6: Estimate z_{Hi} to reproduce the oil recovery between Time 1 and Time 2.

The number of components is not limited for this algorithm as long as it is n-alkanes mixture. In general, this flow-based characterization is easier with more components because of more flexibility allowed in parameter adjustment. Throughput ratio (R_T) is a well characterized parameter defined in DPF to quantify the recovery of bypassed oil in DPF. In next section, the relationship between the two tuning parameters in the fluid characterization method and throughput ratio is investigated.

4.5 Effects of throughput ratio and dimensionality on f_{MW} and z_{Hi}

The flow-based fluid characterization method is repeated for different R_T values for 1-D, 2-D, and 3-D cases for the same reservoir model of 1000 × 1000 × 50 ft^3. The reservoir properties for 1-D, 2-D and 3-D are the same as given in Table 3.1, 3.5, and 3.6. Three-component fluid system given in Table 3.2 is applied in this case. The algorithm in previous section is used to match the recovery prediction for the cases with different throughput ratios.

Figure 4.3 shows the resulting f_{MW} values, which indicate that f_{MW} monotonically decreases with increasing R_T, and is nearly independent of flow dimensionality. For different throughput ratios, the multiplier for MW of C_{H10} is well characterized in different dimensionality. f_{MW} approaches infinity as R_T

tends to be zero because bypassed oil is unrecoverable as in the S_{orm} method. f_{MW} becomes unity for R_T of unity because splitting of oil components is not needed in the absence of capacitance.

The resulting z_{Hi} values in respect of different throughput ratios are given in Figure 4.4. It is observed that z_{Hi} also monotonically decreases with increasing R_T, and must be zero at R_T of unity, which corresponds to the local equilibrium assumption. Unlike f_{MW}, however, z_{Hi} increases with the flow dimensionality. This is likely because the crossflow among flow paths that occurs in 2-D and 3-D flow can make the transport of the bypassed oil to the producer more efficient. That is, once the oil bypassed along the slow-flow (or low-throughput) paths migrates to the flowing fraction, it can travel to the producer using adjacent faster flow (or high-throughput) paths, instead of using the original slow-flow paths. For a fixed R_T, z_{Hi} needs to be increased to counter this effect on PVI_2 relative to PVI_1. However, f_{MW}, which controls the propagation rate (i.e., distance traveled for unit throughput) of oil, is little affected by the effects of crossflow among flow paths.

Similar trends of f_{MW} and z_{Hi} with respect to R_T discussed above are observed by use of different fluids. Once f_{MW} and z_{Hi} are calculated for different R_T values for a given 1-D DPF model, f_{MW} and z_{Hi} can be predicted for a selected R_T value. z_{Hi} should be increased for higher flow dimensionality for a given R_T value.

We confirmed that the method is successfully applied to higher levels of oil bypassing up to 30% in the case presented. However, there is likely an upper limit for the bypassed fraction that the method can handle. Matching oil recovery at breakthrough (i.e., Time 1) may be difficult if the level of oil bypassing is more significant because the corresponding f_{MW} is higher. For such a case, the new method presented in this research can be applied along with the S_{orm} method, which creates unrecoverable bypassed oil.

The objective of the fluid characterization correction presented above is to represent the effects of capacitance on components' propagation using SPF. This fluid characterization method can well characterize capacitance effects with different throughput ratios reproduced by DPF. Fluid model uncertainties is inevitably occur even PVT data is matched as presented in chapter 2. The characterized fluid model to model capacitance effects is confirmed to be within the uncertainties of fluid model. In the next section, core floods data are used to measure flow characteristics using a DPF model. f_{MW} and z_{Hi} can be found for a R_T value estimated for this particular application, where scale dependency of R_T should be taken into account when applied in a larger scale reservoir with more dimensionality.

4.6 Core flooding case of C_1, C_3 and C_{16} mixture

This case study uses the core flooding data from Burger et al. (1996) presented in section 3.4.1. The fluid properties are the same as given in Table 3.7. The reservoir properties used in the single-porosity flow is from Table 3.8 but combining the bypassed and flowing fraction in each grid block.

The core floods recovery history cannot be matched using the 1-D SPF models with and without the S_{orm} method as shown in Figure 4.5. The DPF which explicitly consider capacitance effects in bypassed grid block is able to accurately reproduce the recovery data of the core flooding experiment. The new flow-based characterization method proposed is also tested to match the recovery prediction in next section.

We correct the fluid model in Table 3.7 by splitting the C_{16} components into C_{16} and C_{H16}. The algorithm in previous section yields the corrected fluid model in Table 4.2. With this corrected fluid model, the coreflood recovery history is successfully reproduced using the 1-D SPF model as shown in Figure 4.5.

Three more cases are created using the 1-D DPF model with three different R_T values, 0.468, 0.630, and 0.750 to generate the relationship between two tuning parameters and throughput ratios. The oil recovery histories from these DPF

models are matched using 1-D SPF with fluid characterization correction as shown in Figure 4.6.

Each of these cases gives f_{MW} and z_{Hi} values corresponding to its throughput ratio (R_T). Figure 4.7 presents f_{MW} and z_{Hi} for the four R_T values used; 0.365, 0.468, 0.630, and 0.750. Their trends with respect to R_T are consistent with the case in the previous section 4.5. This correlation is useful in estimating the potential throughput ratios in larger scale and more dimensionality case as throughput ratios tend to be larger when process time become longer.

The correlation obtained from core flooding experiments is used for modelling the recovery bypassed oil in a 2-D vertical field-scale simulation with reservoir properties given in Table 3.5. First we estimate a throughput ratio for the 2-D reservoir model. R_T is estimated to be 0.50 in this case considering that R_T (0.365 for 1-D core scale) becomes higher for a longer recovery process. The previous section showed that z_{Hi} increases with increasing flow dimensionality. Therefore, z_{Hi} must be increased for 2-D flow compared to that for 1-D flow at a given R_T. Then, we estimate that f_{MW} is 1.215 and z_{Hi} is 0.40 for this selected case.

The 2-D gas injection is simulated using SPF models with three schemes: (a) SPF with the local equilibrium assumption, (b) SPF with the S_{orm} method, and (c)

SPF with fluid characterization correction presented in this research. Figure 4.8 gives the distributions of the C_{16} concentration at 10 PVI for the three cases.

Marked differences are observed for residual oil distribution in the reservoir, indicating the importance of considering properly capacitance effects in field-scale simulation. The profiles of C_{16} at 10 PVI for layer 9 are compared in Figure 4.9. The SPF with fluid characterization correction properly models the delayed propagation of C_{16} due to capacitance effects compared to single-porosity flow with local equilibrium assumption. SPF with the S_{orm} method overestimates the residual oil because of capacitance effects because the bypassed oil is excluded from flash calculate and it will never be recovered.

Figure 4.10 shows the C_{16} recovery histories for the three cases. Cases a and b are the two limiting cases that can be modelled using commercial simulators. Case a will overestimate the oil recovery because capacitance effects in sub-scale can never be modelled. Case b will underestimate the oil recovery because recovery of bypassed oil cannot be modelled. The method presented in this research (case c) can consider efficiently capacitance effects using a SPF model with the change of the fluid model.

The case study showed an application of the new method with core floods data. Flow with capacitance effects in the core floods was characterized using a

1-D DPF model. The flow-based fluid characterization then generated the f_{MW} and z_{Hi} parameters with respect to R_T. R_T for a field-scale simulation was estimated based on the R_T value in the corefloods. f_{MW} and z_{Hi} corresponding to the estimated R_T were used in a SPF simulation for gas injection in a vertical 2-D reservoir. Results show the importance of properly considering capacitance effects in simulation. Prediction of residual oil distribution within a reservoir depends significantly on how bypassed oil is modelled in the simulation.

The method presented in this chapter requires no change in the governing equations to quantitatively reproduce flow characteristics in the presence of capacitance. The computational time is just half of it because of the reduced gird blocks for the bypassed region compared to DPF used in chapter 3. The new flow-based characterization method can quantitatively model capacitance effects at the sub-grid scale in conventional compositional simulation without the dual-porosity method. Mixtures of n-alkanes are used here because correlation of Kumar and Okuno (2012) based on MW is needed to limit the flexibility to make the fluid characterization method to be more systematic. In next chapter, we extend our method to real reservoir fluid by directly changing attraction (a) and covolume (b) parameters.

TABLE 4.1 – PROPERTIES FOR CORRECTED FLUID MODEL OF C_1, C_2 AND C_{10} MIXTURES FOR CAPACITANCE.

	Oil (mole fraction)	Gas (mole fraction)	MW (g/mol)	T_C (℉)	P_C (psia)	ω	V_C (ft^3/lb-mol)	$C_{pen(D)}$
C_1	0.20	0.00	16.043	-116.590	667.20	0.0080	1.59	0.000
C_2	0.00	1.00	30.070	90.050	708.35	0.0980	2.37	0.380
C_{10}	0.37	0.00	142.285	644.620	321.78	0.5032	9.66	0.000
C_{H10}	0.43	0.00	142.285	792.624	251.72	0.7009	9.66	0.303

TABLE 4.2 – PROPERTIES FOR CORRECTED FLUID MODEL OF C_1, C_3 AND C_{16} MIXTURES FOR CORE FLOODING CASE 1.

	Oil (mole fraction)	Gas (mole fraction)	MW (g/mol)	T_C (℉)	P_C (psia)	ω	V_C (ft^3/lb-mol)	$C_{pen(D)}$
C_1	0.00	0.74	16.043	-116.59	667.20	0.0080	1.59	0.570
C_3	0.35	0.26	44.097	205.97	615.76	0.1520	3.25	0.570
C_{16}	0.38	0.00	226.400	839.51	233.72	0.7634	14.74	0.000
C_{H16}	0.27	0.00	226.400	957.13	197.00	0.9190	14.74	0.110

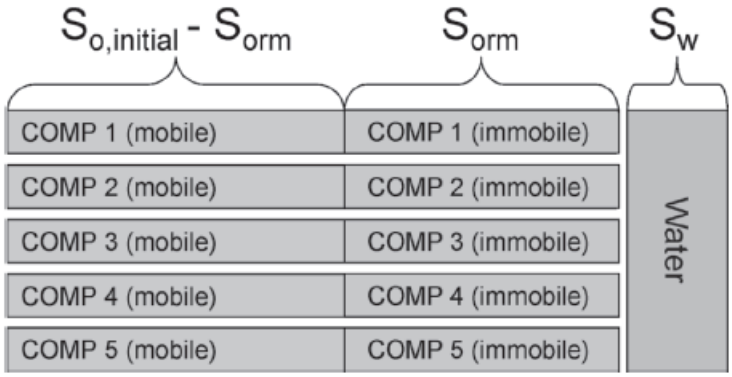

Figure 4.1 Partition of the fluid system to consider the non-vaporizing residual oil saturation in Hiraiwa and Suzuki (2007).

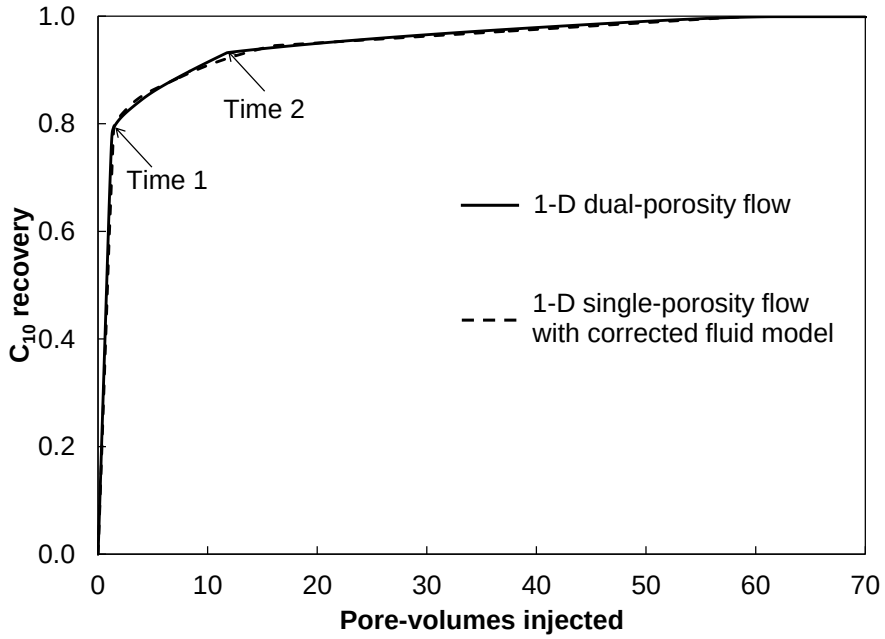

Figure 4.2 C_{10} recovery for the 1-D DPF with a C multiplier of 100 is reproduced by the 1-D SPF with fluid characterization correction. The corrected fluid model is presented in Table 4.1.

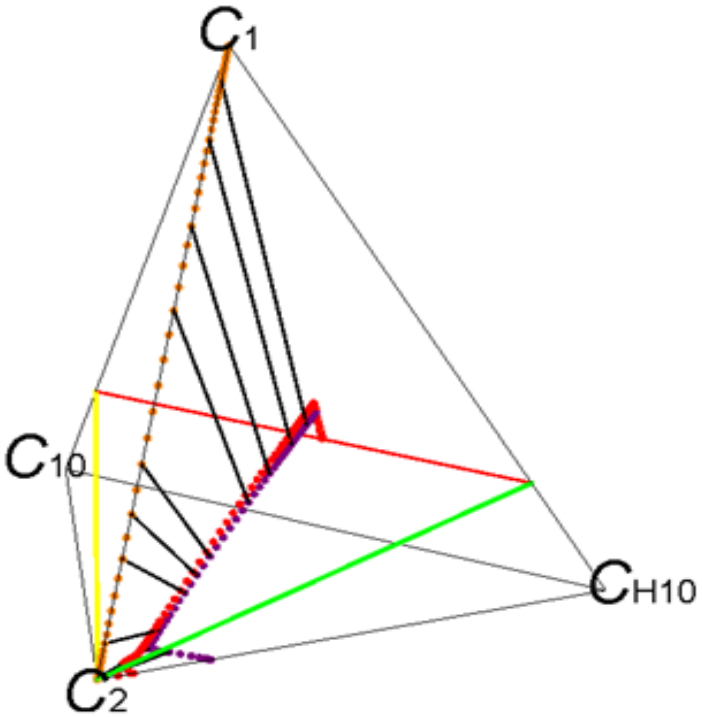

Figure 4.3 Quaternary diagram for the fluid system corrected for capacitance effect at 0.8 PVI.

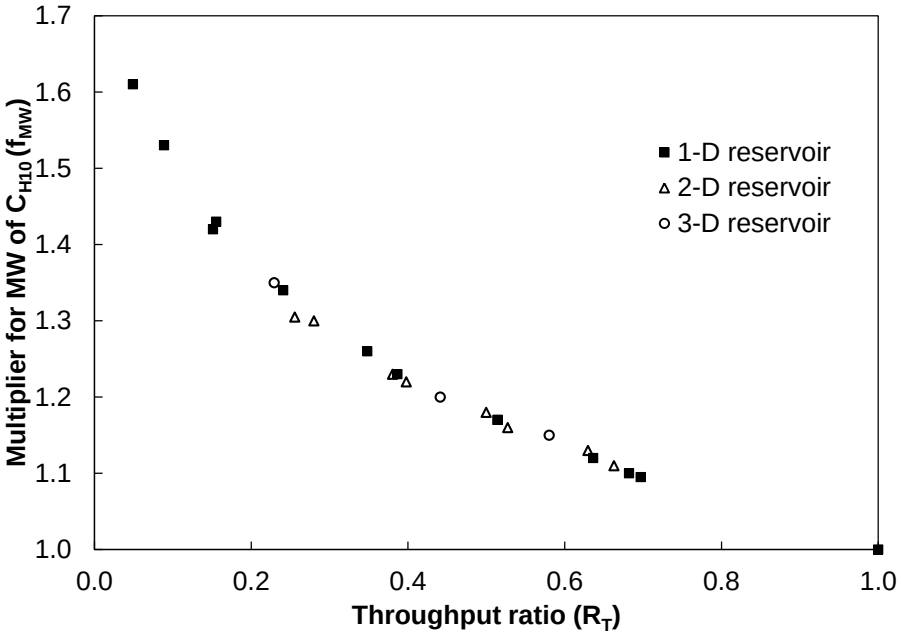

Figure 4.4 f_{MW} monotonically decreases with increasing R_T, and is nearly independent of flow dimensionality.

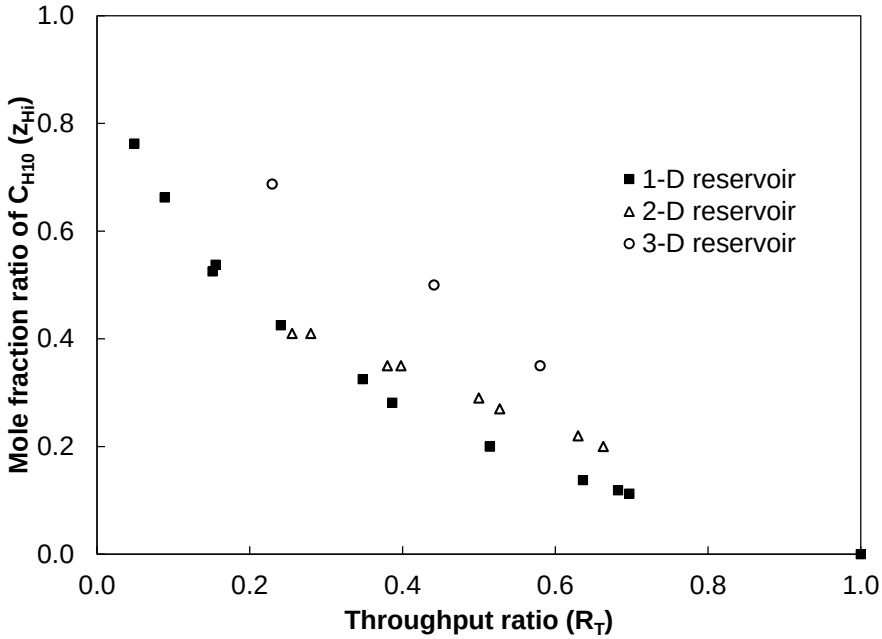

Figure 4.5 z_{Hi} monotonically decreases with increasing R_T, and must be zero at R_T of unity, which corresponds to the local equilibrium assumption. Unlike f_{MW}, z_{Hi} increases with the flow dimensionality.

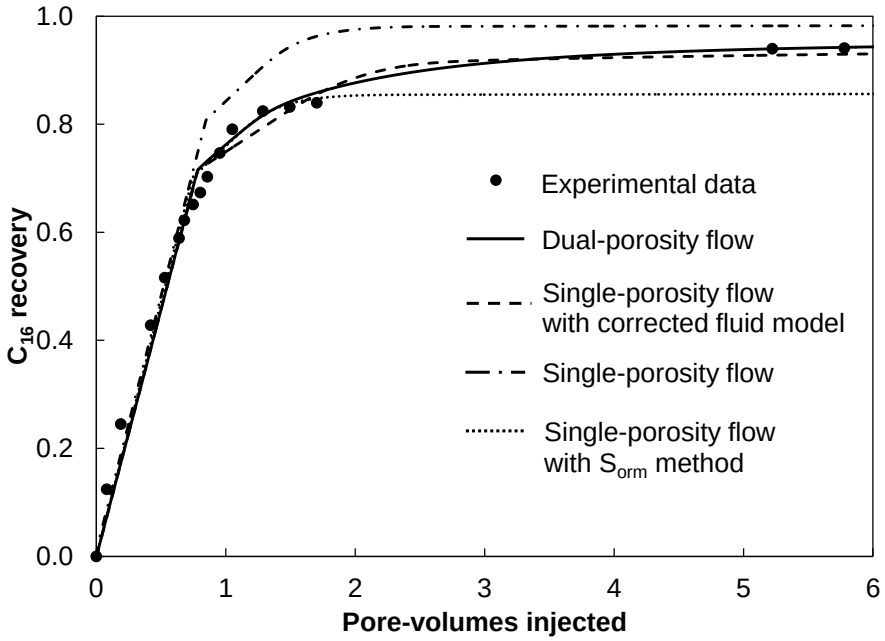

Figure 4.6 1-D SPF model with corrected fluid model significantly improves the recovery prediction compared to core floods data. The coreflood recovery cannot be reproduced using the 1-D SPF models with and without the S_{orm} method unless the fluid model is corrected.

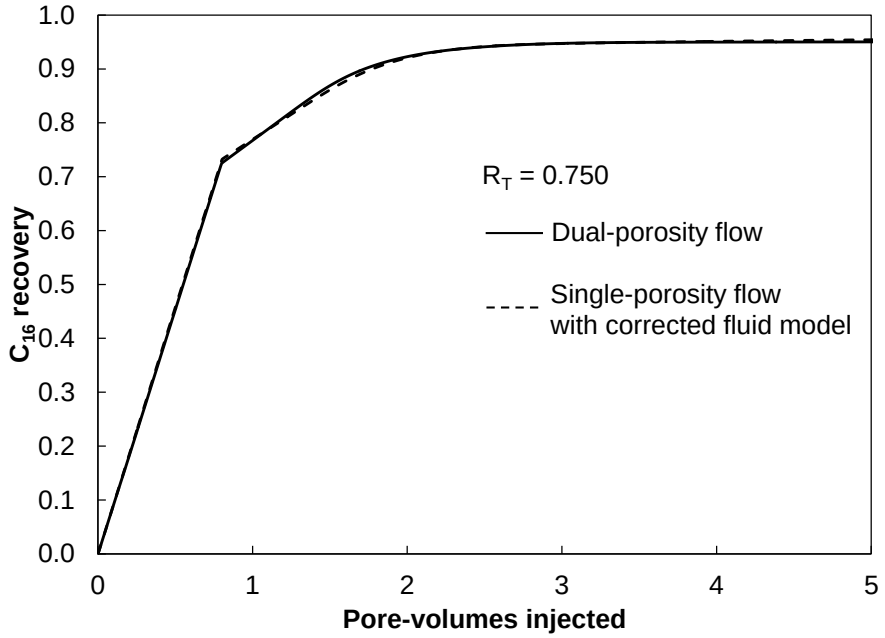

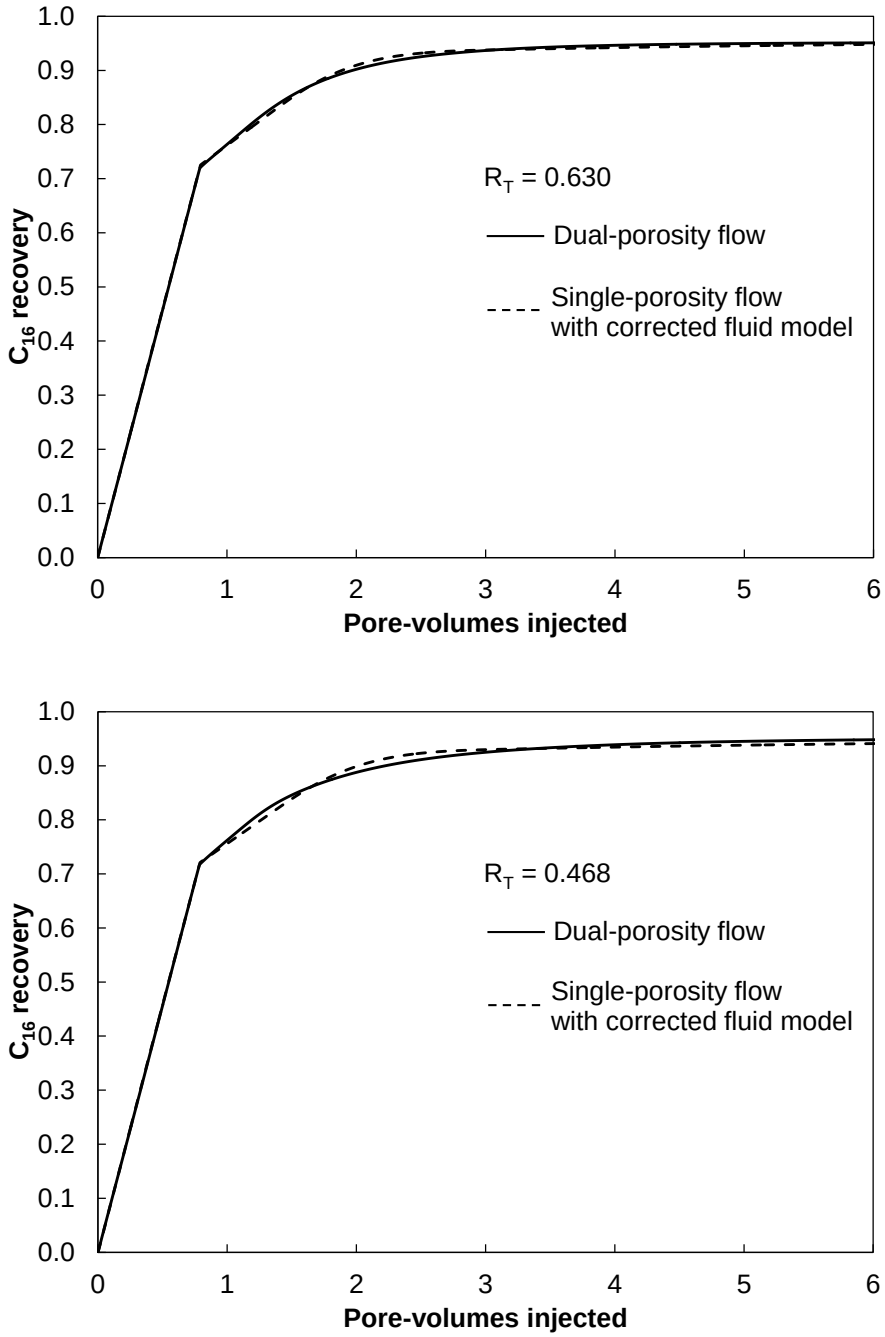

Figure 4.7 1-D SPF cases with corrected EOS for different throughput ratios for C_1, C_3 and C_{16} mixtures. The fluid characterization method can accurately reproduce the flow characteristics modelled by 1-D DPF. The cases are generated for different R_T values. Values for f_{MW} and z_{Hi} resulting from these cases are used to correlate f_{MW} and z_{Hi} with respect to R_T as given in Figure 4.7.

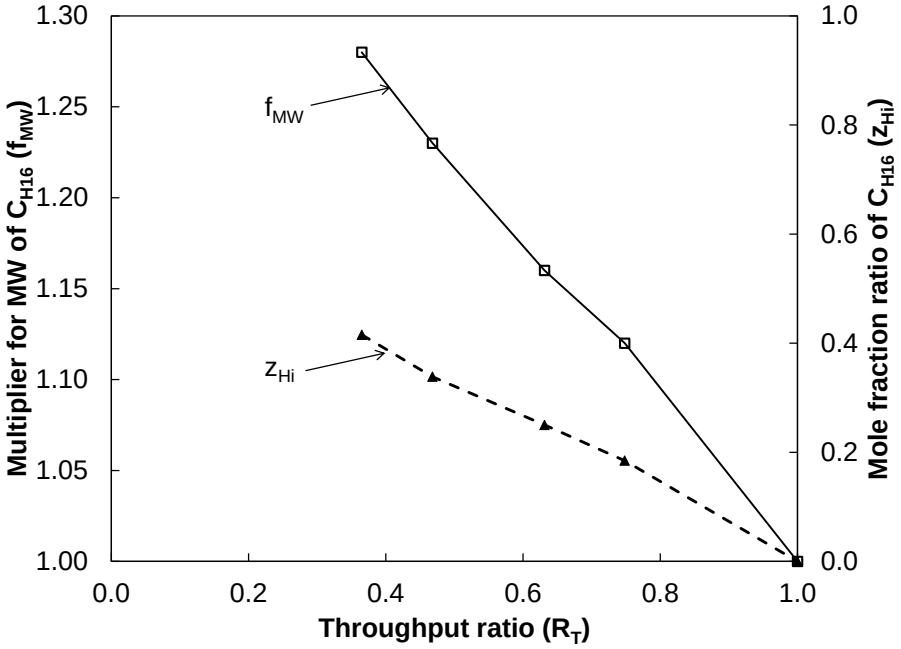

Figure 4.8 Correlations of f_{MW} and z_{Hi} with respect to R_T based on fluid characterizations for four R_T values (0.365, 0.468, 0.630, and 0.750).

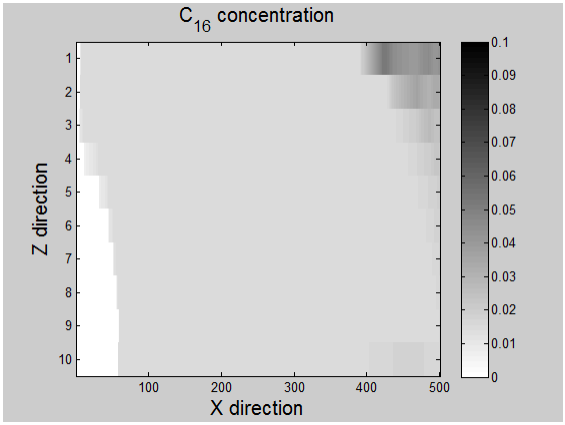

a. SPF with local equilibrium assumption

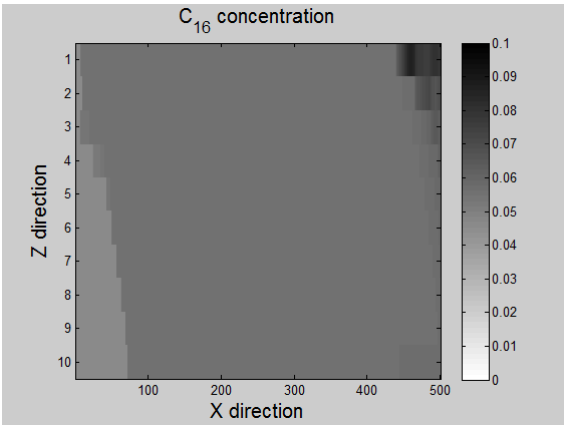

b. SPF with the S_{orm} method

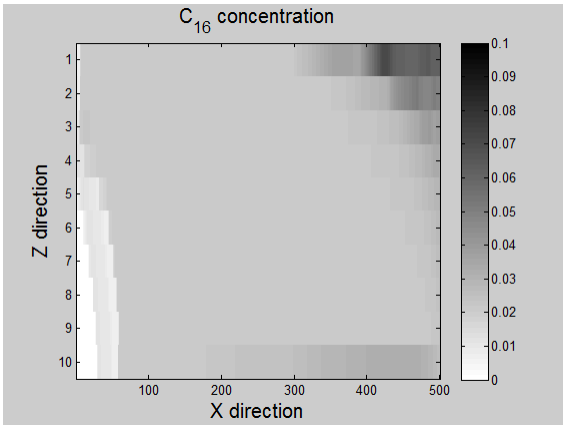

c. SPF with fluid characterization method

Figure 4.9 Distributions of the C_{16} concentration at 10 PVI in vertical 2-D simulations. Three cases are presented as follows: (a) SPF (local equilibrium assumption), (b) SPF with the S_{orm} method, and (C) SPF with fluid characterization correction ($R_T = 0.5$).

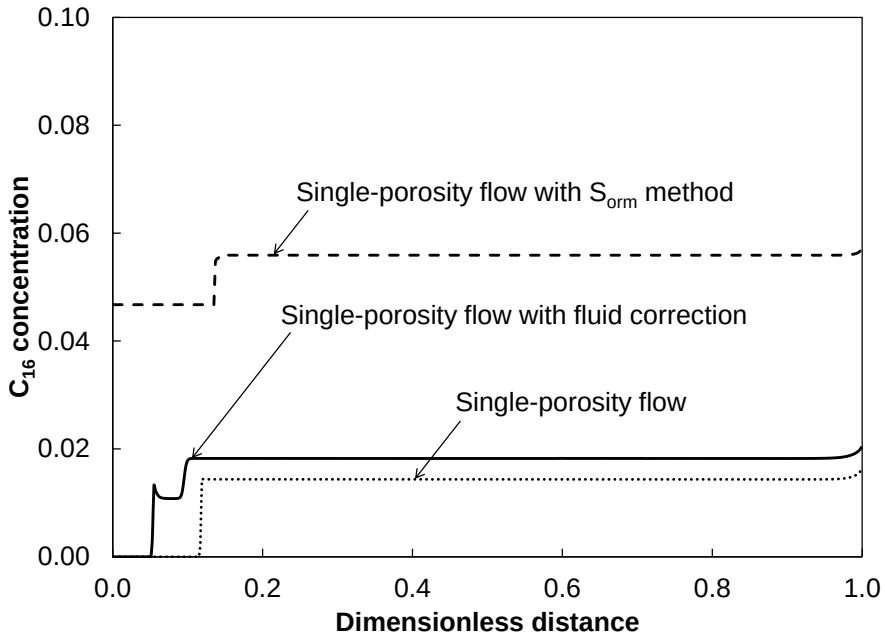

Figure 4.10 C_{16} profiles for layer 9 at 10 PVI in the vertical 2-D simulations. SPF, SPF with the S_{orm} method, and SPF with fluid characterization correction are compared.

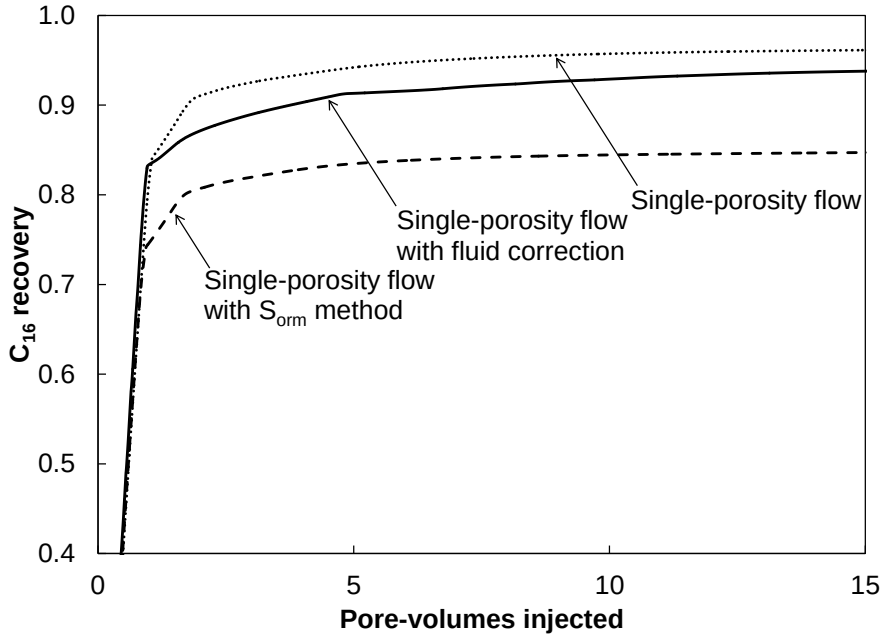

Figure 4.11 Recovery predictions for vertical 2-D simulations based on coreflood data. SPF with fluid characterization correction can model capacitance efficiently.

CHAPTER 5: FLUID CHARACTERIZATION METHOD FOR CAPACITANCE EFFECTS FOR RESERVOIR FLUIDS

The fluid characterization method modelling capacitance effects for n-alkane mixtures is successfully applied in conventional compositional simulator with local equilibrium assumption in previous chapter. Original oil components are split into two fractions: one with original oil and the other with introduced heavy oil components to represent the bypassed oil. The EOS properties for the introduced component are characterized based on the multiplier for the molecular weight f_{MW}. The increased MWs are applied in the correlation of Kumar and Okuno for n-alkanes to generate the T_C, P_C and ω for introduced heavy oil components. We recommend using volume-shift parameters to retain the density and viscosity of the original oil. Both of the two tuning parameter f_{MW} and z_{Hi} change monotonically with throughput ratios used to characterize capacitance effects.

In this section, the fluid characterization method is extended to characterize real reservoir fluid which is not necessary to be n-alkanes. The attraction (a) and covolume (b) parameters of the PR EOS are directly changed for the introduced heavy oil component to account for capacitance effects. The tuning parameters used have an empirical liner relationship with throughput ratio (R_T) for the corresponding DPF model for the case presented. Our fluid characterization

method successfully reproduces the recovery prediction in fine-scale simulation considering capillary effects.

5.1 Attraction and covolume parameters

The PR EOS (1976) is still used to model the phase behaviour in this chapter. The most important two parameters attraction (a) and covolume (b) parameters in the PR EOS are calculated based on the critical pressure, temperature and acentric factors for a fixed temperature. In a word, directly changing both attraction and covolume parameter equals to tuning T_C, P_C, and ω in previous chapter.

According to the PR EOS and van der Waals mixing rule, attraction (a) and covolume (b) parameters for each components are the key parameters to estimate the phase behaviour of the fluid system. The physical trend of both a and b parameters for different levels of aromaticity is plotted in Kumar and Okuno (2013) as shown in Figure 5.1. With the increase of carbon numbers, both a and b parameters monotonically increase. However, it is not necessary to increase both a and b for the introduced heavy oil component because the aromaticity is not known for the original oil component and introduced heavy oil component,.

The propagation speed of the introduced heavy oil component is required to be slower to reproduce the slower evaporation wave due to capacitance effects. Either increasing attraction parameter or decreasing covolume parameter can

decrease the propagation speed for the introduced heavy oil component. Two core flooding cases in section 3.4.1 and 3.4.2 are both tested to decide the best way to minimize the change on attraction and covolume parameter for the introduced heavy oil component. The first way is increasing both attraction and covolume parameters to respect the physical trend of them. The other way is increasing attraction and decrease covolume parameter to decrease the propagation speed together. The recovery predictions for SPF with corrected EOS are matched with the given core flooding data for the two different ways in changing attraction and covolume parameters.

Figure 5.2 presents the deviation of a and b parameters for C_{16H} compared to original component C_{16} in core flooding case 1 from Burger et al. (1996) given in section 3.4.1. The deviation of a and b parameters in core flooding case 2 from Bardon et al. (1994) is illustrated in Figure 5.3. From these two figures, it is observed that the fluid characterization method which increases a and decreases b exhibits a better performance in minimizing the change of attraction and covolume parameters for the introduced heavy component. Thus, the influence of fluid characterization method on phase behaviour can also be minimized.

5.2 Attraction and covolume indices

The attraction and covolume index are defined to quantify the dissimilarity of attraction (a) and covolume (b) parameter for the introduced heavy oil component compared to original oil component following the same form as transverse flux index (τ):

$$\gamma_A = \frac{a_{Hi}-a_i}{a_{Hi}+a_i}\ , \tag{5.2.1}$$

$$\gamma_B = \frac{b_{Hi}-b_i}{b_{Hi}+b_i}\ . \tag{5.2.2}$$

The change of a and b parameter for the introduced heavy oil component is quantified as a dimensionless number from zero to unity. The attraction and covolume index become zero when the introduced heavy oil component is the same as original component. The same introduced heavy oil component as original component would not affect the propagation speed of displacement front and evaporation wave so it would be exactly the same as local equilibrium assumption. The attraction and covolume index approaches unity when the introduced heavy oil components have much larger a and b parameters compared to original components. Thus, the propagation speed of the introduced heavy component is slow enough to be neglected. This is corresponding to S_{orm} option in commercial simulator when the recovery of bypassed oil is zero as the bypassed oil is excluded from flash calculation.

5.3 Algorithm for the fluid characterization method based on attraction and covolume parameters

The procedure for changing attraction and covolume parameter is explained with a DPF sample case with a C multiplier of 200. The reservoir properties and fluid properties are the same as the 1-D cases in chapter 3 given in Table 3.1 and Table 3.2, respectively. The oil recovery prediction of the DPF model is presented in Figure 5.4. The throughput ratio is 0.32, which indicates that capacitance effects are moderate between the local equilibrium assumption and S_{orm} option. Time 1 is the PVI at the breakthrough time and Time 2 is when the evaporation wave reaches the outlet in the flowing region.

The first step is to split oil component in the original EOS into two fractions: one with the original components and the other with introduced heavy oil components. For this fluid model given in Table 3.2, we only split C_{10} into C_{10} and C_{H10} (heavier C_{10}). The mole fraction of C_{10} in original model is the summation of C_{10} and C_{H10} in the new EOS model, where z_{Hi} is the mole fraction of C_{H10} in the mixture of C_{10} and C_{H10}.

The value of γ_A and γ_B is determined by increasing the attraction parameter and decreasing the covolume parameter until the recovery after Time 2 is matched. The value of γ_A and γ_B are 0.069 and 0.032 for this selected case. After estimation

of the correct γ_A and γ_B, the volume-shift parameter for the introduced heavy oil component is determined to retain the original oil density. Then the volume-shift parameter for the injected gas components needs to be approximated to retain the original gravity number and oil recovery before breakthrough (Time 1 in Figure 5.4). The last step is to determine the mole fraction of the heavier components C_{H10} to match oil recovery between Time 1 and Time 2. The resulting z_{Hi} for this selected case is 0.4.

The algorithm for the fluid characterization method by directly changing attraction and covolume parameters is summarized as below:

Step 1: Split the oil component in original EOS into two fractions: one with original components and the other with introduced heavy oil components.

Step 2: Estimate the attraction index γ_A and covolume index γ_B based on the matching result for the oil recovery prediction for SPF with fluid correction and DPF after Time 2.

Step 3: Determine the volume-shift parameter for the introduced heavy oil component to match the original oil density and viscosity for the case with and without fluid correction.

Step 4: Approximate the volume-shift parameter for injected gas components to match the original gravity number and recovery at breakthrough time (Time 1).

Step 5: Estimate the mole fraction of heavy oil component (z_{Hi}) to match the recovery of DPF and SPF with fluid correction between Time 1 and Time 2.

This algorithm is applied for different fluids in the case studies showing the application case study of the characterization method for real reservoir fluid with up to 12 components and the recovery prediction is still accurate without loss of simplicity. The influence of the corrected EOS for capacitance effects in gas injection process is tested in pure water injection. The three phase relative permeability is given in Table 5.1. Figure 5.5 shows that the recovery of pure water flooding is not affected by the correction of fluid model considering capacitance effects. The corrected EOS is generated for the case with $R_T = 0.32$ as it shows in Figure 5.4. The corrected EOS does not affect the oil recovery prediction in continuous water injection because the original density, viscosity are retained for the corrected EOS so the fractional flow is identical for the EOS with and without fluid characterization for capacitance effects in gas flooding process.

By use of the algorithm above, our fluid characterization method is tested in the same fluid and reservoir properties but with different throughput ratios (R_T). An almost linear relationship between the three fluid characterization parameters (γ_A, γ_B and z_{Hi}) and the throughput ratio (R_T) is found in the next section.

5.4 Empirical linear relationship between the tuning parameters in fluid characterization method and throughput ratios

The relationship between the three key characterization parameters and throughput ratio is investigated in this section. We generate a series of SPF cases with new fluid characterization method to mimic the recovery prediction in DPF cases with different throughput ratios: 0.21, 0.32, 0.51, 0.65 and 0.81. As the case with a throughput ratio of 0.32 is already shown in section 5.3, Figure 5.6 gives the recovery prediction matching result for the other four cases.

Figure 5.7, 5.8 and 5.9 present that the three dimensionless characterization parameters all monotonically decrease with increasing throughput ratio. Attraction index (γ_A), covolume index (γ_B) and mole fraction of the introduced heavy oil component (z_{Hi}) have an almost linear relationship for this ternary system of C_1, C_2 and C_{10}. They become 0 for the case ($R_T = 1$) because there is no need to introduce heavy oil component in local equilibrium assumption. The extrapolations of them at $R_T = 0$ are the estimated value which represents that the evaporation wave speed of the introduced component is slow enough to have a reasonable accuracy with S_{orm} option.

The resulting densities in the PR EOS for the introduced heavy oil components are larger compared to original component because the corresponding a parameter

is larger and b parameter is smaller. Negative volume-shift parameters are needed to retain the original oil density. The dimensionless volume-shift parameters used also have a linear relationship with throughput ratios as Figure 5.10 shows. It becomes zero when throughput ratio is unity because original C_{10} is accurate for local equilibrium assumption.

The three tuning parameters γ_A, γ_B, and z_{Hi} exhibit an almost linear relationship with the throughput ratios which characterize the recovery of bypassed oil systematically in DPF. The extrapolated value of γ_A, γ_B, and z_{Hi} for the trend line at R_T of 0 is applied for the corrected EOS model to test the linearity near R_T of 0. The recovery prediction is compared with SPF with S_{orm} option. The extrapolated values at R_T of zero for γ_a, γ_b, z_{Hi} are 0.1051, 0.0487 and 0.6117, respectively. The recovery prediction is reasonable compared to SPF with the S_{orm} method as shown in Figure 5.11. Ideally, the attraction and covolume index should be 1 for the case which recovery of bypassed oil is 0 so that the introduced heavy oil component has an evaporation wave with zero wave velocity. It is not feasible to use this "solid" component in conventional composition simulations. The extrapolations of the three parameters at R_T of 0 giving reasonable accuracy means that the propagation speed of the introduced heavy oil component is slow enough to mimic the zero bypassed oil recovery.

This linear relationship shows that our fluid characterization method is systematic in oil recovery prediction once the throughput ratios are estimated in DPFs which reproduce the sub-grid scale capacitance effects in fine-scale heterogeneous simulation or core floods data. In the next section, the effects on phase behaviour due to the changes of attraction and covolume parameters are going to be discussed.

5.5 The effects of fluid characterization method on phase behaviour

The effects of fluid characterization method by changing attraction and covolume parameters on phase behaviour is analyzed for the cases with different throughput ratios is investigated in this section. The change of P-T diagram, P-x diagram for different throughput ratios will also be discussed to quantify the effects on phase behaviour in P-T-x space. The effects on the prediction MMP is also studied with different throughput ratios.

Attraction and covolume parameters are the two decisive parameters to determine the phase behaviour in the PR EOS. The change of attraction and covolume parameters are discussed first for the C_1, C_2 and C_{10} mixture. The corresponding attraction and covolume parameters for C_{10H} are plotted in Figure 5.12 to compare with original C_{10} with different throughput ratios. We increase attraction parameters and decrease the covolume parameters because this method is

better to minimize the effects on phase behaviour as presented in section 5.1. It is observed that the original oil component corresponding to throughput ratio of 1 is the lower and upper boundary for a and b parameters for C_{10H}, respectively. The corresponding attraction and covolume parameters have the largest deviation wht smaller throughput ratio of 0.21 because capacitance effects are more severe compared to other cases.

Minimum miscibility pressure (MMP) is an important property to design the optimized gas injection process. The MMPs for the corrected EOS model with different throughput ratios are inevitably changed because attraction and covolume parameters are changed. The original MMP for the fluid system in Table 3.2 is 1174 psia. Figure 5.13 illustrates that MMP tends to be larger for the case with smaller throughput ratio because the deviation of attraction and covolume parameter is relatively larger. From this figure, the prediction of MMP is not significantly affected because the largest deviation for MMP prediction at R_T of 0.21 is 11%. This difference in MMP prediction is normal compared to fluid model uncertainties.

The phase behaviour of mixtures is often explained in Pressure-Temperature (P-T) diagram and Pressure-Composition (P-x) diagram. Two phases can coexist in a planar region in P-T space for a multicomponent mixture. The phases coexist

only along a line which is called P-T envelope. The upper boundary of the phase envelope is the bubble point curve and the lower boundary is the dew point curve. The critical point is the point when bubble point curve and dew point curve intersect. However, in gas injection process, gas is injected into the reservoir so the composition of the injected gas is always changing. P-x diagram is plotted to analyze the phase behaviour when gas is injected. In this section the P-T diagram and P-x diagram for corrected EOS with different throughput ratios are both investigated here.

P-T diagrams for the 3 component system with different throughput ratios are plotted in Figure 5.14. The reservoir condition is above the bubble point curve for all the cases with different throughput ratios. It shows that the fluid characterization method do not change the phase condition for the original oil at reservoir condition. The P-T envelope deviates from the original EOS applied in local equilibrium assumption when throughput ratio is approaching zero from unity. The reason is that the deviation for attraction and covolume parameter for introduced C_{H10} becomes higher when capacitance effects are more severe.

Pure C_2 is injected into the reservoir oil consisting of 0.2 C_1 and 0.8 C_{10} for the selected case. The P-x diagram in Figure 5.15 illustrates the saturation pressure change in respect of mole fraction of C_2 with the corrected EOS at different

throughput ratios. The saturation pressure is higher for the case with smaller throughput ratio. If C_2 is mixed with the original oil, the original oil represented by the corrected EOS model with smaller throughput ratio will enter the two phase region with less C_2.

It is concluded that the effects on phase behaviour because of the fluid characterization for capacitance effects systematically increases with the decrease of throughput ratio. However, this change on phase behaviour is still reasonable compared to the fluid model uncertainties as explained in chapter 2. The detailed comparisons for the corrected EOS considering capacitance effects and fluid model uncertainties caused by different characterization methods will be presented in chapter 6.

5.6 Comparison of different tuning strategies for changing the attraction and covolume parameters

In previous sections, we increase the attraction parameters and decrease the covolume parameters to correct the EOS model to model capacitance effects. However, it makes sense to only increase attraction parameter or decrease covolume parameter to achieve the same objective. The different tuning strategy for attraction and covolume parameters are tested in this part to determine that which is the best option to minimize the effects on phase behaviour.

The single-porosity simulation cases with corrected EOS model which increase only attraction parameter or decrease only covolume parameter are conducted for different throughput ratios. Figure 5.16 presents that different tuning strategy can result in same accuracy in recovery prediction for the given case with a throughput ratio of 0.21. Figure 5.17 shows that the attraction index (γ_a) also exhibits an almost linear relationship for the case which only increases attraction parameter to model capacitance effects but has a relatively larger corresponding attraction index with same throughput ratio. The reason is that covolume parameter is not changed anymore so that capacitance effects have to be accounted by attraction parameter increase only. The covolume index (γ_b) is observed to decrease linearly with the increase of throughput ratio for the case which covolume parameter is only decreased to model capacitance effects as shown in Figure 5.18. Similarly, the case which only covolume parameter is changed tends to have a higher corresponding covolume index. Figure 5.19 presents that the MMPs calculated by use of different tuning strategies are almost the same. That is another proof that different tuning strategies can have same accuracy in modelling capacitance effects with the corrected EOS model.

The P-T and P-x diagrams for the corrected EOS model with small, moderate and larger throughput ratios are plotted to determine which tuning strategy can

minimize the effects on phase behaviour. Figure 5.20 presents the P-T diagram for the corrected EOS model using different strategies of changing attraction and covolume parameters with throughput ratios of 0.21, 0.51 and 0.81. It is observed that the difference is the largest for the case with smallest throughput ratio which has a slower recovery of bypassed oil. The effects on phase behaviour is minimized by the case which only changes attraction parameter as clearly shown when throughput ratio is 0.21.

The P-X diagram for the three different tuning strategies with small, moderate and larger throughput ratios are also plotted to confirm whether only increasing attraction parameter will have a smaller effect on phase behaviour. Figure 5.21 presents that the saturation pressure is systematically lower for the case which only attraction parameter is changed. As the phase behaviour for a gas flooding process is determined in a P-T-x space, we can conclude that the increasing attraction parameter can have a smaller effect on phase behaviour. It also repsect the physical trend that attraction parameter monotonically increases when the hydrocarbon component becomes heavier. The flexibility is also decreased as covolume parameter is not changed anymore. It is recommended that only attraction parameter is increase in the fluid characterization method.

5.7 Case studies considering capillary effects

It is explained in section 3.5.3 that capillary crossflow can significantly enhance the recovery of bypassed oil. The fluid characterization method will be applied for the case which is capillary dominant using the fluid characterization method to improve the prediction in the bypassed oil recovery.

The relative permeability and capillary function used in this section is the same as it shows in section 3.5.3. Figure 5.22 presents the C_{10} recovery prediction for the dual-porosity flow with and without capillary effects and the corresponding single-porosity flow with corrected EOS and capillary effects. The fluid characterization method is possible to reproduce the recovery prediction in the dual-porosity flow when capillary pressure is considered. The resulting attraction index and mole fraction ratio of C_{10} (z_{Hi}) are 0.123 and 0.125. The corresponding z_{Hi} is much smaller for the case with capillary because the bypassed fraction (0.025) estimated in section 3.5.4 is also smaller.

The effects on phase behaviour for the fluid characterization method are studied for this selected case with a throughput ratio of 0.46. According to Figure 5.23 showing the P-T and P-x diagram, the effects on phase behaviour is not significant for this case with a moderate throughput ratio.

Simulation cases with different throughput ratios are generated by changing the C multiplier in DPF. The recovery predictions are matched for the DPF and SPF with corrected EOS model for the cases with different throughput ratios when capillary effects are considered. The linear relationship still can be observed in Figure 5.24 which presents the attraction index (γ_A) and mole fraction ratio of C_{H10} (z_{Hi}) in respect of throughput ratio (R_T).

5.8 Core flooding case of C_1, C_3 and C_{16} mixture

This case study uses the core flooding data from Burger et al. (1996) presented in section 3.4.1 and 4.6. The fluid properties are the same as given in Table 3.7. The reservoir properties used in the single-porosity flow is from Table 3.8 with the combined bypassed and flowing fraction is each gird block.

The corrected fluid model in this section is generated by changing attraction and covolume parameter rather than used the correlation of n-alkanes. Figure 5.25 shows that this fluid characterization by changing attraction and covolume parameter has a good recovery prediction result compared to experimental data. The recovery prediction is similar for the two single-porosity cases with two different methods for corrected EOS model. These two methods are equivalent because T_C, P_C and ω calculated by the correlation is used for flash calculation in conventional composition simulation. The method used in this section can also be

considered as a more straightforward method because attraction and covolume parameter will be directly used to calculate the equilibrium phase. The resulting attraction index, covolume index and mole fraction ratio of C_{16} are 0.0138, 0.0183 and 0.415, respectively.

Figure 5.25 presents that both dimensionless attraction and covolume parameter for mixtures used in the PR EOS monotonically increase from injected gas to original oil. However, the original oil point can be different with different mole fraction ratio for the introduced heavy oil component. The value of z_{Hi} can be considered as ratio of the deviation between lower boundary and corrected EOS and distance from the boundary case with zero and unity mole fraction ratio of introduced heavy oil component.

The calculated MMP for original EOS model and corrected EOS model are 2975.90 psia and 3243.17 psia, respectively. The difference of the MMP for the corrected EOS model is 8.9% for C_1, C_3 and C_{16} ternary system which is still reasonable compared to fluid model uncertainties.

Figure 5.26 presents that the SPF with corrected EOS model successfully reproduce the faster displacement front observed in DPF which is consider to be one the most important characteristics of capacitance effects. The difference of dimensionless attraction and covolume parameter between the dual-porosity flow

and single-porosity flow with corrected EOS lies in a reasonable range. It is a good example that the new fluid characterization method can reproduce capacitance effects without loss of the accuracy in modelling expected phase behaviour.

5.9 Fluid characterization method applied to reproduce the fine-scale simulation recovery prediction

The dual-porosity method is validated in fine-scale heterogeneous simulation and successfully reproduces the recovery prediction as Figures 3.33 and 3.34 show. The fluid characterization method is tested in the cases with and without capillary pressure to validate it in coarse-scale simulation to match the fine-scale result.

The reservoir and fluid properties are identical to the case in section 3.5.4. The fluid characterization method is applied based on the algorithm given in section 5.3. Case 3 is selected because capacitance effects are still important for the capillary dominant case. The estimated γ_A is 0.487 and z_{Hi} is 0.3125 for the case without capillary pressure as shown in Figure 5.28. The corrected EOS improves the recovery prediction in the coarse-scale simulation and it is almost identical to that in fine-scale simulation. Figure 5.29 gives the recovery predictions for the case with capillary pressure and the fluid characterization also

improves the recovery prediction for the case considering capacitance effects. The corresponding value for γ_A and z_{Hi} are 0.64 and 0.1, respectively.

The figure for the matching result is shown as below:

In next chapter, a two-step method for modelling capacitance effects are proposed based on a case study for the gas injection process conducted in the Shengli oil field. The detailed procedure for reproducing capacitance effects in heterogeneous fine-scale simulation and core flooding experiment will also be explained in the case studies.

TABLE 5.1 – RELATIVE PERMEABILITY FOR PURE WATER INJECTION

Relative permeability model	Corey
Residual saturation (Oil/Gas/Water)	0.24/0.0/0.2
Endpoint relative permeability (Oil/Gas/Water)	1.0/0.6/0.55
Exponent (Oil/Gas/Water)	2.1/1.8/2.0

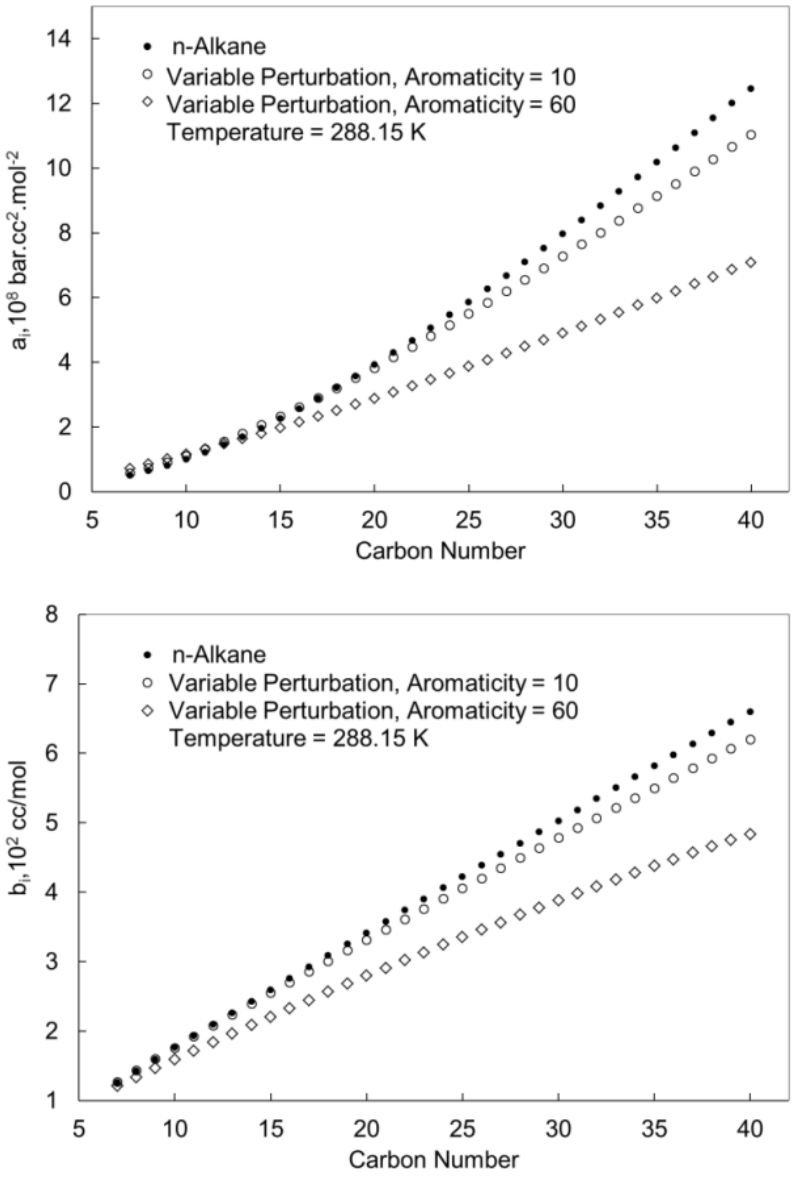

Figure 5.1 The physical trend of attraction (a) and covolume (b) parameter for three levels of aromaticity 0, 10, and 60 in the paper of Kumar and Okuno (2013). The original correlations of Kumar and Okuno (2012) are used for n-alkanes. The perturbation values from n-alkanes are fitted to Yarborough's trend curves for the aromaticity levels 10 and 60.

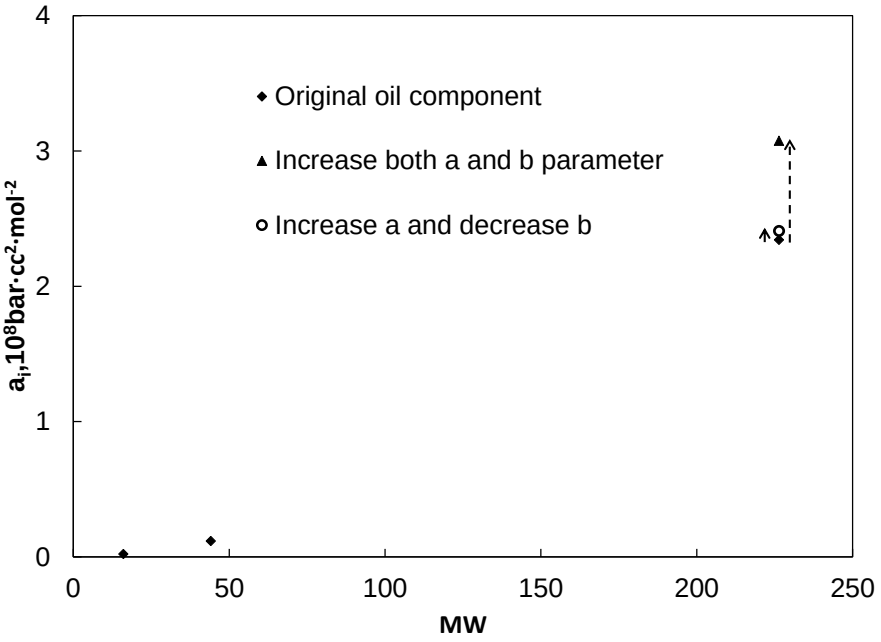

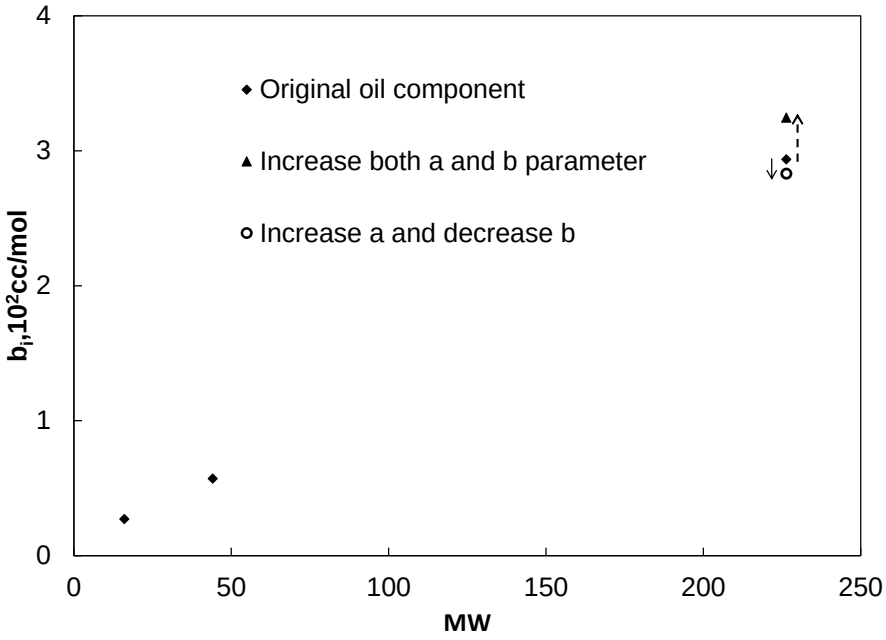

Figure 5.2 The attraction (a) and covolume (b) parameter for original EOS and two different method for corrected EOS applied in core flooding case 1 in Burger et al (1996). One is increasing both attraction and covolume parameter to respect the physical trend of a and b in same aromaticity. The other is increasing a and decrease b to minimize the change on phase behaviour.

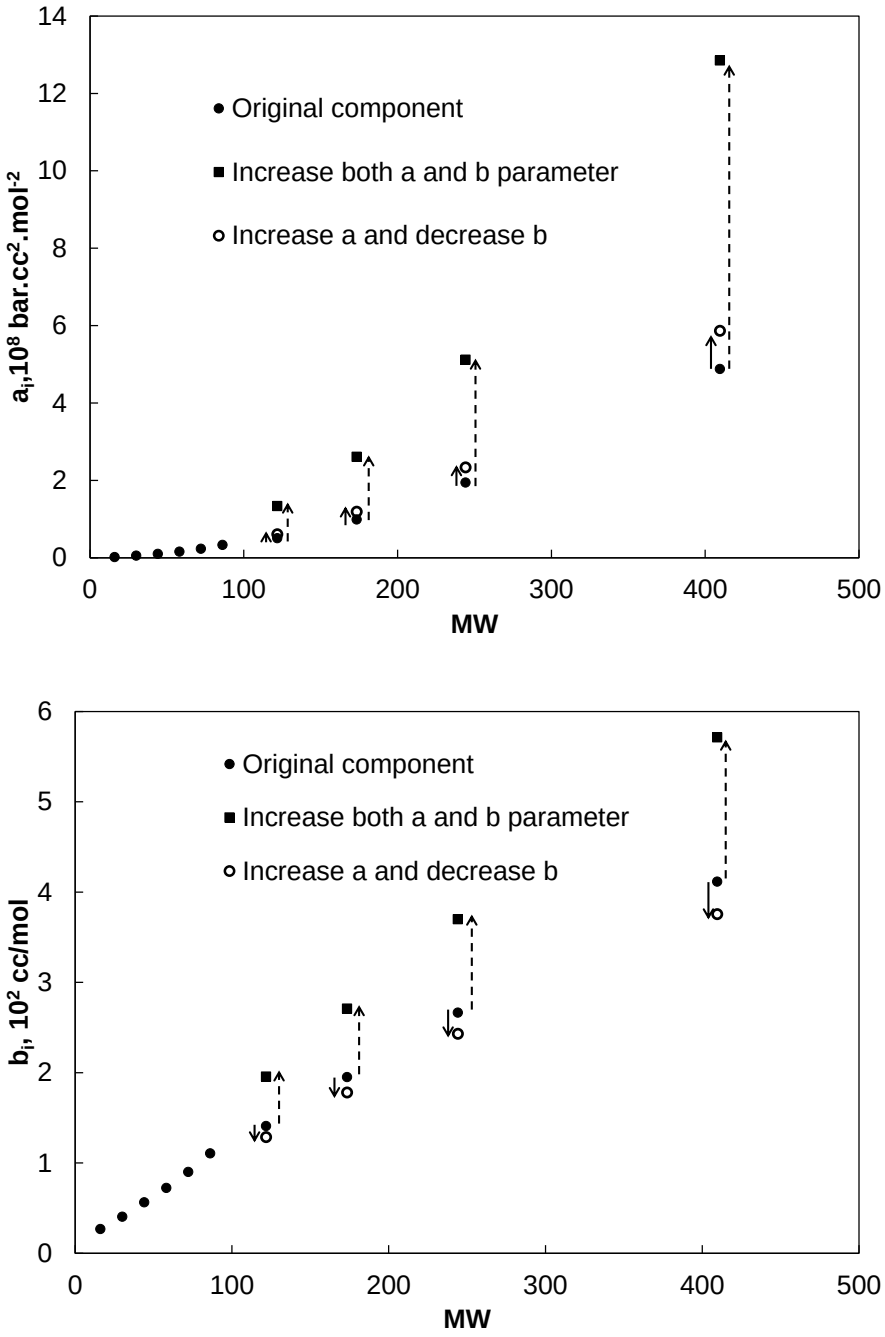

Figure 5.3 The attraction (a) and covolume (b) parameter for original EOS and two different method for corrected EOS applied in core flooding case 2 from Hassi-Messaoud field in Bardon et al. (1994).

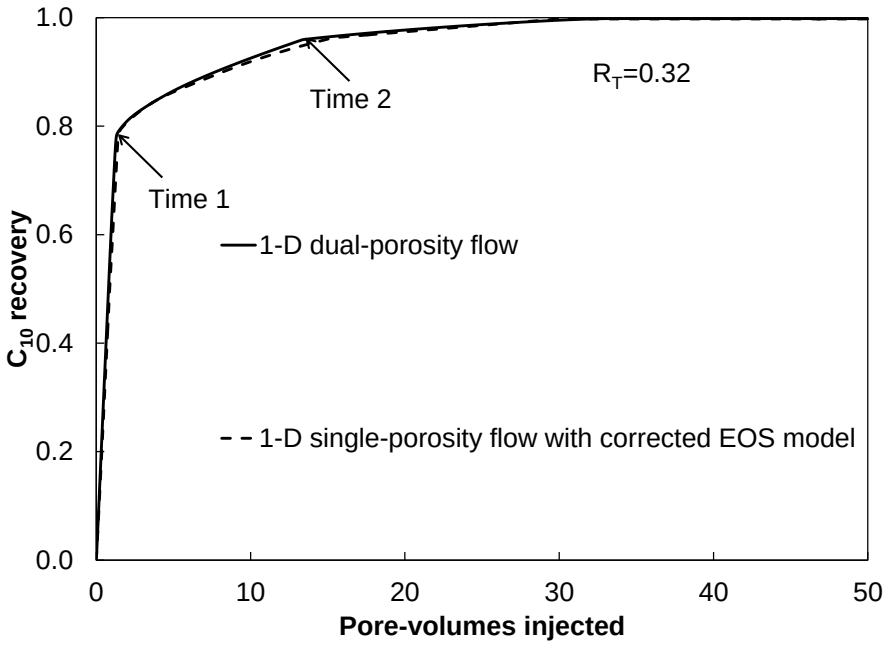

Figure 5.4 C_{10} recovery for the 1-D DPF with a C multiplier of 200 is reproduced by the 1-D SPF with fluid characterization correction by changing attraction and covolume parameter

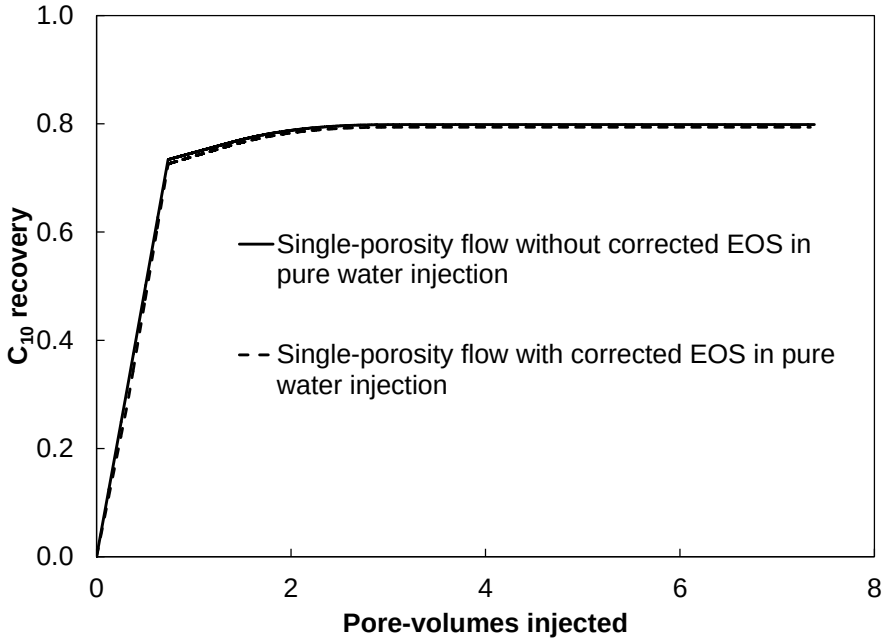

Figure 5.5 C_{10} recovery for the 1-D SPF with and without corrected EOS in pure water injection process.

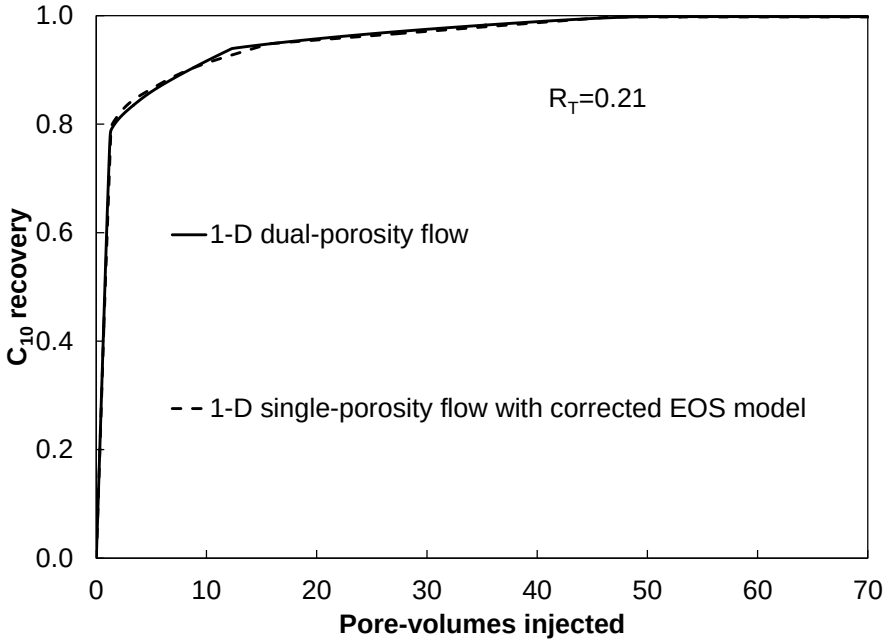
1.0
0.8
0.6
0.4
0.2
0.0
C_{10} recovery
R_T=0.21
1-D dual-porosity flow
1-D single-porosity flow with corrected EOS model
0
10
20
30
40
50
60
70
Pore-volumes injected

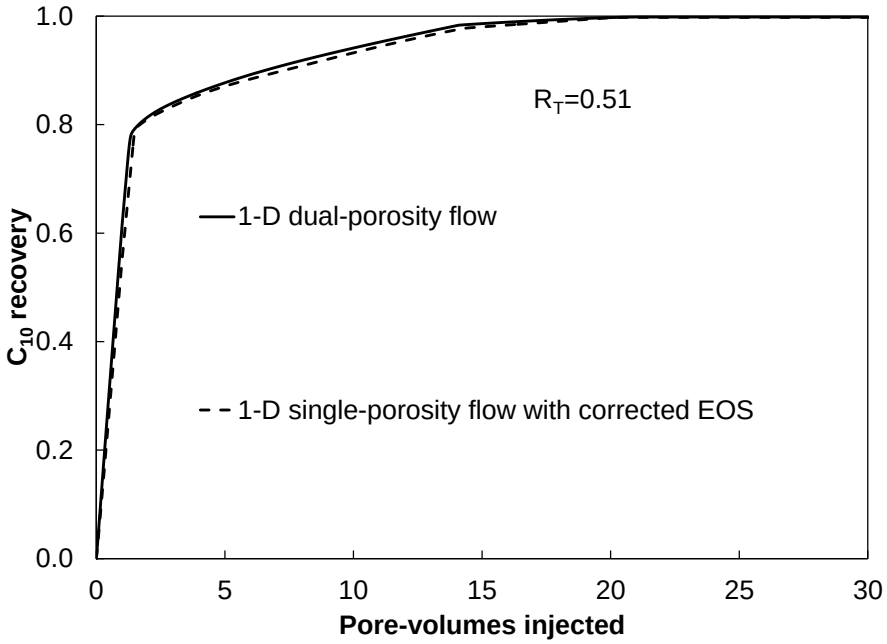
1.0
0.8
0.6
0.4
0.2
0.0
C_{10} recovery
R_T=0.51
1-D dual-porosity flow
1-D single-porosity flow with corrected EOS
0
5
10
15
20
25
30
Pore-volumes injected

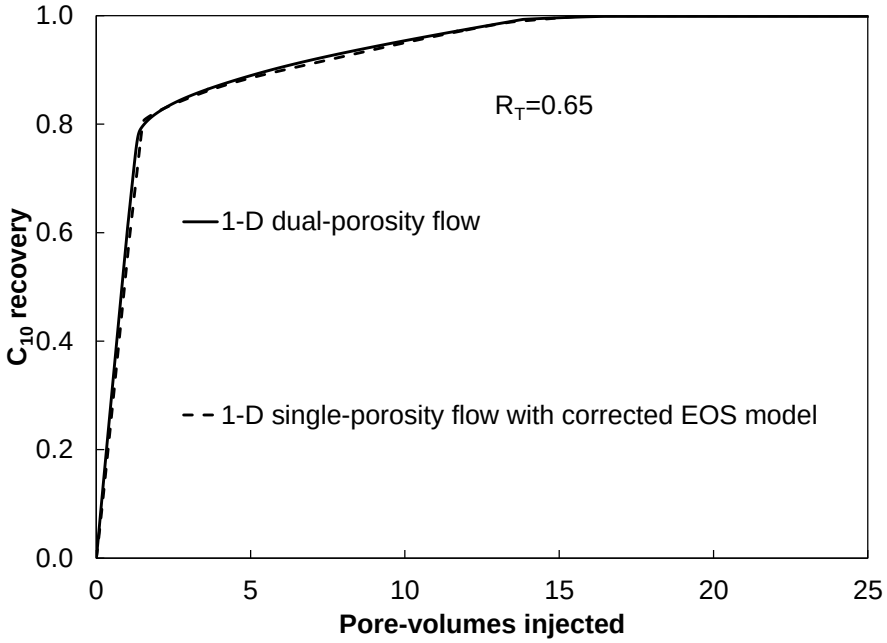

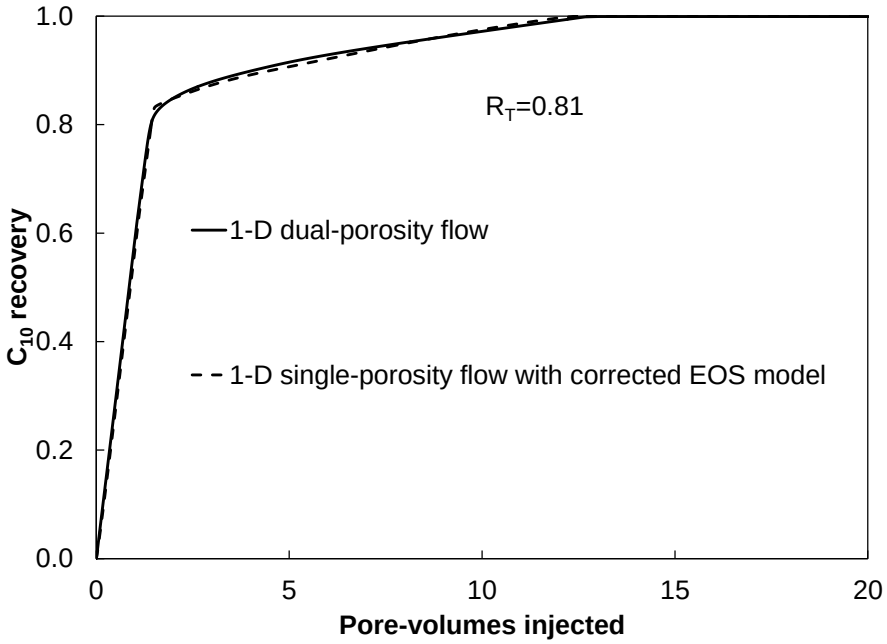

Figure 5.6 C_{10} recoveries for the 1-D DPF with throughput ratios of 0.21, 0.51, 0.65 and 0.81 is reproduced by the 1-D SPF with fluid characterization correction by changing attraction and covolume parameter.

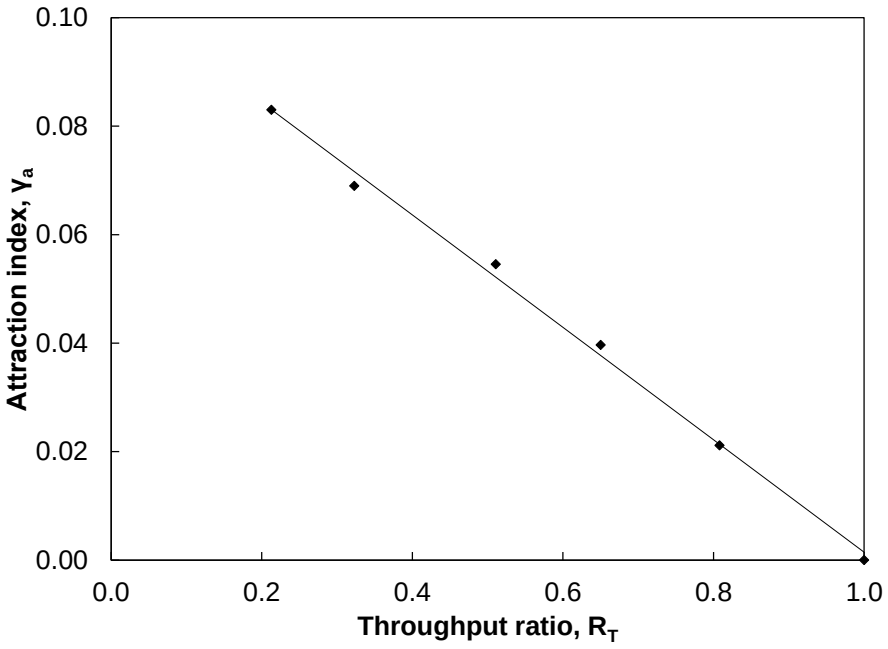

Figure 5.7 γ_A monotonically decreases with increasing R_T and is nearly linear for this case.

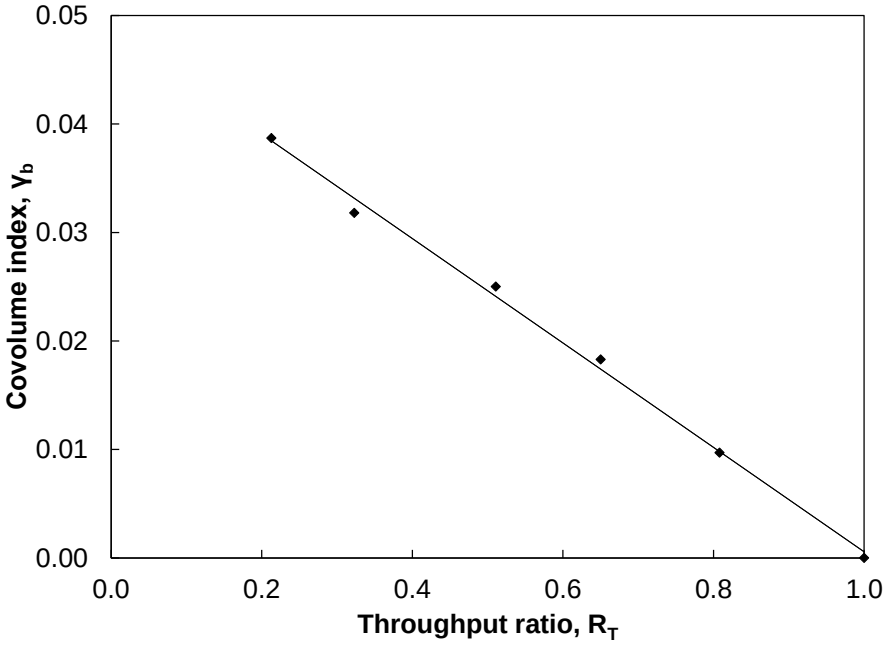

Figure 5.8 γ_B is also monotonically decreasing with the increase of τ and nearly linear for this case.

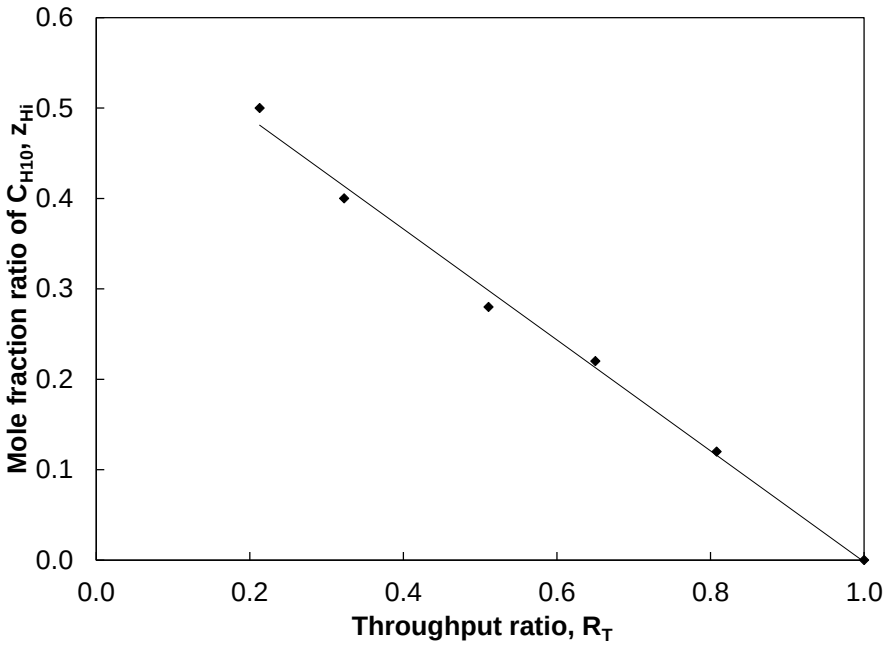

Figure 5.9 z_{Hi} monotonically decreases with increasing R_T and is nearly linear for this case.

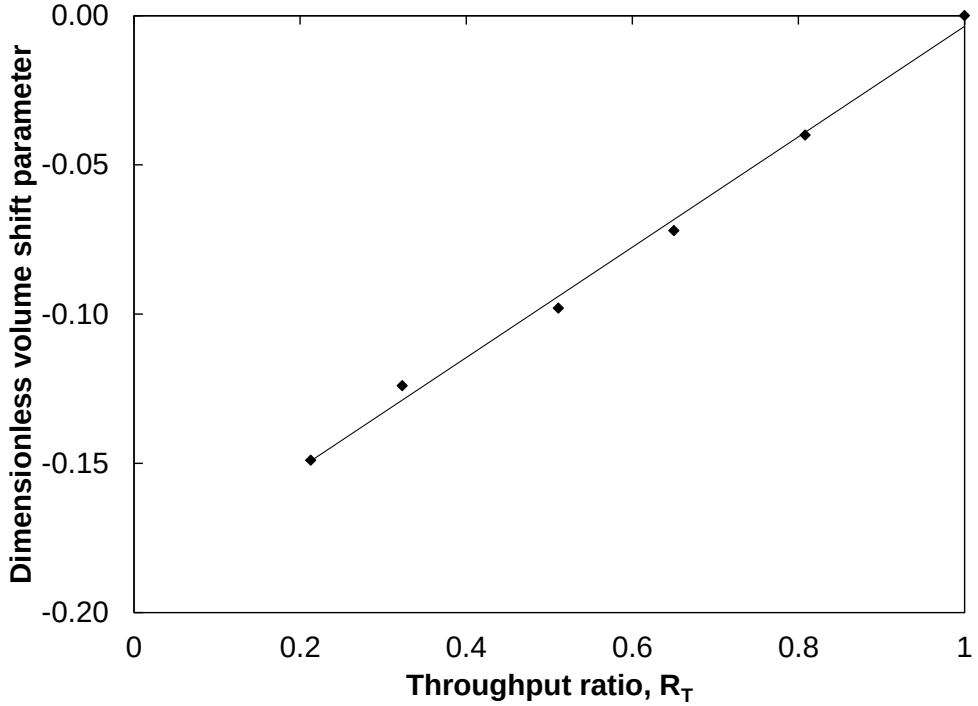

Figure 5.10 Dimensionless volume-shift parameter ($C_{pen(D)}$) monotonically increases with the increase of R_T and is nearly linear for this case.

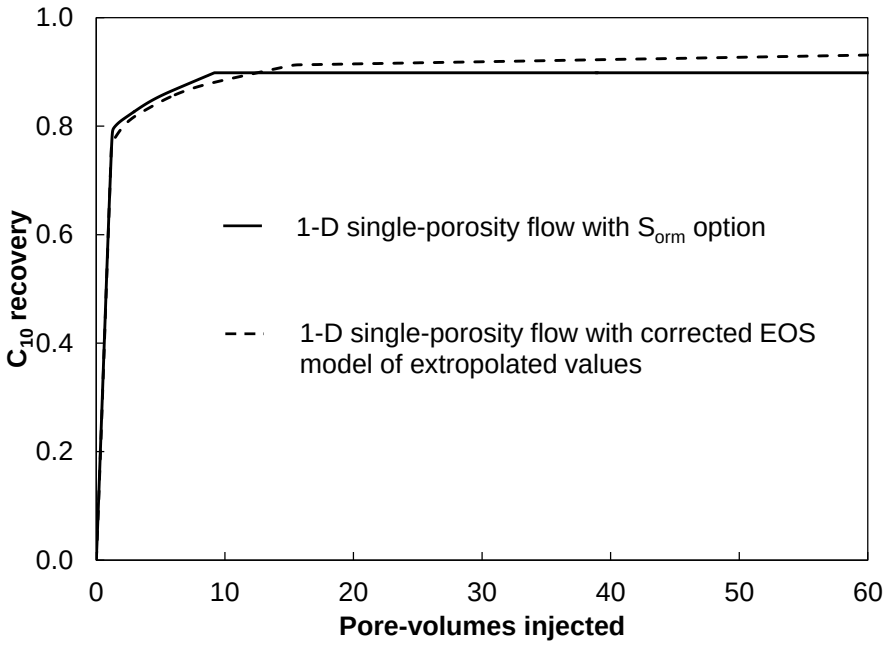

Figure 5.11 C_{10} recovery predictions for single-porosity flow with S_{orm} option and corrected EOS model with extrapolated value at R_T of 0.

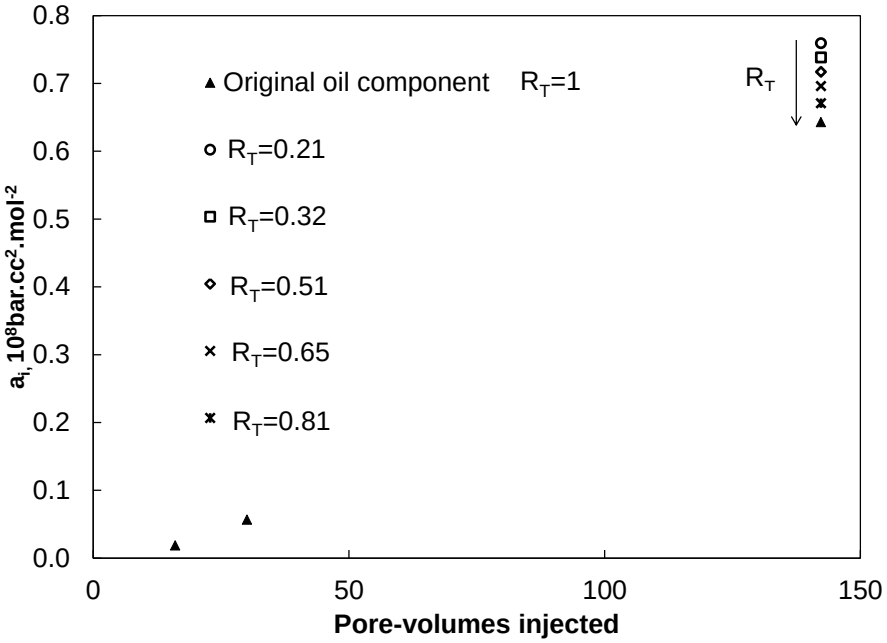

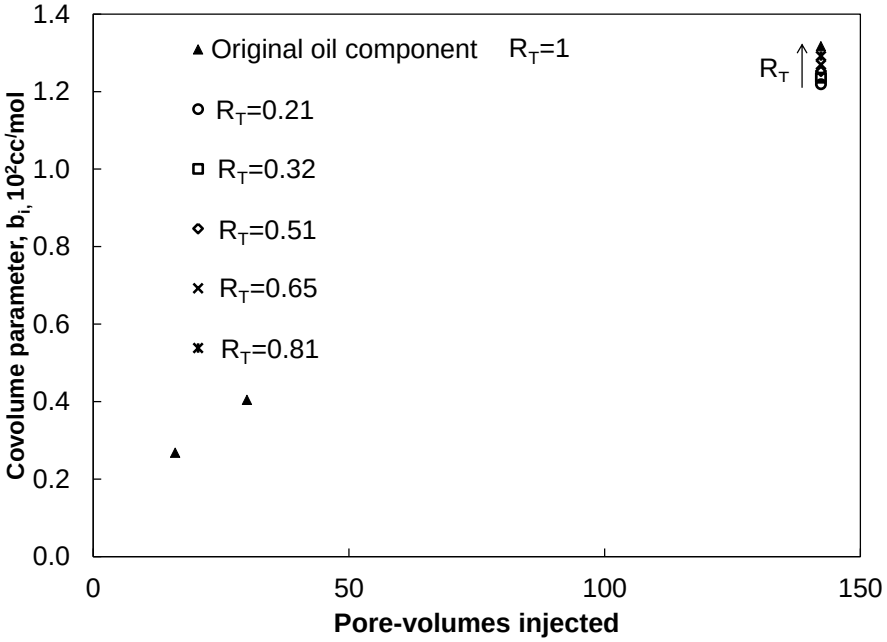

Figure 5.12 Attraction and covolume parameters of C_{10H} with different throughput ratios compared to original C_{10}.

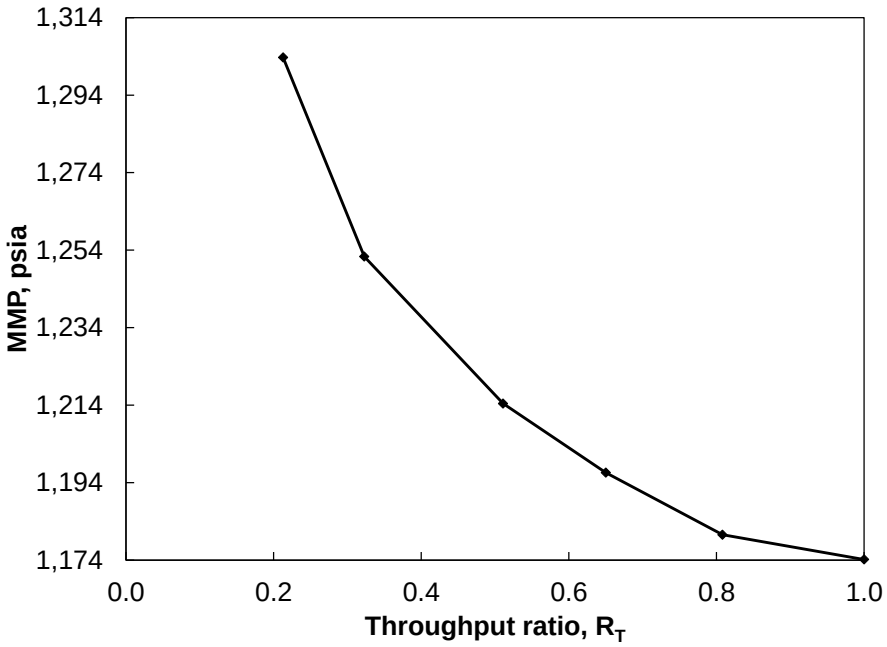

Figure 5.13 MMP predictions for the corrected EOS models with different throughput ratios from 0.21 to 1.

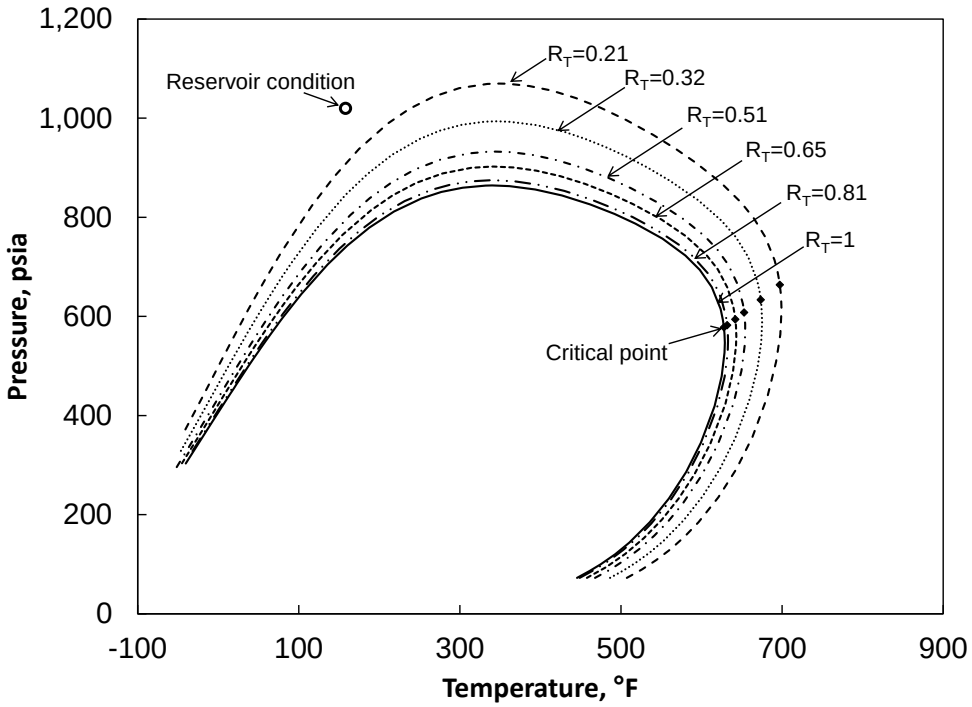

Figure 5.14 P-T diagrams for the corrected EOS models with different throughput ratios from 0.21 to 1.

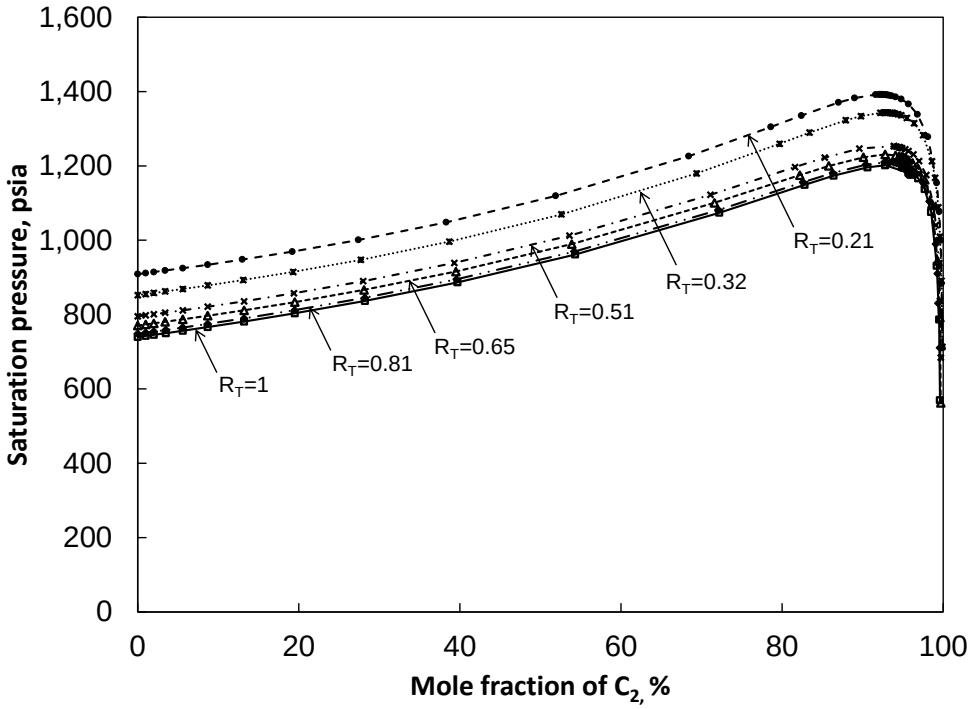

Figure 5.15 P-x diagrams for the corrected EOS models with different throughput ratios from 0.21 to 1.

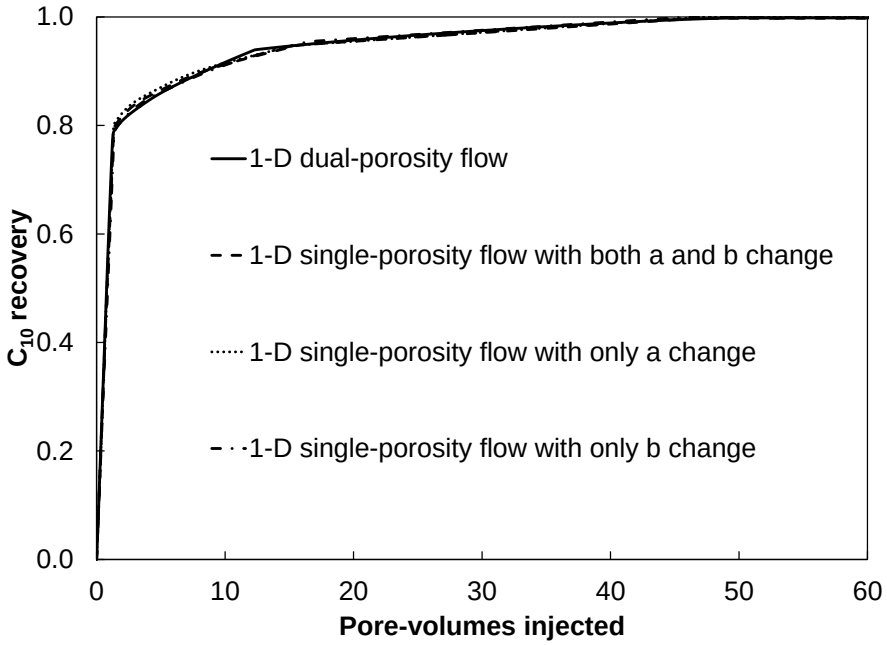

Figure 5.16 Different tuning strategies of changing attraction and covolume parameter can achieve the same accuracy in recovery prediction matching result with the dual-porosity flow with a throughput ratio of 0.21.

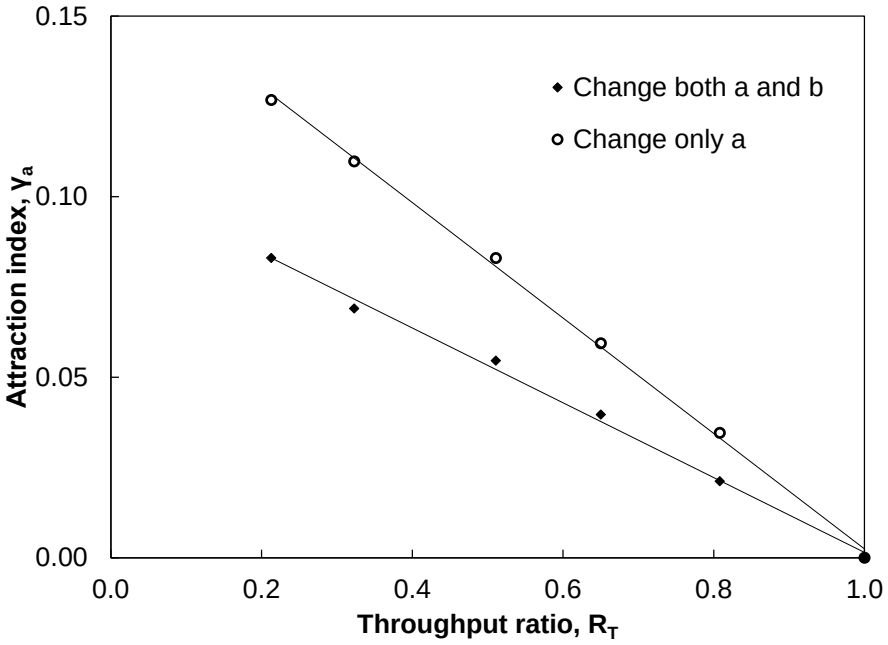

Figure 5.17 Attraction index values for the two different tuning strategies in respect of throughput ratios. The case resulting in a higher attraction index is when only attraction parameter is changed to account for capacitance effects.

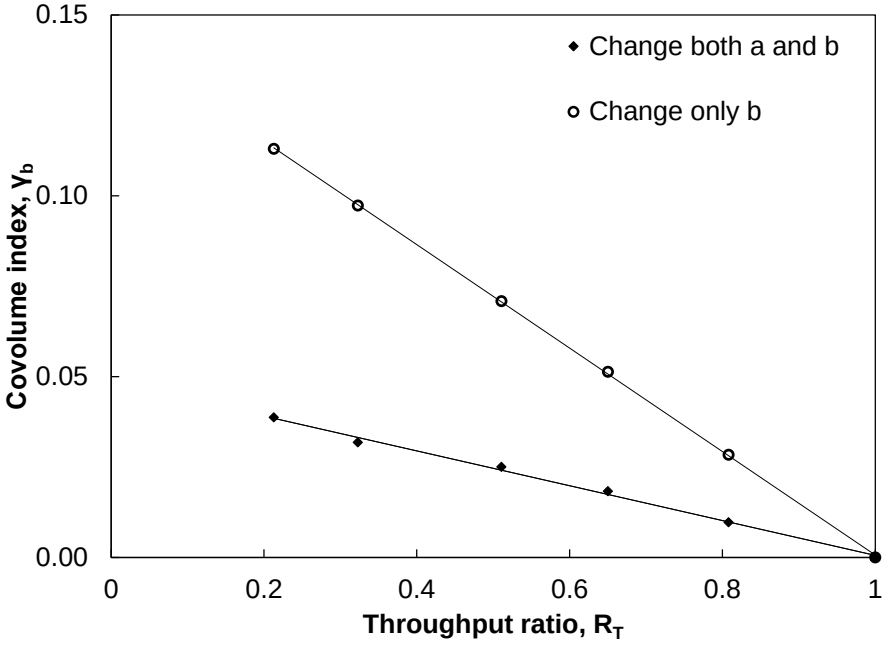

Figure 5.18 Covolume index values for the two different tuning strategies in respect of throughput ratios. The case which only attraction parameter is changed to account for capacitance effects has a higher corresponding covolume index.

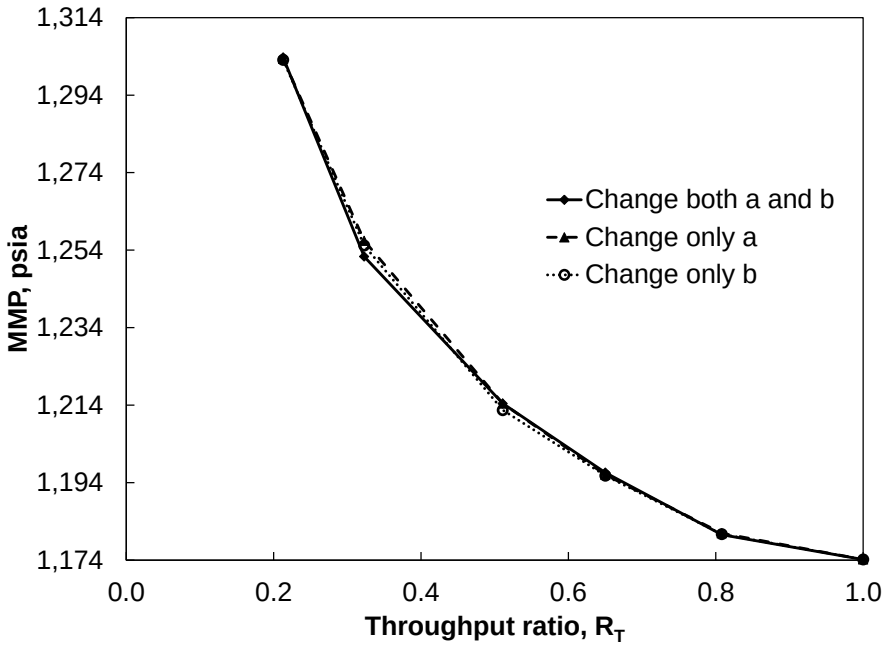

Figure 5.19 MMP predictions are almost the same for three different tuning strategies.

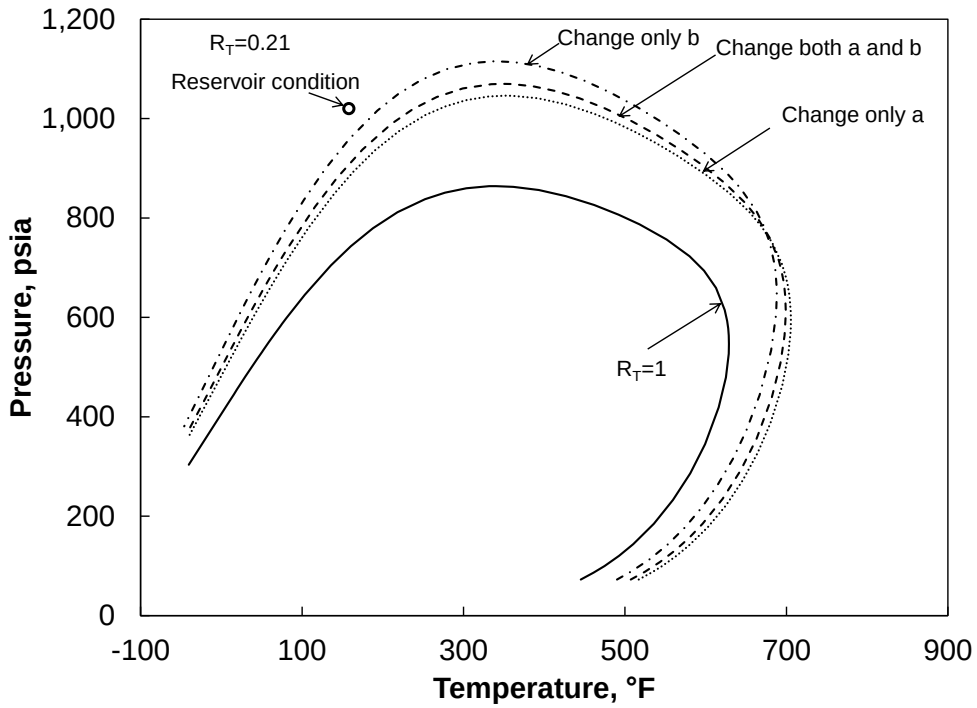
1,200
1,000
800
600
400
200
0
Pressure, psia
-100
100
300
500
700
900
Temperature, °F
R_T=0.21
Reservoir condition
Change only b
Change both a and b
Change only a
R_T=1

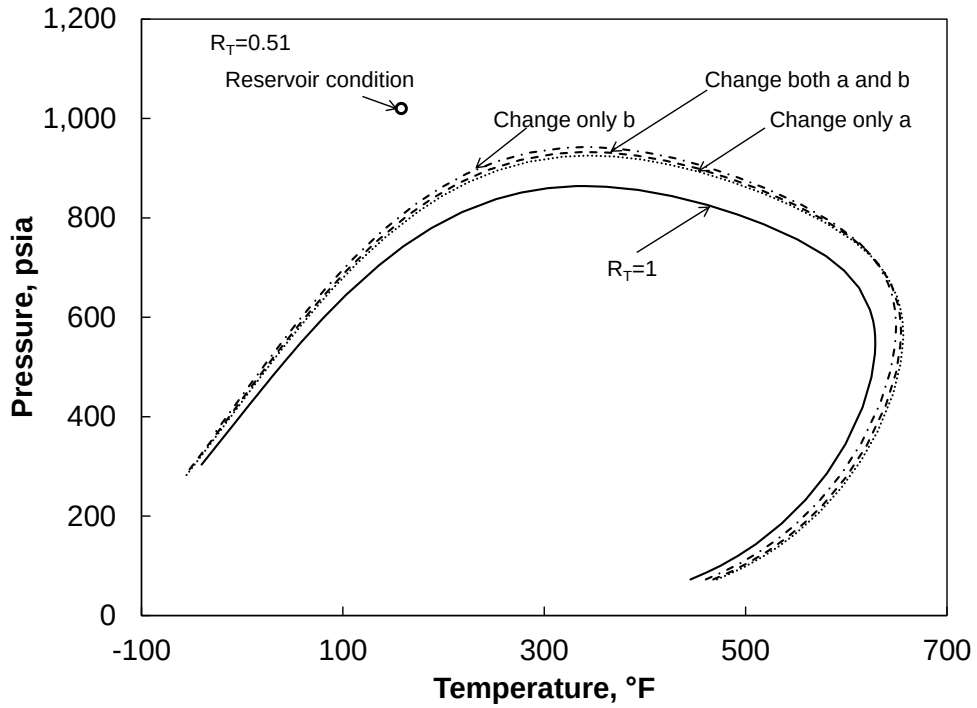
1,200
1,000
800
600
400
200
0
Pressure, psia
-100
100
300
500
700
Temperature, °F
R_T=0.51
Reservoir condition
Change only b
Change both a and b
Change only a
R_T=1

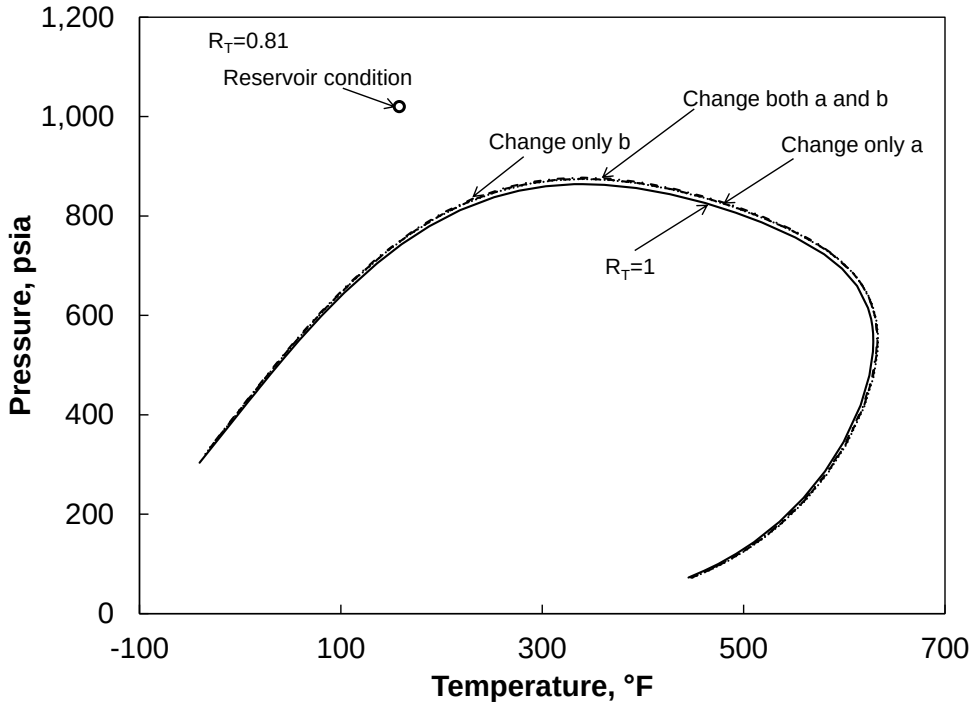

Figure 5.20 P-T diagrams for the corrected EOS models using different strategies of changing attraction and covolume parameters with throughput ratios of 0.21, 0.51 and 0.81.

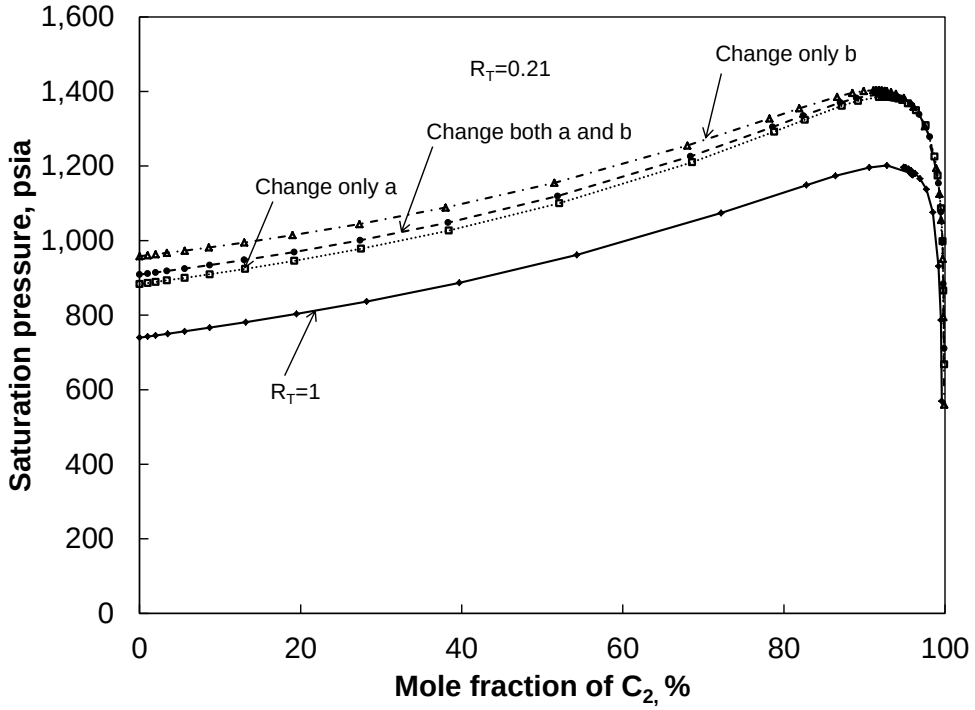

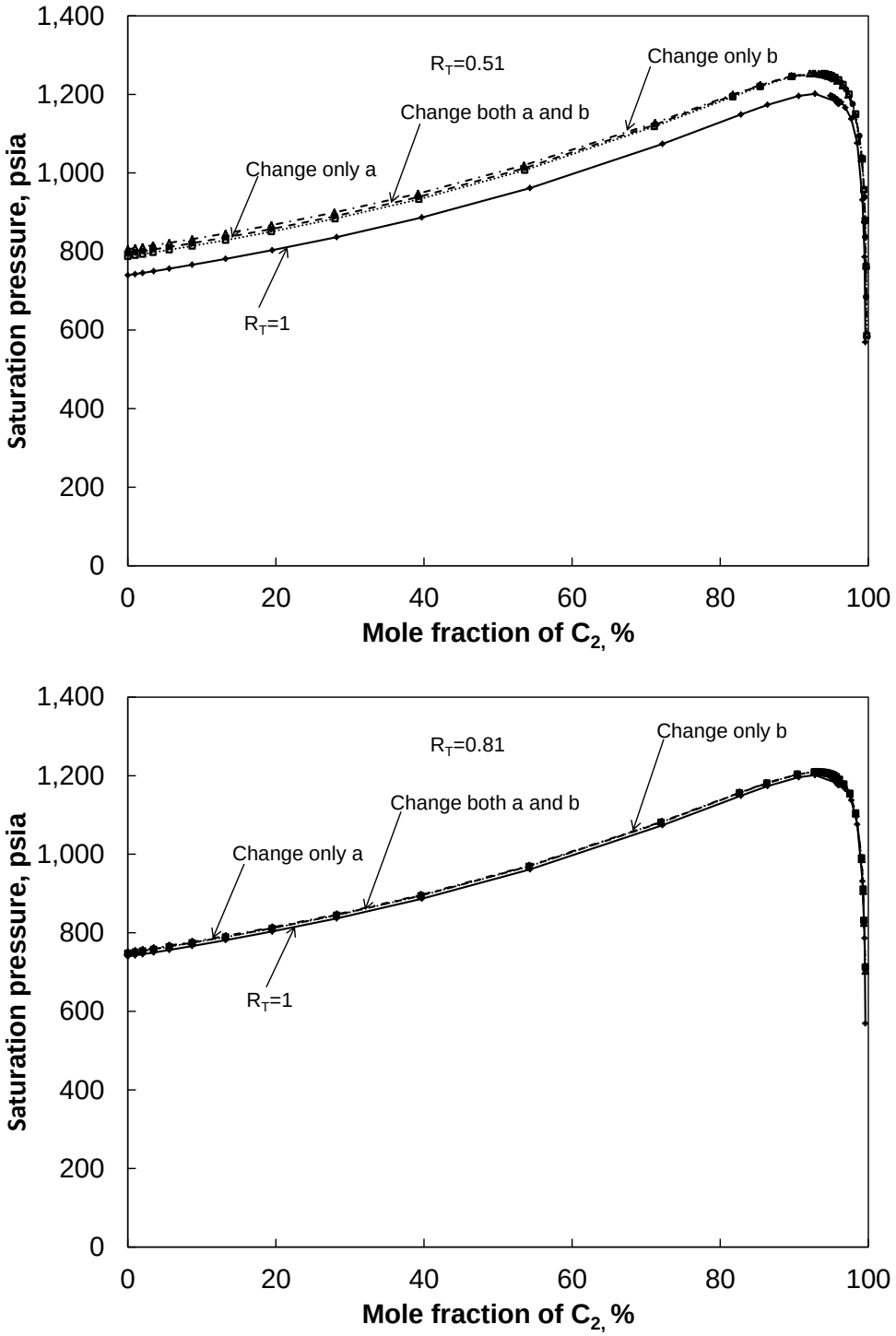

Figure 5.21 P-x diagrams for the corrected EOS models with throughput ratios of using different strategies of changing attraction and covolume parameters 0.21, 0.51 and 0.81.

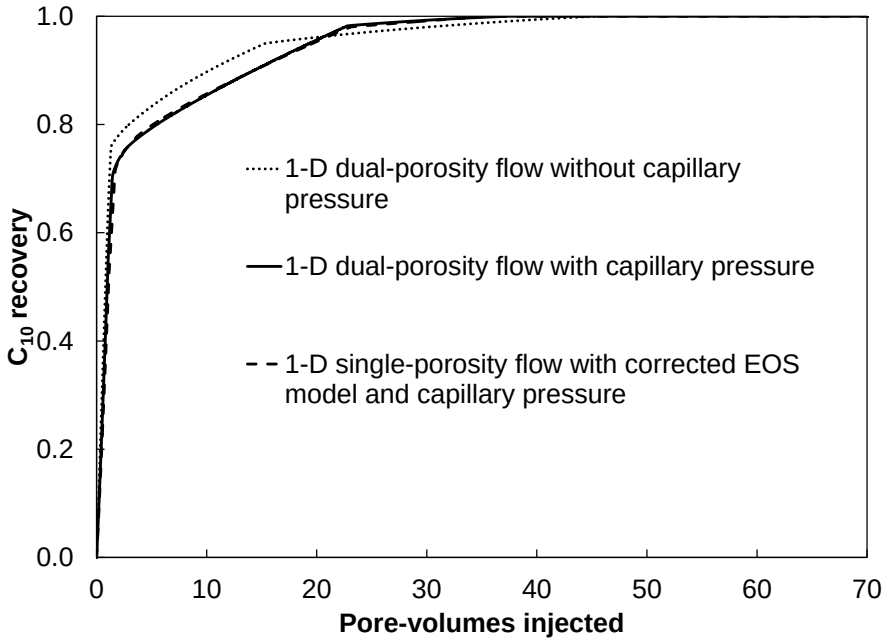

Figure 5. 22 C_{10} recovery predictions for the dual-porosity flow with and without capillary effects and the corresponding single-porosity flow with corrected EOS and capillary effects.

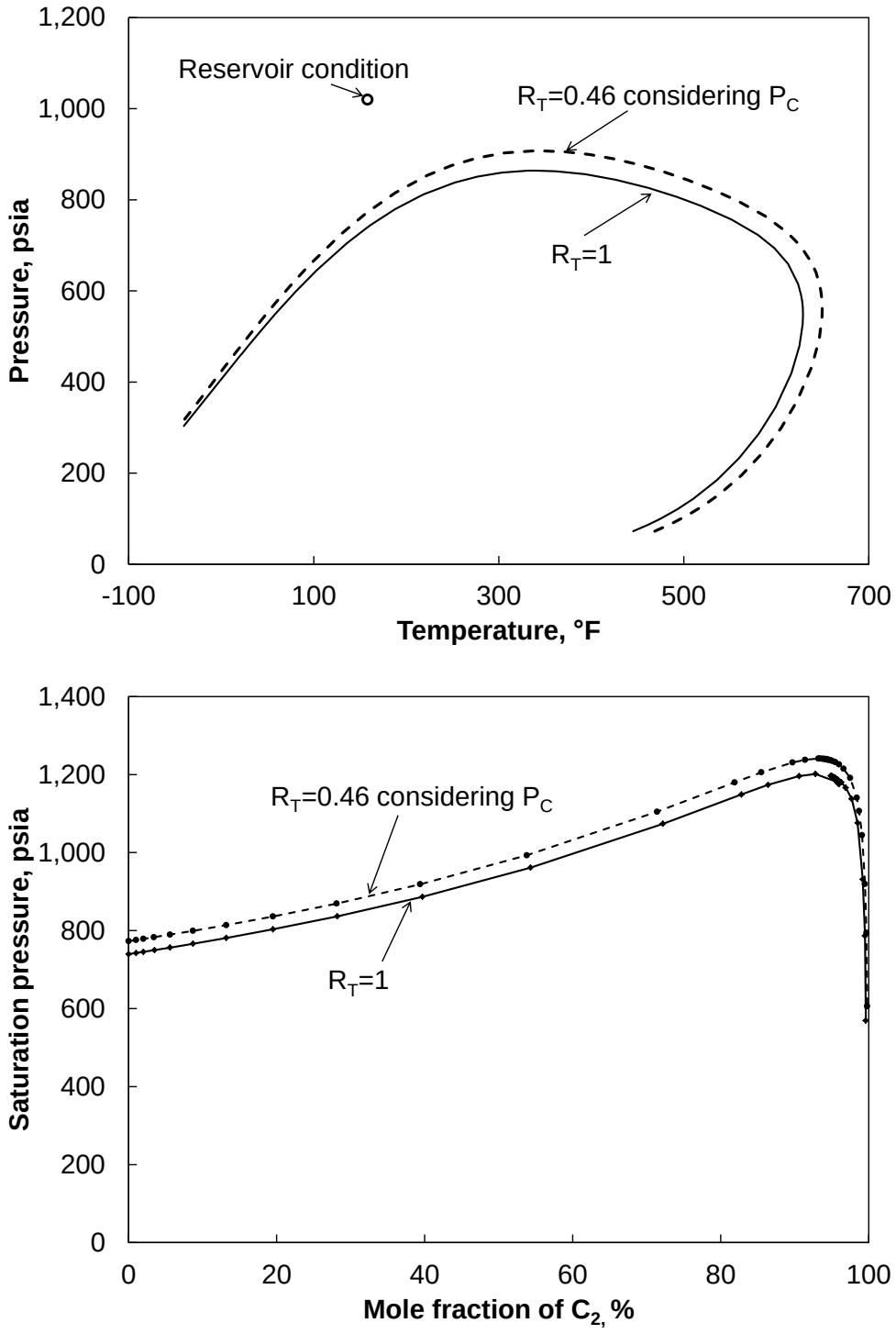

Figure 5. 23 P-T and P-x diagram for the corrected EOS model with a throughput ratios of 0.46 when capillary effects are considered.

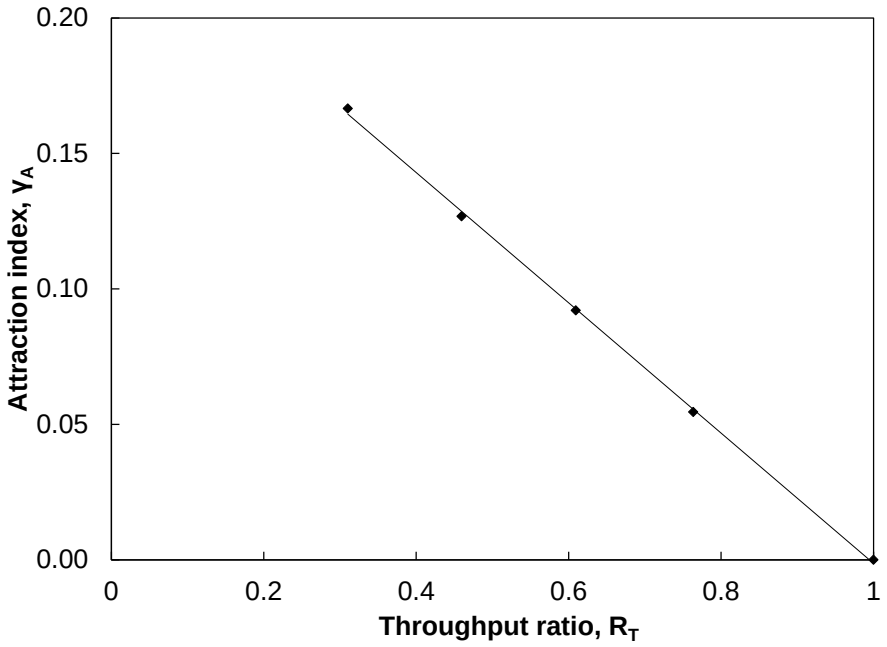

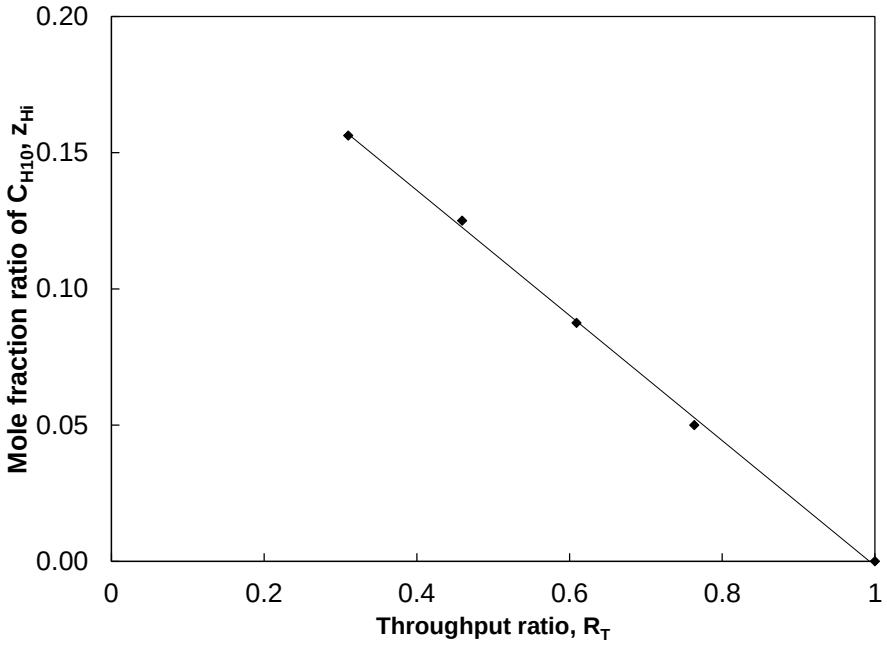

Figure 5.24 Attraction index (γ_A) and mole fraction ratio of C_{H10} (z_{Hi}) show a linear relationship with throughput ratio (R_T) for the case considering capillary effects.

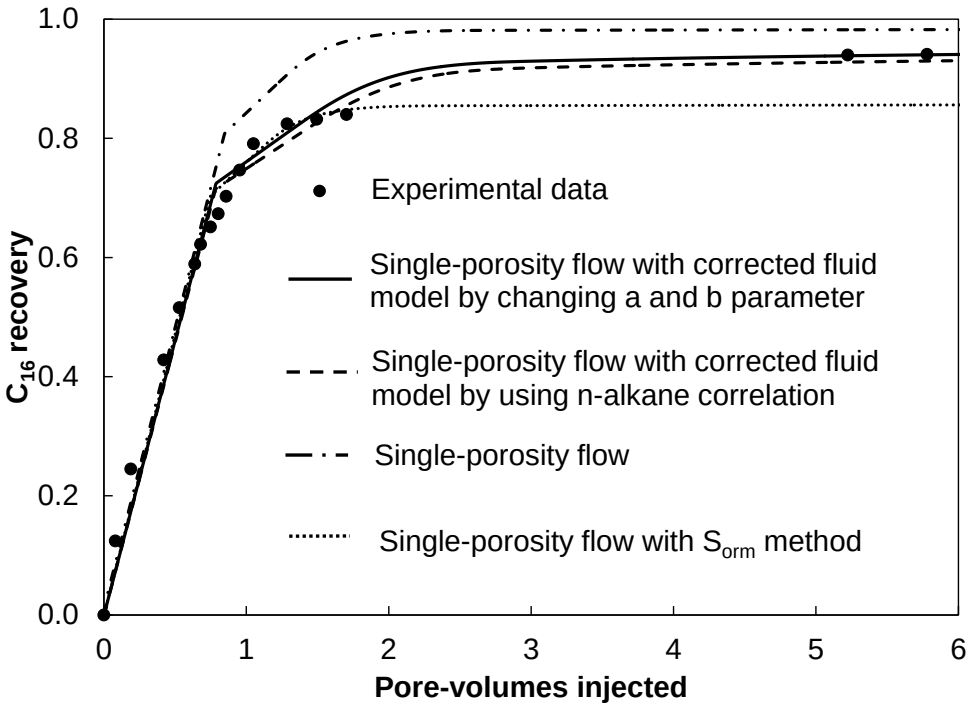

Figure 5.25 C_{16} recovery predictions for the single-porosity flow with corrected fluid model by changing attraction and covolume parameter is well fitted to experimental data.

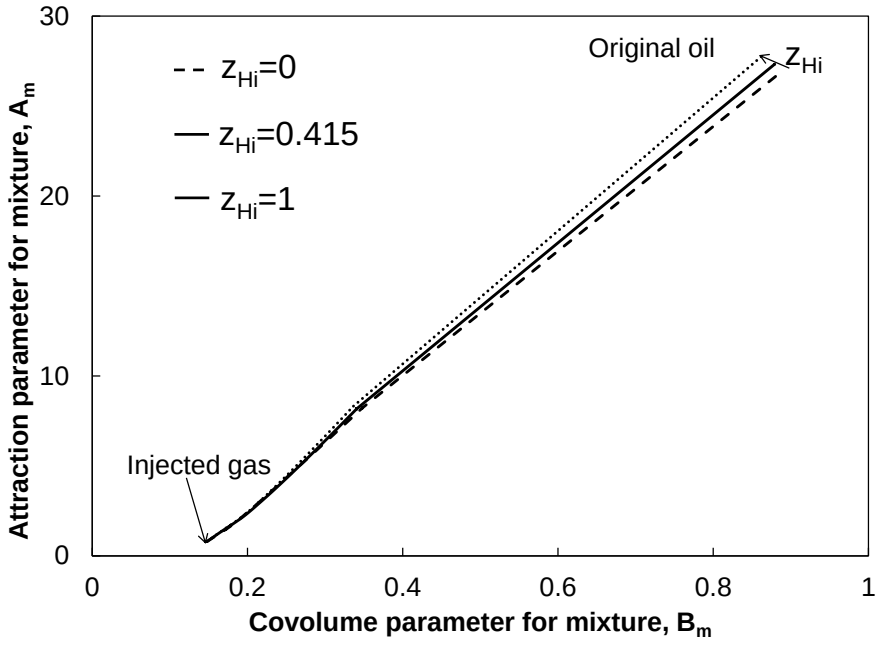

Figure 5.26 Relationship between the dimensionless attraction and covolume parameters for mixtures. z_{Hi} can be considered as the deviation from the lower boundary where no heavy oil component is introduced and compared to the distance from lower boundary and upper boundary.

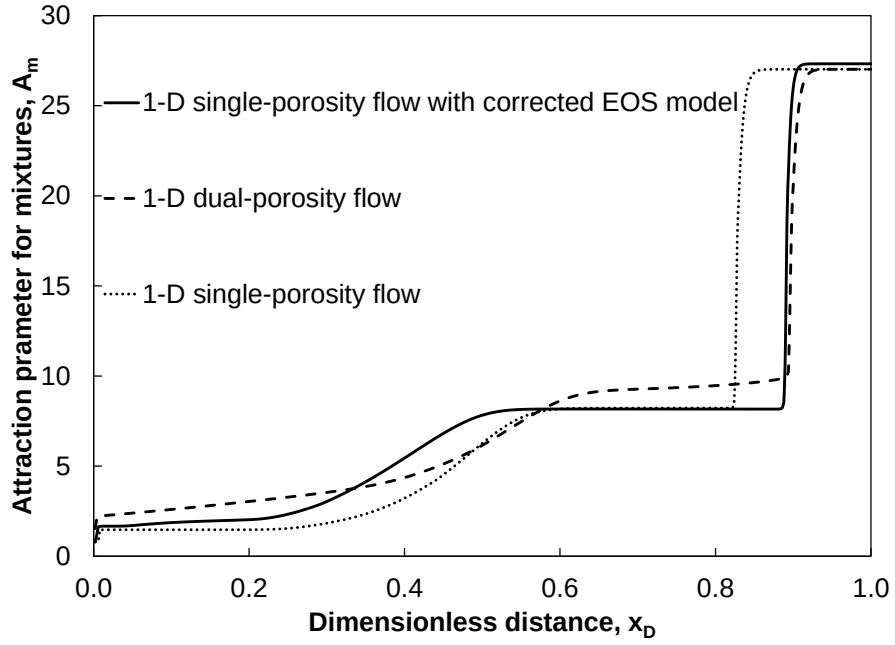

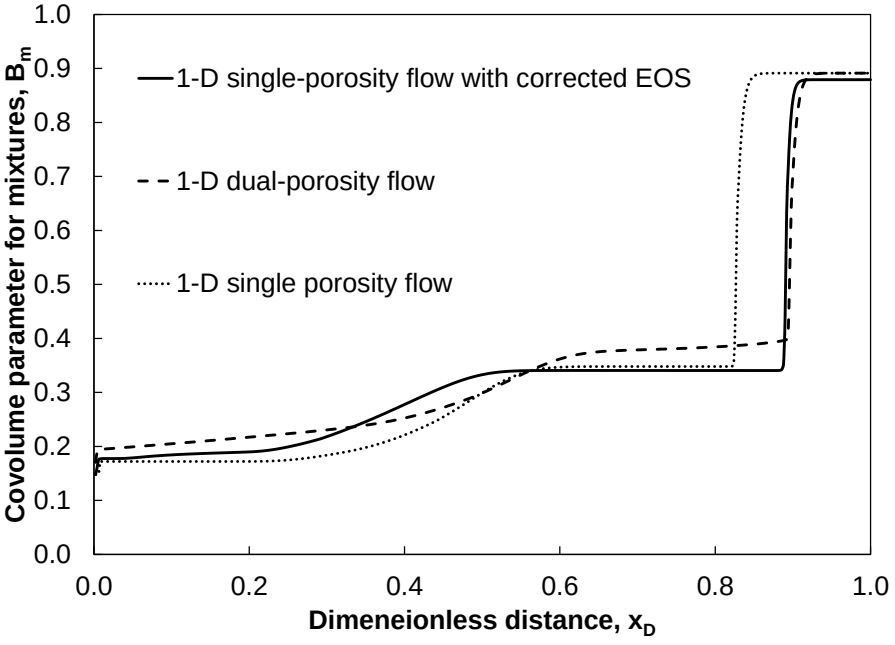

Figure 5.27 Profiles of dimensionless attraction and covolume parameters for dual-prosity flow and single-porosity flow with and without corrected EOS model at 0.7 PVI.

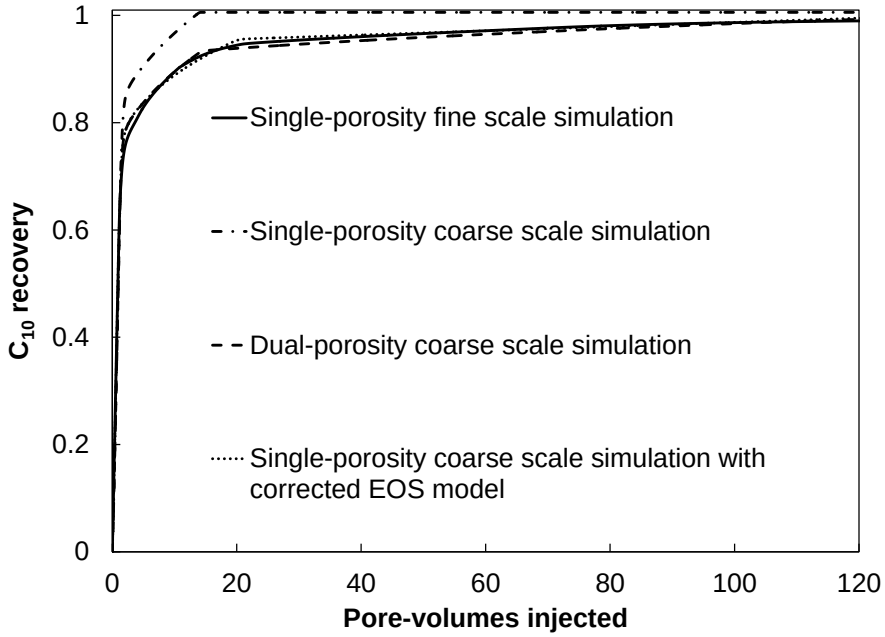

Figure 5.28 Recovery predictions for the XY-2D heterogeneous reservoir with C_1, C_2 and C_{10} mixtures which do not consider capillary effects.

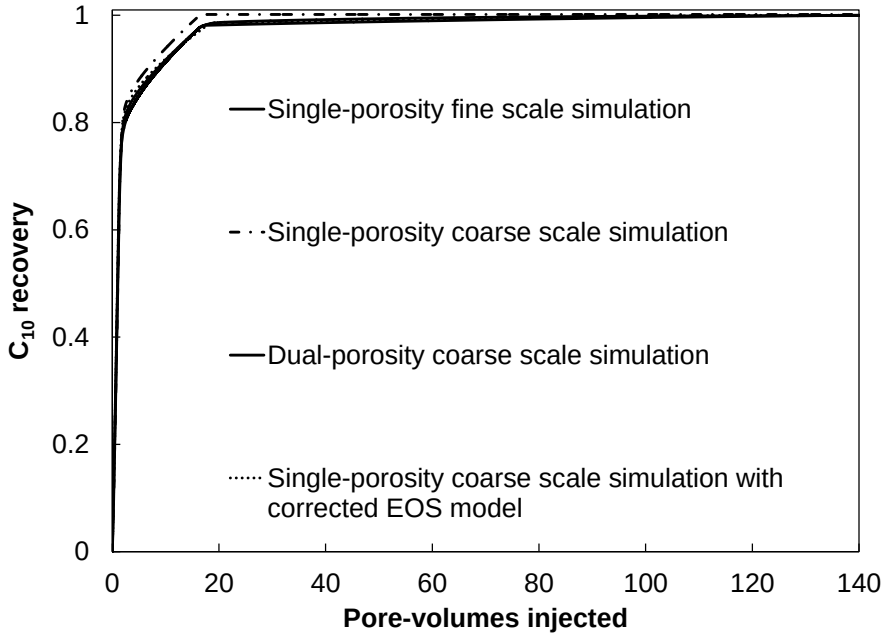

Figure 5.29 Recovery predictions for the XY-2D heterogeneous reservoir with C_1, C_2 and C_{10} mixtures considering capillary effects.

CHAPTER 6: TWO-STEP FLUID CHARACTERIZATION METHOD APPLIED IN CASE STUDYDIES

Gas injection into oil reservoirs is a favourable and promising enhance oil recovery method in terms of high gas injectivity and good displacement/sweeping efficiency over water injection. Particularly, CO_2 injection is the best option due to its superior miscibility effects with oil and in consideration of geological storage of the greenhouse gas. In this chapter, the two-step fluid characterization method is applied to assess a CO_2 injection project at near-miscible condition in the G89 Block of the Shengli Oilfield located in east China.

The two-step method is an algorithm combining the dual-porosity method quantifying capacitance effects and flow-based fluid characterization method in SPF to reproduce the flow characteristics of the capacitance effects. The two-step algorithm is presented as below:

Step 1: Quantify capacitance effects in the dual-porosity flow with corresponding bypassed fraction and throughput ratio. The first step varies for different objectives.

1. For core flooding experimental data:

Characterize the flow characteristics using a 1-D DPF to take a representative flow path.

2. For fine-scale heterogeneous reservoir:

Reproduce the fine-scale simulation result by use of a coarse-scale simulation with the dual-porosity flow.

Step 2: Correct the fluid model in SPF model to mimic capacitance effects modelled in step 1.

This two-step method is validated in the case studies of CO_2 injection at partially miscible condition. The characteristics of the capacitance effects in both core floods experiment and fine-scale heterogeneous reservoir simulation are modelled by the proposed two-step method in the single-porosity flow with the local equilibrium assumption.

6.1 Applications to reproduce the core flooding data

The objective of the core flooding test is to determine the influence of operating pressure on oil recovery and evaluate the displacement/sweep efficiency of CO_2 in near miscible pressure regimes. The detailed information for the core flooding apparatus and core properties is given in Ren et al. (2011). The compositions of the reservoir fluid and the corresponding PVT properties are also listed in the literature. The MMP determined from slim-tube experiments is around 3800 psia.

Table 6.1 gives the reservoir fluid system characterized by use of the characterization method proposed by Kumar and Okuno (2013) to avoid the usage of volume-shift parameter. The reservoir properties for the 1-D SPF simulation are listed in Table 6.2. The temperature in the core flooding experiment is fixed to be 258.80 °F. Three different injection pressures are tested in the experiments to test the influence of pressure on capacitance effects. All of the injection pressures are below MMP in the core flooding test to determine the optimum injection pressure because the reservoir pressure drops below MMP after depletion in the recent several years.

The 1-D single-porosity flow simulations are first generated based on fluid and reservoir properties in Table 6.1 and 6.2 at three different pressures. No capacitance effects at the sub-grid scale can be modelled in the single-porosity flow because of the local equilibrium assumption as shown in the solid lines in Figure 6.1, 6.2 and 6.3. The resulting Péclet number is 661 with 500 girds and 0.01 hour time step.

The first step for the fluid characterization method is quantifying capacitance effects using a 1-D DPF. The recovery prediction of the core flooding experiment at the pressure of 3263.36 psia is fitted by the 1-D DPF with a bypassed fraction of 0.14 illustrated in Figure 6.1. The estimated throughput ratio is 0.48. Figures 6.2

and 6.3 present that the core floods data with the other two injection pressures (2842.65 psia and 3727.48 psia) are both reproduced by the corresponding 1-D DPF simulations. The corresponding bypassed fraction and throughput ratio are given in the captions below the figures.

The introduced heavy oil components are only introduced for the heaviest four pseudo components as most of the bypassed oil comes from heavy components in the EOS. Following the algorithm of the fluid characterization method given in section 5.3, the corrected EOS model successfully models the capacitance effects at the pressure of 3263.36 psia as shown in Figure 6.1. The corresponding attraction index and mole fraction ratios for the four pseudo heavy components are 0.12 and 0.36, respectively. Only attraction parameters are changed in this chapter to minimize the influences on phase behaviour. The tuning parameters in fluid characterization method are strong functions of throughput ratios as the empirical linear relationship shows in section 5.4. Same γ_A and z_{Hi} are applied in the SPF simulations with corrected EOS for the other two injection pressures (2842.65 psia and 3727.48 psia) because the characterized throughput ratios in DPF are almost identical. According to Figure 6.2 and 6.3, the recovery predictions are accurate by use of the same corrected EOS from the case under injection pressure of 3263.36

psia. The recovery prediction capability for the flow-based fluid characterization is excellent concluded from the three cases with different injection pressures.

Injection rate is kept constant during the continuous CO_2 injection in the core flooding tests, so the pressure drop should keep changing with the increase of throughputs as shown in Figure 6.4. The reason is that the mobility ratio between the oil left in the reservoir and the gas injected is changing. However, the pressure drop differences during the continuous gas injection do not affect the accuracy of the correct EOS in predicting bypassed oil recovery as illustrated in Figure 6.1, 6.2 and 6.3. The change of pressure difference between the injection and production well does not affect the prediction capability of the corrected EOS. The pressure insensitivity for the fluid characterization method to model capacitance effects is important in real gas injection project because the operation pressure will inevitably change due to different reasons.

Figure 6.5 presents the comparisons for the attraction parameters for introduced heavy components and original components with respect to molecular weight. It is observed that the deviations of attraction parameters are just minor for this selected case with a throughput ratio of 0.48. Dimensionless attraction parameters for the mixtures of injected gas and original oil only have a tiny difference between the original EOS and corrected EOS along the composition path

as shown in Figure 6.6. The difference caused by the composition difference is excluded in this figure. The largest difference of A_m is corresponding to the original oil near the outlet.

Figure 6.7 illustrates the P-T diagram for the original oil in place for the characterized EOS by use of Kumar and Okuno's method. All of the three injection pressures are above saturation pressure and below MMP. Our method is confirmed to be efficiently in partially miscible condition. Case studies for gas floods with reservoir pressures above MMP show that the fluid characterization method is not capable to mimic the characteristics of capacitance effect. The reason is that it is not possible to control the wave velocity to model the longer tailing in MCM or FCM condition. On the basis of the case studies demonstrated above, MMP is the upper boundary for the efficient application for our fluid characterization method.

The uncertainties in the fluid model can be observed if different characterization methods are used. Table 3.3 presents the EOS model characterized by PVTsim to match PVT data given in the literature. T_C, P_C and ω are changed for the four pseudo components compared to Table 3.1. The PVT data is well matched for the two different characterization methods according to Table 6.4. However, the deviations in phase behaviour predictions in P-T-x space

can still be significant as shown in Figures 6.8 and 6.9. The original EOS stands for the EOS characterized by use of Kumar and Okuno's method for the original oil used for core flooding experiment. Original EOS (PVTsim) is generated by PVTsim to match the given PVT data. As the above two figures show, the deviation on P-T-x space caused by fluid model uncertainties is larger compared to corrected EOS. The corrected EOS is able to consider capacitance effects and respect the phase behaviour of the original oil compared to fluid model uncertainties.

The linear relationship between the tuning parameters in fluid characterization and throughput ratios is presented in sections 5.4, 5.6 and 5.7 for 3 component n-alkane mixtures. The linearity is tested in the 12 component EOS characterized for the oil from the Shengli Oil field. Four cases with different throughput ratios are generated beside the core flooding case with a throughput ratio of 0.48. The recovery predictions for the cases using corrected EOS in SPF is well matched with DPF cases as illustrated in Figures 6.10, 6.11, 6.12 and 6.13. The linear relationship is also observed for the 12 component EOS characterized for the oil from the Shengli Oil field in Figures 6.14 and 6.15. The phase diagrams in P-T space and P-x space for the cases with different throughput ratios are shown in Figures 6.16 and 6.17. The P-T envelopes for the oil in place deviate from local

equilibrium assumption with the decrease of throughput ratio. Similarly, the P-x envelopes are monotonically larger when the recovery of bypassed oil becomes slower.

6.2 Applications to reproduce the results of fine-scale heterogeneous simulation

The application of the two-step fluid characterization method is successful in case studies of core flooding tests of CO_2 injection at partially miscible condition in the G89 Block of the Shengli Oilfield. The two-step method is also validated in the fine-scale heterogeneous simulation in X-Z direction. The porosity and permeability distribution used are the same as that in section 3.5.1 except that the original Y direction is changed to Z direction. The reservoir pressure is 3263.36 psia and temperature is 258.8 °F. The pressure between the injector and producer is kept as 10 psia to maintain the phase behaviour. Table 6.1 is used as the fluid properties in this section. Cases with and without capillary pressures are also generated based on the relative permeability and capillary function shown in section 3.5.3.

Figure 6.18 illustrates the CO_2 concentration at 0.4 and 1.0 PVI in the X-Z 2-D fine-scale simulation without capillary pressure. The channelling is severe because the shale accumulates at the bottom of the reservoir near the inlet. Also

the gravity segregation should be another reason for the channelling. Comparing the concentration of the CO_2 for the fine-scale X-Z 2-D simulations with and without capillary pressure, it is observed that the sweep efficiency is much better for the case with capillary pressure as Figure 6.19 shows. The CO_2 in top layer is migrated to the bottom layer by the capillary crossflow. Figure 6.20 present that recovery efficiency for the case with capillary crossflow is better compared to the case without capillary pressure.

According to the equation 3.5.2 for N_{cv}, the capillary number for this X-Z 2D case is 44.03. The scaling number for capillary force and viscous force is calculated as below:

$$0.2 < \frac{MN_{cv}}{1+M} = 1.02 < 5.0. \quad (6.2.1)$$

It is concluded that the case with capillary pressure lies in the transition zone where both viscous and capillary effects are important.

The characterized gravity number is also defined to compare the gravity force and viscous force. The definition for the characterized gravity number is:

$$N_{gv} = \frac{\Delta\rho g L k_{av}}{H v \mu_o}. \quad (6.2.2)$$

The scaling number for gravity force and viscous force for the X-Z 2-D case is:

$$\frac{MN_{gv}}{1+M} = 42.63 > 5.0. \quad (6.2.3)$$

It is corresponding to Figure 6.18 that gravity segregation is notable in the CO_2 concentration profile.

The fine-scale simulation is characterized by the coarse-scale simulation with corrected EOS using the two-step method. In the first step, the 120×30 fine-scale heterogeneous reservoir is upscaled to a 12×3 coarse-scale reservoir following the procedure in section 3.5.5 with a bypassed fraction distribution. The dual-porosity flow significantly improves the recovery prediction for the upscaled coarse-scale simulation without capillary pressure as it shows in Figure 6.21. The resulting bypassed fraction is 0.1 and throughput ratio is 0.22. In step 2, the fictitious heavy oil components for the four pseudo componentsa are introduced to model capacitance effects in single-porosity flow. Figure 6.21 demonstrates that the corrected EOS applied in the coarse-scale simulation successfully models capacitance effects in the fine-scale heterogeneous reservoir. The corresponding γ_A and z_{Hi} are 0.531 and 0.12, respectively.

Figure 6.22 illustrates that recovery prediction by single-porosity flow with local equilibrium assumption in coarse-scale simulation considering capillary effects is relatively good compared to the case without capillary pressure. The reason is that capillary crossflow enhances the recovery of bypassed oil in fine-scale simulation so the sub-grid capacitance effects can be neglected. The

DPF for the case with capillary pressure is generated to confirm this statement. The resulting bypassed fraction and throughput ratio for the DPF with capillary pressure are 0.04 and 0.32, respectively. Comparing to the case without capillary pressure, the bypassed fraction is decreased and throughput ratio is increased, hence the recovery of bypassed oil is faster. Accordingly, the corresponding γ_A and z_{Hi} tend to be smaller to make the introduced heavy oil component lighter and occupy less mole fraction ratio. The estimated γ_A and z_{Hi} are 0.421 and 0.03, respectively. The recovery prediction is slightly improved with the minor changes in DPF and SPF with corrected EOS as it presents in Figure 6.22. Figure 6.23 gives the CO_2 concentration profiles for the dual-porosity coarse-scale simulation with and without capillary pressure at 1.0 PVI. Compared to the concentration profile in fine-scale simulation, the dual-porosity coarse-scale simulation models the averaged capacitance effects in individual grid blocks for the corresponding region in the fine-scale simulation. The gravity segregation in the case without capillary pressure and capillary crossflow enhancement in the recovery of bypassed oil in the case with capillary pressure are also shown in Figure 6.23.

TABLE 6.1 – PROPERTIES OF THE FLUID SYSTEM APPLIED IN CORE FLOODING EXPERIMENT OF THE SHENGLI OIL FIELD

	Oil (mole fraction)	Gas (mole fraction)	Molecular weight (g/mol)	T_C (℉)	P_C (psia)	ω	V_C (ft^3/lb-mol)
N_2	0.003	0.000	28.01	-232.51	492.26	0.0400	1.44
CO_2	0.005	1.000	44.01	87.89	1069.80	0.2250	1.51
C_1	0.244	0.000	16.04	-116.59	667.18	0.0080	1.59
C_2	0.023	0.000	30.07	90.05	708.37	0.0980	2.37
C_3	0.031	0.000	44.10	205.97	615.83	0.1520	3.25
C_4	0.030	0.000	58.12	305.69	551.15	0.1930	4.08
C_5	0.038	0.000	72.15	385.61	489.36	0.2510	4.87
C_6	0.069	0.000	86.18	453.65	430.62	0.2960	5.93
PC1	0.215	0.000	122.99	775.74	510.68	0.1761	10.11
PC2	0.153	0.000	173.09	927.18	406.40	0.2776	11.94
PC3	0.114	0.000	231.28	1056.90	334.17	0.3975	14.6
PC4	0.076	0.000	350.53	1229.94	251.21	0.6096	17.38

TABLE 6.2 – RESERVOIR PROPERTIES USED FOR 1-D SPF OF COREFLOODING SIMULATION OF THE SHENGLI OIL FIELD

Dimensions	$0.0123 \times 0.8723 \times 0.8723$ in^3
Number of gird blocks	$500 \times 1 \times 1$
Porosity	0.1529
Permeability	19.49 md (X, Y, Z)
Reservoir pressure	2842.65/3263.36/3727.48 psia
Reservoir temperature	258.80 ℉
Injection rate	4.39 in^3/min
Production pressure	2842.65/3263.35/3727.48 psia
Relative permeability model	Corey
Residual saturation (Oil/Gas)	0.1/0.0
Endpoint relative permeability (Oil/Gas)	1.0/0.5
Exponent (Oil/Gas)	1.5/3.0
Initial saturation (Oil/Gas)	1.0/0.0

TABLE 6.3 – PROPERTIES OF THE FLUID SYSTEM APPLIED IN CORE FLOODING EXPERIMENT OF THE SHENGLI OIL FIELD GENERATED BY PVTSIM.

	Oil (mol%)	Gas (mol%)	Molecular weight (g/mol)	T_C (℉)	P_C (psia)	ω	V_C (ft^3/lb-mol)
N_2	0.003	0.000	28.01	-232.51	492.26	0.0400	1.44
CO_2	0.005	1.000	44.01	87.89	1069.80	0.2250	1.51
C_1	0.244	0.000	16.04	-116.59	667.18	0.0080	1.59
C_2	0.023	0.000	30.07	90.05	708.37	0.0980	2.37
C_3	0.031	0.000	44.10	205.97	615.83	0.1520	3.25
C_4	0.030	0.000	58.12	305.69	551.15	0.1930	4.08
C_5	0.038	0.000	72.15	385.61	489.36	0.2510	4.87
C_6	0.069	0.000	86.18	453.65	430.62	0.2960	5.93
PC1	0.215	0.000	122.99	**705.857**	**483.91**	**0.1780**	10.11
PC2	0.153	0.000	173.09	**897.589**	**412.34**	**0.2396**	11.94
PC3	0.114	0.000	231.28	**990.797**	**344.68**	**0.3702**	14.6
PC4	0.076	0.000	350.53	**1584.505**	**273.43**	**0.5055**	17.38
The bold parameters are different from Table 6.1							

TABLE 6.4 – PVT DATA REPRODUCED BY TWO DIFFERENT CHARACTERIZATION METHOD FOR THE FLUID SYSTEM APPLIED IN CORE FLOODING EXPERIMENT OF THE SHENGLI OIL FIELD.

Characterization method	Characterized by PnA method	Characterized by PVTsim
Saturation pressure @ 258.8 ℉ (psia)	1638.36	1641.18
FVF @1638.36 psia	1.226	1.223
FVF @3263.36 psia	1.199	1.196
Density @ 1638.36 psia (lb/ft3)	47.82	47.68
Density @ 3263.36 psia (lb/ft3)	48.91	48.77
Viscosity @ 1638.36 psia (cp)	1.342	1.342
Viscosity @ 3263.36 psia (cp)	1.748	1.745
MMP @ 258.8 °F (psia)	3777.52	3771.94

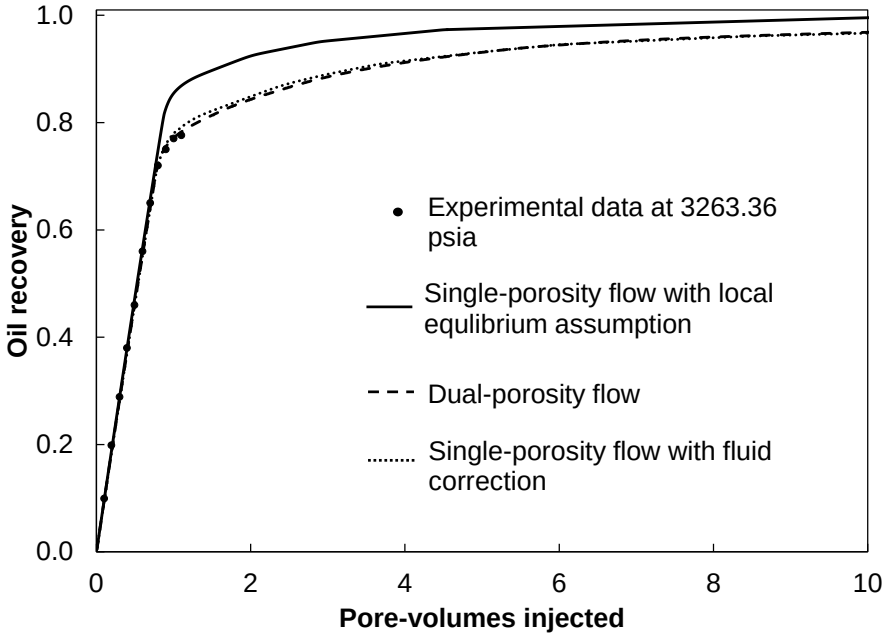

Figure 6.1 1-D DPF model fitted to core floods data in the Shengli Oil field (P = 3263.36 psia) gives a bypassed fraction of 0.14 and a throughput ratio of 0.48. The recovery prediction cannot be reproduced using the 1-D SPF models unless the fluid model is corrected.

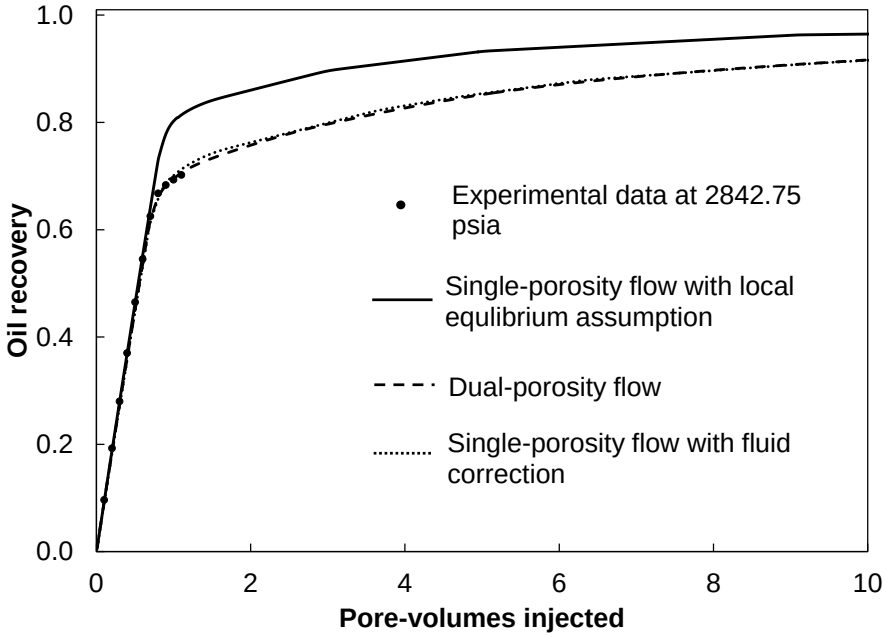

Figure 6.2 1-D DPF model fitted to core floods data in the Shengli Oil field (P = 2842.75 psia) gives a bypassed fraction of 0.18 and a throughput ratio of 0.48.

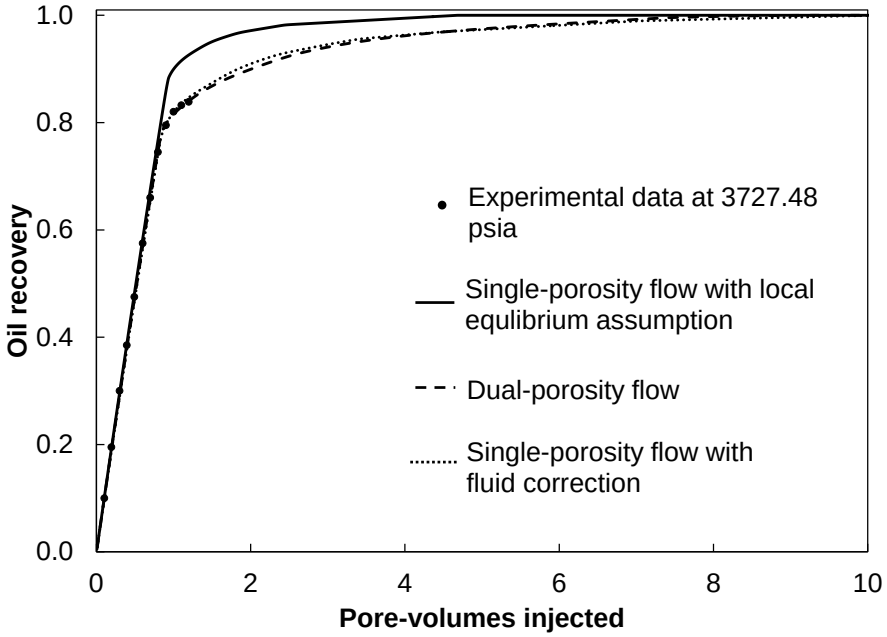

Figure 6.3 1-D DPF model fitted to core floods data in the Shengli Oil field (P = 3727.48 psia) gives a bypassed fraction of 0.14 and a throughput ratio of 0.472.

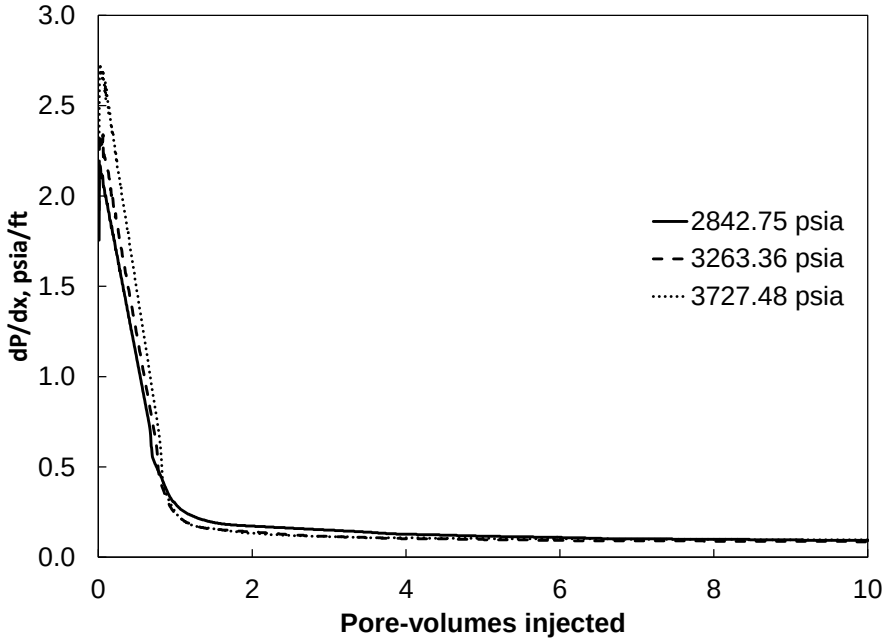

Figure 6.4 Pressure drops keep decreasing during the gas injection process for three different injection pressures with constant injection rate. Different pressure drop has no influence on the applicability of the correct EOS in SPF to reproduce the recovery predictions modelled in 1-D DPF model as shown by Figure 6.1, 6.2 and 6.3.

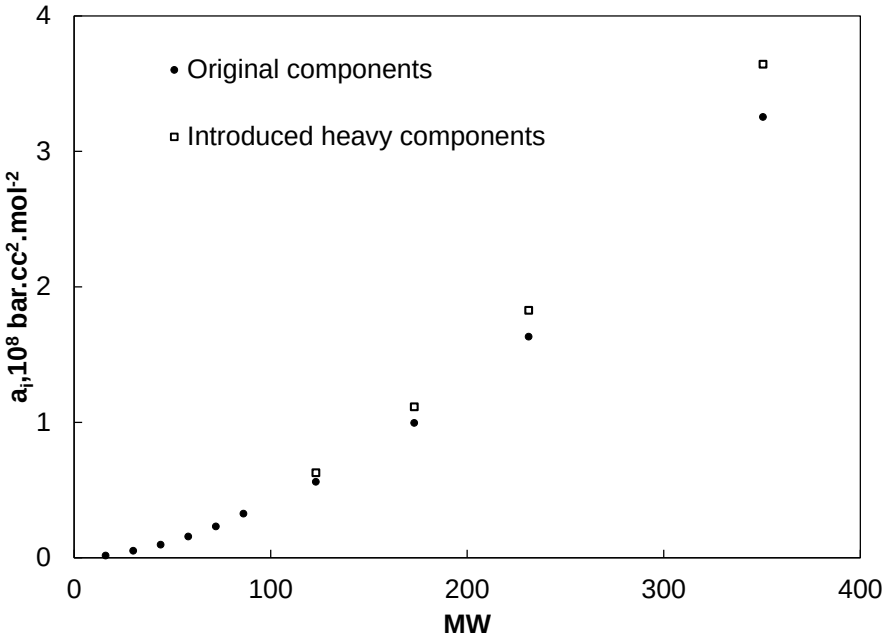

Figure 6.5 Attraction parameters of the introduced heavy components are larger compared to original components.

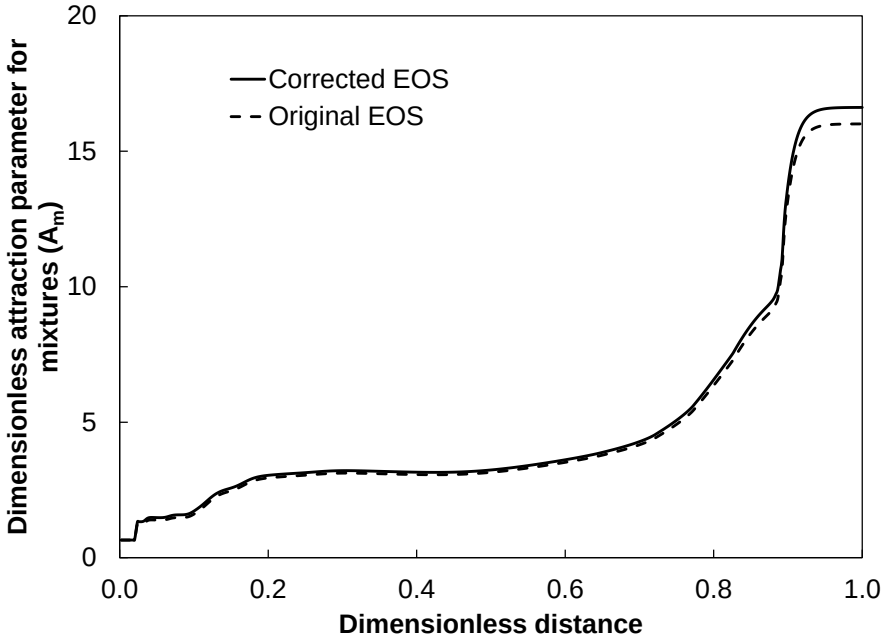

Figure 6.6 Dimensionless attraction parameters for the mixtures of reservoir oil and injected gas have tiny difference between the corrected EOS and original EOS along the composition. The largest difference near the outlet is the original oil.

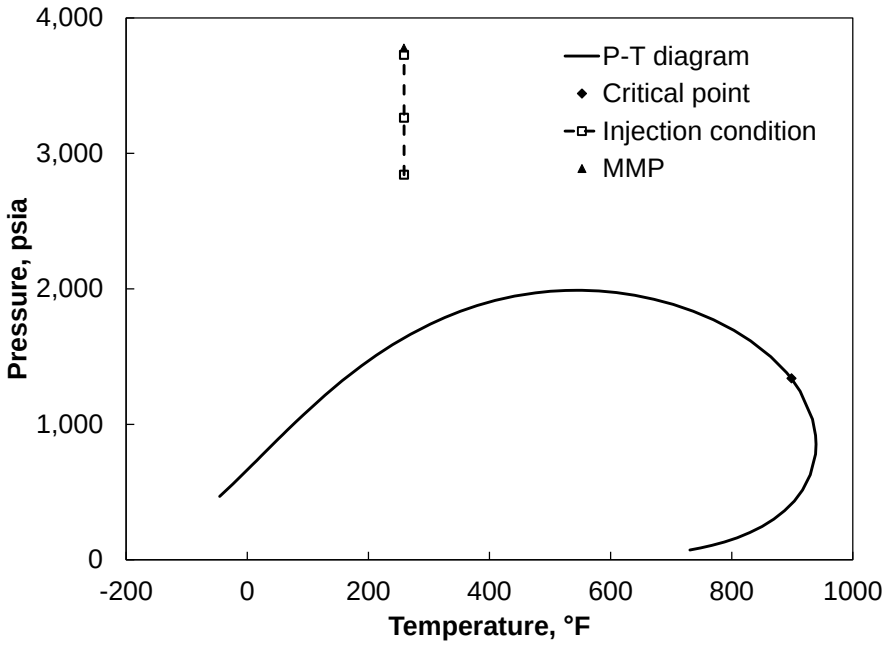

Figure 6.7 P-T diagram for the original oil used in the core flooding experiment for the Shengli Oil field. The original oils at three injection pressures are all in liquid phase and below MMP.

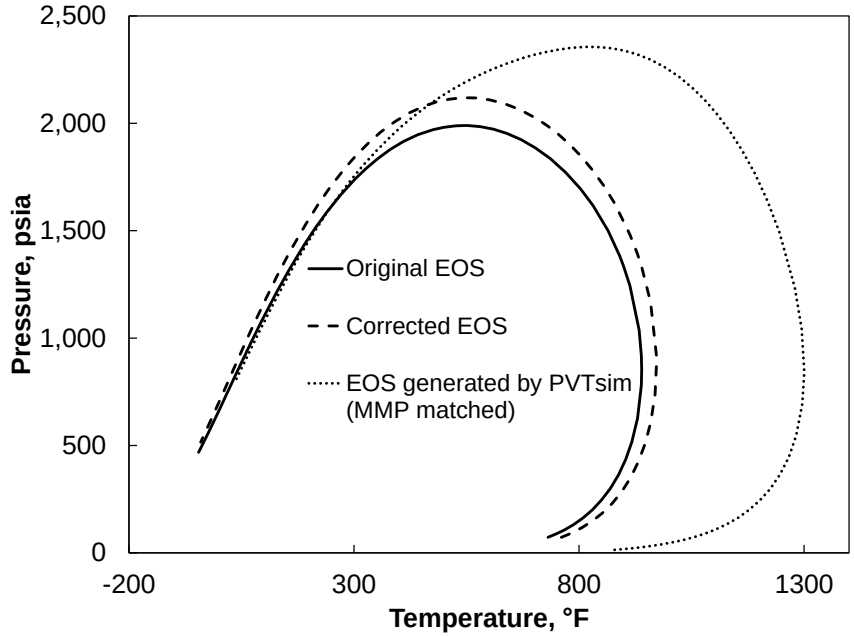

Figure 6.8 P-T diagrams for the original EOS and corrected EOS. The original EOS is characterized by two different methods showing the uncertainties in fluid characterization. The deviation on P-T diagram for the corrected EOS is reasonable compared to fluid model uncertainties.

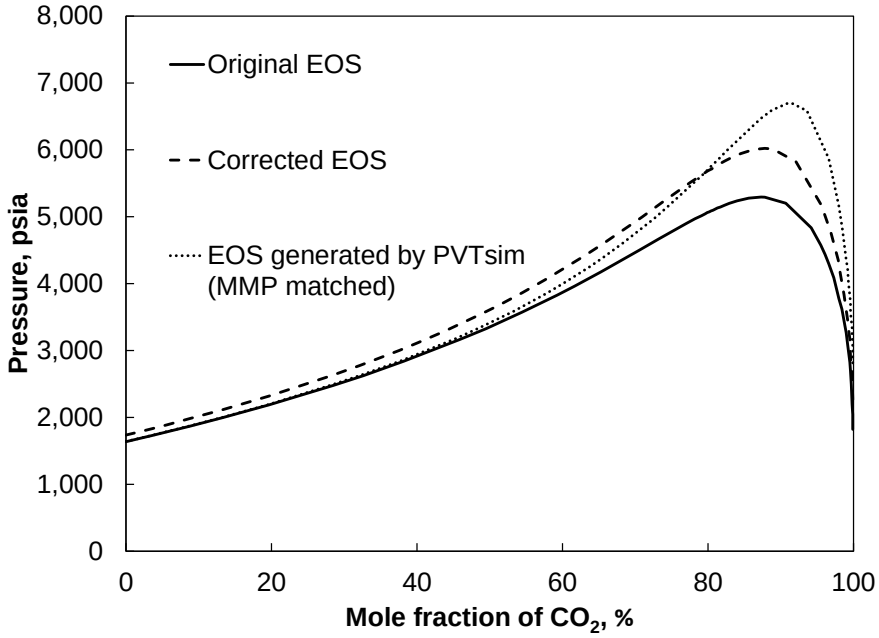

Figure 6.9 P-x diagrams for the original EOS and corrected EOS. The original EOS is characterized by two different methods showing the uncertainties in fluid characterization. The deviation in P-x diagram for the corrected EOS is reasonable compared to fluid model uncertainties.

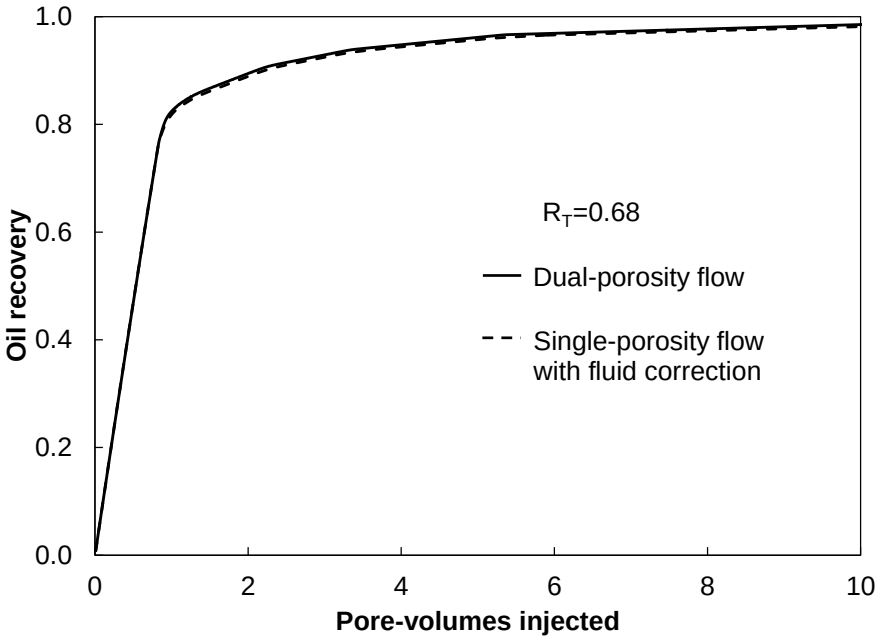

Figure 6.10 Recovery predictions for the dual-porosity flow and single-porosity flow with fluid correction with a throughput ratio of 0.68.

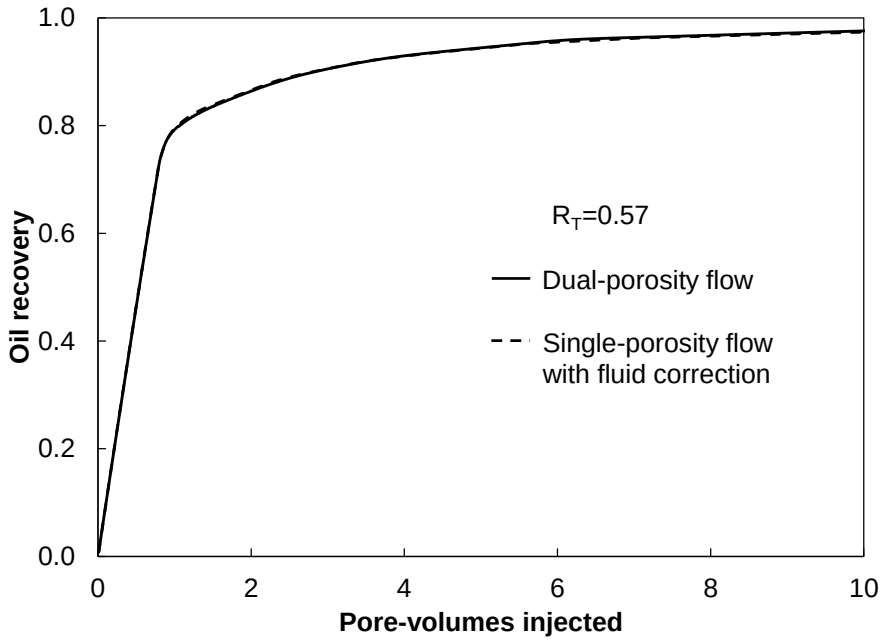

Figure 6.11 Recovery predictions for the dual-porosity flow and single-porosity flow with fluid correction with a throughput ratio of 0.57.

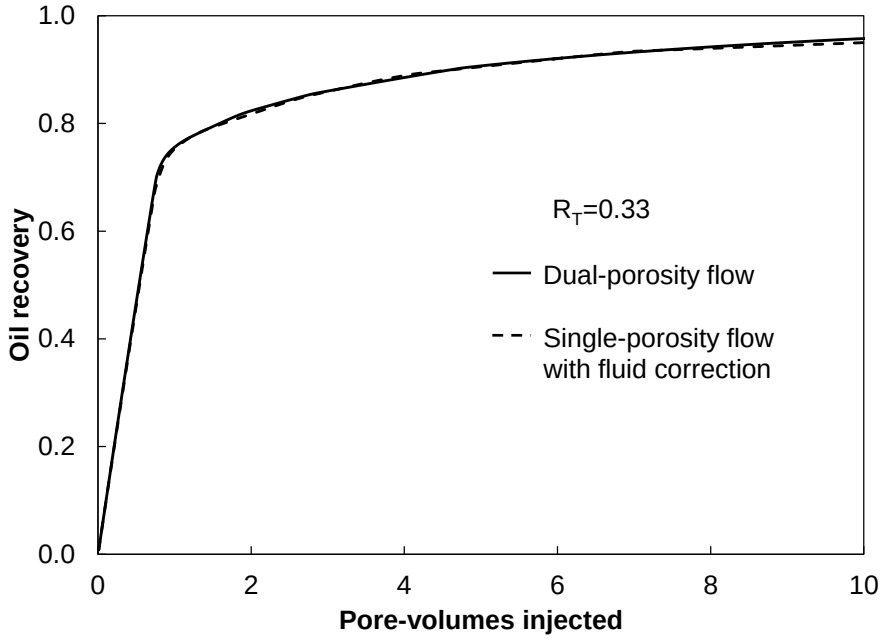

Figure 6.12 Recovery predictions for the dual-porosity flow and single-porosity flow with fluid correction with a throughput ratio of 0.33.

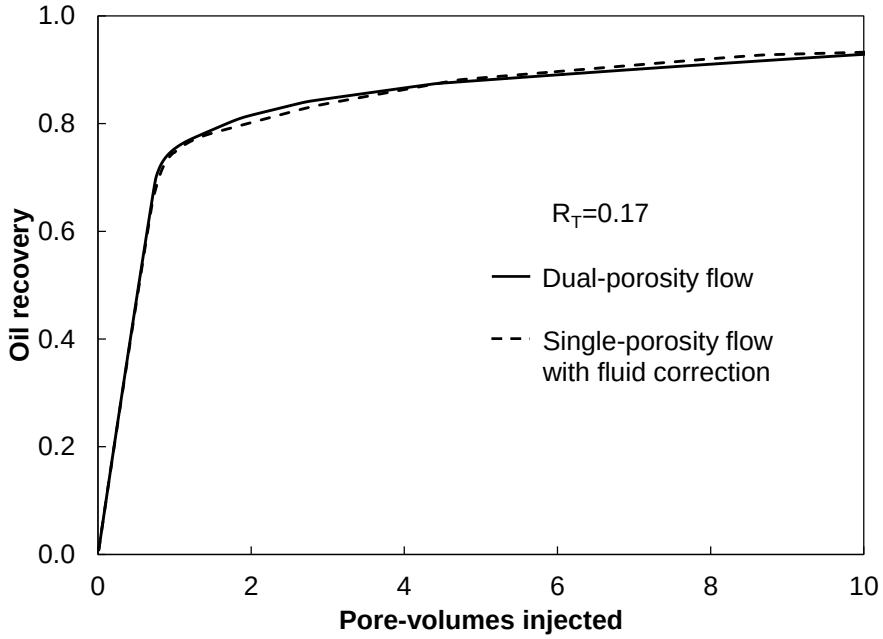

Figure 6.13 Recovery predictions for the dual-porosity flow and single-porosity flow with fluid correction with a throughput ratio of 0.17.

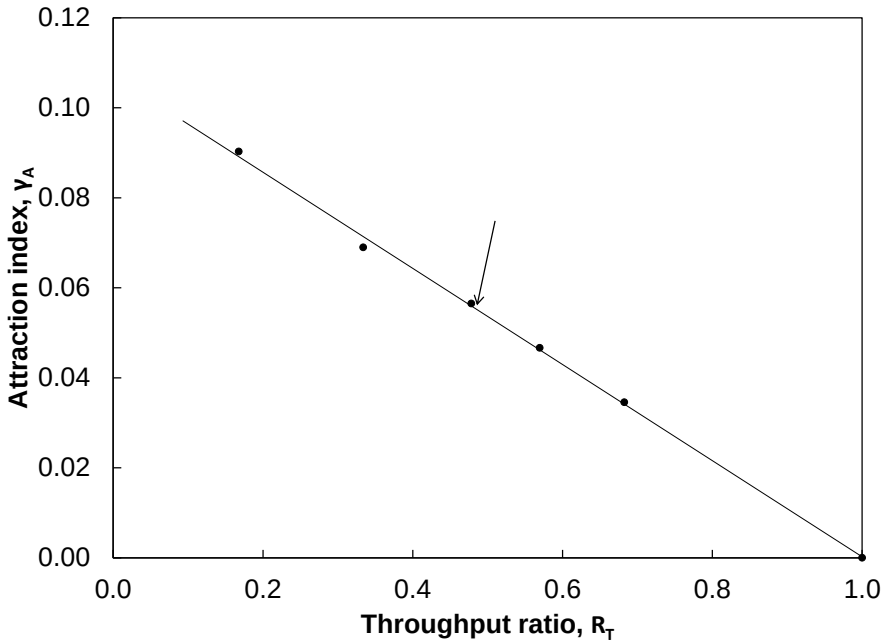

Figure 6.14 Linear relationship between attraction index and throughput ratios at pressure of 3263.36 psia. The core flooding case is corresponding to the point marked by the arrow.

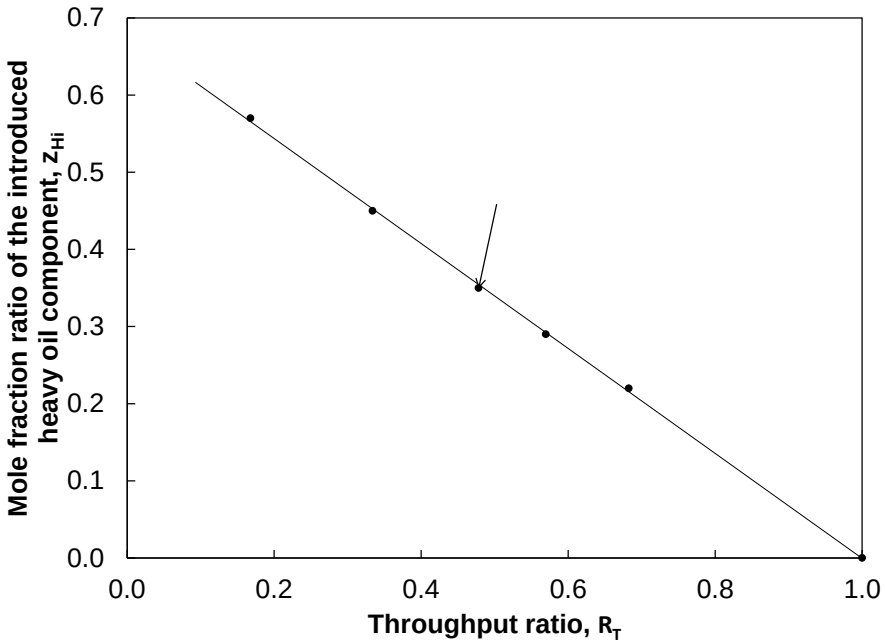

Figure 6.15 Linear relationship between mole fraction ratios of the introduced heavy oil component and throughput ratios at pressure of 3263.36 psia. The core flooding case is corresponding to the point marked by the arrow.

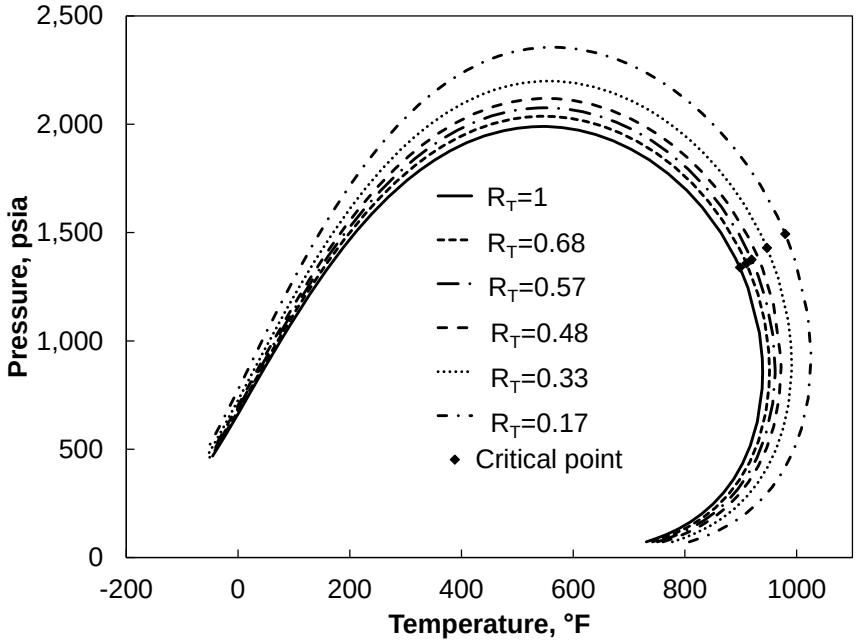

Figure 6.16 P-T diagrams for the cases with different throughput ratios at pressure of 3263.36 psia for 12-component EOS characterized for the Shengli Oil field. With the decrease of throughput ratios, the P-T envelopes deviate from local equilibrium assumption.

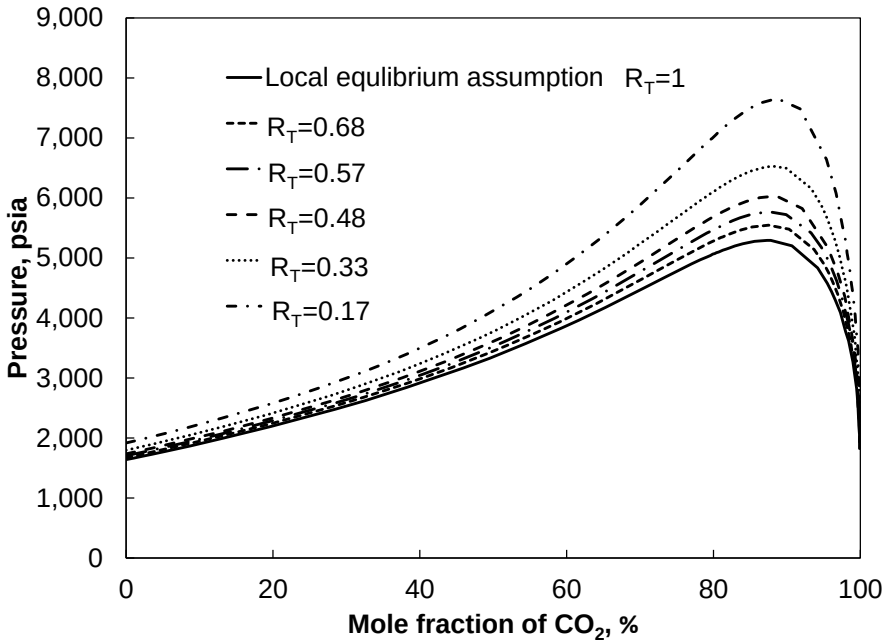

Figure 6.17 P-x diagrams for the cases with different throughput ratios at pressure of 3263.36 psia for 12-component EOS characterized for the Shengli Oil field. With the decrease of throughput ratios, the P-x envelope deviate from local equilibrium assumption.

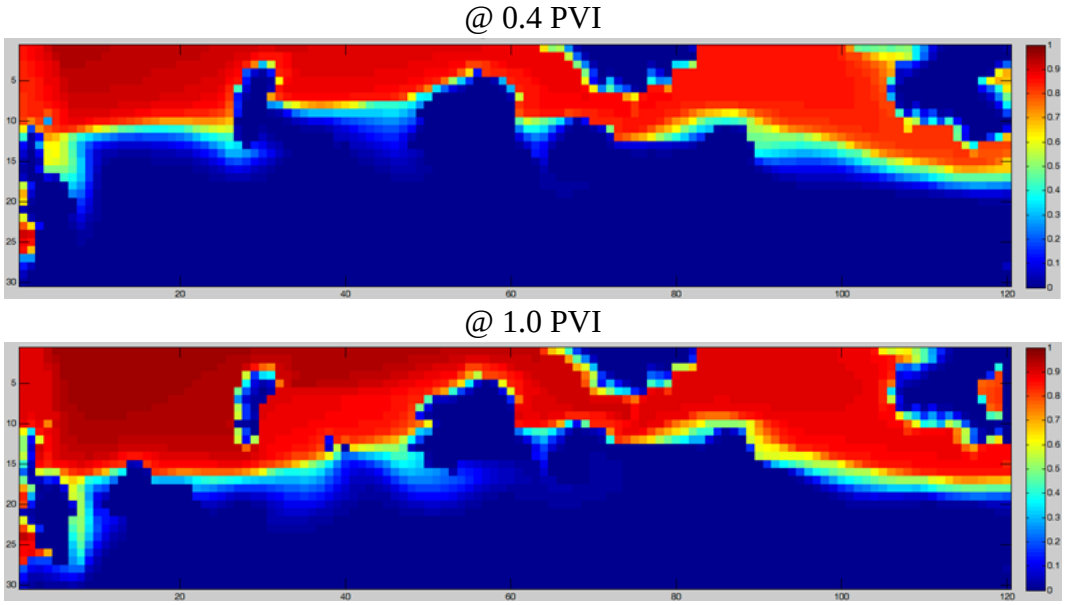

Figure 6.18 CO_2 concentration profile at 0.4 and 1.0 PVI in the X-Z 2-D fine-scale simulation without capillary pressure. CO_2 channelling is severe because of gravity effects.

@ 0.4 PVI

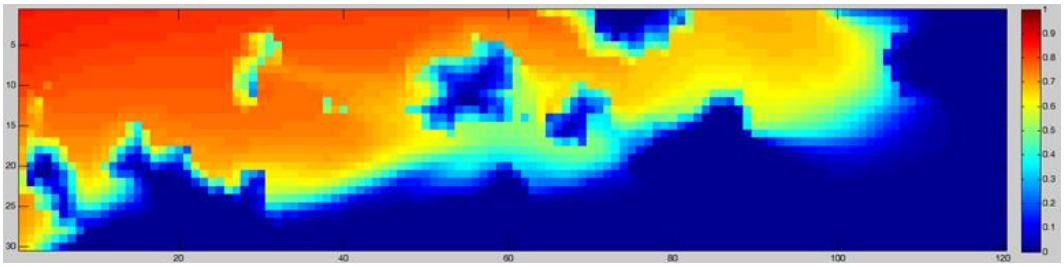

@ 1.0 PVI

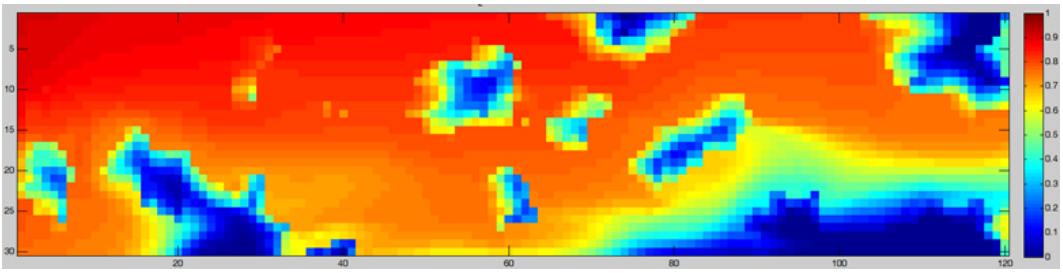

Figure 6.19 CO_2 concentration profile at 0.4 and 1.0 PVI in the X-Z 2-D fine-scale simulation with capillary pressure. The sweep efficiency is much better compared to Figure 6.18 because capillary crossflow enhances the communication between different layers in Z direction.

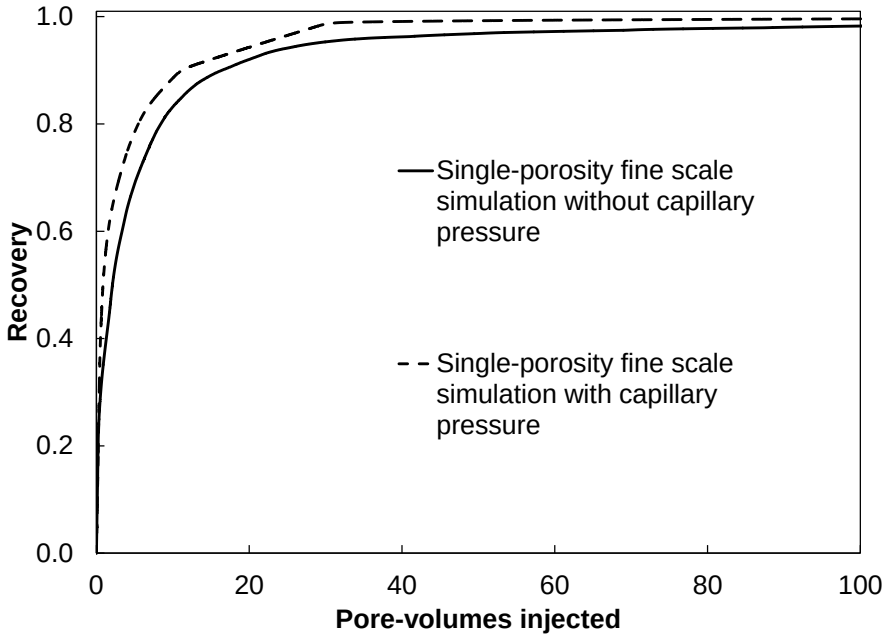

Figure 6.20 Recovery predictions for the X-Z 2-D fine-scale simulation without and with capillary pressure. The recovery efficiency for the case with capillary pressure is better because of the improved sweep efficiency by capillary crossflow.

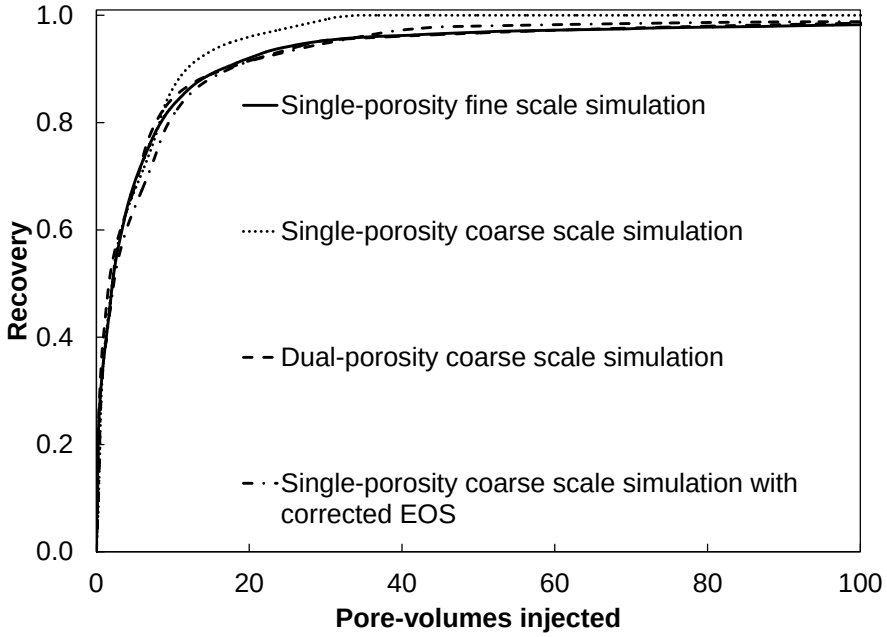

Figure 6.21 Recovery predictions for the X-Z 2-D case without capillary pressure. DPF is successfully applied in the coarse-scale simulation to mimic the recovery prediction in fine-scale simulation. SPF with local equilibrium assumption in conventional composition simulation is not able to reproduce the recovery prediction until the corrected EOS is generated.

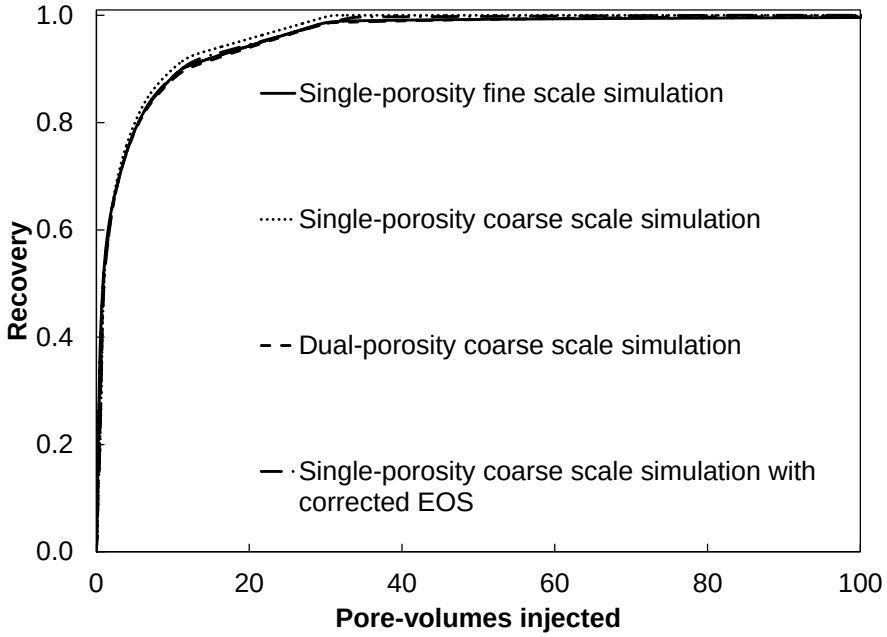

Figure 6.22 Recovery predictions for the X-Z 2-D case with capillary pressure. The recovery prediction is relative good for SPF with local equilibrium assumption because capillary crossflow significantly enhances the recovery of bypassed oil as Figure 6.19 presents.

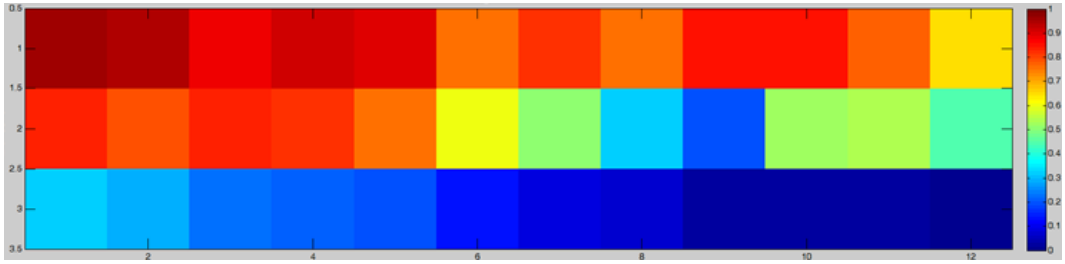

a. The dual-porosity coarse-scale simulation without capillary pressure at 1.0 PVI

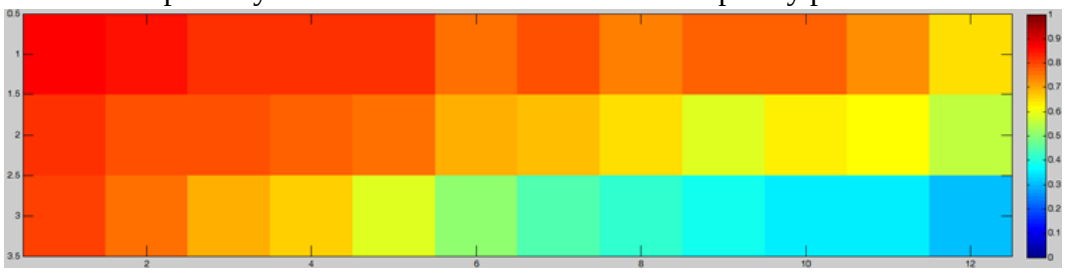

b. The dual-porosity coarse-scale simulation with capillary pressure at 1.0 PVI

Figure 6.23 CO_2 concentration profile for the dual-porosity coarse-scale simulation with and without capillary pressure by use of bypassed fraction distribution.

CHAPTER 7: Conclusions, Limitations and Recommendations for Future Research

7.1 Conclusions

Modelling of capacitance effects at the sub-grid scale is a long existing problem due to the local equilibrium assumption in conventional compositional simulation. This research attempted to deal with this problem by use of a two-step flow-based characterization method. The first step is to quantify the capacitance effects in a dual-porosity flow with three dimensionless groups presented in chapter 3. The contributions for the proposed dual-porosity method are listed as below:

1. The flow characteristics of capacitance effects at the sub-grid scale can be captured by the DPF with the intra-block mass flux in the transverse direction between the flowing fraction and bypassed fraction for each individual grid block. Oil stored in the secondary-pore volume gradually migrates to the the primary-pore volume through the intra-block mass flux. Flow in the presence of capacitance cannot be modelled using conventional SPF models with and without the S_{orm} method.
2. The three dimensionless groups are introduced to quantify the level of capacitance effects in core floods data or fine-scale simulation results with the DPF. The characterization parameters used in this research are the bypassed

fraction, throughput ratio (R_T), and longitudinal Péclet number. The throughput ratio is defined as the ratio of the throughputs required to achieve the ultimate oil recovery without and with intra-block mass flux. R_T of zero corresponds to SPF with the S_{orm} method. The dual-porosity flow is reduced to the traditional SPF with the local equilibrium assumption when R_T is unity. The throughput ratio is a strong function of recovery process time.

3. Capillary crossflow enhances the recovery of bypassed oil significantly as shown in fine-scale simulation. The DPF method is also successfully applied in the coarse-scale simulation case to reproduce the simulation results of the fine-scale capillary dominant case.
4. Distribution of bypassed fractions is confirmed to be useful in improving the concentration prediction because of the additional flexibility introduced.

In chapters 4 and 5, the flow-based fluid characterization method is developed to reproduce the characteristics of capacitance effects in conventional composition simulation. The algorithm is implemented in both core flooding experiment and heterogeneous fine-scale simulation for different reservoir and fluid properties. The conclusions of the fluid characterization method are:

1. The new fluid characterization method is developed to characterize the flow in the presence of capacitance. Oil components are split into two fractions: one

with original components and the other with heavier components. The attraction and covolume parameters are altered for the introduced heavy oil components according to the throughput ratio estimated.

2. The three characterization parameters γ_A, γ_B and z_{Hi} in SPF are well characterized with the throughput ratio in the DPF and exhibit an empirical linear relationship for the cases studied. The extrapolation of the three characterization parameters at R_T of zero applied in the correct EOS can have a reasonable accuracy compared with the S_{orm} option.
3. The volume-shift parameters used retain the volumetric phase behaviour together with the composition phase behaviour considering capacitance effects. The effects on phase behaviour are kept within the fluid model uncertainties by use of the correct tuning strategy proposed in this research.
4. This fluid characterization method is validated in different core flooding experiments with different fluids at partially miscible conditions. Once the corrected EOS is generated for one pressure in partially miscible conditions, it can be successfully applied in different pressures with little loss of accuracy.
5. The method presented in this research requires no change in the governing equations to quantitatively reproduce the flow characteristics in the presence of capacitance.

In chapter 6, the two-step method was tested for a CO_2 gas injection process at partially miscible conditions in the Shengli Oil field. It successfully reproduced the capacitance effects in core floods and vertical X-Z 2-D fine-scale simulations. The effects on phase behaviour was compared with uncertainties in fluid model and confirmed that the change on phase behaviour to model capacitance effects was kept within the uncertainties in EOS fluid model.

The recommended stepwise descriptions for our two-step method in field applications are also proposed as below:

Step 1: Generate a series of the 1-D dual-porosity model with different throughput ratios based on the fluid model characterized for the reservoir oil

Step 2: Reproduce the recovery prediction of the corresponding dual-porosity flow by use of the fluid characterization method for different throughput ratios

Step 3: Obtain the relationship between the tuning parameter (γ_A, γ_B & z_{Hi}) in the fluid characterization method and throughput ratios characterized in the dual-porosity flow

Step 4: Estimate the three dimensionless groups, including the throughput ratio, for the field application based on the given information such as core floods data or fine-scale simulation result

Step 5: Apply the fluid characterization method based on the relationship obtained in step 3.

7.2 Limitations and Recommendations for future work

7.2.1 Limitations for fluid characterization method

Our flow-based fluid characterization method was developed to model the incomplete mixing at the sub-grid scale with the local equilibrium assumption in conventional compositional simulation. The fluids in individual grid blocks are still completely mixed but the corrected EOS controls the component propagation speed to mimic the characteristics of capacitance. The earlier breakthrough and longer tailing modelled by the dual-porosity flow are reproduced by the fluid characterization method in the single-porosity flow by introduction of pseudo heavy component in partially miscible condition.

However, the proposed fluid characterization method is not applicable at pressures above MMP. The main reason is that the evaporation wave and displacement front merge into a single wave so it is not possible to control the wave velocity to mimic the capacitance effect with the corrected EOS in single-porosity flow. We recommend using the dual-porosity flow to model the recovery of bypassed oil for gas floods at pressures above MMP due to the limitation of our fluid characterization method in MCM and FCM condition.

7.2.2 Recommendations for future work

In the first step, we proposed to quantify the capacitance effect by use of three dimensionless groups: bypassed fraction, throughput ratio and longitudinal Péclet number. On the basis of the three dimensionless groups, the corrected EOS is generated by use of the flow-based fluid characterization method to mimic the characteristics of capacitance effect modelled in the dual-porosity flow. In chapter 3 and chapter 6, a 2-D realization of heterogeneous reservoir is used in both X-Y and X-Z direction. Case studies show that the fluid characterization method can be successfully applied in single-porosity coarse-scale simulation to reproduce the recovery prediction of fine-scale simulation including the macroscopic heterogeneities based on the characterized dimensionless groups in the dual-porosity flow. However, we recommend to test whether the same corrected EOS could have reasonable accuracy in recovery prediction for different realizations of heterogeneous reservoir with same fluid model. The corresponding bypassed fraction and throughput ratio characterized for different realizations should be the key dimensionless groups to determine the predictability of the corrected EOS. It is also an interesting topic to investigate whether the same linear function between tuning parameters in fluid characterization method and throughput ratios could be applicable for different fluid models.

Applications of this fluid characterization method in WAG processes are not tested in this research. The fluid EOS model is corrected to model the capacitance effects in the gas injection period. The original density and viscosity are retained for the corrected EOS so the recovery prediction is not affected in the water injection period. As a result, the overall influences of the corrected EOS on recovery predictions still require further investigation.

Mixtures of reservoir oil and CO_2 can exhibit complex phase behaviour, especially at temperatures typically below 120 ℉ where a CO_2-rich liquid (L_2) phase can coexisit with the oleic (L1) phase, or the L1 and gaseous (V) phases. The displacement efficiency involving complex three-phase behaviour is extensively investigated recently. However, capacitance effects including the three-phase behaviour has not been studied. The effects of the three-phase behaviour on the sweep efficiency should be an interesting topic for future work.

SAGD process is widely used in Canada to produce the bitumen in oil sands. The steam chamber keeps increasing with continuous injection. Oil, gas and water phase are coexisting along the chamber edge due to the temperature difference. The effect of non-equilibrium state at the sub-grid scale on SAGD chamber growth prediction is important to be investigated to improve the prediction capability of commercial simulator in SAGD process.

References

Abraham, K.J., Lake, L.W., Steven, B., and James W.J. 2010. Investigation of Mixing in Field-Scale Miscible Displacements Using Particle-Tracking Simulations of Tracer Floods with Flow Reversal. SPE Journal 15(3): 598-609. doi:10.2118/113429-PA.

Al-Wahaibi, Y.M., Muggeridge, A.H., and Grattoni C.A. 2007. Experimental and Numerical Studies of Gas/Oil Multicontact Miscible Displacements in Homogeneous and Crossbedded Porous Media. SPE Journal 12(1):62-76. SPE-92887-PA.

Aronofsky, J.S. and Heller, J.P. 1957. A Diffusion Model to Explain Mixing of Flowing Miscible Fluids in Porous Media. Petroleum Transaction, AIME 210: 345-349. SPE-860-G.

Arya, A., Hewett, T.A., Larson, R.G., and Lake, L.W. 1988. Dispersion and Reservoir Heterogeneity. SPE Reservoir Engineering 3(1): 139-148. SPE-14364-PA.

Bahralolom, I., Bretz, R.E., and Orr Jr., F.M. 1988. Experimental Investigation of the Interaction of Phase Behaviour with Microscopic Heterogeneity in a CO_2 Flood. SPE Reservoir Engineering 3(2): 662-672. SPE-14147-PA.

Ballin, P.R., Clifford P.J., and Christie, M.A. 2002. Cupiagua, Modelling of a Complex Fractured Reservoir Using Compositional Upscaling. SPE Reservoir Evaluation & Engineering 5(6): 488-498. SPE-81409-PA.

Barker, L.E. 1977. Effects of Dispersion and Dead-End Pore Volume in Miscible Flooding. SPE Journal 17(3): 219-227. SPE-5632-PA.

Barker, J.W. and Evans, S.C. 1995. Predictive Model for Viscous Fingering in Compositional WAG Floods. SPE Reservoir Engineering 10(2): 116-122. SPE-27835-PA.

Barker, J. W. and Fayers, F.J. 1994. Transport Coefficients for Compositional Simulation with Coarse Grids in Heterogeneous Media. SPE Advanced Technology Series 2(2): 103-112. SPE-22591-PA.

Bardon, C., Longeron D.G., Baudoin F., Delhomme, A., and Naili, N. 1994. Gas/Oil Relative Permeabilities and Residual Oil Saturations in a Field Case of a Very Light Oil, in the Near-Miscibility Conditions. Paper SPE 28625 presented at the SPE Annual Technical Conference and Exhibition, New Orleans, Louisiana, 25-28 September.

Barker, J.W., Prevost, M., and Pitrat, E. 2005. Simulating Residual Oil Saturation in Miscible Gas Flooding Using Alpha-Factors. Paper SPE 93333 presented at the SPE Reservoir Simulation Symposium, 31 January-2 February, The Woodlands, Texas, USA.

Batycky, J.P., Maini, B.B., and Fisher, D.B. 1982. Simulation of Miscible Displacement in Full-Diameter Carbonate Cores. SPE Journal 22(5): 647-657. SPE-9233-PA.

Blunt M. and Christie M. 1994. Theory of Viscous Fingering in Two Phase, Three Component Flow. SPE Advanced Technology Series 2(2):52-60. SPE-22613-PA.

Bourgeois, M.J., Gommard, D.R., and Gouas, H. 2012. Simulating Early Gas Breakthrough in Undersaturated Oil Using Alpha-Factors. Paper SPE 161460 presented at the Abu Dhabi international Petroleum Exhibition and Conference, Abu Dhabi, UAE, November 11-14.

Bourgeois, M.J., Thibeau, S., and Guo J. 2011. Modelling Residual Oil Saturation in Miscible and Immiscible Gas Floods by Use of Alpha-Factors. Paper SPE 143379 presented at the SPE EUROPEC/EAGE Annual Conference and Exhibition in Vienna, Austria, 23-26 May.

Bretz, R.E. and Orr Jr. F.M. 1987. Interpretation of Miscible Displacements in Laboratory Cores. SPE Reservoir Engineering 2(4): 492-500. SPE-14898-PA.

Brigham, W.E., 1974. Mixing Equations in Short Laboratory Cores. SPE Journal 14(1): 91-99. SPE-4256-PA.

Brock, D.C. and Orr Jr., F.M. 1991. Flow Visualization of Viscous Fingering in Heterogeneous Porous Media. Paper SPE 22614 prepared for SPE Annual Technical Conference and Exhibition held in Dallas, TX, October 6-9.

Brown, J.S., Al-Kobaisi, M.S., and Kazemi,H. 2013. Compositional Phase Trapping in CO2 WAG Simulation. Paper SPE 165983 presented at the SPE Reservoir Characterization and Simulation Conference and Exhibition, Abu Dhabi, UAE, Sep 16 - 18.

Burger, J.E., Bhogeswara, R., and Mohanty K.K. 1994. Effect of Phase Behaviour on Bypassing in Enriched Gasfloods. SPE Reservoir Engineering 9(2): 112-118. SPE-25254-PA.

Burger, J.E. and Mohanty, K.K. 1997. Mass Transfer From Bypassed Zones During Gas Injection. SPE Reservoir Engineering 12(2): 124-130. SPE-30768-PA.

Burger, J.E., Springate, G.S., and Mohanty K.K., 1996. Experiments on Bypassing During Gasfloods in Heterogeneous Porous Media. SPE Reservoir Engineering 11(2): 109-115. SPE-28626-PA.

Campbell, B.T. and Orr, Jr., F.M. 1985. Flow Visualization for CO_2/Crude-Oil Displacements. SPE Journal 25(5): 665-678. SPE-11958-PA.

Christie, M.A. and Clifford, P.J., 1998. Fast Procedure for Upscaling Compositional Simulation. SPE Journal 3(3): 272-278. SPE-50992-PA.

Chatzis, I., Norman, M.R., and Hau, L.T. 1983. Magnitude and Detailed Structure of Residual Oil Saturation. SPE Journal 23(2):311-326. SPE-10681-PA.

Cinar, Y., Jessen, K., Berenblyum, R., Juanes, R., and Orr. Jr., F.M. 2006. An Experimental and Numerical Investigation of Crossflow Effects in Two-Phase Displacements. *SPE Journal* **11**(2): 216-226. SPE-90568-PA.

Coats, K.H. and Smith, B.D. 1964. Dead-End Pore Volume and Dispersion in Porous Media. SPE Journal 4(1): 73-84. SPE- 647-PA.

Coats, K.H., Thomas, L.K., and Pierson, R.G. 2007. Simulation of Miscible Flow Including Bypassed Oil and Dispersion Control. SPE Reservoir Evaluation & Engineering 10(5): 500-507. SPE-90898-PA.

Constantinou, L. and Gani, R., 1994. New Group Contribution Method for the Estimating Properties of Pure Compounds. AIChE J. 40, 1697-1710.

Dai, K.K. and Orr, Jr., F.M. 1987. Prediction of CO_2 Flood Performance: Interaction of Phase Behaviour with Microscopic Pore Structure Heterogeneity. SPE Reservoir Engineering 2(4): 531-542. SPE-13115-PA.

Daridon J.L., Xans P., and Montel F. 1996. Phase boundary measurement on a methane+decane+multi-paraffins system. Fluid phase equilibria 117(1):241-248.

Deans, H.A. 1963. A Mathematical Model for Dispersion in the Direction of Flow in Porous Media. SPE Journal 3(1): 49-52. SPE-493-PA.

Dindoruk, B. 1992. Analytical Theory of Multiphase, Multicomponent Displacement in Porous Media. PhD dissertation, Stanford University, Stanford, CA.

Eclipse 300 Users' Manual. 2011. Schlumberger

Fayers, F.J., Barker, J.W., and Newley, T.M.J. 1992. Effects of Heterogeneities on Phase Behaviour in Enhanced Oil Recovery. The Mathematics of Oil Recovery edited by P.R. King. Oxford University Press, NY.

Fayers, F.J., Blunt, M.J., and Christie, M.A. 1992. Comparisons of Empirical Viscous-Fingering Models and Their Calibration for Heterogeneous Problems. SPE Reservoir Engineering 7(2): 195-203. SPE-22184-PA.

Gao, W., Robinson Jr. R.L., and Gasem K.A.M. 2001. Fluid Phase Equilibrium 179: 207-216.

Gardner, J.W. and Ypma, J.G.J. 1984. An Investigation of Phase-Behaviour/Macroscopic- Bypassing Interaction in CO_2 Flooding. SPE Journal 24(5): 508-520. SPE-10686-PA.

Garmeh, G., Johns, R.T., and Lake, L.W. 2009. Pore-Scale Simulation of Dispersion in Porous Media. SPE Journal 14(4): 559-567. SPE-110228-PA.

Hill, R. 1963. Elastic properties of reinforced solids: Some theoretical principles. Journal of the Mechanics and Physics of Solids 11(5):357-372.

Hiraiwa, T. and Suzuki, K. 2007. New Method of Incorporating Immobile and Nonvaporizing Residual Oil Saturation into Compositional Reservoir

Simulation of Gasflooding. SPE Reservoir Evaluation & Engineering 10(1): 60-65. SPE-88719-PA

Iizuka, R., Al-Shehhi, H.R., and Al-Hammadi H.M. Derivation of Immobile and Non-vaporizing Residual Oil Saturation Under Miscible Flood from CO_2 Coreflood Experiments. Paper SPE 161568 Abu Dhabi International Petroleum Conference and Exhibition, Abu Dhabi, UAE 11-14 November 2012.

Jasti, J.K., Vaidya, R.N., and Fogler, H 1988. Capacitance Effects in Porous Media. SPE Reservoir Engineering 3(4): 1207-1214. SPE-16707-PA.

Jhaveri, B.S. and Youngren, G.K. 1988. Three-parameter modification of the Peng-Robinson equation of state to improve volumetric predictions. SPE Reservoir Engineering 3(3):1033–1040. SPE-13118-PA

Joergensen, M. and Stenby, E.H. 1995. Optimization of Pseudocomponents Selection for Compositional Studies of Reservoir Fluids. Paper SPE 30789 presented at Annual Technical Conference and Exhibition, Dallas, Texas, Oct. 22−25.

Johns, R.T. 1992. Analytical Theory of Multicomponent Gas Drives with Two-Phase Mass Transfer. PhD dissertation, Stanford University, Stanford, CA.

Khosravi M., Alireza B., Emadi M., Rostami B., and Roayaie E. 2014. Mechanistic investigation of bypassed-oil recovery during CO_2 injection in matrix and fracture. Fuel 117: 43-49.

Kim, J.S. 1993. Tracking Injected Components in Fully Compositional Reservoir Simulations. Paper SPE 26638 presented at the SPE Annual Technical Conference and Exhibition, Houston, Texas, 3-6 October.

Koval, E.J. 1963. A Method for Predicting the Performance of Unstable Miscible Displacement in Heterogeneous Media. SPE Journal 3(2): 145-154. SPE-450-PA.

Kumar, A. and Okuno, R. 2012. Critical Parameters Optimized for Accurate Phase Behaviour Modelling for Heavy n-Alkanes up to C_{100} using the Peng-Robinson Equation of State, Fluid Phase Equilibria 335: 46-59.

Kumar, A. and Okuno, R. 2013. Characterization of Reservoir Fluids using an EOS based on Perturbation from n-Alkanes. Fluid Phase Equilibria 358: 250-271.

Kumar, A. and Okuno, R. 2014a. Reservoir Oil Characterization for Compositional Simulation of Solvent Injection Processes. Industrial & Engineering Chemistry research 53(1): 440-455.

Kumar, A. and Okuno, R. 2014b. Direct Characterization of the Peng-Robinson EOS Attraction and Covolume Parameters for Reservoir Fluids (Processing).

Lange E.A. 1998. Correlation and Prediction of Residual Oil Saturation for Gas Injection EOR Processes. SPE Reservoir Evaluation & Engineering 1(2): 127-133. SPE-35425-PA

Lake L.W. 1989. Enhanced Oil Recovery. Department of Petroleum and Geosystems Engineering at the University of Texas at Austin.

Lake, L.W. and Hirasaki, G.J. 1981. Taylor's Dispersion in Stratified Porous Media. SPE Journal 21(4): 459-468. SPE-8436-PA.

Lohrenz, J., Bray, B.C., and Clark, C.R. 1964. Calculating Viscosities of Reservoir Fluids from Their Compositions. Journal of Petroleum Technology 16(10): 1171-1176.

McGuire, P.L., Spence, A.P., Stalkup, F.I., and Cooley, M.W. 1995. Core Acquisition and Analysis for Optimization of the Prudhoe Bay Miscible-Gas Project. SPE reservoir engineering 10(2): 94-100. SPE-27759-PA.

Mohanty, K.K. and Johnson S.W. 1993. Interpretation of Laboratory Gasfloods with Multidimensional Compositional Modelling. SPE Reservoir Engineering 8(1):59-66. SPE-21204-PA.

Nghiem, L.X. and Sammon, P.H 1997. A Non-Equilibrium Equation-of-State Compositional Simulator. Paper SPE 37980 presented at the SPE Reservoir Simulation Symposium, 8-11 June 1997, Dallas, Texas, USA.

Nguyen, Q.P., Rossen, W.R., and Zitha P.L.J. and P.K.Currie 2009. Determination of Gas Trapping With Foam Using X-Ray Computed Tomography and Effluent Analysis. SPE Journal 14(2):222-236. SPE-94764-PA.

Okuno, R. 2009. Modelling of Multiphase Behaviour for Gas Flooding Simulation. PhD dissertation, University of Texas at Austin, Austin, Texas.

Orr, Jr., F.M. 2007. Theory of Gas Injection Processes. Tie-Line Publications, Holte, Denmark.

Orr, Jr., F.M. and Taber, J.J. 1984. Displacement of Oil by Carbon Dioxide. Contract No. AS19-80BC10331, U.S. DOE, Washington, D.C.

Pande, K.K. 1992. Effects of Gravity and Viscous Crossflow on Hydrocarbon Miscible Flood Performance in Heterogeneous Reservoirs. Paper SPE 24935 prepared for SPE Annual Technical Conference and Exhibition held in Washington, D.C. October 4-7.

Pande, K.K. and Orr, Jr., F.M. 1994a. Effect of Viscous Crossflow on Miscibility Development in a Two-Layer Flow System: Part I - Ternary Vaporizing Gas Drives. SPE Advanced Technology Series 2(2): 7-16. SPE-19668-PA.

Pande, K.K. and Orr, Jr., F.M. 1994b. Effect of Viscous Crossflow on Miscibility Development in a Two-Layer Flow System: Part II - Ternary Condensing Gas Drives. SPE Advanced Technology Series 2(2): 17-25. SPE-22635-PA.

Pedersen K.S. and Christensen P.L. 2010. Phase behaviour of peterogleum reservoir fluids. Denmark.

Peng, D.-Y. and Robinson, D.B. 1976. A New Two-Constant Equation of State, Industrial & Engineering Chemistry Fundamentals, 15(1): 59-64.

PVTsim, 20.0, 2011. Calsep A/S, Lyngby, Denmark.

Peneloux, A., Rauzy, E., and Fréze, R. 1982. A consistent correction for Redlich-Kwong-Soave volumes. Fluid Phase Equilibria 8(1): 7–23.

Ren, Bo., Xu,.Yang., Niu, baolun., Ren, Shaoran., Li, Xiangliang., Li, Pingguo., and Song, Xinwang. 2011. Laboratory Assessment and Field Pilot of Near Miscible CO_2 Injection for IOR and Storage in a Tight Oil Reservoir of ShengLi Oilfield China. Paper SPE 144108 presented at the SPE Enhanced Oil Recovery Conference, Kuala Lumpur, Malaysia, 19-21 July.

Salehi, A., Voskov D.V., and Tchelepi H.A. 2013. Thermodynamically Consistent Transport Coefficients for Upscaling of Compositional Processes. Society of Petroleum Engineers, 2013. doi:10.2118/163576-MS.

Salter, S.J. and Mohanty, K.K. 1982. Multiphase Flow in Porous Media: I. Macroscopic Observations and Modelling. Paper SPE 11017 presented at the SPE Annual Technical Conference and Exhibition, New Orleans, Louisiana, September 26-29.

Shelton, J.L. and Schneider F.N. 1975. The Effects of Water Injection on Miscible Flooding Methods Using Hydrocarbons and Carbon Dioxide. SPE Journal 15(3): 217-226. doi:10.2118/4580-PA.

Smith, D.H. and Jikich, S.A. 1994. Characterization of Trapped Gas Saturation and Heterogeneity in Core Samples Using Miscible-Displacement Experiments. Paper SPE 29161 presented at the SPE Eastern Regional Conference & Exhibition held in Charleston, WV, U.S.A., 8-10 November 1994.

Spence Jr., Andrew, P., and Watkins R.W. 1980. The Effect of Microscopic Core Heterogeneity On Miscible Flood Residual Oil Saturation. Paper SPE 9229 prepared for SPE Annual Technical Conference and Exhibition held in Dallas, TX, September 21-24.

Spence, A.P. and Watkins, R.W. 1980. The Effect of Microscopic Core Heterogeneity on Miscible Flood Residual Oil Saturation. Paper SPE 9229 presented at the SPE Annual Technical Conference and Exhibition, Dallas, September 21-24.

Stalkup F.I. 1970. Displacement of Oil by Solvent at High Water Saturation. SPE Journal 10(4): 337-348. SPE-2419-PA.

Stern D. 1991. Mechanisms of Miscible Oil Recovery: Effects of Pore-Level Fluid Distribution. Paper SPE 22652 prepared for 66th Annual Technical

Conference and Exhibition of the Society of Petroleum Engineers held in Dallas, TX, October 6-9.

Todd, M.R. and Longstaff, W.J. 1972. The Development, Testing, and Application of a Numerical Simulator for Predicting Miscible Flood Performance. Journal of Petroleum Technology 24(7). SPE-3484-PA.

Wylie, P. and Mohanty, K.K. 1997. Effect of Water Saturation on Oil Recovery by Near-Miscible Gas Injection. SPE Reservoir Evaluation & Engineering 12(4). SPE-36718-PA.

Wylie, P. and Mohanty, K.K. 1999. Effect of Wettability on Oil Recovery by Near-Miscible Gas Injection. SPE Reservoir Evaluation & Engineering 2(6). SPE-59476-PA.

Wilke, C.R. 1950. Diffusional Properties of Multicomponent Gases. Chemical Engineering Progress: 95-105.

Young, L.C. 1990. Use of Dispersion Relationships To Model Adverse-Mobility-Ratio Miscible Displacements. SPE Reservoir Engineering 5(3): 309-316. SPE-14899-PA.

Zhang, B. and Okuno, R. 2013. A New Method for Modelling Bypassed Oil Recovery in EOS Compositional Simulation. Paper SPE 166371 presented at the SPE Annual Technical Conference and Exhibition, New Orleans, Louisiana. USA, Sep 30-Oct 2.

Zhou, D., Fayers, F.J., and Orr Jr., F.M. 1997. Scaling of Multiphase Flow in Simple Heterogeneous Porous Media. *SPE Reservoir Engineering* **12**(3): 173-178. SPE-27833-PA.